The effect of a nonlinear Power Take Off on a Wave Energy Converter

Helen Bailey

Submitted in satisfaction of the requirements
for the degree of *Doctor of Philosophy* in

THE UNIVERSITY OF EDINBURGH

2009

Timothy Garn,

1982 – 2010

This thesis is dedicated to the memory of Tim.

He was a constant source of support and inspiration during my PhD.
Missed so much, everyday.

Abstract

This thesis is titled *The influence of a nonlinear Power Take Off on a Wave Energy Converter*. It looks at the effect that having a nonlinear Power Take Off (PTO) has on an inertial referenced, slack moored, point absorber, Wave Energy Converter (WEC). The generic device studied utilizes relative heave motion between an axi-symmetric cylinder and an internal mass, for the PTO to operate between.

The PTO is the part of the WEC that transforms the relative motion into electricity. In this work, three different types of nonlinear PTO and a linear PTO are presented, tested, analysed and compared. The three nonlinear PTO types are:

- A PTO that extracts energy in only one direction, either in relative compression or expansion.
- A linear PTO and an additional endstop or peripheral PTO, that can only extract energy when the relative position of the internal mass has reached a pre-determined position.
- A PTO that has damping forces that are quadratically proportional to the relative velocity.

A numerical simulation has been built based upon a Runge-Kutta time series progression. The model uses the summation of the excitation force from the waves, the radiation force from the movement of the cylinder, the buoyancy force and the PTO forces. These combine to cause acceleration of the mass of the external cylinder, with an equal and opposite PTO force acting on the internal mass. The excitation force and added mass values are obtained from the boundary element method software, WAMIT. Prony's method is used to obtain an approximate radiation force, based upon the radiation time force history. This numerical model operates on both a 1:40 scale and a full sized model.

The numerical model finds the optimal PTO parameters, for different PTO setups, in irregular sea states. This optimum is based on the power extracted as well as indications of the reliability and lifetime of the system. The numerical simulation presents results showing how the non-linearity of the PTO influences the motions of the WEC, resulting in dissimilarities between the Response Amplitude Operator (RAO) results, obtained from regular seas, and the Linear Transfer Function (LTF), found from irregular sea testing.

The experimental model has been tested in the Curved Wave Tank facility at the University of Edinburgh, with a 1:40 scaled model. It used a central rod both as a support structure and to limit the movement of the cylinder and internal mass to heave. Between the cylinder and internal mass a spring and pneumatic damper operate in parallel, in various setups. It was tested in regular and irregular sea states and the position of the internal mass and cylinder was monitored. The experimental model was tested to ascertain the time series motions, RAO, LTF, the relative phase between the bodies and the power extracted for different wave climates.

The numerical and experimental work were compared to allow confidence in both models. They showed relatively good agreement for the RAOs, LTFs and predictions of the relative phase but there was discrepancies in the predicted power for both regular and irregular seas. This difference is due to the difficulties in obtaining the relative velocities in the experimental model, resulting in a significant error in power prediction, since the power is proportional to the square of the relative velocities.

The conclusions show that having a mono-directional PTO as opposed to a bi-directional PTO results in an approximately equal or greater power extraction in a variety of different sea states. An additional endstop or peripheral damper can increase the total power that a WEC extracts, in some situations, and may be advantageous depending upon the other potential benefits it brings to the WEC.

Acknowledgements

A great many people have enabled me to complete this thesis, and I thank them for all their help over the past three years.

Work-related acknowledgments

I would like to first, thank my supervisor Ian Bryden for his advice, assistance and support throughout this project.

For interesting technical discussions: I would like to thank Ben Child for spotting my mistakes, Ally Price for questioning everything, and Henry Jeffery for having a fresh perspective. For general advice and support I'd also like to thank David Forehand and Scott Couch.

For teaching and assisting me with using the Curved Wave Tank and ideas in the design of my physical model. For suggestions, advice and lots of patience, I would like to thank Gregory Payne, Remy Pascal, Jorge Lucas and especially Jamie Taylor.

Thanks to INORE (International Network in Offshore Renewable Energy) I have developed international friendships and a wide range of people that I have had the pleasure of asking for advice. I would especially like to thank Miguel Lopes, from IST, for discussions on experimental testing. Griet De Baker, from Gent University, for assistance with the Prony's method and other numerical modelling discussions. Marco Alves, from the Wave Energy Center, for assistance and information. Jorgen Hals,for suggesting new ideas and Nicolai Lovdal for inspiring me, both from NTNU.

For building and helping in the design of the physical model, and for fixing things that I break, I'd like to thank Neil Wood and Laird Parker.

Personal acknowledgments

I would like to thank my friends for helping make my life fun. For coming out climbing, kayaking, mountaineering and biking and generally getting cold, wet, muddy and exhausted. Enabling me to regularly forget all about the "day job".

And finally, and most importantly, I'd like to thank Timothy Garn. Without his encouragement and support, his ability to make me laugh, his stern looks when I'd been procrastinating all day, I don't know how I would have managed to write a thesis. I would especially like to thank him for his proof reading skills and his obsession with the difference between "effect" and "affect" and between "where" and "were". Any remaining errors with respect to this are entirely my own fault.

Declaration

I declare that this thesis was composed by myself, that the work contained herein is my own except where explicitly stated otherwise in the text, and that this work has not been submitted for any other degree or professional qualification except as specified.Those parts of this work which have been published, or submitted for publication, are as follows:

“The influence of a mono-directional PTO on a self-contained inertial WEC”
H. Bailey & I.G. Bryden
8th European Wave and Tidal Energy Conference (EWTEC 2009)
Uppsala, September 2009

“Experimental testing on the effect of nonlinear Power Take Off on the motions of Wave Energy Converters"
H. Bailey & I.G Bryden
2nd International Conference on Ocean Energy (ICOE 2008), Brest, France.

“Nonlinear modelling of Power Take Off"
H. Bailey & I.G Bryden
Oceans 2007 Conference, Aberdeen, UK.

Helen Bailey

Contents

List of Figures

List of Tables

Chapter 1

Introduction

1.1 Summary

The ability to extract useful energy from ocean waves is exciting. The concept of wave energy conversion describes the process of absorbing and utilizing the energy of waves by the addition of a Wave Energy Converter (WEC) to the marine environment. In this thesis, numerical simulations and experimental wave tank testing is used on a generic WEC. The effects that different nonlinear Power Take Offs (PTOs) have on the motions and resulting power extracted are investigated.

This chapter introduces the concepts and background information for this thesis. In Section 1.2 the reasons why wave energy has the potential to provide a significant contribution to the total energy production of many countries is presented. In Section 1.3 a brief history of wave energy is presented and the different types of WEC, with examples, are discussed. The PTO, the part of the WEC that produces electricity from the WEC's relative motion, is discussed and the three main types of PTO are presented in Section 1.4. Section 1.5 presents the wave resource and introduces both regular and irregular waves. Section 1.6 presents linear wave theory and the associated limitations and assumptions. The numerical modelling principles are presented in Section 1.7, which are used as the basis for the numerical simulation that is developed in this thesis. The type of generic device that is being investigated in this thesis and the advantages and disadvantages of different components of this concept, is presented in Section 1.8. In Section 1.9, an outline of the thesis is presented.

1.2 Why wave energy?

The reasons why energy should be extracted from ocean waves are numerous. It is needed as one of the mix of low carbon technologies to help reduce the effects of climate change and as a source of energy which will not "run out". It is an emerging new industry, with potential for commercial gains and employment.

The potential amount of energy that can be extracted from the waves is large. Estimates vary

significantly with Panicker (1976) suggesting that an order of 1 TW of power is hitting coastlines worldwide.

The successful development and deployment of commercial WECs would result in an emerging new industry, with the potential for new jobs and GDP for the countries that host this new industry. In Scotland, there is the potential to extract 20 GW from marine renewable energy. The Scottish government aims to have 1 GW of power being extracted by 2020. This would result in 2600 direct jobs in Scotland and 12500 gross jobs (FREDS Marine Energy Group, 2009).

Fossil fuels are a finite resource and they will require increasing amounts of energy to extract as the "easily" accessible resource fields are used up. They will eventually run out – the estimates as to when fluctuate and are varied and disputed. They all emit carbon dioxide among other unwanted gases into the atmosphere.

Nuclear fission power is a potential alternative means of energy production but the costs may become prohibitive, and the issues associated with waste disposal, safety of the reactors and public perception are substantial. All but one of the current UK nuclear power stations are due to be decommissioned by 2025 (Department of Energy and Climate Change, 2009). Nuclear fusion as a commercially viable energy source, is still considered to be a long way off.

It has been declared by the Intergovernmental Panel on Climate Change (IPCC) that there is

> "very high confidence that the global average net effect of human activities since 1750 has been one of warming" (Solomon, 2007)

The effects of climate change would adversely affect some of the world's poorest people. The electricity produced from wave energy would have a lower amount of released carbon associated with it compared to traditional fossil fuels. However, carbon would still be released in the manufacture, installation, maintenance and decommission of WECs (Parker *et al.*, 2007).

Wave energy complements other renewable energy sources, such as wind and solar. The energy in waves is greatest at latitudes of around 40 – 50 degrees (Falnes, 2007). Therefore, in countries where there is a significant wave resource, the potential energy from solar tends to be less. Since the waves are formed from the wind, but travel at different speeds, then the wind and waves are often present at different times, which can help provide a more continuous electricity supply from a combination of these energy resources.

1.2.1 Why not wave energy?

There are still significant challenges involved with wave energy.

To be able to get WECs that are reliable and can survive the harsh marine environment is a substantial issue; to do this whilst keeping costs low is incredibly difficult. The cost per kWhr needs to be competitive (with or without a government–run artificial pricing model) compared to other traditional and renewable energies. If artificial pricing structures are used, then this has the potential to increase households energy bill, leading to a greater number of people in fuel poverty.

The survivability of WECs is one of the major challenges facing the industry. A number of devices have failed, often resulting in sinking, in the past. The reasons for this have varied, from small component failures, flaws in the installation process, to mooring failures.

The intermittent electricity supply from WECs is undesirable. Although waves can be forecast within certain levels of accuracy a few days in advance, it is unpredictable on an hour-by-hour and especially on a wave-by-wave time scale. The electricity grid network needs to be able to cope with this irregular and sporadic supply, in addition to other potentially varying renewable energy sources, and be able to “keep the lights on”. The electricity grid also needs to be able to cope with periods when there is little energy extracted from the waves. A secondary associated problem is the need to have a high voltage cable able to take large quantities of energy, from the often sparsely populated nearby areas where WECs are installed to the population centers of the country.

Other challenges facing this industry are of a social and political nature. Negotiating with local communities and the fishing industry, especially with regard to spatial planning of the ocean, is required. The completion of environmental assessments of WECs and the local governments willingness for renewable energy is necessary in order to obtain consents to build a WEC or a farm of WECs.

1.3 The history and development of wave energy

The history and development of wave energy has been influenced by many factors, such as material development, computational power, general mechanical knowledge and the skills, ideas and inspiration of a few key people. Political will has been a significant factor (both positively and negatively), from the interest in renewable energy during the oil crises of the 1970s, to the lack of interest after the price of crude oil stabilised (Ross, 1979), to the renewed current interest with the desire for energy security, the variable oil prices and the desire for low carbon energy.

There are a large number of WECs in various stages of development, from concept, tank tested

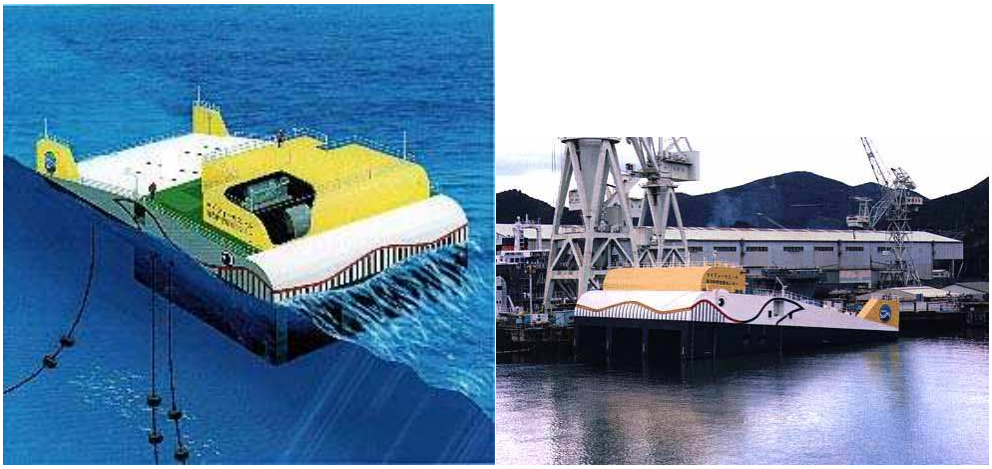

(a) Concept. **(b)** Prototype.

Figure 1.1: The Mighty Whale, (from http://www.jamstec.go.jp).

models, sea trials to full scale devices. A few of what the author considers to be significant WECs with regard to the focus of this thesis, will be discussed.

1.3.1 Early devices

Mighty Whale

The concept of extracting energy from the waves was considered by Yoshio Masuda, in Japan, in the late 1940s, (Falnes, 2007). The research group in Japan continued to work on various devices especially Oscillating Water Columns (OWCs), and their most famous concept is the "Mighty Whale", a floating OWC developed in the 1990s, prototypes of which have been deployed. A concept picture and prototype photo is presented in Figure 1.1.

Salter's Duck

Stephen Salter at the University of Edinburgh originated the concept of "Salter's Duck", photographed in Figure 1.2. Initially a single body that "nodded" in the waves with a PTO from hydraulics, but different PTOs have been considered such as a gyroscopic system. There have been many concepts based around this idea, from a spine of Salter's Ducks, to a desalination unit (Lucas *et al.*, 2008).

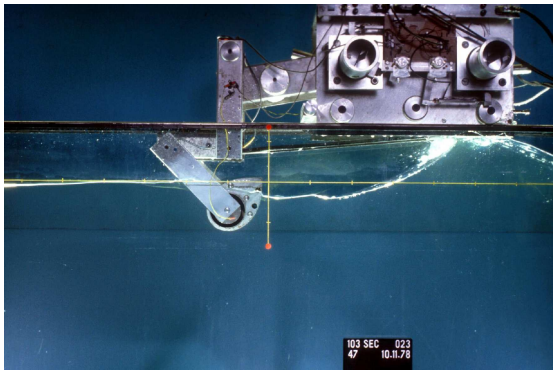

Figure 1.2: Salter's duck in the narrow test tank, photo by Jamie Taylor.

1.3.2 Long devices

Long devices are WECs that operate perpendicular [1] to the main wave front direction, their length is significant with respect to the wave length. Often called *Attenuators*, they experience different parts of the wave cycle at the same time. They have the potential to extract considerable amounts of energy.

Pelamis

Pelamis is developed by Pelamis Wave Power and consist of a number of axi-symmetric cylinders with a horizontal axis of symmetry. Different modules react against each other by moving at different times relative to an incoming wave. They move in both heave and pitch, driving hydraulic motors which in turn drive a conventional generator (Henderson, 2006). A photo of a full scale prototype is presented in Figure 1.3.

1. They can also operate parallel to the wave front. These type of device are often called *Terminators* and are not considered in this thesis.

Figure 1.3: A photo of the Pelamis device - a full scale prototype (from http://www.pelamiswave.com/).

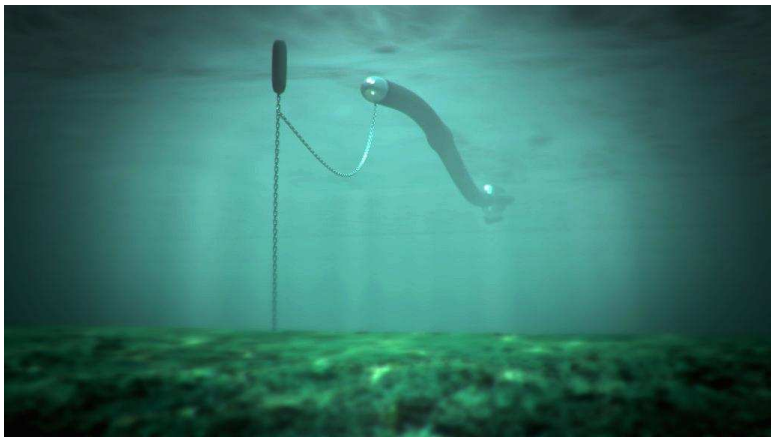

Figure 1.4: The anaconda WEC (from http://www.checkmateuk.com/seaenergy/).

Anaconda

Anaconda comprises a distensible rubber tube that is pressurised as the wave passes, resulting in a *bulge wave* passing through the tube. This pressurised fluid within the tube is used by the PTO system to obtain electricity (Checkmate, 2009). An artist's impression of the Anaconda WEC is presented in Figure 1.4.

1.3.3 Point absorbers attached to the seabed

A point absorber is a WEC where the dimensions of the the device are small compared to the wavelength. Having a point absorber directly attached to the seabed means that the reaction force that is required for the PTO is easily obtained from the ocean floor. Various devices fit into this category, examples of which are given.

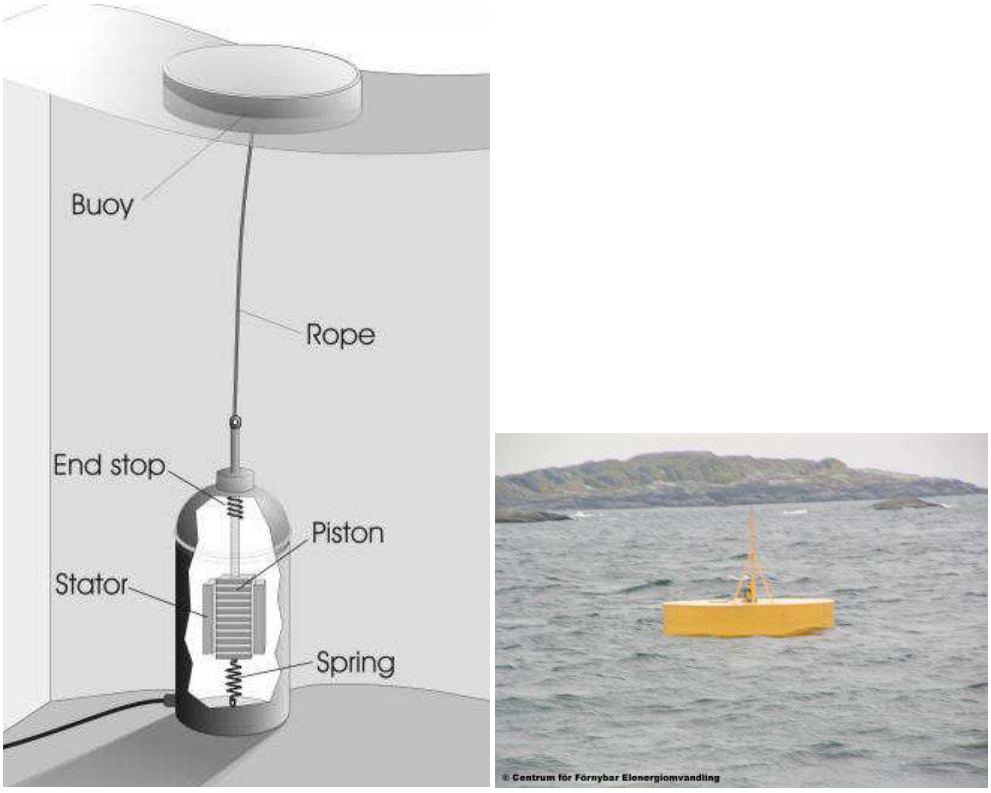

Figure 1.5: The Seabased's WEC (from http://www.el.angstrom.uu.se/).

Seabased AB

The Lysekil wave project was developed by Upsalla University (Tyrberg *et al.*, 2008), and is being commercialised by Seabased AB (Seabased AB, 2008). The Lysekil / Upsalla University project has a number of buoys attached to tethers that are connected to the sea bed, where a seabed mounted direct drive system harnesses the energy from the waves. A schematic diagram and photo of a device at the Lysekil test site are presented in Figure 1.5.

Archimedes Waveswing

The Archimedes Waveswing is developed by AWS Ocean energy (AWS Ocean energy Ltd., 2008). The waveswing is attached to the seabed. It has a floater that moves with the incoming waves and a hydraulic PTO system is used to extract the energy. An artists impression of a farm of these devices is presented in Figure 1.6.

Figure 1.6: AWS, (from http://www.awsocean.com).

1.3.4 Inertial point absorbers

This thesis will focus on this type of generic WEC. They are related to the point absorbers that are attached to the seabed (Section 1.3.3), except that the reaction force occurs within the device. The reaction force for long devices (Section 1.3.2) also occurs from within the device, however these devices are larger and therefore experience different parts of the wave cycle at the same time.

IPS (sloped) buoy

The initial concept of the IPS buoy, named after its Swedish proposer, Inter Project Services, is a submerged cylinder, that floats vertically and its lower end is open to the water. Within the cylinder is a piston that acts with the mass of water, to react against the overall motion of the buoy and generates electricity by a hydraulic system. This was further developed by Salter in 1995, to move at a 45 degree angle, hence the name *IPS sloped buoy*, to increase the resonance response of the system over a wider range of frequencies, and to respond to both heave and surge waves (Lin, 1999). The wave tank tested model of the IPS sloped buoy is presented in Figure 1.7.

AquaBuOY

Finavera Renewables have designed a WEC, based on the concept of the IPS buoy, and have had a prototype in the ocean, called the *AquaBuOY* (Finavera Renewables, 2009). It uses a long hose-pump which extends well below the water surface and reacts against the main body of the device. It pressurises water, as its volume changes with the hose stretching and contracting

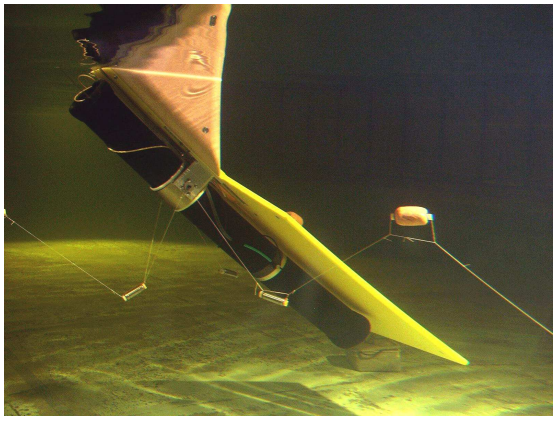

Figure 1.7: Photo of a tank test model of a sloped IPS buoy, (from http://www.mech.ed.ac.uk).

Figure 1.8: Finerva's AquaBuoy, (from Finavera Renewables (2009)).

during the wave cycle (Weinstein *et al.*, 2007). The pressurised water is used to drive a turbine. The prototype is presented in Figure 1.8.

PS - Frog

The University of Lancaster have been working on the concept of the PS-Frog. Initially conceived by the group led by Michael French, the Frog stands for French's Reactionless Oceanic Generator. This WEC is based on an internal inertial mass moving in heave, which is reacting against the outer body of the device (French and Bracewell, 1985). It was later extended to work in Pitch and Surge and hence became the PS-Frog. An artists impression of the PS-Frog is presented in Figure 1.9.

OE buoy

The OE buoy, being developed by OceanEnergy, is a floating OWC (Lewis, 2003) where the oscillating water and hence air column is reacting against the body of the device. It is designed for survivability with "only a single moving part" . It has been tested at a 1:50 scale in a wave tank, and a 1:4 scale in a sheltered ocean site, a photo of the device is presented in Figure 1.10. Currently a 3/4 scale model is in development (OceanEnergy, 2009).

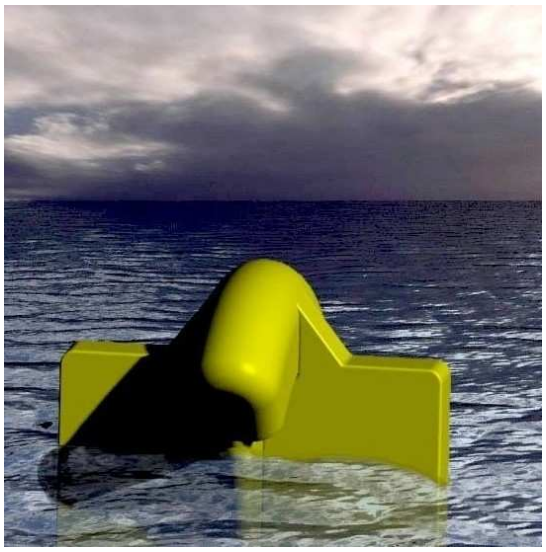

Figure 1.9: Artisitic impression of the PS-Frog, (from http://www.engineering.lancs.ac.uk/lureg).

Figure 1.10: The OE Buoy, (from OceanEnergy (2009)).

Figure 1.11: ECN's SEAREV, (from http://www.icoe2008.com).

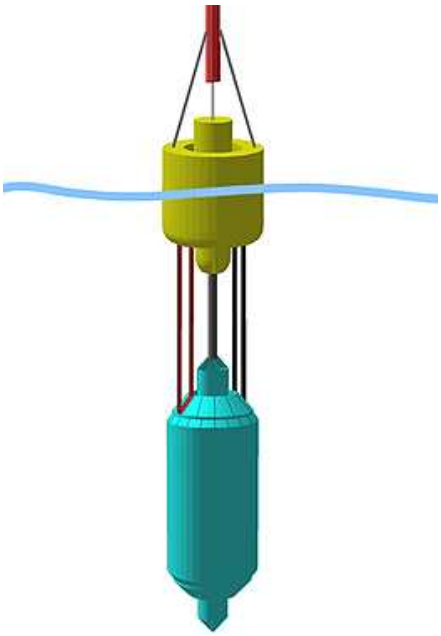

(a) Schematic.

(b) Photo.

Figure 1.12: Wavebob (from http://www.wavebob.com).

SEAREV

SEAREV is a concept developed at l'Ecole Centrale de Nantes. It is a self-contained device, designed to move in pitch but movement in other directions is not constrained. It has a rotating internal horizontal axis disc that reacts against the main body, with a hydraulic PTO between them (Babarit *et al.*, 2006). A photo of a scaled model is presented in Figure 1.11.

Wavebob

Wavebob, developed by Wavebob Ltd. comprises two bodies. A surface piercing body and a submerged body, which primarily operate in heave to extract energy. It has an axi-symmetric shape and the moorings are slack (Wavebob Ltd., 2009). A photo and schematic view of Wavebob, are presented in Figure 1.12.

Korde's concept

Korde (1999) concept involved using a body that moves in heave. The body reacts against an internal mass which attempts to remain stationary with respect to the seabed. The internal mass is kept stationary due to a combination of additional undamped smaller masses that are controlled. Korde completed frequency domain analysis, using complex conjugate control (see Section 4.2 and Falnes (2002)) to try and obtain optimal power extraction.

1.4 Power Take Off

The PTO is the part of the device that utilizes the relative motion that occurs in the WEC to produce electricity. The majority of WECs produce electricity, the notable exception of this being the desalination of sea water, and an additional benefit of both is in coastal defense. The PTO can be made up of a number of components, which may incorporate a form of temporary energy storage, some way of transforming the relative motion into a different mechanical motion, an electrical machine to produce the electricity, some form of control to increase the energy production, and power electronics to enable the electricity to be connected to the country's national grid. It is stated by Falnes (2007) that the PTO is often nonlinear.

1.4.1 Principles of PTO

For a WEC to produce electricity it needs a PTO system that allows it to use the differential motion of the device and transform it into electricity. The differential motion can occur in many forms:

- A long device that is perpendicular to the wave front will experience different wave forces over its length due to the different phase of the waves. This causes relative motion within the device. Examples of this are the Pelamis and the Anaconda.
- Similarly, a long device parallel to the wave front also experiences a different wave forces, especially due to multi-directional waves, resulting in relative motion. An example would be a spine of Salter's ducks.
- From reacting against a stationary platform, such as the ocean floor, for example, the Seabased system and AWS's waveswing.
- Reacting against a separate body of the device which is likely to be situated away from the most energetic part of the waves, such as Finerva's AquaBOuy and the Wavebob.
- Reacting against an inertial mass within the device, such as the PS-frog and SEAREV.
- It can react against a body of fluid. This is the case for both floating and fixed OWC such as the OE buoy and for devices which operate with a low head of water such as overtopping devices.

1.4.2 Hydraulic PTO

Hydraulic PTO systems comprise a combination of a prime mover, high and low pressure gas accumulators, a hydraulic motor and an electrical generator, one way valves and pipes connecting these components (Falcao, 2007). The hydraulic fluid is initially pressurized by the relative motion of the WEC. High and low pressure accumulators operate by having a flexible membrane within the accumulator which has the pressurized fluid on one side and a fixed amount of compressible air on the other. This allows the pressure to be temporally stored.

The advantages of a hydraulic PTO over other forms of PTO for WECs are (Kugi, 2001):

- Many of the components of hydraulic systems are currently commercially available. They have been used for years in other applications - there is reliability data and knowledge about their maintenance needs and lifetime analysis.
- The electricity can be compatible with national electricity grids without (many) further alterations.
- The power that can be generated from a hydraulic system is much greater for the same overall weight, than most types of PTO.

However, hydraulic PTO systems have a number of disadvantages such as:

- There are a greater number of steps compared to some other PTOs, for the energy flow to go from the relative motion to electricity (Mueller *et al.*, 2007).
- The efficiency of hydraulic machines rapidly reduces if they are not working in their designed optimal parameter space.
- If oil is used as the hydraulic fluid, potential leaks could adversely affect the marine environment.

The hydraulic system is highly nonlinear unless a control system is used to deliberately make the response linear. The force provided by the pressure at the entrance to the first gas accumulator is proportional to the square of the velocity of the differential movement within the hydraulic system, if any frictional and inertial forces are ignored and the fluid is assumed to be incompressible (Falcao, 2007).

A second type of hydraulic system is where a low head of pressure is generated and used to drive a turbine. This low head of pressure is produced from a body of water higher than the mean sea level. The waves, which are often amplified in height via an artificial or real coastal structure, overtop into a basin that is above the prevailing sea level. This results in a temporary storage of water and the ability to control the rate and timings of energy generated. However, overtopping types of WEC are not going to be further considered as it is not relevant to the subject of this thesis.

Figure 1.13: Prototype of a direct drive generator (from http://www.see.ed.ac.uk).

1.4.3 Electromagnetic direct drive

Whilst a conventional electric generator rotates at a high speed - typically 1500 Hz for grid integration, a potentially more suitable generator for wave energy utilizes the slow speeds and high forces of the waves. Direct drive generators, often called linear machines, have a relatively slow moving rotor that moves in either a cyclic locus or in reciprocal linear motion. A photo of an example of a linear generator is presented in Figure 1.13.

The advantages of electromagnetic direct drive generators over other types of PTO, are:

- Potentially overall simpler design.
- No gearboxes are needed, that add complexity and potential sources of failure.
- Possibly easier to implement control strategies.

However, the disadvantages of direct drive electromagnetic generators are:

- Not fully proven technology for wave energy.
- Expensive power electronics are needed to change the electricity produced to what is acceptable for the national electricity grids.
- The weight of the machine and the amount of iron and structual material needed is large.

A standard direct drive electromagnetic machine, would become highly nonlinear when the iron cored windings are saturated with current. When not saturated, the main source of nonlinearities would be in any implemented control strategy.

1.4.4 Pneumatic PTO

A pneumatic PTO is a PTO where the fluid which directly results in the energy production, is air. Typical examples of this are fixed and floating OWCs. In OWCs the motion of the waves results in a body of air being pressurised and depressurised relative to atmospheric pressure, as the volume of water in a partially enclosed body changes. This results in air being forced out of the device through a bi-directional turbine, typically a Wells turbines (Boyle, 1996), which drives a conventional generator.

1.5 The wave resource

Waves are primarily the result of winds blowing across the water surface. Over long periods of time, the energy from the wind is transfered to the sea, in the form of waves. These waves continually transfer energy between kinetic and potential energy, to move the energy across the surface of the oceans.

The ocean resource varies with the position of land masses, the size of the fetch[2] and the latitude. The average amount of power per metre of coastline for the world is presented in Figure 1.14. It can be seen that the UK, especially Scotland, has a particularly high power available, at around 70 KW/m. Other places of very high wave energy in Europe are Portugal, Spain, Ireland and Norway. Parts of Australia, New Zealand and the Western coast of North and South America also have a high resource (Trinnaman and Clarke, 2004).

1.5.1 Regular waves

Waves which are described as regular, consist of a single frequency, sinusoidal wave. In the oceans, these waves do not exist but the real sea can be approximated by a summation of these type of waves. These waves have a frequency, amplitude and a phase to define them, as presented in Equation 1.1,

$$\eta = A\cos(\omega t + \phi). \tag{1.1}$$

where η [m] is the wave elevation, A [m] is the wave amplitude, ω [1/s] is the angular velocity of the wave, t [s] the time of the wave and ϕ[-] the phase of the wave.

2. The fetch is the length of the ocean that the wind blows over to make the wave.

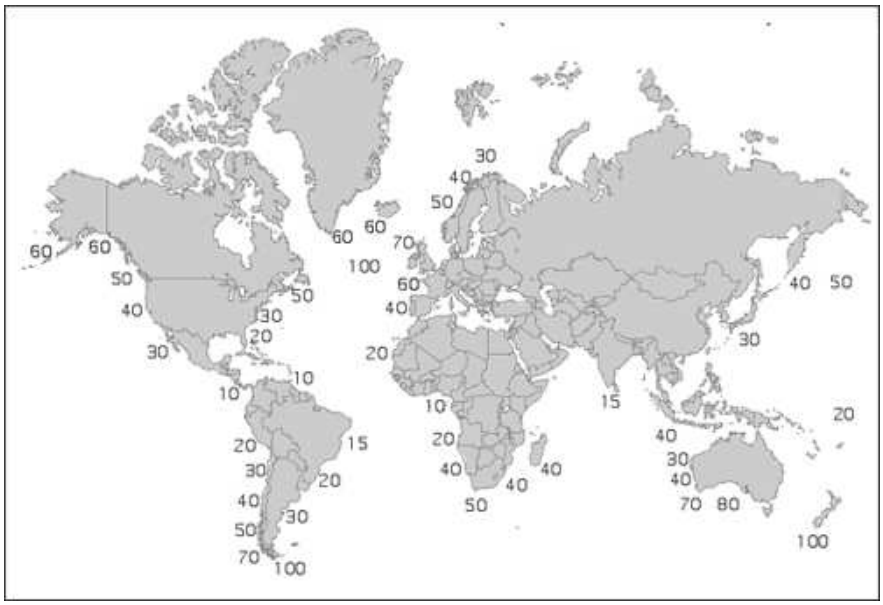

Figure 1.14: KW/m power available from the world's coastlines (from Trinnaman and Clarke (2004)).

1.5.2 Irregular waves

If a linear sea is assumed, then a more realistic sea state would be a combination of regular waves with different amplitudes, frequencies and phases, referred to as irregular waves, such as presented in Equation 1.2,

$$\eta = \sum_{i=1}^{N} H_i \cos(\omega_i t + \phi_i). \tag{1.2}$$

Different sea states have different characteristics and are more representative of different areas of offshore and coastal waters. A typical sea state is the Pierson-Moskowitz spectrum which will be used in this thesis, other sea states that will not be included are the JONSWAP and the Bretschneider (Rogers and King, 1997).

1.5.3 Pierson-Moskowitz spectrum

The Pierson-Moskowitz (PM) spectrum is a wave spectrum originally based on experimental data about wind speed and the corresponding wave heights. Pierson and Moskowitz (1964) assumed that if the wind blows constantly over a large sea, for a long time, then the resulting waves would be in equilibrium with the wind. This is described as a fully developed sea. The data was obtained empirically, and fitted to an equation. Further work was done on this equation to directly link the frequency of the waves and the wave height, without reference to the wind

speed. The equation linking these variables is defined in Equation 1.3 (Rogers and King, 1997),

$$S_\zeta(f) = 8.1 \times 10^{-3} g^2 (2\pi)^{-4} f^{-5} exp\left(-\frac{5}{4}\left[\frac{f_p}{f}\right]^4\right), \tag{1.3}$$

where $S_\zeta(f)$ [m^2/s] is the PM power spectrum, f [1/s], is the wave frequency, f_p [1/s] is the peak frequency and g [m/s^2] is the acceleration due to gravity. The amplitude of the different waves is then calculated from $\sqrt{4\pi S_\zeta \Delta f}$.

This wave spectrum is similar to the actual spectrum obtained from the North Atlantic ocean, since it is considered to be fully developed.

Multi-directional sea states

All the sea states previously mentioned have assumed a mono-directional sea state, a sea state where all the waves come from the same known direction. This is reasonably realistic in some circumstances, where the bathymetry and coast shape lead to the waves being refracted near to shore and seemingly coming from one direction. Realistically, most sea states will have a directional spectra of the waves coming from multiple directions. The waves are often coming from a main wind direction, with additional waves from storms or other wind directions from previous days. This can be incorporated into the different sea spectra. However, in this thesis, only mono-directional waves have been considered because the model is a symmetric point absorber therefore the directionality of the waves will have little influence.

1.6 Linear wave theory

In this thesis (in Chapter 2) numerical simulations will be developed. The basis of these simulations is linear wave theory, also known as the Airy wave theory. The following work is based on Dean and Dalrymple (1992) and Payne (2006). This theory allows us to know the velocities of the water surrounding the WEC, and hence the forces that the waves exert on the body and the body exerts on the water.

The assumptions of linear wave theory are:

- Irrotational motion: the fluid particles do not “spin”. This means that turbulent and wake effects are not present.
- Inviscid: the fluid is inviscid so there is no friction between the particles of the fluid and themselves or any bodies in the water.
- Incompressible fluid: the water can not be compressed.
- Forces from the surface tensions of the fluid are small compared with the forces experienced by the fluid.

- Small waves: the ratio of the wavelength to the wave height is very small, hence the waves are not steep.

The validity of these assumptions varies. Irrotational motion and an inviscid fluid are probably the least valid. Irrotational motion implies that there will be no turbulence or wake effects at all, while inviscid fluid implies that the friction between the fluid particles, as they move relative to each other, as well as against the model and seabed is negligible. In any physical model these effects will occur and they will influence the forces and pressures acting on the body. However, their influence when the amplitude of the body is low are assumed to be minimal and the computational cost of including them is incredibly high.

The incompressibility assumption is valid since the speed of the fluids in the waves are not high, resulting in a low Mach number. Assuming that the surface tension is small is correct when the waves are large enough that they are dominated by gravitational forces, which occurs for the wave heights used in the experiments presented.

The assumption of small waves is valid in regular waves, since the wave height used for experimental testing is 20 mm and a 1 Hz frequency wave has a wavelength of 1.56 m [3]. In irregular waves the frequency range is greater, so a 2 Hz wave which has a wavelength of 0.39 m is less "small" compared to the wave heights used.

The governing equation is based on the concept that the mass is conserved and the fluid is incompressible and has a constant density, resulting in Equation 1.4,

$$\nabla \cdot \mathbf{u} = 0, \tag{1.4}$$

where the velocity of the fluid is $\mathbf{u} = u\mathbf{i} + v\mathbf{j} + w\mathbf{k}$, and $\mathbf{i}$, $\mathbf{j}$ and $\mathbf{k}$ are orthogonal unit vectors.

Due to the irrotational property of the fluid, the scalar velocity potential $\xi(x,y,z,t)$ is represented in Equation 1.5,

$$\mathbf{u} = -\nabla\xi. \tag{1.5}$$

Combining Equations 1.4 and 1.5 results in the Laplace Equation,

$$\nabla^2\xi = 0. \tag{1.6}$$

The boundary conditions on the fluid are based on the limitations of each surface or edge of the fluid domain. The boundary condition at the seabed states that fluid does not flow though the seabed, shown in Equation 1.7, for a uniform depth fluid domain,

$$\frac{\partial\xi}{\partial z} = 0, \text{ for } z = -h, \tag{1.7}$$

3. The method for calculating this is described later in this section, and uses Equation 1.12.

where h [m] is the water depth.

At the free surface, there are two boundary conditions. The kinematic boundary condition states that a particle at the surface remains at the surface, shown in Equation 1.8,

$$\frac{\partial \eta}{\partial t} + \frac{\partial \xi}{\partial x}\frac{\partial \eta}{\partial x} + \frac{\partial \xi}{\partial y}\frac{\partial \eta}{\partial y} - \frac{\partial \xi}{\partial z} = 0, \text{ on } z = \eta(x,y,t), \tag{1.8}$$

where $z = \eta(x,y,t)$ is the water surface.

Using the assumption that the wave height is small compared to both the wave length and the water depth (hence the product of two terms is negligible), Equation 1.8 reduces to Equation 1.9,

$$\frac{\partial \eta}{\partial t} = \frac{\partial \xi}{\partial z}. \tag{1.9}$$

The dynamic boundary condition states that the pressure along the surface must be equal to atmospheric pressure. It is obtained from Bernoulli's Equation and assumes that the atmospheric pressure p_a [N/m^2] is constant over the entire surface of the water. By choosing a sensible constant of integration, Equation 1.10 is obtained on the water surface,

$$-\frac{1}{\rho}(p - p_a) = \frac{\partial \xi}{\partial t} + \frac{1}{2}\nabla\xi.\nabla\xi + gz = 0 \tag{1.10}$$

where $p(x,y,z,t)$ [N/m^2] is the pressure of the fluid, ρ [kg/m^3] is the density of the water and g [m/s^2] the acceleration due to gravity.

By substituting the free surface into Equation 1.10 and neglecting any second order terms, we obtain Equation 1.11,

$$\eta = \frac{1}{g}\frac{\partial \xi}{\partial t}. \tag{1.11}$$

With the full boundary conditions and the governing equation, then the equations can be solved for a linear system.

The dispersion equation obtained from the manipulation of the above equations links the wave length L[m] with the wave period T[s], when there is no body present in the water, as shown in Equation 1.12,

$$L = \frac{gT^2}{2\pi}\tanh\left(\frac{2\pi h}{L}\right). \tag{1.12}$$

The preceding linear wave theory does not make assumptions about the waves being present or a floating body within the fluid domain. These factors are included by using the linearity of the fluid to separate the situation into two separate problems and finding the boundary conditions for each. The resulting combination, along with the preceding boundary conditions, results in an analytical solution for an axi-symmetric cylinder, which can be found to determine the velocity potential, and hence the force experienced by the floating body (Bhatta and

Rahman, 2003). The two situations are:

- Diffraction: the floating body is held stationary and experiences an incoming wave field.
- Radiation: the floating body is forced to oscillate in still water, with the same frequency as the incoming waves. This produces waves which radiate away from the body.

The velocity potential of these two situations linearly combines to form the overall velocity potential,

$$\xi = \xi_r + \xi_d, \tag{1.13}$$

where ξ_r [m^2/s] is the radiated velocity potential, and ξ_d [m^2/s] is the diffracted velocity potential.

Radiated velocity potential

The boundary condition for the radiated velocity potential, is that on the surface of the floating body, the velocity of the fluid has the same velocity as the body. This is presented in Equation 1.14,

$$\frac{\partial \xi_r}{\partial z} = \mathbf{u.n}, \text{ on the wetted surface,} \tag{1.14}$$

where **n** is the normal to the boundary surface.

For an axi-symmetric cylinder limited to move in heave, such as is being studied in this thesis, this boundary condition becomes Equation 1.15,

$$\frac{\partial \xi_r}{\partial z} = \dot{x}_e, \text{ on } z = -b, \tag{1.15}$$

where $\dot{x}_e$ is the velocity of the external axi-symmetric cylinder and b is the draft of the cylinder. For linear theory, this draft is considered to be the average draft over time.

Diffraction velocity potential

The floating body is held fixed in incoming waves resulting in the diffraction potential, which is further separated into:

- The incident wave field velocity potential, ξ_i: the velocity potential due to the incoming waves without the floating body being present.
- The scattering velocity potential, ξ_s: the disturbed wave field which is directly caused by the floating body.

These combine together to form the diffraction velocity potential:

$$\xi_d = \xi_i + \xi_s. \tag{1.16}$$

As the diffraction velocity can not flow though the floating body, the boundary condition is as

shown in Equation 1.17,

$$\frac{\partial \xi_s}{\partial n} + \frac{\partial \xi_i}{\partial n} = 0, \text{ on the wetted surface of the body.} \tag{1.17}$$

The far field radiation condition states that both the radiation and scattering potential velocity fields will equal zero at an infinite distance away from the floating body, which results in Equation 1.18 (Bhatta and Rahman, 2003).

$$lim_{r\to\infty}\sqrt{r}\left(\frac{\partial \xi_r}{\partial r} - \frac{i\,\xi_r}{L}\right) = 0, \tag{1.18}$$

where r is the polar coordinate distance from the origin at the center of the cylinder.

Equation 1.18 is also valid for the scattering potential velocity field, where ξ_s is present instead of ξ_r.

Forces on the body

The forces on the body are calculated from summing the pressures over the surface of the floating body. In this case, the cylinder, which can only move in heave, is shown in Equation 1.19,

$$F = \int\int_S p.\mathbf{n}dS \tag{1.19}$$

where p [N/m^2] is the pressure in the fluid. From Bernoulli's equation, the pressure is related to the velocity potential by Equation 1.20,

$$p = -\rho\left(\frac{\partial \xi}{\partial t} + gz\right). \tag{1.20}$$

For this dynamic situation $gz\rho$ is the hydrostatic pressure, which will be accounted for separately, and $\Xi = real(\xi e^{-i\omega t})$, therefore the force in heave is,

$$F = real(fe^{-i\omega t}),$$

where

$$f = i\rho\omega\int\int_S(\xi_d + \xi_r)dS, \tag{1.21}$$

and S is the wetted surface area that is integrated over.

1.7 Numerical modelling principles

1.7.1 Added mass and damping

The added mass is the effective fluid that surrounds a body and is accelerated as the body accelerates. The added damping is the additional damping that the body feels due to being close to the free surface and making waves (Newman, 1977).

The added mass and damping are directly linked to the radiation force, with the added mass equal to the component of the radiation force in phase with the body's acceleration, and the added damping in phase with the body's velocity. In the frequency domain, this equates to Equations 1.22 and 1.23 (Bhatta and Rahman, 2003).

$$F_{rad} = -\left(M\frac{d^2x_e}{dt^2} + N\frac{dx_e}{dt}\right), \tag{1.22}$$

$$F_{rad} = Real\left[\omega^2 x_e(M + i\frac{N}{\omega})\right], \tag{1.23}$$

where M [kg] is the added mass, and N [kg/s] is the added damping.

1.7.2 WAMIT

WAMIT is a boundary element method software, which uses a panel method and is based on linear wave theory. The panel method splits the body into either quadrilateral, triangular panels or if a higher order method is used, a B-Spline - a continuous piecewise polynomial parametric curve. The velocity potential is then calculated for each of the panels assuming it is constant over the panels. For further details on the panel method and how WAMIT calculates the hydrodynamic coefficients, see Payne (2006) and the WAMIT user manual (WAMIT, 2000.). For this work, output from WAMIT is used to obtain the added mass and excitation force, for both the full scale and tank scale models.

1.7.3 Time domain analysis

Time domain analysis has been used to simulate the floating body when there are nonlinearities present in the motion of the body, although the fluid is still considered to be linear. Further details on the methodology are given in Section 2.3. It is used for finding the different forces that occur at progressive time steps, and using these to predict the resulting motions.

The time domain method has been often used for control strategies, where the control strategy results in nonlinear motion. Latching is the process of holding or latching the main body and releasing it at a different point in the wave cycle, in an attempt to increase the power extraction (Falcao, 2008). The main body is held fixed against the object it is reacting against, for example, the second body of a two body device or a fixed platform. It is more effective in regular seas than

irregular seas and for higher efficiencies in real seas future knowledge of the waves is desired. Initially, it was thought that the latching would be done mechanically, but current designs use a hydraulic valve in a hydraulic PTO or use electrical control in a direct drive machine.

Time domain modelling has been used for latching initially by Greenhow (1982), and since in work by Falcao (2008), Korde (2002) and in the SEAREV models (Babarit *et al.*, 2005).

Time domain modelling has also been used for simulations on the AWS, in order to determine the motions of the body in irregular waves, when the body parameters such as the internal and external air and water pressures, electrical linear generator and water dampers change with time (Sa da Costa *et al.*, 2005).

A hybrid frequency / time domain model has been developed by the research group at NTNU (Norwegian University of Science and Technology), using state-space models and the bond graph method (Taghipour *et al.*, 2008). The purpose for this type of model is to reduce the computational time requirement for the Cummin's convolution (see Section 2.3), and to make models similar to other simulations of "motion control systems".

The nonlinearities could have also been modelled using a higher order frequency domain approach, based on Volterra functional representations. This method uses simplified bi-linear and tri-linear frequency response functions (Bendat, 1998). However, it can only model steady-state processes, therefore it would not be able to model all of the different PTO setups used in this thesis.

1.7.4 Computational Fluid Dynamics Methods

Computational Fluid Dynamics (CFD) methods, including Boundary Element Methods (BEM), can be used to model systems were the fluid is fully nonlinear. These involve producing a mesh of the fluid domain or the fluid's boundaries and calculating the velocity potential over this mesh. The accuracy of these models is highly dependent on the general size of the panels in the mesh and the size of the panels near places of interest or high activity, the area that the mesh covers and the type of mesh used. Intelligent boundary conditions need to be implemented to avoid spurious data, vibrations and the simulation "exploding" (Chung, 2002). These type of models, although useful, are highly computational expensive and typically require specialist supercomputers or clusters of powerful computers to run. For this reason, completing a large number of runs with different parameters or finding optimized parameters is not practical due to the computational time required. Hence, for this thesis, these type of models have not been used.

1.8 The model

This thesis will concentrate on one type of generic device and investigate how it responds to a nonlinear PTO. The type of device being considered is an inertial point absorber, as discussed in Section 1.3.4. More specifically, it is a self-contained device, so the inertial mass is within the main body and is slack moored.

It comprises an internal mass reacting against an axi-symmetric cylinder, both only moving in heave. The PTO operates between the internal mass and the cylinder and is modelled as a spring and damper. It utilizes the relative motion between the two bodies. A schematic diagram of the model is presented in Figure 1.15.

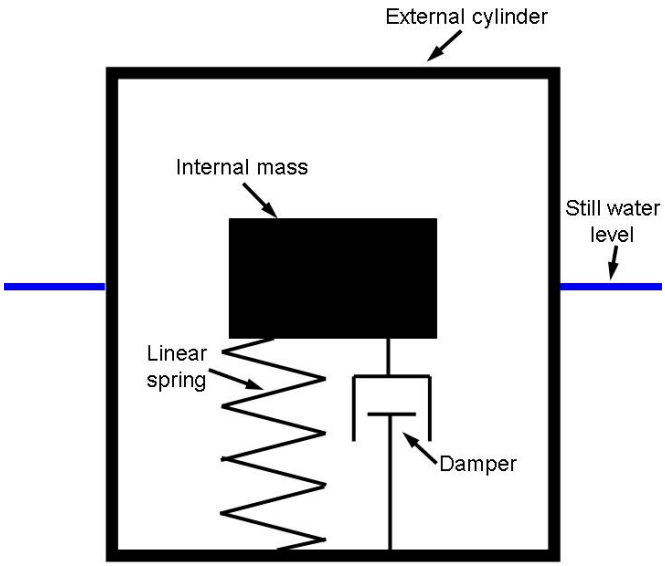

Figure 1.15: Schematic sketch of the model.

The device only moves in heave in order to, simplify the concept, the numerical requirements and the experimental model, allowing the focus to be purely on the nonlinearities of the PTO. Therefore, it is easier to ascertain that the effects are due to the PTO rather than, for example, a cross coupled effect from the different directions that the device is moving in.

The device studied is a point absorber (Budal and Falnes, 1975) which means that its overall dimensions are much smaller than the wavelength. The advantages of a point absorber over a larger device are,

- It can produce a greater amount of energy per unit of active material as it radiates waves which act to cancel out incoming waves. This can increase the efficiency of the device to over 100%, i.e., it can absorbs more energy than is available in the length of wave front

that is in direct contact with the device.

- Planned or unplanned maintenance operations of a point absorber has less impact on the overall rated power of a large wave farm, comprising a number of WECs.

The disadvantages of a point absorber are,

- The actual amount of energy extracted per device can be lower than a larger device. Multiple devices would be needed in order for the energy extracted to be equal to that of a modern wind turbine, with large farms of devices needed to equal a traditional fossil fuel power station.
- The costs of installation, the moorings and some electrical cables would potentially be larger for a number of point absorbers than for one larger device, for the same power output.
- Having an array of point absorbers will take up more space than a single larger device, with implications for the spatial use of the sea and planning consent.
- Marine mammals may find more difficulties in avoiding an array of devices than a single device, resulting in a higher chance of collisions.

The device will be slack moored, which means that the moorings are not associated with the PTO system and the moorings allow some movement within the system. The advantages to being slack moored are (Beatty *et al.*, 2007),

- There would be less mechanical stresses on the body in extreme sea conditions.
- There would potentially be less forces going through the moorings in high energy sea states.
- Any changes in the water level due to tides will have less of an effect on the power extracted from the WEC.

Disadvantages of a slack moored system are,

- The PTO system cannot be incorporated within the mooring system, so a reaction force needs to be obtained from another (often more complex) source.
- The position of the device in the sea not accurately known.

The WEC considered is self-contained, meaning that all the components of the device except the moorings and electrical connection are held within a waterproof exterior. The advantages of this are the ease of deployment and the ability to bring the device to shore when required. Also, there are potential reliability and maintenance savings due to not having seawater in contact with the majority of the device, including any bearings and moving parts. However, the disadvantages of having a self-contained device are that it may be harder to maintain at sea and the reaction force has to be obtained from within the device.

1.8.1 The nonlinear PTOs

Three different types of nonliner PTO and a linear PTO are to be investigated. These will all operate between the cylinder and internal mass, using the relative heave motion between them.

Linear PTO
This PTO comprises a linear spring and a linear damper. In the experimental model, a pneumatic damper and a conventional spring is used. The purpose of testing this PTO setup is mainly as a comparison for the other, nonlinear PTOs.

Mono-directional PTO
The mono-directional PTO comprises a linear spring and a damper that only produces a damping force in one direction of movement - either expansion or compression and negligible force in the opposite direction. This is tested using different mono-directional pneumatic dampers and a conventional spring in the experimental model.

Quadratic PTO
The quadratic PTO uses a linear spring and a damper that produces a damping force that is proportional to the square of the relative velocity. The sign of the damping force is kept the same as the sign of the relative velocity. It represents a hydraulic PTO, were the initial fluid pressure is proportional to the square of the velocity (Falcao, 2007). This PTO is modelled using the numerical simulations only.

Endstop dampers
Endstop or peripheral dampers are used as an addition to a linear damper. They can either be used to extract extra energy in high energy sea states or (with a higher damping constant) to limit the relative amplitude of the motion, such as considered by Sa da Costa *et al.* (2005). In the experimental testing endstop dampers which only operate when the internal mass makes contact with them, are used.

1.9 Thesis outline

This thesis looks at the type of device that has been described in Section 1.8. It presents results of both a 1:40 tank scale model and a full sized model. A numerical simulation that operates in the time domain, is used to model the device and is described in Chapter 2, for both scales of WEC. The results obtained from the numerical simulations are presented and discussed in Chapter 3, for the full scale model. This considers the optimisation of the PTO for power extraction and reliability, and the influence of the nonlinearity of the PTO. The experimental model is tested in the University of Edinburgh's Curved Wave Tank and is described in Chapter 4,

with a discussion of the parameters chosen and a detailed description of the physical model and the calibration process. The experimental results are presented, analysed and discussed in Chapter 5 for regular waves and Chapter 6 for irregular waves. These results chapters present the response of the device to the waves, the relative phase between the two bodies, the power extracted and the phenomena associated with the nonlinearities of the PTO. In Chapter 7 the numerical simulation of the 1:40 scale model results are presented in order to compare these with the experimental model. Conclusions from the thesis are drawn in Chapter 8.

Chapter 2

The numerical simulation

2.1 Summary

This chapter considers the methodology used to develop a numerical simulation to model the positions of both the external cylinder and the internal mass of the WEC. Details of part of the methodology used in this chapter have been reproduced in Bailey and Bryden (2011).

In this chapter, Section 2.2 describes the dimensions of the full scale model and the tank scale device and presents the WAMIT results for the added mass and the excitation force for these. This section also discusses the phenomena that are not included in the numerical simulation. Section 2.3 presents the time domain equations that are used and Section 2.4 uses Prony's method, a numerical technique, to reduce the computational time of the radiation force of these time domain equations. Section 2.5 details how the linear, mono-directional, quadratic and end-stop PTOs that are used in the simulation are modelled. Section 2.6 presents attempts at quantifying the friction and unwanted damping in the physical model in ways that can be incorporated into the numerical simulation to give a more realistic simulation of the tank scale model.

2.2 The system being modelled

The WEC that is to be modelled in this thesis has been described in Section 1.8. It comprises an outer axi-symmetric cylinder and an internal mass. These both move in heave and relative to each other. Between these bodies, the PTO operates on the relative motion and is represented by a spring and damper in parallel. A schematic drawing of the model is presented in Figure 2.1.

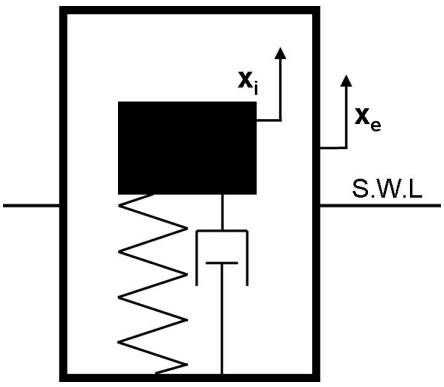

Figure 2.1: Schematic drawing of the model.

2.2.1 Full scale model

The model, at full scale, resides in 48 m of water, and has a draft of 10 m below the Still Water Level (SWL). The radius of the cylinder is 4.6 m, its depth is 20 m and the weight of the internal mass is 3.32×10^5 kg. The internal mass was chosen to be half of the overall mass of the device, due to the linear theory results showing a greater power extraction for a larger internal mass, for the same combined internal and body mass (see Section 4.2). The center of mass of the body is at its geometric center.

The model being tested is unstable and would tip over if placed in water unsupported, therefore this exact geometry would not be suitable for an actual prototype model. However, since this model is used for numerical simulations and experimental work were the body is supported so that it cannot move in pitch, this instability is not important.

The panel size is the area of each of the panels that WAMIT splits the submerged parts of the external cylinder into. Once WAMIT has performed this paneling, it calculates the added mass, added damping the excitation force for each discrete frequency specified by the user. The panel size in WAMIT affects the accuracy of the model; having a small panel size increases the accuracy of the results but also increases the computational time. The full scale model has a WAMIT panel size of 0.5 m^2.

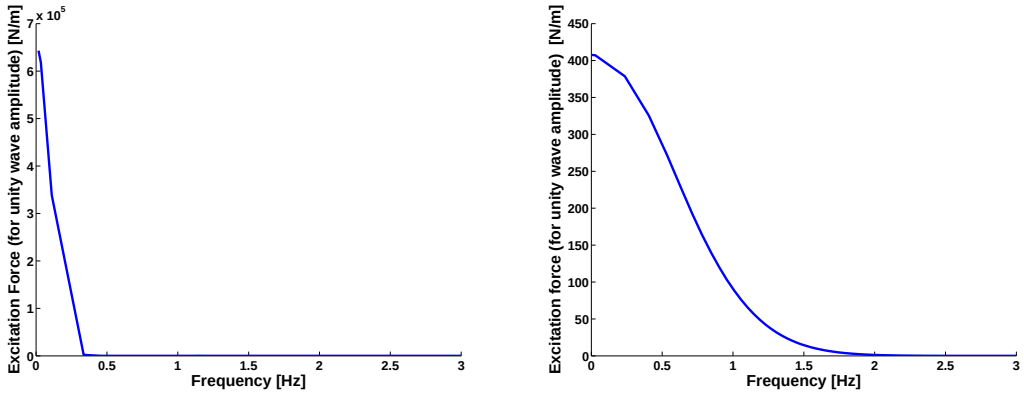

(a) Full scale model.

(b) Tank scaled model.

Figure 2.2: Results from WAMIT: the excitation force in heave, for unity wave amplitude.

2.2.2 Tank scale model

The tank scale model is based on a 1:40 scale representation of the full scale model, although not all the dimensions scale exactly due to the designing and building process. It resides in 1.2 m of water. The cylinder has a draft of 0.285 m, a radius of 0.115 m and a depth of 0.5 m. It has an internal mass of 6.7 kg and a body mass, without the internal mass, of 4.9 kg. The center of geometry is at its geometric center. This model has a WAMIT panel size of 0.01 m^2.

2.2.3 Results from WAMIT

The excitation force experienced by the device in heave due to unity amplitude incident waves, as a function of frequency, is presented in Figure 2.2. This shows the magnitude of the excitation force, as provided by WAMIT, for both the experimental tank scaled model and for the full scale WEC.

The added mass of the body in heave, for different frequencies, for both the full scale model and the tank scaled model is presented in Figure 2.3. It should be noted that for high frequencies the value of the added mass converges to a constant value.

The excitation force and added mass of the bodies have been made dimensionless by dividing by the buoyancy force required to submerged the body one meter and the mass of the body, respectively. This has been done for ease of comparison between the two scales of model and is presented in Figure 2.4.

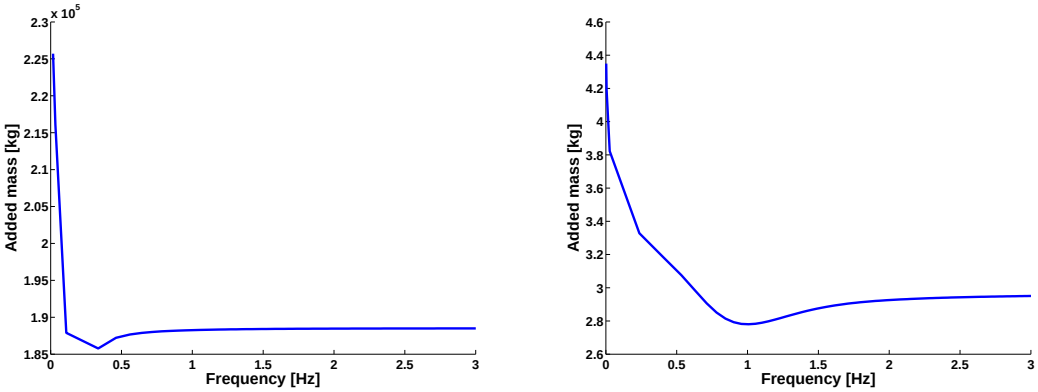

(a) Full scaled model.

(b) Tank scaled model.

Figure 2.3: Results from WAMIT: the added mass, in heave.

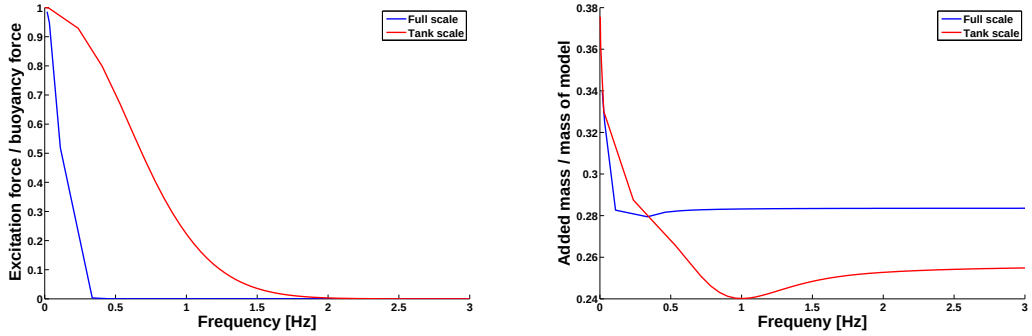

(a) Excitation force / buoyancy force per meter submerged.

(b) Added mass / mass of model.

Figure 2.4: Results from WAMIT: Dimensionless excitation force and added mass.

2.2.4 Phenomena not included in the model

The waves in the numerical simulation and the experimental model are assumed to behave as predicted by linear wave theory. This requires that, relative to the body, the height of the waves is small, the waves are not steep, and the water motion is assumed to be irrotational. In addition, body motions are assumed to be small relative to the body dimensions. Hence, nonlinear water effects, such as wakes and turbulence are not included in this model. These would tend to reduce the amplitude of the larger motions of the external cylinder disproportionately when compared with smaller motions of the cylinder. It is assumed that all motions of the cylinder result in some additional damping from the nonlinear effects but larger motions of the cylinder have a much higher proportion of additional damping from these effects.

For the full size model, the internal mass and cylinder are constrained to move in heave. The details of how this is achieved have not been considered for this model. However, in the process of constraining the model in one degree of freedom, it is likely that there would be additional friction and damping that occurs, such as the effects that are included in the tank scaled model (see Section 2.6) and additional relevant effects, and these have not been included in this simulation.

The heave motion of the cylinder results in its wetted area changing with the incoming waves. This has the potential to affect the excitation force and added mass of the cylinder, and has been considered for a body who's primary motion was in pitch in McCabe *et al.* (2006). However, since in this thesis there is not such significant body motions and change in the wetted body geometry as occurred in McCabe's work, the disadvantage of having the additional computational burden was deemed to be too high for the small advantage in accuracy gained.

As the position of the internal mass moves within the cylinder, the center of gravity of the cylinder changes. This would affect the forces and added masses associated with non-heave degrees of freedom. However, since the cylinder is limited to move in heave, the only effect would be to alter the friction felt on the experimental model due to the model wanting to move in pitch and surge. If motions other than heave were being considered, this effect would have more influence.

2.3 Time domain equations of motion

The equations of motion for this model are based on the theory from Section 1.6. Equations are needed for the forces on the internal mass and on the external cylinder separately. They are given for the cylinder in Equation 2.1 and for the internal mass in Equation 2.2,

$$M_e\ddot{x}_e + Sx_e = F_{ex} + F_r + F_{PTO}, \tag{2.1}$$

$$M_i\ddot{x}_i = -F_{PTO}, \tag{2.2}$$

where M [kg] is the mass of a body and x [m] is the position of a body. The subscripts of e and i represent the external cylinder and internal mass respectively.

F_{ex} [N] is the excitation force which is a function of time. This is the force exerted on a stationary cylinder in incident waves and it is provided by WAMIT for a pre-defined number of frequencies. For regular waves, linear interpolation is used to find the corresponding excitation force for the incident wave frequency, with the excitation force being the real component of $F_{ex}e^{-i\omega(t+\phi)}$, where ϕ is the phase of the incident wave. In irregular waves, the excitation force is a summation of the real component of the linear interpolations of each individual frequency, taking into account the phase of each incident wave.

S [kg/s^2] is the hydrostatic stiffness of the buoy, and is equal to $\rho g \pi r^2$, where ρ [kg/m^3] is the density of water, assumed to be 1025 kg/m^3, g [m/s^2] is the acceleration due to gravity with the value of 9.81 m/s^2 used and r [m] is the radius of the cylinder.

F_{PTO} [N] is the time dependent force from the PTO that operates on both the internal mass and, due to Newton's third law of motion, its equal and opposite force operates on the external cylinder. It varies depending on the type of PTO setup being tested and further details are given in Section 2.5.

F_r [N] is the time dependent radiation force. In the frequency domain, the radiation force is the product of the complex radiation term, $G(i\omega)$, and the complex motion of the cylinder, $Z(i\omega)$, as described by Jefferys (1984),

$$F_r(i\omega) = G(i\omega)Z(i\omega), \tag{2.3}$$

where the radiation term contains the added mass and added damping, which are discussed in Section 1.7.1, as shown in Equation 2.4,

$$G(i\omega) = \omega^2 m(\omega) - i\omega N(\omega). \tag{2.4}$$

The added mass at infinity is a constant and is removed from the radiation force, to obtain the new radiation term, $G^\star(i\omega)$,

$$G^\star(i\omega) = G(i\omega) - \omega^2 m_\infty. \tag{2.5}$$

In the time domain, a step in the position of the cylinder as demonstrated in Equation 2.6, is

the equivalent to an impulsive response in the velocity of the cylinder.

$$\begin{aligned} x_e &= 0, \text{when } t < 0, \\ x_e &= 1, \text{when } t \geq 0. \end{aligned} \tag{2.6}$$

The equivalent in the frequency domain is multiplication by $\frac{1}{i\omega}$. For this time step, the radiation force response would therefore be

$$H(i\omega) = \frac{G^\star}{i\omega} = -N(\omega) - i\omega[m(\omega) - m_\infty] \tag{2.7}$$

where $H(i\omega)$ is defined as the radiation response to a velocity impulse.

To find the radiation force time history for an impulsive velocity in the time domain, the *Fourier inversion theorem* of $H(i\omega)$ is found, then the function can be obtained from Equations 2.8 and 2.9, for the in-phase and out-of-phase components of the response.

$$K(t) = -\frac{2}{\pi}\int_0^\infty \omega[m(\omega) - m_\infty]\sin(\omega t)d\omega, \tag{2.8}$$

$$= -\frac{2}{\pi}\int_0^\infty N(\omega)\cos(\omega t)d\omega, \tag{2.9}$$

where $K(t)$ is the inverse fourier transform of $H(i\omega)$.

The radiation force, F_r [N] is obtained from the convolution of the velocity of the cylinder, and the force response of the cylinder to a velocity impulse, in Equations 2.10 and 2.11. Due to the linear assumption of the water waves, because of superposition, by convolving the known velocities of the body at all past times, up until the present time with the radiation force from an impulsive velocity, the radiation force can be calculated.

$$F_r = -m_\infty \ddot{x}_e - I(t), \tag{2.10}$$

where

$$I(t) = \int_0^t \dot{x}_e K(t-\tau)d\tau. \tag{2.11}$$

The added mass at infinity is a constant and is removed from the radiation force kernel term in Equation 2.5 and it is, hence, included separately in Equation 2.10. This removal from Equation 2.5 is to allow the integral of Equation 2.8 to converge.

2.4 Prony's Method

In order to reduce the computational time, Prony's method was used. This method was first developed by Gaspard Riche de Prony in 1795, and has been used to reduce the radiation kernel $K(t)$ into a summation of exponential functions (Duclos *et al.*, 2001). Equation 2.12 sets $K(t)$ approximately equal to the summation of the exponential functions, which uses the two constants, α_n and β_n, which together form a couple.

$$K(t) \simeq \sum_{n=1}^{N} \alpha_n e^{\beta_n t}. \tag{2.12}$$

The couples α_n and β_n are calculated by setting $t_m = t_0 + m\Delta t$, where Δt is the time step and t_0 is the starting time. Using this substitution and Equation 2.12 this results in Equation 2.13,

$$K(t_m) = \sum_{n=1}^{N} \alpha_n e^{\beta_n t_0} e^{\beta_n m \Delta t}. \tag{2.13}$$

New coefficients are defined in Equations 2.14 and 2.15, for Equation 2.13,

$$c_n = \alpha_n e^{\beta_n t_0}, \tag{2.14}$$

$$Q_n = e^{\beta_n \Delta t} \tag{2.15}$$

and noting that $Q_n^m = e^{m\beta_n \Delta t}$, Equation 2.16 can be defined

$$\begin{bmatrix} Q_1 & Q_2 & \cdots & Q_N \\ Q_1^2 & Q_2^2 & \cdots & Q_N^2 \\ \vdots & \vdots & \ddots & \vdots \\ Q_1^M & Q_2^M & \cdots & Q_N^M \end{bmatrix} \begin{bmatrix} c_1 \\ c_2 \\ \vdots \\ c_N \end{bmatrix} \simeq \begin{bmatrix} K(t_1) \\ K(t_2) \\ \vdots \\ K(t_M) \end{bmatrix}. \tag{2.16}$$

The variables q and s_i are defined as shown in Equation 2.17,

$$\prod_{n=1}^{N}(q - Q_n) = (q - Q_1)(q - Q_2)\cdots(q - Q_N) = \sum_{n=0}^{N} s_{N+1-n} q^n, \; s_0 = 1. \tag{2.17}$$

The first $N+1$ rows of Equation 2.16 are each multiplied by one of the coefficients $s_N, s_{N-1}, \cdots, s_0$, where the $(N+1-n)^{th}$ row is multiplied by s_n, resulting in Equation 2.18.

$$\begin{aligned} s_N Q_1 c_1 + s_N Q_2 c_2 + \cdots + s_N Q_N c_N &\simeq s_N K(t_1), \\ s_{N-1} Q_1^2 c_1 + s_{N-1} Q_2^2 c_2 + \cdots + s_{N-1} Q_N^2 c_N &\simeq s_{N-1} K(t_2), \\ &\vdots \\ s_0 Q_1^{N+1} c_1 + s_0 Q_2^{N+1} c_2 + \cdots + s_0 Q_N^{N+1} c_N &\simeq s_0 K(t_{N+1}). \end{aligned}$$

$$\Leftrightarrow \sum_{n=1}^{N} s_{N+1-m} Q_n^m c_n \simeq s_{N+1-m} K(t_m), \text{ for } m = 1,2, \text{ to } N+1. \tag{2.18}$$

Equation 2.19 is obtained from summing Equation 2.18,

$$\begin{aligned} c_1(s_N Q_1 + s_{N-1} Q_1^2 + \cdots + s_0 Q_1^{N+1}) + \cdots + c_N(s_N Q_N + s_{N-1} Q_N^2 + \cdots + s_0 Q_N^{N+1}) \\ \simeq s_N K(t_1) + s_{N-1} K(t_2) + \cdots + s_0 K(t_{N+1}), \end{aligned}$$

$$\Leftrightarrow \sum_{n^\star=1}^{N} c_{n^\star} Q_{n^\star} \sum_{n=0}^{N} s_{N-n} Q_{n^\star}^n \simeq \sum_{n=1}^{N+1} s_{N+1-n} K(t_n). \tag{2.19}$$

The second summation on the LHS of Equation 2.19 equals zero because this summation is just Equation 2.17 with q replaced by $Q_{n^\star}$ for some $n^\star$ between 1 and N (i.e. one of the parenthesis on the LHS of Equation 2.17 will always be zero). This results in Equation 2.19 reducing to Equation 2.20,

$$\sum_{n=1}^{N} s_{N+1-n} K(t_n) \simeq -K(t_{N+1}). \tag{2.20}$$

Repeating the process of Equations 2.18 – 2.20 using a different starting row, results in Equation 2.21,

$$\begin{bmatrix} K(t_1) & K(t_2) & \cdots & K(t_N) \\ K(t_2) & K(t_3) & \cdots & K(t_{N+1}) \\ \vdots & \vdots & \ddots & \vdots \\ K(t_{M-N}) & K(t_{M-N+1}) & \cdots & K(t_{M-1}) \end{bmatrix} \cdot \begin{bmatrix} s_N \\ s_{N-1} \\ \vdots \\ s_1 \end{bmatrix} \simeq - \begin{bmatrix} K(t_{N+1}) \\ K(t_{N+2}) \\ \vdots \\ K(t_M) \end{bmatrix}. \tag{2.21}$$

$K(t)$ is known from Equation 2.8 therefore, s_n can be found. From Equation 2.17, the roots of the polynomial equation Q_n can be calculated. Hence β_n can be obtained from Equation 2.15, and c_n from Equation 2.16. This results in α_n being found from Equation 2.14. Examples of exponential functions formed from these α_n and β_n couples can be seen in Figure 2.5, where the 20 most significant couples are shown, for a full scale model.

The variables for finding the α_n and β_n couples and determining the accuracy of Prony's method, are the positive integer M and N. Larger values results in higher accuracy, although there is less computational effort in finding the α_n and β_n couples for a higher value of M than of N. The value of N indicates the number of couples, so an increased number of couples results in the final numerical simulation running slower. The accuracy of $K(t)$ for increasing values of N is shown in Table 2.1, for an M value of 900 . To enable a 99.9% accurate representation of the kernel function, 20 sets of α_n and β_n have been used for both models. Figure 2.6 shows $K(t)$ and the effect of the different number of couples used in order to approximate $K(t)$.

Substituting Equation 2.12 into Equation 2.11 gives an equation for $I(t)$, which is further

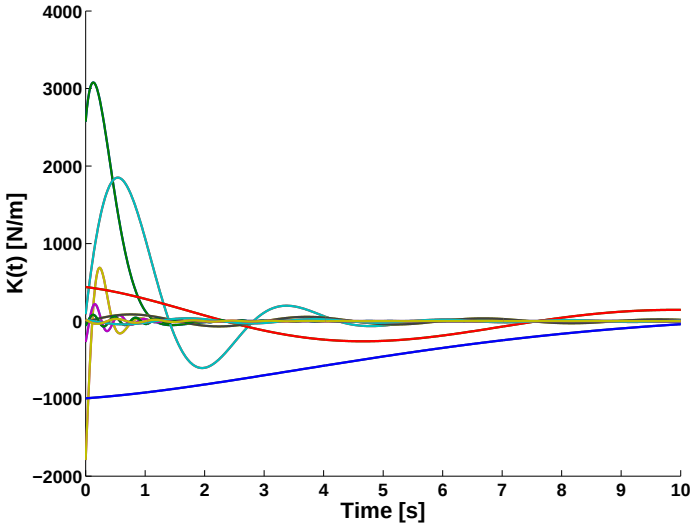

Figure 2.5: Twenty different exponential functions that make up the $K(t)$ function.

Value of N	Error for full sized (%)	Error for physical model (%)
5	6.34	1.17
10	0.546	0.273
15	0.257	0.111
20	0.100	0.0929

Table 2.1: Accuracy of the different numbers of couples compared to the kernel obtained from the added mass.

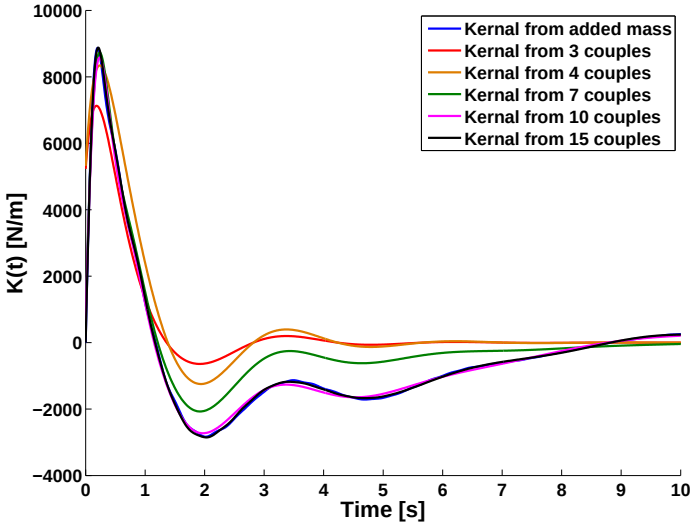

Figure 2.6: The $K(t)$ function obtained from the added mass, and from the summation of exponential functions.

From Equation 2.25	Equivalent from Equation 2.22
$a(x)$	0
$b(x)$	t
$f(x,t)$	$\alpha_n e^{\beta_n(t-\tau)}\frac{dx_e(\tau)}{d\tau}$
t	τ
x	t

Table 2.2: Table showing the relationships between $I_n(t)$ and the method of *differentiating under the integral sign*.

manipulated to obtain Equation 2.22.

$$I(t) = \int_0^t \sum_{n=1}^{N} \alpha_n e^{\beta_n(t-\tau)}\frac{dx_e(\tau)}{d\tau}d\tau,$$
$$I(t) = \sum_{n=1}^{N}\int_0^t \alpha_n e^{\beta_n(t-\tau)}\frac{dx_e(\tau)}{d\tau}d\tau = \sum_{i=1}^{N} I_n, \tag{2.22}$$

where

$$I_n(t) = \int_0^t \alpha_n e^{\beta_n(t-\tau)}\frac{dx_e(\tau)}{d\tau}d\tau. \tag{2.23}$$

The derivative of I_n with respect to time is obtained using the mathematical technique *differentiating under the integral sign*, which states that assuming the functions are continuous and Equation 2.24 holds,

$$F(x) = \int_{a(x)}^{b(x)} f(x,t)dt, \text{ where } x_0 \le x \le x_1. \tag{2.24}$$

Then the differential of $F(x)$ with respect to x can be calculated using Equation 2.25,

$$\frac{d}{dx}F(x) = \left(\frac{\partial F}{\partial b}\right)\frac{db}{dx} - \left(\frac{\partial F}{\partial a}\right) + \int_{a(x)}^{b(x)}\frac{\partial}{\partial x}f(x,t)dt,$$
$$= f(x,b(x))b'(x) - f(x,a(x))a'(x) + \int_{a(x)}^{b(x)}\frac{\partial}{\partial x}f(x,t)dt, \tag{2.25}$$
$$\text{for } x_0 \le x \le x_1.$$

where, for the time derivative of Equation 2.23, Table 2.2 has the equivalent terms in Equation 2.25.

By setting $g(t,\tau) = \alpha_n e^{\beta_n(t-\tau)}\frac{dx_e(\tau)}{d\tau}$, the equivalent of $f(x,t)$, results in Equation 2.26,

$$\begin{aligned} \dot{I}_n &= g(t,t).1 - g(t,0).0 + \int_0^t \frac{\partial}{\partial t} g(t,\tau)d\tau, \\ &= \alpha_n e^{\beta_n(t-t)}\frac{dx_e(t)}{dt} + \int_0^t \beta_n\alpha_n e^{\beta_n(t-\tau)}\frac{dx_e(\tau)}{d\tau}d\tau, \\ \dot{I}_n &= \beta_n I_n + \alpha_n \frac{dx_e}{dt}. \end{aligned} \tag{2.26}$$

Therefore, we have the differential equation for $I_n(t)$, using only the α_n and β_n couples, and the instantaneous velocity of the external cylinder.

2.4.1 Runge-Kutta

The fourth order Runge-Kutta numerical method is based on a numerical integration that uses a weighted average to obtain a more accurate numerical code than lower order methods for the same sized time step (Greenberg, 1998). The basic equations are given in Equation 2.27.

$$\begin{aligned} y_{n+1} &= y_n + \frac{1}{6}(k_1 + 2k_2 + 2k_3 + k_4), \\ \text{where} & \\ k_1 &= hf(x_n, y_n), \\ k_2 &= hf(x_n + \frac{h}{2}, y_n + \frac{1}{2}k_1), \\ k_3 &= hf(x_n + \frac{h}{2}, y_n + \frac{1}{2}k_2), \\ k_4 &= hf(x_{n+1}, y_n + k_3), \end{aligned} \tag{2.27}$$

where h is the time step and $f(x,y)$ is the function to be evaluated.

A fourth order Runge-Kutta numerical method was used on Equations 2.1 and 2.2. The radiation force was obtained from the added mass at infinity and from the α_n,β_n couples. Equation 2.26 was used to find the differential of $I(t)$ with respect to time. To numerically obtain the time domain results, the MATLAB function *"ode45"* was used. This function uses a variable step size. The input values and their differentiated outputs are presented in Table 2.3.

The initial positions and velocities of the internal mass and cylinder are zero. This is assuming that the body starts at rest, with the mass and cylinder positioned at their SWL positions. The values of the I_n and $\dot{I}_n$ are also zero at $t = 0$.

Value	Differential
x_e	$\dot{x}_e$
$\dot{x}_e$	$\frac{F_e+F_r+F_{PTO}-Sx_e-I(t)}{M_e+m_\infty}$
x_i	$\dot{x}_i$
$\dot{x}_i$	$\frac{-F_{PTO}}{M_i}$
I_n	$\beta_n I_n + \alpha_n \frac{dx_e}{dt}$, for $n = 1$ to N

Table 2.3: The differentials that are used in the numerical solver.

2.5 Modelling the different PTOs

2.5.1 Linear PTO

The linear PTO combines the linear spring and the linear bi-directional damper. The PTO force in this case is shown in Equation 2.28,

$$F_{PTO} = k(x_e - x_i) + c_{linear}(\dot{x}_e - \dot{x}_i). \tag{2.28}$$

where k [N/m] is the linear spring constant and c_{linear} [Ns/m] is the linear damping constant.

2.5.2 Quadratic PTO

The quadratic PTO is modelled as a combination of a linear spring and a quadratic damper. The equation for the PTO force is,

$$F_{PTO} = k(x_e - x_i) + c_{hydraulic}(\dot{x}_e - \dot{x}_i)|\dot{x}_e - \dot{x}_i|, \tag{2.29}$$

where $c_{hydraulic}$ [Ns^2/m^2] is the quadratic damping constant.

2.5.3 Mono-directional PTO

The mono-directional PTOs provide a resistive damper force for when the damper is either expanding or contracting and no damping force in the opposite direction. This is modelled as an *"if loop"*. When the relative velocity experienced by the expansion damper is causing the damper to expand the PTO force is calculated from Equation 2.30, and, when the damper is contracting, the force is calculated from Equation 2.31.

$$\text{if } (\dot{x}_e - \dot{x}_i) > 0,\ F_{PTO} = k(x_e - x_i) + c_{MD-E}(\dot{x}_e - \dot{x}_i), \tag{2.30}$$

$$\text{if } (\dot{x}_e - \dot{x}_i) \leq 0,\ F_{PTO} = k(x_e - x_i), \tag{2.31}$$

where c_{MD-E} [Ns/m] is the expansion mono-directional damping constant.

For a compression damper, the PTO forces are shown in Equations 2.32 and 2.33,

$$\text{if } (\dot{x_e} - \dot{x_i}) < 0,\ F_{PTO} = k(x_e - x_i) + c_{MD-C}(\dot{x_e} - \dot{x_i}), \tag{2.32}$$

$$\text{if } (\dot{x_e} - \dot{x_i}) \geq 0,\ F_{PTO} = k(x_e - x_i), \tag{2.33}$$

where c_{MD-C} [Ns/m] is the compression mono-directional damping constant.

2.5.4 Endstop PTO

The endstop PTO comprises a linear damper and either one endstop damper positioned (in this thesis) above the internal mass or two endstop dampers positioned both above and below the internal mass. The linear damper exerts a resiting force over the entire time duration when there is relative motion. The endstop damper only exerts a resistive force when the position of the internal mass is a set distance away from its SWL position and the endstop damper is being compressed. The distance from the SWL position of the internal mass to the endstop damper(s), and the damping constant of the endstop damper(s) and the linear damper are variables.

The PTO force with two endstop dampers combined with a linear spring and damper, is presented in Equations 2.34 and 2.35,

$$\text{if } (x_e - x_i) > A \text{ and if } (\dot{x_e} - \dot{x_i}) > 0 \text{ or if } (x_e - x_i) < A \text{ and if } (\dot{x_e} - \dot{x_i}) < 0,$$

$$F_{PTO} = k(x_e - x_i) + (c_{endstop} + c_{linear})(\dot{x_e} - \dot{x_i}), \tag{2.34}$$

$$\text{else, } F_{PTO} = k(x_e - x_i) + c_{linear}(\dot{x_e} - \dot{x_i}). \tag{2.35}$$

where A [m] is the distance that the endstop damper is positioned away from the SWL position of the internal mass, and $c_{endstop}$ [Ns/m] is the endstop damping constant.

For the PTO with one endstop damper above the internal mass, the PTO force would be

$$\text{if } (x_e - x_i) < A \text{ and if } (\dot{x_e} - \dot{x_i}) < 0,$$

$$F_{PTO} = k(x_e - x_i) + (c_{endstop} + c_{linear})(\dot{x_e} - \dot{x_i}), \tag{2.36}$$

$$\text{else, } F_{PTO} = k(x_e - x_i) + c_{linear}(\dot{x_e} - \dot{x_i}). \tag{2.37}$$

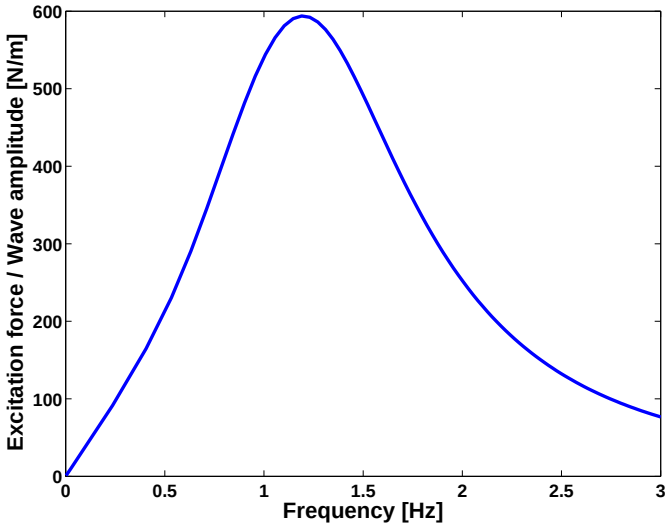

Figure 2.7: The excitation force for unit amplitude incident wave, in surge, for the tank scaled model.

2.6 Friction and unwanted damping of the tank scaled physical model

To summarize the description of the experimental setup (in Chapter 4), the cylinder is kept to move in heave by a stainless steel central rod which is held in place by an upper and lower external rod-end bearings, with Polytetrafluoroethylene (PTFE) liners. The internal mass is also limited to move in heave by being positioned on the central rod. The internal mass has a PTFE bearing in contact with the central rod.

2.6.1 Friction between the rod and the PTFE bearings

The friction that occurs between the central rod and the PTFE bearings has been modelled, using the coefficient of friction between the stainless steel rod and the PTFE bearing liner in air of 0.15 and, in water, of 0.05 (Wang *et al.*, 2009). The excitation force in surge is calculated using results from WAMIT for the different incident wave frequencies, presented in Figure 2.7, and the bearing friction calculated from Equation 2.38. This assumes that the surge force is exerted evenly on the upper and lower bearing, and using an average of the dry and wet bearing coefficient of friction and ignores the effect of any pitching force.

$$F_{bearing\ friction} = 0.1\ F_{surge\ on\ cylinder}. \tag{2.38}$$

2.6.2 Friction on the internal mass

The internal mass has a PTFE bearing and runs in heave upon the stainless steel central rod. Below the internal mass, the spring is positioned on the central rod and at certain points it is in contact with the central rod . The forces on the internal mass in the non-heave directions are caused by the possible imbalance on the internal mass and non-perfect alignment of the internal mass on the central rod. It is assumed that there is a constant static friction caused by any imbalance in the weight, non-perfect alignment and the spring rubbing on the central rod. This constant is determined from placing weights on the internal mass (without any dampers attached) and observing when there is any slight movement of the mass. It was observed that for an 80 g mass there was no movement, but for higher masses there was movement. Therefore, the constant static frictional force is assumed to be 0.8 N $\pm$0.1 N, opposing the relative motion.

2.6.3 Unwanted damping on the internal mass

Between the internal mass and the central rod there is assumed to be a force proportional to the relative velocity of the two bodies. This is calculated from measuring the position of the internal mass, with the Qualysis Motion Capture system (see Section 4.5.1 for a full description) and a single marker attached to the internal mass, recorded at 64 Hz. The internal mass is manually held up (or down) from its resting position, for approximately 1 s, and released. The position of the mass as it returns to its original position, with a certain amount of overshoot, is then recorded. The positions of the internal mass, for both directions of hold, can be seen in Figures 2.8 and 2.9. A close up view showing the occurrence of the recorded data is shown in Figure 2.10. The values are smoothed with a moving average filter which works on the previous 5 values (as discussed in Section 5.5). The position of the internal mass is shifted so that the final resting position for the internal mass after it has been held up or down is zero. Three sets of three data values are obtained from the time when the internal mass is moving from its held position to its SWL position, the overshoot motion is not used. The average position, the average velocity and acceleration is calculated for each set. The unwanted damping is calculated from the equation of motion for the internal mass, for each data set, from Equation 2.39,

$$c_{fric} = \frac{M_i \ddot{x}_i + k x_i}{\dot{x}_i}, \tag{2.39}$$

where c_{fric} [Ns/m] is the frictional damping constant and M [kg] is the weight of the internal mass.

The frictional damping constant was found for 278 different data sets, for both when the mass was held up and held down. The highest and lowest 10% of the results are discarded due to the likelyhood of experimental errors. The mean was found to be 24 Ns/m, with a standard deviation of 17 Ns/m. There was no significant difference in this value for the results from when the mass was held up compared to when the mass was held down.

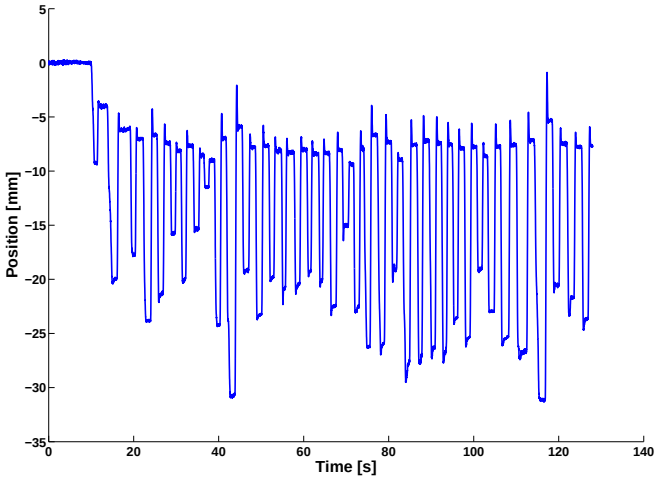

Figure 2.8: The position of the internal mass during calibration of the friction between the internal mass and the external cylinder – the internal mass is held below the rest position and released.

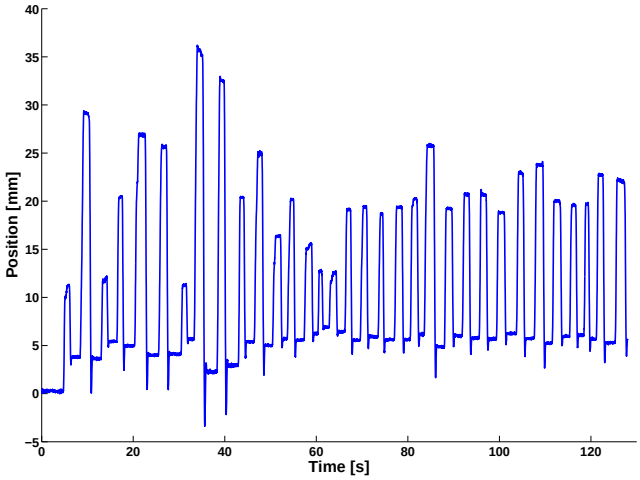

Figure 2.9: The position of the internal mass during calibration of the friction between the internal mass and the external cylinder – the internal mass is held above the rest position and released.

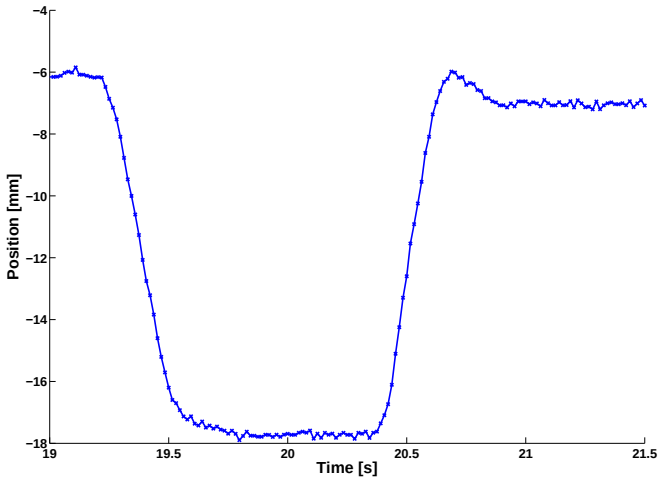

Figure 2.10: A closer view of the position of the internal mass during calibration of the friction between the internal mass and the external cylinder – the internal mass is held above the rest position and released.

The error in the calculation of the damping is large, which implies that the equation of motion used to determine the damping constant does not include all the variables that are affecting the results. The variables not included are

- when the spring comes into and out of contact with the rod,
- the dynamic friction,
- any nonlinear relationships between the relative velocity and the fricitional damping forces.

However this value of the frictional damping constant does give an approximate indication of the unwanted damping between the internal mass and the central rod that occurs when the cylinder is experiencing incident waves, regardless of what other PTO damping is present.

2.6.4 The influence of these frictional effects

The inclusion of these frictional effects affect the outcomes from the numerical simulation. A 0.8 Hz regular wave of 0.2 m amplitude, was tested with the numerical simulation, sized for the experimental model, with a spring constant of 200 N/m, and an expansion mono-directional damper, with a damping constant of 300 Ns/m.

The effect of the friction from the surge force on the external PTFE bearings and the central rod is presented in Figure 2.11, on both the positions and velocities of the external cylinder, the internal mass and the relative motion between the bodies. A reduction of both the positions and velocities of both the cylinder and internal mass is observed, leading to a reduction in the relative motion and velocity.

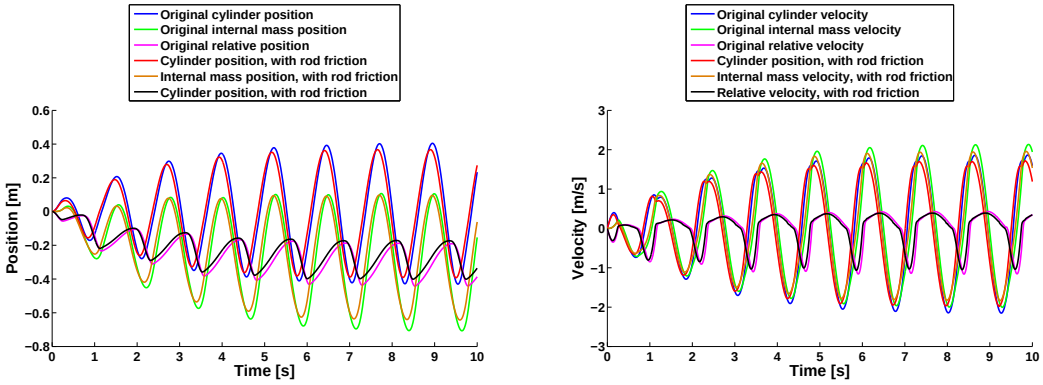

(a) Positions of the bodies. **(b)** Velocities of the bodies.

Figure 2.11: The original positions and the velocities, compared with the positions and velocities with friction from between the central rod and the external bearings included.

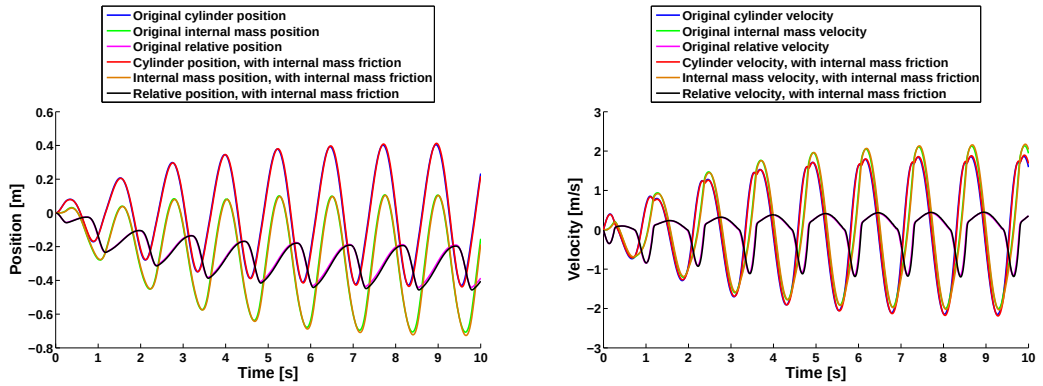

(a) Positions of the bodies. **(b)** Velocities of the bodies.

Figure 2.12: The original positions and the velocities, compared with the positions and the velocities with friction from between the internal mass and the central rod included.

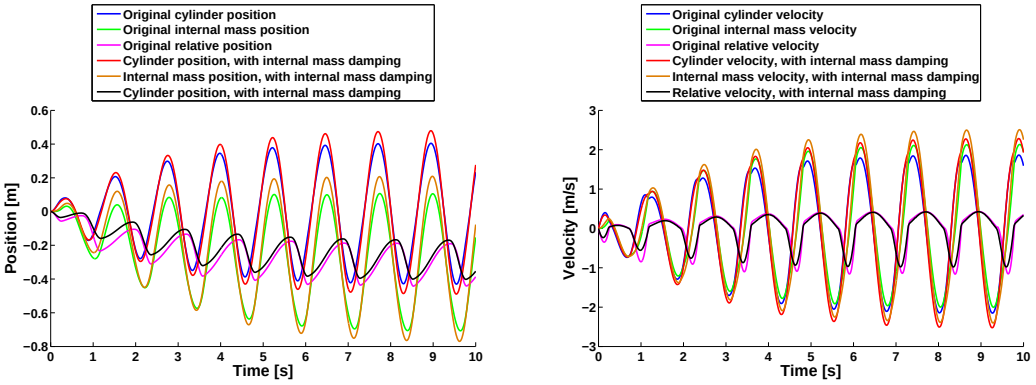

(a) Positions of the bodies. **(b)** Velocities of the bodies.

Figure 2.13: The original positions and the velocities, compared with the positions and the velocities with damping from between the internal mass and the central rod included.

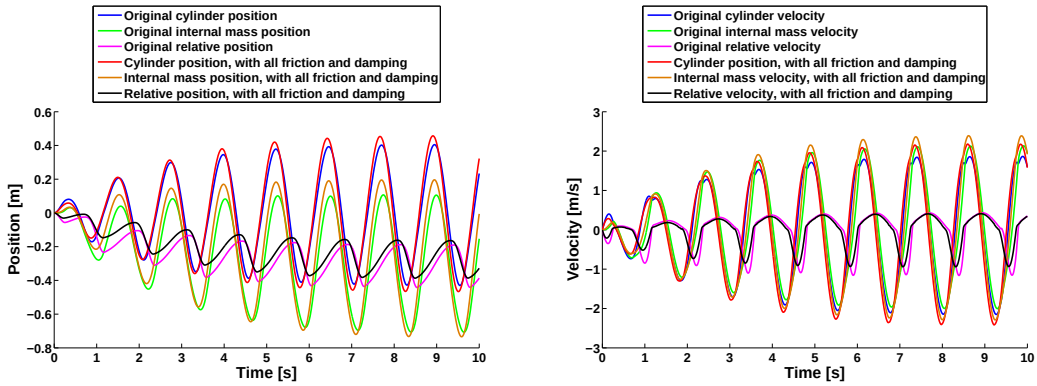

(a) Positions of the bodies. **(b)** Velocities of the bodies.

Figure 2.14: The original positions and the velocities, compared with the positions and the velocities with all the unwanted frictions and damping included.

The effect of the constant frictional force between the internal mass and the cylinder is presented in Figure 2.12. There is very little influence of this frictional force on the motions of the cylinder and the internal mass, in this example.

The effect of the frictional damping between the internal mass and the cylinder is presented in Figure 2.13. There is increased motion in both the cylinder and the internal mass positions, which results in a reduction in the relative motion, for both the positions and the velocities.

All these effects are combined in Figure 2.14 and shown compared to the numerical simulation with no unwanted friction or damping. In this example, the total influence of all the combined frictions and damping has increased the cylinder's maximum amplitude by 10.6%, the internal mass' maximum amplitude by 14.5%. Therefore, the maximum relative motions between the bodies has decreased by an amplitude of 11.6%. The phase of all the positions has also changed. For the velocities, the cylinder and internal mass absolute maximum velocity increased by 14.4% and 13.3% respectively, and the relative maximum velocity decreased by 15.7%. These would also lead to a reduction in the calculated power extracted.

All the tank scaled numerical simulations in this thesis, will include these unwanted frictional and damping effects, in order to produce more accurate simulations.

Chapter 3

Results from the numerical simulation

3.1 Summary

This chapter presents results from the numerical simulation of the full sized device, considering the linear, quadratic, mono-directional and endstop dampers. The results from the quadratic damper PTO have been reproduced in Bailey and Bryden (2011). For each of the different PTO types, the time series is discussed and spectral analysis of the body positions are presented. The effect of varying the PTO parameters on the power extracted, the integrated displacement (the total relative distance traveled) and the average maximum accelerations are also presented.

In Section 3.2, different types of spectral analysis are discussed and presented, including the linear transfer function and the coherency function. In Section 3.3 results for the linear damper are presented, primarily as a basis to compare the nonlinear PTOs against. Section 3.4 presents results for the mono-directional dampers.The quadratic PTO is presented in Section 3.5, with results and discussion. Section 3.6 presents the results for endstop damper(s), in addition to a linear damper, for both a single endstop damper and two endstop dampers each positioned either side of the internal mass. In Section 3.7 results from the chapter are discussed and briefly concluded, especially with respect to comparing the different PTO types. To aid clarity, the figures for this chapter are presented in Section 3.8 and grouped for ease of comparison between the different damper types.

3.2 Spectral analysis

A nonlinear system, for which there are no sudden changes, can be modelled as (Schetzen, 1989),

$$y(t) = \Sigma_{n=0}^{\infty} \left(\int_{-\infty}^{\infty} \int_{-\infty}^{\infty} \dots \int_{-\infty}^{\infty} h(\tau_1, \tau_2, \dots \tau_n) x(t-\tau_1) x(t-\tau_2) \dots x(t-\tau_n) d\tau_1 d\tau_2 \dots d\tau_n \right) \tag{3.1}$$

where x is the input and y is the output time signal. The time is denoted by t and τ is a dummy variable related to time. $h(\tau_1, \tau_2, ..., \tau_n)$ are called the Volterra kernels of the system (Hall, 1991). For a linear system, $h(t, \tau)$ is the response of this system, when subjected to a unit impulse at time, τ.

Equation 3.1 is typically truncated in order to approximate a real system. Allowing only the first order terms results in an equation that can model a linear system. Including the second order terms as well, defines a system where there are only linear and quadratic components.

This equation is truncated and is manipulated to form the Linear Transfer Function (LTF) and the Quadratic Transfer Function (QTF) (Tick, 1961), as defined in Equations 3.2 and 3.3 respectively,

$$H_1(f) = \frac{S_{xy}(f)}{S_{xx}(f)}, \tag{3.2}$$

$$H_2(f_1, f_2) = \frac{1}{2}\frac{B_{xxy}(f_2, f_2)}{S_{xx}(f_1)S_{xx}(f_2)}, \tag{3.3}$$

where

$$\begin{aligned} S_{xx}(f) &= E\left[\frac{\Delta t}{N}X^\star(f)X(f)\right], \\ S_{xy}(f) &= E\left[\frac{\Delta t}{N}X^\star(f)Y(f)\right], \\ B_{xxy}(f_1, f_2) &= E\left[\frac{(\Delta t)^2}{N}X^\star(f_1)X^\star(f_2)Y(f_1+f_2)\right], \end{aligned}$$

and E denotes the expectation operator, and the superscript * denotes a complex conjugate. A sampling rate of $\frac{1}{\Delta t}$ [1/s] and a length of N is used.

The QTF detects the quadratic phase coupling which occurs in a nonlinear system due to some coherency between the phases of the spectral values (Worden and Tomlinson, 2001). The quadratic phase coupling (Nikias and Petropulu, 1993) causes contributions to the power at the sum and / or difference frequencies.

When the system can not be easily identified as a linear or quadratic (or cubic etc.) system, then another way to look at the influence of the nonlinearities is to compare the LTF and the Response Amplitude Operator (RAO) and to look at how accurately the LTF models the actual system. For a completely linear system the LTF and the RAO should be identical, in the absence of extraneous noise.

The RAO is the ratio of the amplitude of the motion of the body to the wave amplitude. It is calculated using single frequency waves, where the wave height and the average amplitude of motion, after any transient affects have decayed, are recorded. Multiple experiments are

completed to build up the RAO over a range of frequencies.

The difference between the LTF and the RAO is due to the presence of nonlinearities in the system. However, since the LTF is calculated from considerations of the phase of the input and output signal, the difference compared the RAO, is due to the nonlinearities affecting the magnitude of the response of the bodies, when the waves experienced are an irregular mix of frequencies, as opposed to a regular single frequency wave.

The nonlinearities often also result in output frequencies that are not directly part of the input frequencies. These tend to happen when the input is a combination of frequencies to get additional related output frequencies - for example, for a quadratic system additional frequencies tend to occur at the sum and / or difference frequencies.

The LTF only considers when the phases of the input and output time series coincide, and only uses the first term in the Volterra Series (of Equation 3.1). To clarify, it only states that the output is connected to the input by

$$Y(f) = \text{LTF} \times X(f) + \text{Nonlinear components} + \text{Noise}. \tag{3.4}$$

The coherency function provides an indication of the nonlinear components that are not being modelled by the LTF. The coherency is the square root of the ratio of the expected response from the averaged transfer functions to a single measured response (Hall, 1991). For a perfectly linear system, the coherency will be one, for all frequencies. However, nonlinear components will result in the coherency not being equal to unity (as will noise in the measured response, which is more relevant for experimental testing). For a system modelled only with a LTF [1], the coherency is calculated from

$$\gamma^2(f) = \frac{|H_1(f)|^2 S_{xx}(f)}{S_{yy}(f)}, \tag{3.5}$$

where $H_1(f)$ is the LTF which has been calculated from the expectation operator, i.e., the average of a number of S_{xy} and S_{xx} values which have experienced waves with different randomly assigned phases. The S_{xx} and S_{yy} values are obtained from a seperate single numerical simulation.

1. A more complex form of Equation 3.5 is used for higher order transfer functions.

3.3 Linear dampers

To ascertain what influence the nonlinearities have on the body's motion and power extraction and for comparison between the different damper types, the results for the linear PTO setup are presented.

3.3.1 Time series

The time series for a 0.1 Hz peak frequency PM spectrum sea state for predetermined random phases is used for comparison for all the different damper types. The first 100 s of results are presented, starting from rest. The data is collected at a sampling frequency that is high enough to produce representative results.

The time series results showing the positions of the cylinder and the internal mass and the relative position between them are presented in Figure 3.1. The PTO parameters are a spring constant of 0.45 MN/m and a damping constant of 0.2 MNs/m. The figures show a smooth response of the bodies and their relative position.

The absolute and relative velocities of this PTO setup are presented in Figure 3.2. This figure shows how the absolute velocity has similar properties for both positive and negative relative velocities. The instantaneous power extracted is presented in Figure 3.3 and the cumulative power extracted is presented in Figure 3.4, where the power is extracted over the entire time period.

3.3.2 Optimal parameters

A criterion to choose the ideal PTO parameters is required. In this thesis, it is assumed that the WEC needs to provide significant amounts of power while the device needs to be reliable in standard sea conditions.

Power extraction

The time averaged power extracted, measured and sampled at 10 Hz is calculated for a range of spring and damping constants. The PM spectrum sea has equally spaced frequencies with a separation of 0.0032 Hz (0.02 rad/s) and within the range $\frac{0.05\sqrt{6}}{\pi} \leq f \leq \frac{0.05\sqrt{6}+1}{\pi}$. The phases were randomly selected between 0 and 2π with a uniform distribution. The sample was measured over a 1000 s time period, although the repeat time of the system was 312.5 s, so a sample time period of 937.5 s would have been better. Figure 3.11 presents contour plots of the power extraction.

Reliability

The total relative distance or the integrated displacement that the internal mass moves and

Damper type		Power [MW]	Spring [MN/m]	Damper [MNs/m] [MNs^2/m^2]	Distance [m]	Acc'n [m/s^2]
Linear	Max	0.263	1.5	4.4	345	0.819
	2nd max	0.260	0.1	0.95	1271	3.609
Quadratic	Max	0.304	1.5	0.1	1191	3.228
	2nd max	0.284	4.5	2.5	385	1.788
Expansion MD	Max	0.266	3.0	4.0	374	3.315
	2nd max	0.259	0.2	0.95	1254	4.023
Compression MD	Max	0.267	3.5	4.0	351	3.341
	2nd max	0.258	0.3	0.9	1014	4.193

Table 3.1: The maximum and secondary local maximum power extraction and their corresponding spring and damping constants, and the associated integrated displacement and the average of the highest 1% of accelerations, for linear, quadratic and mono-directional dampers.

the value of the average of the largest 1% of the relative accelerations that it experiences are indications of the reliability of the WEC, with respect to the motion of the PTO. A greater relative distance traveled will result in the spring, the damper and the bearings between the bodies operating over a greater relative distance resulting in more wear and maintenance requirements. The relative accelerations result in higher forces on the spring, the damper and the bearing system. Therefore, for a more reliable system, both these values should be as low as possible.

The total distance that the internal mass has traveled relative to the cylinder, over 1000 s, is summated and presented in Figure 3.12. The colour bar shows the total distance travelled for varying spring and damping constants. This range is from 2000 m, which is presented as blue on the figure to 12000 m, which is presented as red, with a linear scale between these values represented using a standard Matlab colour scheme. This figure shows much higher distances are traveled for low values of spring and damper constants.

The average of the top 1% of accelerations over the 1000 s time period is presented in Figure 3.13. This shows that having an increased spring constant results in higher accelerations, while increasing the damping constant results in lower maximum accelerations.

The power extracted contour plot shows two distinct maximums, which are presented in Table 3.1, along with the associated distance traveled and maximum accelerations. The highest power extracted spring and damper parameters also have low values of relative motion and acceleration. Therefore, for this PTO setup, the PTO parameters should be 1.5 MN/m and 4.4 MNs/m for the spring and damper, respectively, for optimal power extraction and reliability.

3.3.3 Spectral analysis

Ten runs of 3140 s, sampled at 0.0076 s intervals, were completed, for different randomly generated phases with a uniform distribution. The repeat time of the run was 314 s. A higher sampling frequency and a longer sampling time than the previous sections was used to allow for more detail in the frequencies of interest in the FFT analysis. The FFT function operated on the separate runs, using a vector length of 524288. The LTF was calculated using the average of these runs (as in Equation 3.2) and is presented in Figure 3.18. The PTO parameters are a linear spring constant of 0.4 MN/m and a linear damping constant of 0.2 MNs/m. The RAO is calculated from using the same frequencies as are in the PM spectrum sea. These single frequency waves are run for 64 s and the average amplitude of the wave and bodies are recorded, after any transient responses have decayed. The RAO is also presented in Figure 3.18. The coherency of the LTF is calculated from the LTF and an additional 3140 s run and is also presented in the same figure.

The RAO is consistently slightly higher than the LTF for the vast majority of all the frequencies. At the resonant peak, which occurs at the same frequency, the RAO is approximately 10% higher than the LTF. This proportion increases slightly at frequencies away from the resonant peak but where there is still a substaintial response. The coherency function is close to one over the frequency range near resonance. Lower frequencies and much higher frequencies have a coherency function that is consistantly lower than one.

The small difference between the LTF and the RAO, and the coherency function that is not always unity, shows that there are some nonlinearities in the system. These could be from a combination of,

- the truncation and Prony's approximation of the radiation force.
- Numerical errors from the level of accuracy chosen in the WAMIT package, for the excitation force and the added mass and damping.

However, as will be presented in this chapter, these difference are smaller than when there is a nonlinear PTO.

3.4 Mono-directional dampers

3.4.1 Time series

The two directions of the mono-directional dampers are compared to each other and to the linear damper. The time series of the positions is visually compared in Figure 3.1 and the velocities are visually compared in Figure 3.2. These are for the first 100 s of a 0.1 Hz peak frequency PM spectrum sea. The instantaneous power extracted is presented in Figure 3.3 and the cumulative power extracted is presented in Figure 3.4.

The positions of the cylinder and the internal mass and their relative positions show obvious influence from the mono-directional dampers. For the local minima of the relative motion, the expansion mono-directional damper is at a more negative position than the linear and compression mono-directional dampers. For the local maxima of motion, the compression mono-directional damper has the largest relative position, with the linear and expansion mono-directional dampers having lower relative positions.

The absolute velocity of the cylinder and the internal mass changes depending on the type of damper used. The differences are also apparent when the relative velocity is studied. The mono-directional dampers relative velocities are different to the linear damper, especially at either the upper or lower components of the motion where higher frequency oscillations occur.

The instantaneous power emphasizes how the linear damper extracts power over the entire time period while the mono-directional dampers only extract power during either expansion or compression of the damper. When the mono-directional dampers are extracting power, the instantaneous power that they extract is greater than the equivalent power extracted from the linear damper.

3.4.2 Optimal parameters

Power extraction

The power extracted from the mono-directional dampers for varying linear spring and mono-directional damping constants is presented in Figure 3.11. The compression and expansion mono-directional results show a near identical amount of power extracted, across the varying parameters. Both dampers have two distinct peaks, where the power extraction is largest. Table 3.1 shows the value of these peaks and the associated reliability parameters.

Reliability

The total relative distance traveled and the average of the highest 1% of relative accelerations are presented in Figures 3.12 and 3.13.

Table 3.1 shows how the PTO parameters with the largest power extraction also coincide with the local maxima that has the lowest accelerations and the total distance traveled. Therefore, these parameters, based on the pre-mentioned criteria, are the optimal values.

3.4.3 Spectral analysis

The LTF, RAO and the corresponding coherency function are presented in Figures 3.19 and 3.20, for the expansion and compression mono-directional dampers respectively. These have been calculated using the same techniques as described in Section 3.3.3. The mono-directional dampers have a spring constant of 0.4 MN/m and a damping constant of 0.2 MNs/m.

The RAO for the mono-directional dampers is consistently significantly higher than the equivalent LTF. This is an indication of the nonlinearities present. Additionally, there is a LTF response at frequencies around 0.25 Hz, where the RAO response is small. This also indicates that there are non-linearities in the system.

For frequencies of less than 0.2 Hz, the coherency function implies that the LTF is accurately representing the system in irregular seas. Above this frequency, the coherency function fluctuates and is much greater than unity. This is due to the LTF not accurately representing these frequencies.

3.5 Quadratic PTO

3.5.1 Time series

The time series for 100 s of motion is presented in Figure 3.5. This figure shows the positions and velocities of the cylinder, internal mass and the relative motion between them. The power extracted, both shown instantly and cumulatively is presented in Figure 3.6. The PTO parameters for this time series are a linear spring constant of 0.45 MN/m and a quadratic damping constant of 0.2 MNs^2/m^2.

The positions and the velocities closely resemble those of the linear damper. However, the instantaneous power extracted is consistently less than the values of the linear damper, over the time period shown.

3.5.2 Optimal parameters

Power extraction

The power extracted when varying the spring and quadratic damper is presented in Figure 3.11. This shows two distinct peaks of local maximum power extraction. Away from these two maxima, the power extracted reduces, especially for increasing spring and damping constants.

Reliability

The integrated displacement and the total average of the highest 1% of accelarations are presented in Figures 3.12 and 3.13, respectively.

Table 3.1 shows the local maximum values for the power extracted. The table also shows the relative distance traveled and the average highest for these parameters.

When the two local peaks of the power extraction are considered, and when these are cross referenced to the associated integrated displacement and the large accelerations, the peak with the lower power extraction has lower accelerations and relative distance traveled. This implies that for a WEC developer, it may be worth choosing parameters that result in slightly less power extracted (a reduction of 0.02 MW or 7%) in exchange for potentially increased reliability.

3.5.3 Spectral analysis

The LTF, RAO and the coherency function are calculated as described in Section 3.3.3 and presented in Figure 3.21. The PTO parameters are a linear spring constant of 0.4 MN/m and a quadratic damping constant of 0.2 MNs^2/m^2.

The difference between the LTF and the RAO is significant for the quadratic damper PTO. The shape of the LTF has a wider range of frequencies that produce the maximum value than the RAO and is shifted to the right. The response of the RAO is approximately double the LTF response, over a wide range of frequencies. This is a strong indicator of nonlinear components in the signals.

The coherency for the frequency region where there is the greatest LTF and RAO response, is close to one. Outside of this range, the coherency is not near to unity, for low frequencies the internal mass coherency is c. 2. At higher frequencies, there is a lot of fluctuation in the coherency function, especially for the cylinder, and the value for the coherency function varies between 0.2 and 2.4.

The coherency functions shows that the LTF is a good indicator of the response of the function in a mixed frequency sea state, at frequencies around resonance. Outside of the resonant frequencies, it is a less accurate indicator.

3.6 Endstop PTO

The device has been tested with endstop damper(s), which could be referred to as peripheral damper(s), to see how they influence the time series response, the power extracted, the relative distance that the internal mass travels, the maximum accelerations of the internal mass and the spectral analysis.

The damping constants are chosen so that the influence of the endstop damper(s) is clear, with the endstop dampers having 20 MNs/n damping constants compared to the linear dampers 0.2 MNs/m damping constant. This difference was chosen as it was deemed important that the endstop effects were the most prevalent in the systems investigated.

The two setups tested are: a single endstop damper that is placed 0.5 m above the SWL position of the internal mass, and two endstop dampers placed both 0.5 m above and 0.5 m below the SWL position of the internal mass.

For high endstop damping constants, the endstop dampers effectively force a maximum amplitude of relative motion. At lower endstop damping constants, the endstop damper(s) extract energy at the peripherals of the larger relative motions that occurs.

3.6.1 Time series

Single endstop

The time series results for an endstop damper, with a linear damping constant of 0.2 MNs/m and a linear spring of 0.45 MN/m, positioned 0.5 m from the SWL position of the internal mass with an endstop damping constant of 20 MNs/m, are presented in Figure 3.7. The time series results show the positions and velocities of the two bodies and the relative position and velocity between them, and the instantaneous power extracted from both the linear damper and the endstop damper.

The relative position shows a clear line where the influence of the endstop damper affects the internal mass, with very limited motion occurring above this virtual line. The relative velocity is also highly influenced by the presence of the endstop damper.

The instantaneous power extracted from the linear damper was presented in Figure 3.8 were significantly less regular than when no endstop damper is present. The power extracted from the endstop damper was very intermittent but was large during the short periods that it did occur. The total power extracted, in this case, was larger for the linear dampers than for the endstop dampers.

Two endstops

Endstop dampers are positioned both above and below the internal mass, away from its SWL position. These dampers both have the same endstop damping constant, and the same distance from the endstop dampers to the SWL of the internal mass.

Figure 3.9 presents an example of the time series of the absolute and relative positions and velocities of the cylinder and internal mass.

The time series results for when the two endstop dampers are present is similar to when there is a single endstop damper. The exception to this is that the relative position is effectively limited in both directions, which results in the relative velocity having twice as many periods of zero or near zero velocity.

The instantaneous power extracted is presented in Figure 3.10 alongside the cumulative power extracted. This is again, similar to the single endstop damper in style, although the power extracted from the endstop damper is greater than from the linear damper.

3.6.2 Optimal parameters

Single endstop

Power extraction

The power extraction has been calculated for various endstop damping constants and distances from the SWL position of the internal mass to the endstop damper. The power extraction is considered for both the linear damper and the endstop damping. The linear spring and damping constant used were 0.4 MN/m and 0.2 MNs/m, respectively. The results are presented in Figure 3.14.

Having a single endstop damper results in an increase in the power extracted from the linear damper, for these parameters. The greatest power extraction from the linear damper occurs when the endstop damping constant is 2.5 MNs/m and the distance from the SWL of the internal mass to the endstop damper is [2] 0 m. The time averaged power extracted for these parameters is 0.75 MW.

The power extracted from the endstop damper is highly variable depending on the endstop parameters chosen. This variability is due to the potentially large damping which occurs in the endstop dampers especially at high endstop damping constants. As such, the power extracted for lower values of endstop damper is also presented. This shows that, as expected, in general the nearer the endstop damper is to the internal mass the more power is extracted from the endstop damper.

Two endstops

The power extracted from the linear damping and the endstop damping is presented in Figure 3.15 for the same linear spring and damping constants as with one endstop damper.

The power from the linear damper is greatest when the distance from the SWL to the endstop damper is 0.75 m, with a 100 MNs/m endstop damper. This is the highest endstop damping constant tested. This implies that the linear damper extracts more energy when the amplitude of its relative motion is limited to a 1.5 m range. The time averaged power extracted, for this sea state was 1.94 MW.

The power extracted directly from the endstop damper is less than from the linear damper (as presented in Figure 3.15). As the endstop dampers position gets nearer to the SWL position of the internal mass, the power extracted from the endstop dampers increases.

Reliability

The integrated displacement is presented in Figure 3.16, for both one and two endstop dampers.

2. The distance is the distance from the SWL of the internal mass to the endstop damper. So with a single endstop damper, a SWL distance of zero implies that the motion is limited in moving in a positive position, and not at all in a negative position.

These both show that for either one or two dampers, the relative distance travelled of the endstop damper is greatest when the distance from the SWL of the internal mass to the endstop damper is highest.

The average of the top 1% of accelerations is presented in Figure 3.17. These figures imply a relationship between when the linear damper extracts the most power and the largest accelerations. As such, to reduce the accelerations and hence increase the reliability of the system would require a significant reduction in extracted power. Therefore, the large accelerations would have to be taken into account in the design of the WEC.

3.6.3 Spectral anaylsis

The LTFs and the RAOs for PTO setups with either one or two endstop dampers are presented in Figures 3.22 and 3.23, respectively. These have linear spring and damping constants of 0.4 MN/m and 0.2 MNs/m, and endstop SWL distance of 0.2 m and endstop damper(s) of 2.0 MNs/m.

The LTFs and the RAOs responses are very similar. The LTFs resonant frequency is shifted to slightly higher frequencies than the associated RAOs, however the height and bandwidth of the resonant response is nearly identical. Both LTFs have additional response at frequencies around 0.25 Hz, as has been seen in other nonlinear PTO setups.

The coherency function is very close to unity for frequencies up to 0.2 Hz, which includes the frequencies where resonance is seen. Above these frequencies, where the LTF has some additional response, the coherency function becomes large and fluctuates considerable.

3.7 Discussion

3.7.1 Comparison between damper types

Power extracted

The power extracted for the different spring and damping constants, for the linear, mono-directional and quadratic dampers, varies. All these damper setups have two local maximums of power extracted. The value of the maximum power extraction for the linear and mono-directional dampers is similar. However, the mono-directional dampers have higher power extraction for the non-optimal damping constants than the linear damper. The quadratic damper has the highest power extraction over a wide range of spring and damper constants.

Since the endstop damper's power extraction concentrates on the effect of different parameters to the other damper types, a comparison between them would be artificial.

Reliability

The linear, mono-directional and quadratic damper types all have the highest relative distance

traveled for the lowest spring and damper constants. The highest values of relative distance traveled are significantly higher than the distance traveled for the PTO parameters that are likely to be chosen due to their high power extraction.

The integrated displacement is generally higher for the mono-directional dampers than for the linear case. The quadratic damper, for the "same" damping constant, has a lower relative distance traveled than the linear damper PTO.

The maximum relative accelerations experienced by the linear, mono-directional and quadratic dampers, have a similar response to the varying spring and damper constants. The mono-directional dampers have a higher average top 1% of accelerations than the linear damper.

Spectral analysis

The LTF and the RAO are the most similar for the linear damper. For the mono-directional and quadratic dampers, the RAO is considerably higher than the associated LTF. This is due to the nonlinearities in the PTO affecting the motion of the two bodies.

The endstop LTF and RAO are similar, with a small frequency shift being the main difference.

The coherency function for the linear damper is closest to one, with the mono-directional dampers being further from unity than the quadratic dampers. Therefore, the LTF is best at representing the linear dampers, and then the quadratic damper and finally the mono-directional dampers. The endstop dampers coherency is very close to one for frequencies lower than 0.2 Hz but above this frequency the coherency is highly fluctuating and at times very large.

For all the damper types, the LTF was best at representing the system at frequencies close to the resonant frequency of the system. Further from the resonance frequency, particularly when additional frequency responses were present in the LTF which were not present in the RAO, the LTF was not as accurate at representing the model, shown by the coherency function being further from unity.

3.7.2 General discussion and conclusions

The information derived from the reliability parameters has allowed us to decide whether the PTO parameters that result in the highest power extraction are desirable for the reliability of the device. If the reliability parameters are high, this could mean that the costs involved with building the WEC are greater, that more maintenance is required and / or that the WEC will be more likely to fail. The results presented in this chapter show that for the linear and mono-directional dampers, the PTO parameters which have the highest power extraction also have low values of the indicators of reliability. Therefore, a designer would, from only considering the parameters discussed, want to build a WEC with these parameters, providing the associated costs are acceptable.

The maximum power extracted from the mono-directional dampers compared to the linear dampers is comparable, with the expansion mono-directional damper extracting 1.1% more and the compression mono-directional damper, 1.5% more. Due to the effects that chosing different randonly generated phases could have on the power extracted, and considering that the sea states would be different, then this difference is small. To obtain the maximum power extraction, the mono-directional dampers require a higher spring constant than the linear dampers, although the damping constants used are similar. The integrated displacement is again compariable. However, the maximum accelerations experienced is much greater for the mono-directional dampers. The mono-directional average maximal acceleration is 4.06 times the maximal accerlation of the linear dampers. The larger accelerations are due to the internal mass moving from when there is no damping force to when there is a damping force present. The question that a developer will need to answer is: whether having a potentially cheaper mono-directional damper will be countered by the costs associated with this increased relative acceleration that the internal mass will experiance, since the power extracted is similar.

The quadratic PTO has a higher maximum accelerations and integrated displacement for the maximum power extraction parameters than for the second highest local maxima. Therefore it is necessary for the developer to make an informed choice about whether the 7% reduction in power extraction is worth the savings associated with having a 68% reduction in the total relative distance travelled and a 45% reduction in the average of the highest 1% of accelerations, for the tested sea state.

The addition of the endstop dampers for the sea state tested, with the model parameters of the linear spring and damping constant as described, resulted in an increase in the power extracted. This is obviously desirable. Having two endstop dampers, as opposed to a single endstop damper, increased the maximum time averaged power extracted from 0.75 MW to 1.94 MW, the two endstop dampers extracted 2.59 times as much as the single endstop damper. However, this assumes a perfect linear damper that can extract energy with a force exactly proportional to the relative velocity. Figure 3.9 shows the time series of an example of a PTO setup with two endstop dampers. From this figure, the relative velocity of the internal mass is shown to be close to zero for the majority of the time, with spikes of large relative velocity as the internal mass moves from one endstop damper to the other. An actual linear damper may have problems with absorbing energy in this “impulsive” form.

When the endstop dampers (both a single and two endstop dampers) are set at the parameters to extract the maximum amount of power, the values for the average of the highest 1% of accelerations are approximately the largest. This would be due to the high accelerations that are experienced when the internal mass collides with the endstop damper. The accelerations increase as the endstop damping constant increases, since the internal mass is colliding with a less compliant object. The accelerations also increase as the endstop SWL distance gets closer to its optimal value, possible due to the internal mass experiancing the highest levels of relative

velocity at these parameters.

The spectral analysis shows the significant differences between the RAO and the LTF, as well the accuracy that the LTF manages to represent the data, especially for the mono-directional and quadratic dampers. This emphasizes the importance of using numerical simulations that can model the nonlinearities present, rather than standard frequency domain models, which would not include these nonlinear effects. It also illustrates how, for both numerical and experimental work, unless there is high confidence that the model is completely linear, the RAO should not be used to estimate the WECs response to mixed frequency sea states. For the mono-directional and quadratic dampers tested in this thesis, using the RAO to estimate the response of the WEC in mixed frequency seas, would result in a significant overestimation of the motions and hence power extracted.

In the next chapters, experimental modelling procedures and results will be presented. In Chapter 7, the numerical simulations will be used to model the 1:40 scale physical model in order to directly compared this to the experimental results. This is done separately to the simulation of the full scale WEC since the model scale is not exact in all dimensions.

3.8 Figures

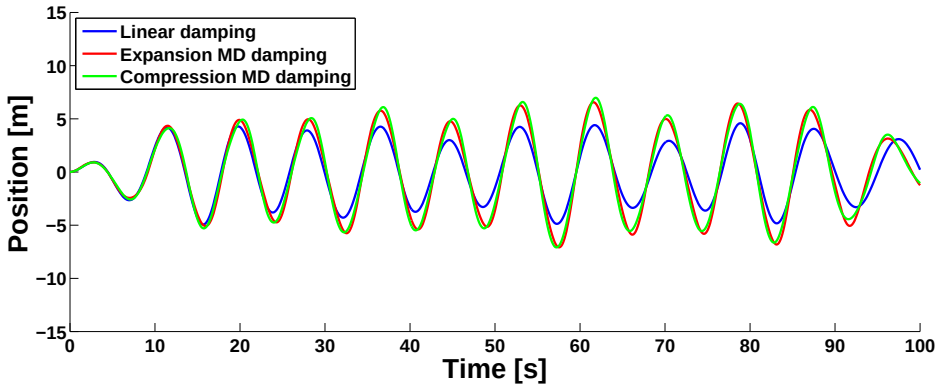

(a) Position of the cylinder.

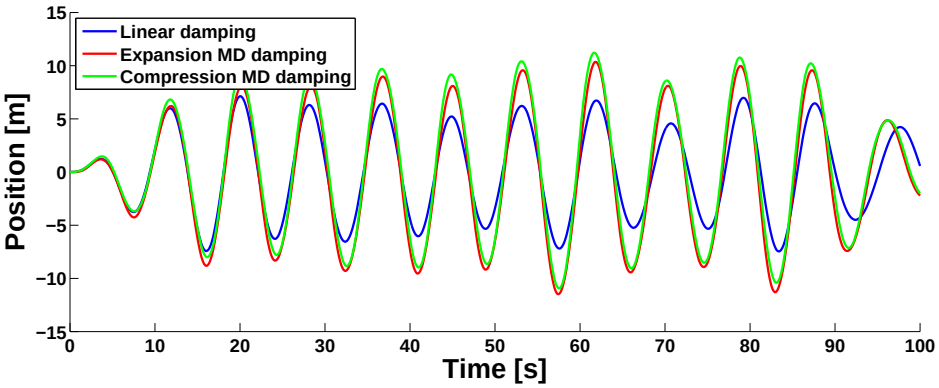

(b) Position of the internal mass.

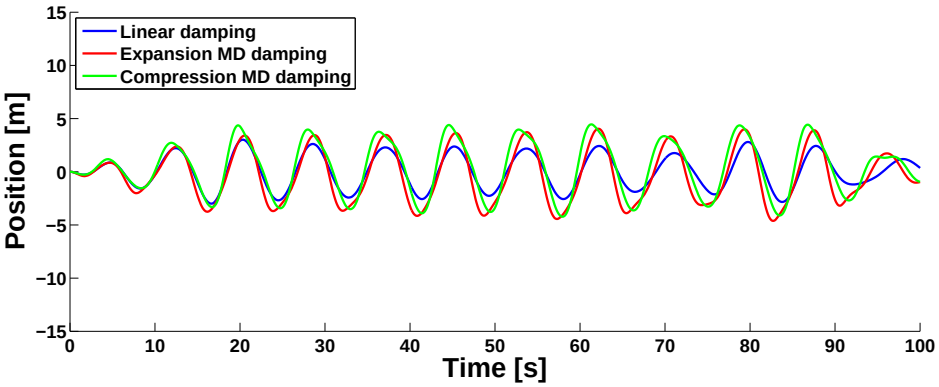

(c) Relative position of the internal mass.

Figure 3.1: The positions of the two bodies and their relative position, for linear and mono-directional dampers, with a linear spring constant of 0.45 MN/m and a damping constant of 0.2 MNs/m.

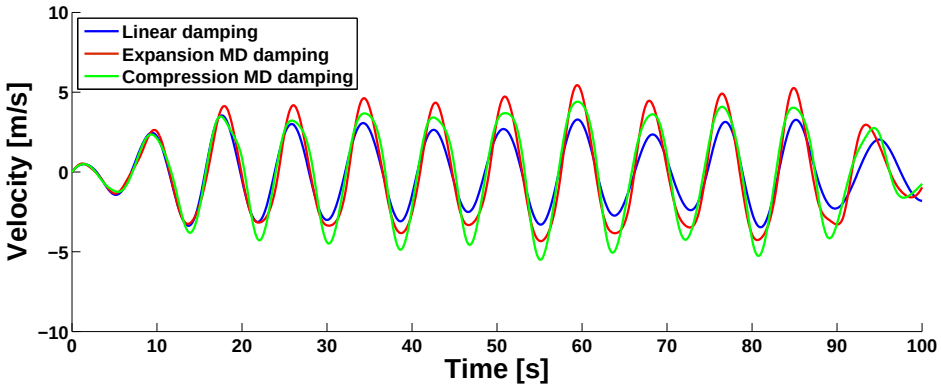

(a) Velocity of the cylinder.

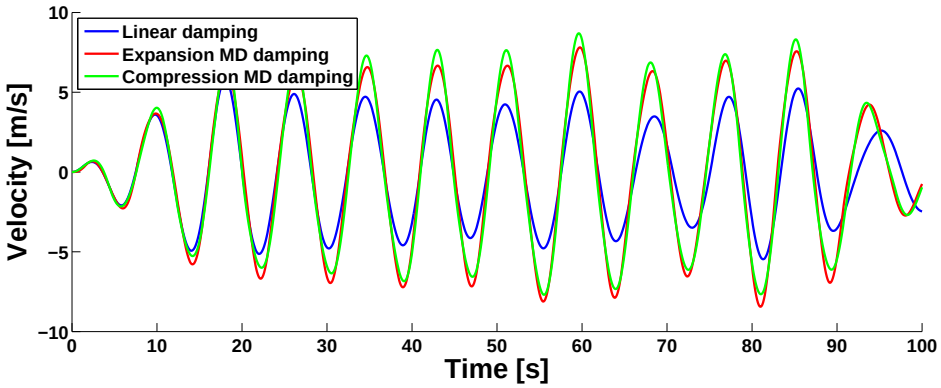

(b) Velocity of the internal mass.

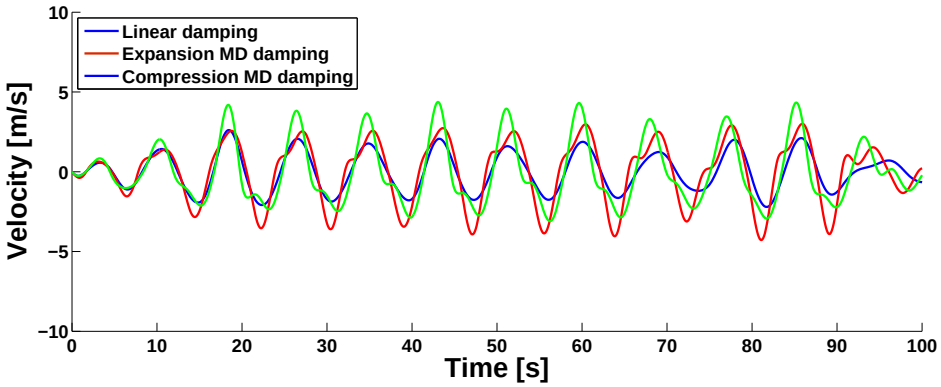

(c) Relative velocity of the internal mass.

Figure 3.2: The velocities of the two bodies and their relative velocity, for linear and mono-directional dampers, with a linear spring constant of 0.45 MN/m and a damping constant of 0.2 MNs/m.

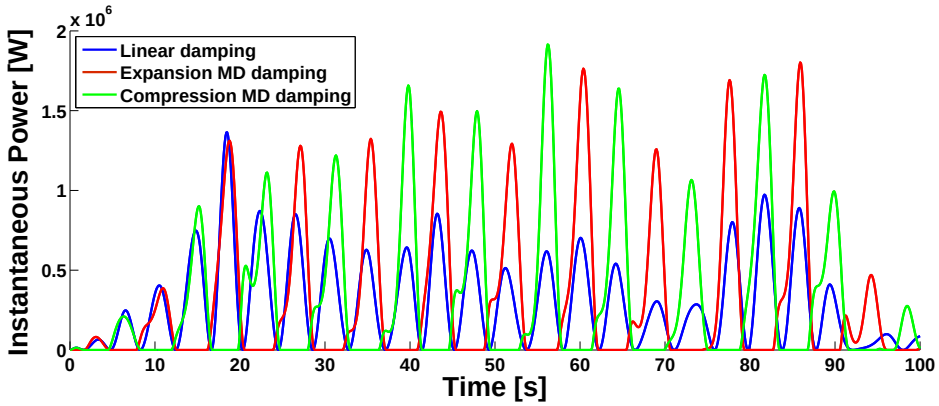

Figure 3.3: The instantaneous power for the linear and mono-directional dampers, with a linear spring constant of 0.45 MN/m and a damping constant of 0.2 MNs/m.

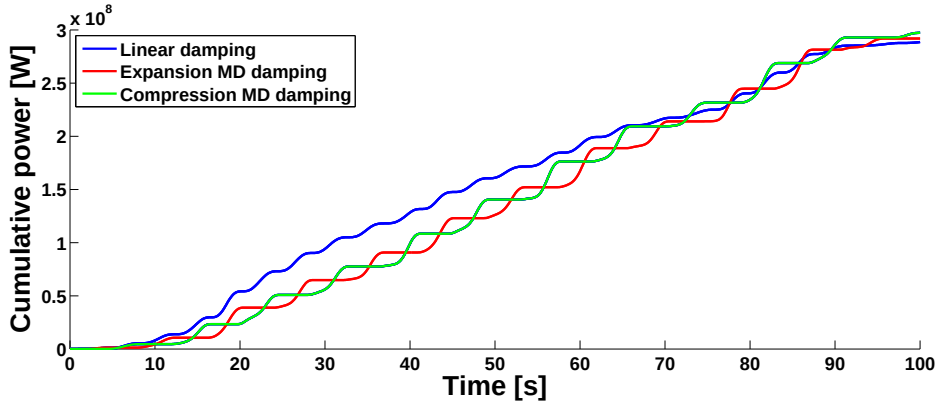

Figure 3.4: The cumulative power for the linear and mono-directional dampers, with a linear spring constant of 0.45 MN/m and a damping constant of 0.2 MNs/m.

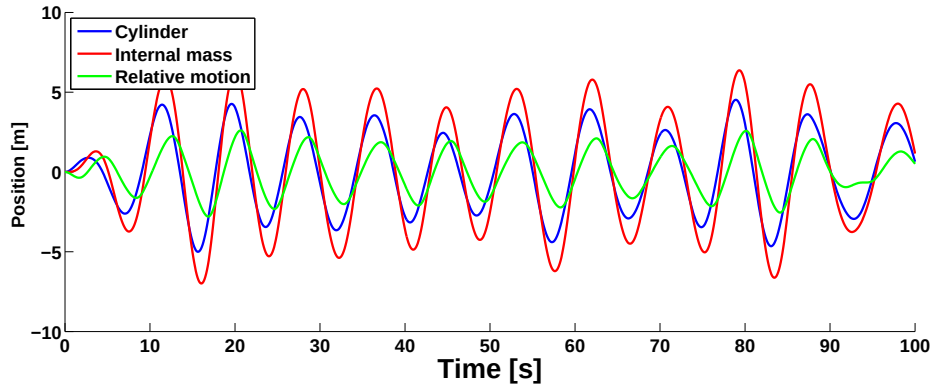

(a) Positions.

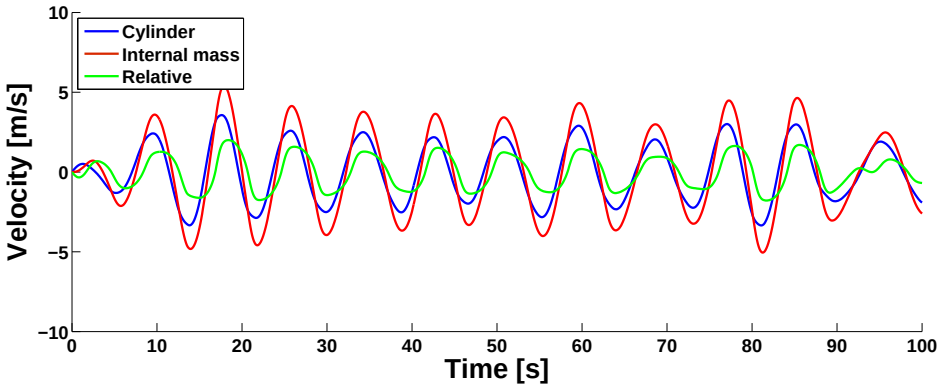

(b) Velocities.

Figure 3.5: Time series showing the position and velocities of the bodies with a quadratic PTO damper and a linear spring, with a damping constant of 0.2 MNs^2/m^2 and a linear spring of 0.45 MN/m.

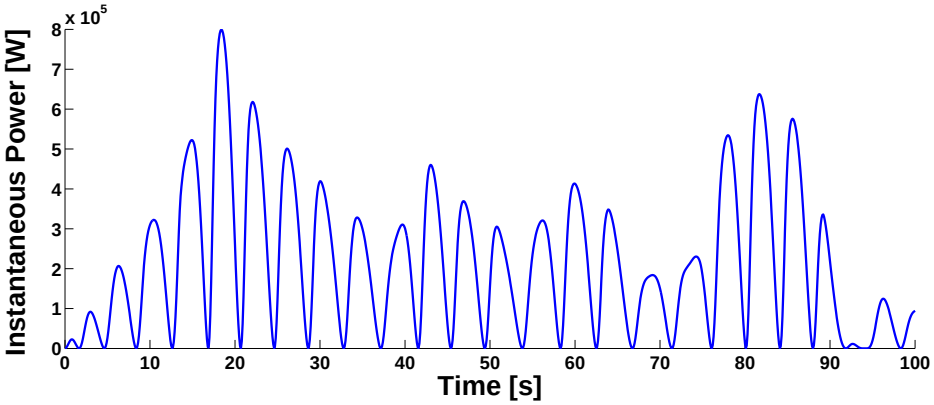

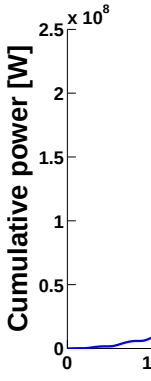

(a) Instantaneous power extracted.

Figure 3.6: The power extracted with a quadratic PTO damper and a linear spring, with a damping constant of 0.2 MNs^2/m^2 and a linear spring of 0.45 MN/m.

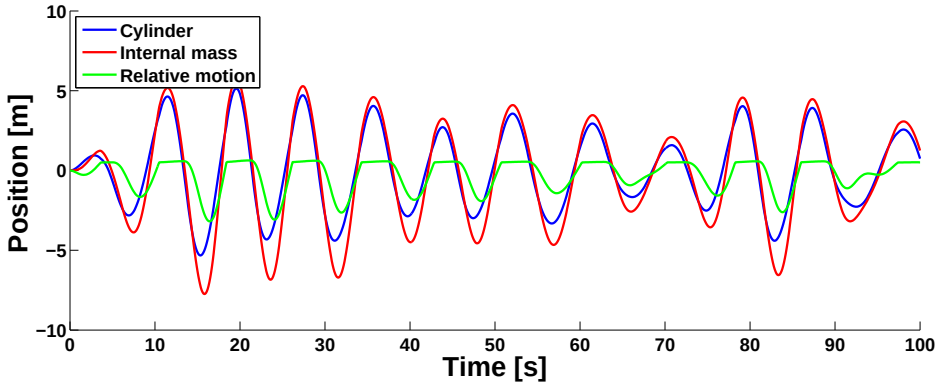

(a) Positions.

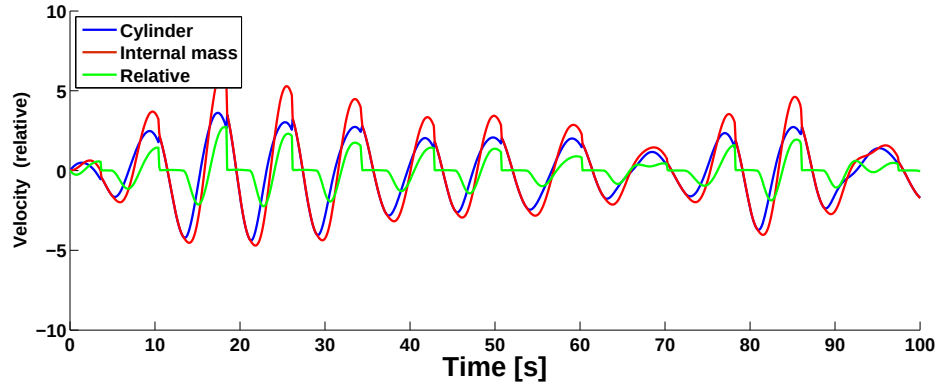

(b) Velocities.

Figure 3.7: Time series showing the position and velocities of the bodies, with a single endstop damper positioned 0.2 m from the SWL of the internal mass, with an endstop damping constant of 20 MNs/m, linear damping of 0.2MNs/m and linear spring of 0.45 MN/m.

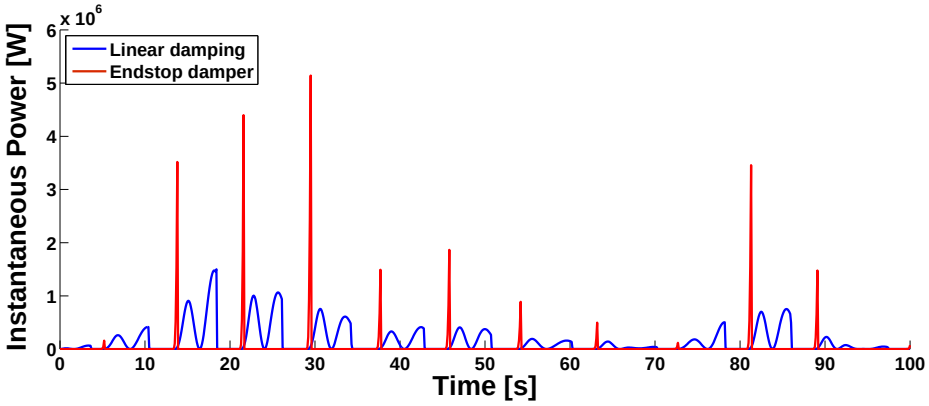

(a) Instantaneous power extracted.

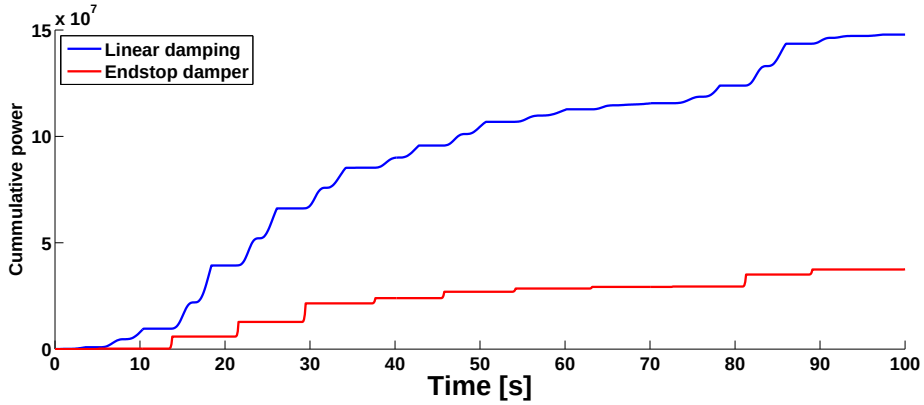

(b) Cumulative power extracted.

Figure 3.8: Power extracted with a single endstop damper positioned 0.5 m from the SWL of the internal mass, with an endstop damping constant of 20 MNs/m, linear damping of 0.2MNs/m and linear spring of 0.45 MN/m.

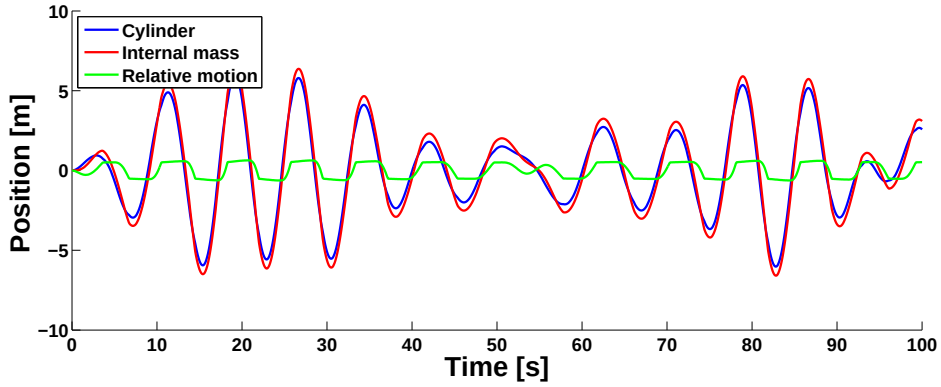

(a) Positions.

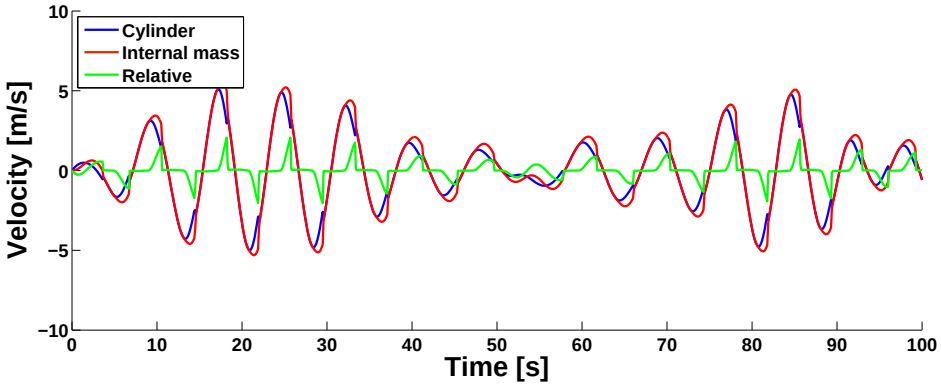

(b) Velocities.

Figure 3.9: Time series showing the position and velocities of the bodies with two endstop dampers positioned 0.2 m from the SWL of the internal mass, with an endstop damping constant of 20 MNs/m, linear damping of 0.2MNs/m and linear spring of 0.45 MN/m.

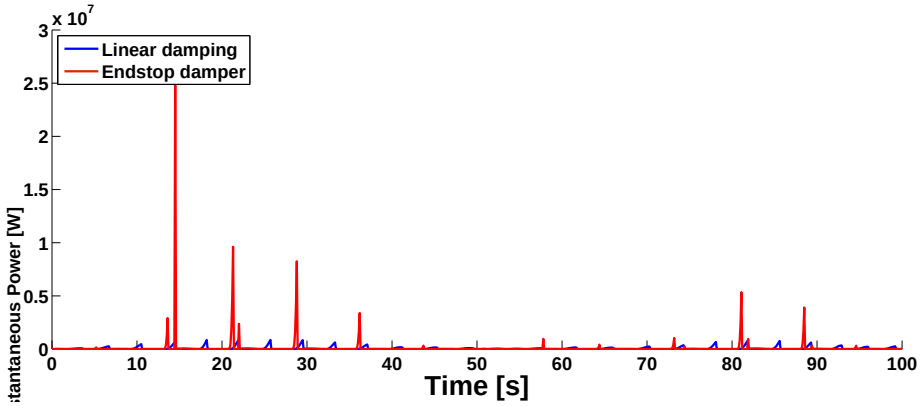

(a) Instantaneous power

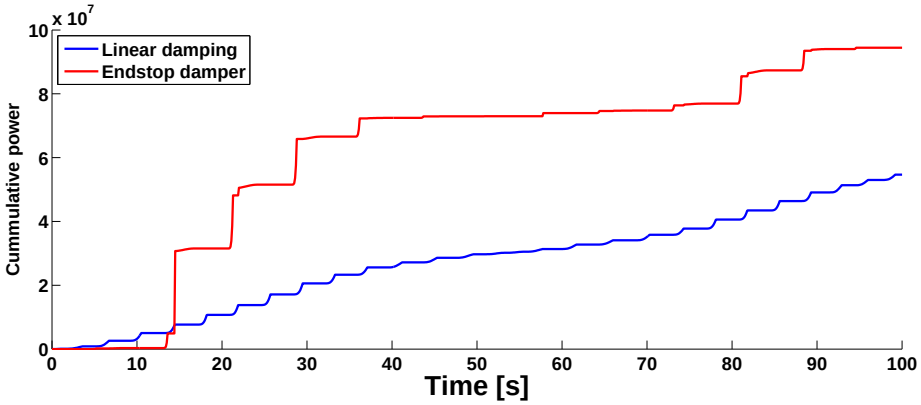

(b) Cumulative power

Figure 3.10: Power extracted with two endstop dampers positioned 0.2 m from the SWL of the internal mass, with an endstop damping constant of 20 MNs/m, linear damping of 0.2MNs/m and linear spring of 0.45 MN/m.

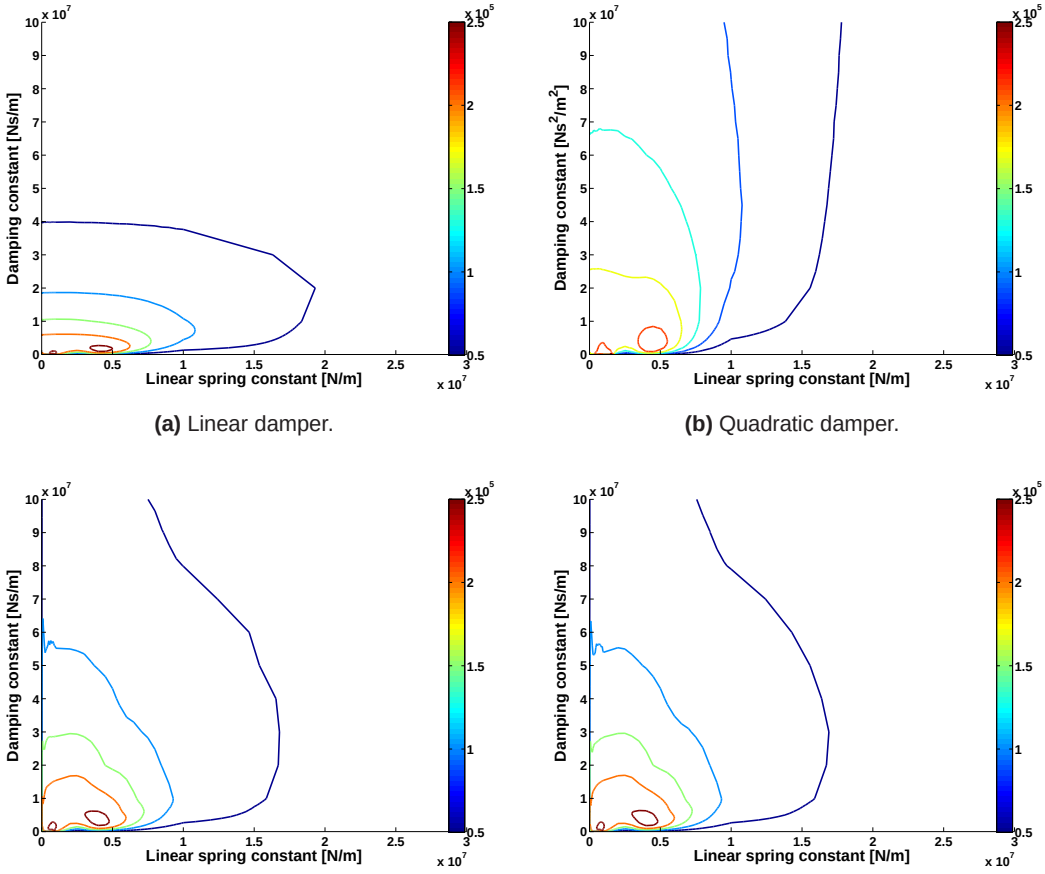

(a) Linear damper.

(b) Quadratic damper.

(c) Expansion mono-directional damper.

(d) Compression mono-directional damper.

Figure 3.11: The time averaged power extraction [W] for the linear, quadratic and mono-directional dampers, showing variation with spring and damping constants. The power extraction is represented by the colour of the lines and this scale is shown on the colour bar.

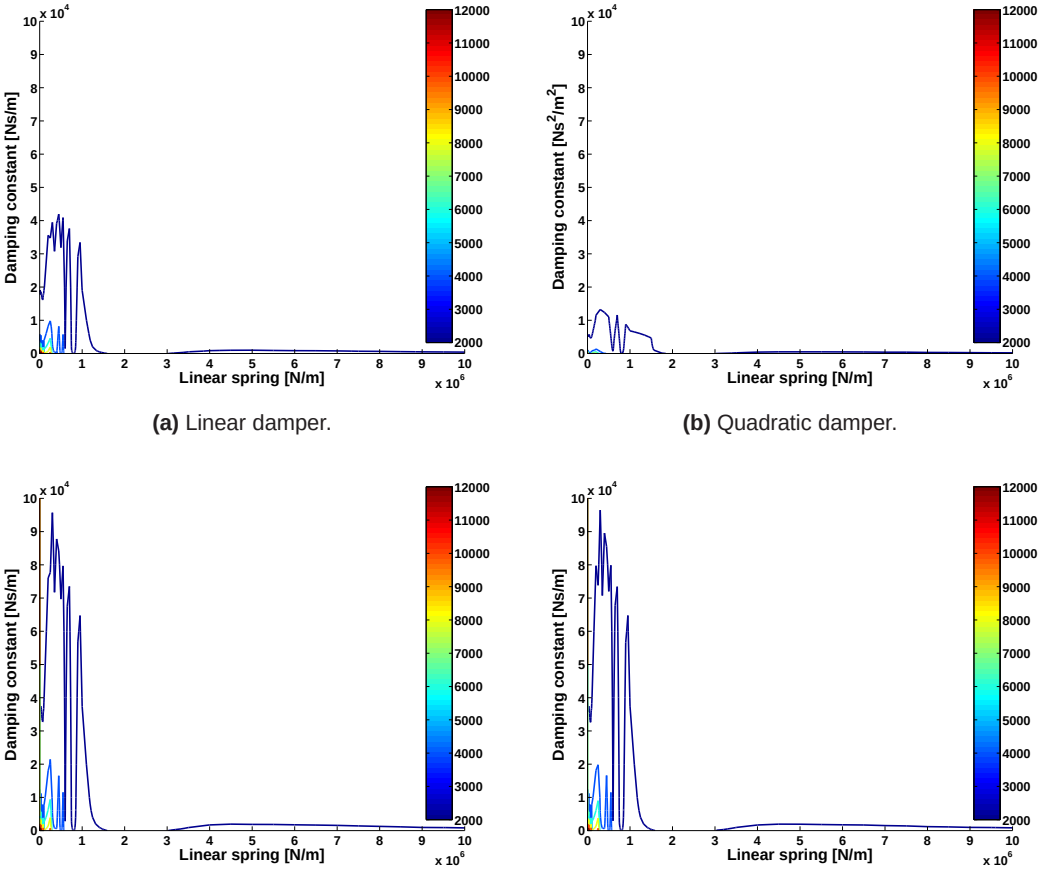

(a) Linear damper.

(b) Quadratic damper.

(c) Expansion mono-directional damper.

(d) Compression mono-directional damper.

Figure 3.12: The summation of the total relative distance travelled [m] for the linear, quadratic and mono-directional dampers, for each of the spring and damping constants tested. The distance travelled is represented by the colour of the lines and this scale is shown on the colour bar.

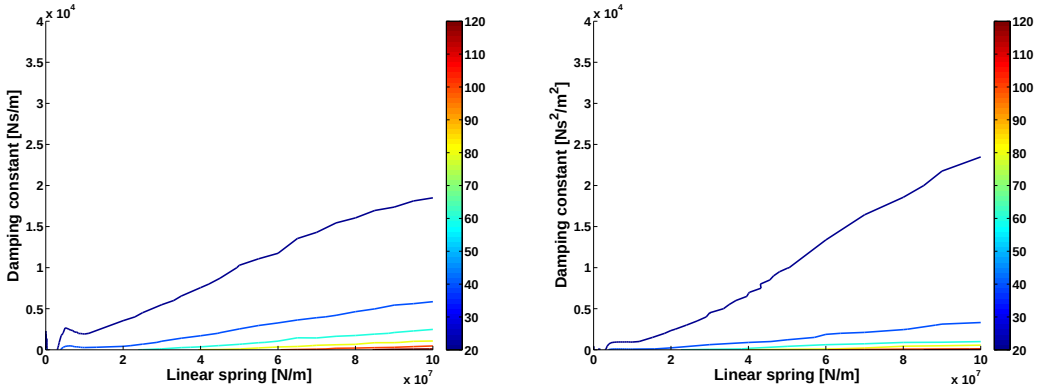

(a) Linear damper.

(b) Quadratic damper.

(c) Expansion mono-directional damper.

(d) Compression mono-directional damper.

Figure 3.13: The average of the highest 1% of accelerations [m/s^2] for the linear, quadratic and mono-directional dampers, showing variation with spring and damping constants. The accelerations are represented by the colour of the lines and this scale is shown on the colour bar.

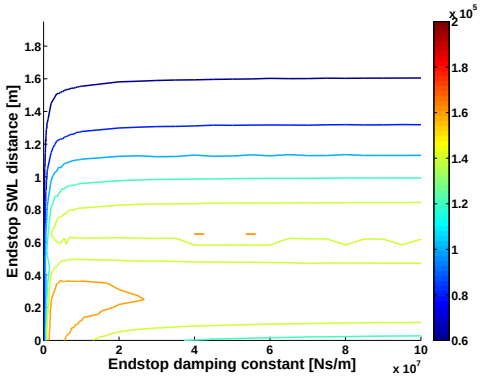

(a) Linear damper.

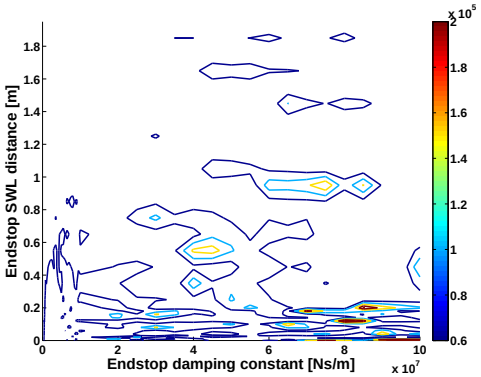

(b) Endstop damper.

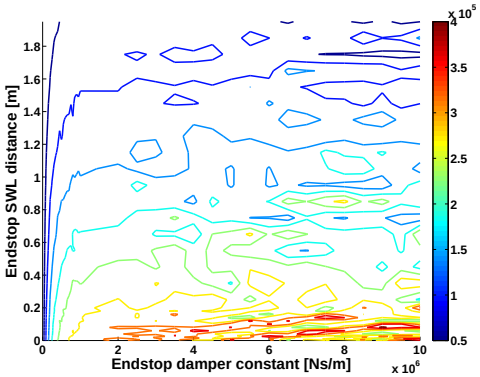

(c) Endstop damper (lower endstop damping constant).

Figure 3.14: The time averaged power extraction [W], with a single endstop damper, with a linear damping and spring constant of 0.2 MNs/m and 0.4 MN/m respectively. The power extraction is represented by the colour of the lines and this scale is shown on the colour bar.

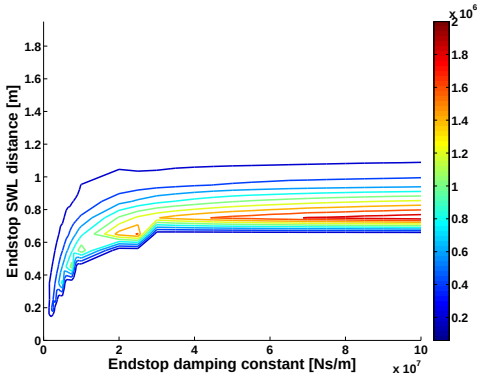

(a) Linear damper.

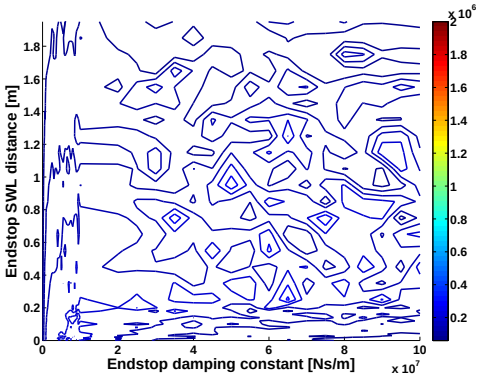

(b) Endstop damper.

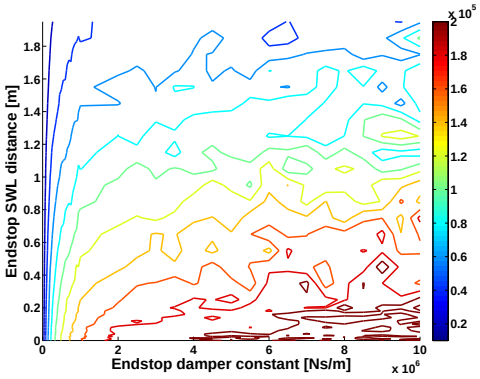

(c) Endstop dampers(lower endstop damping constant).

Figure 3.15: The time averaged power extraction [W], with two endstop dampers, with a linear damping and spring constant of 0.2 MNs/m and 0.4 MN/m respectively. The power extraction is represented by the colour of the lines and this scale is shown on the colour bar.

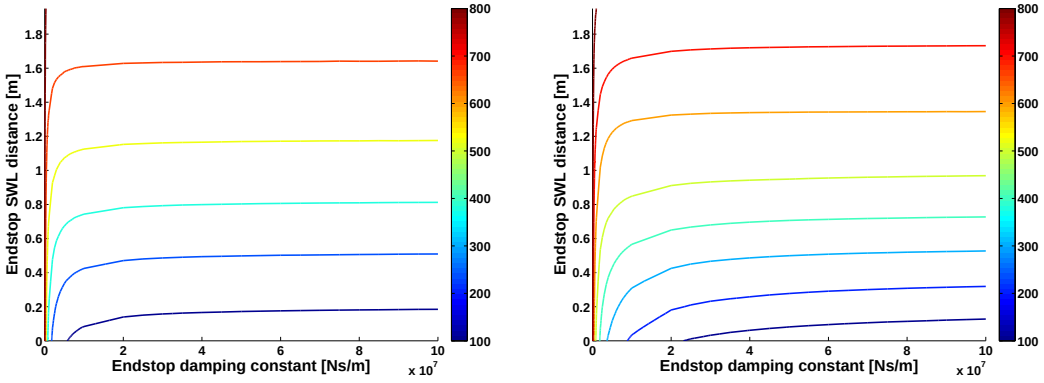

(a) Single damper. **(b)** Two dampers.

Figure 3.16: The total relative distance travelled, with endstop damper(s), with a linear damping and spring constant of 0.2 MNs/m and 0.4 MN/m respectively. The distance travelled is represented by the colour of the lines and this scale is shown on the colour bar.

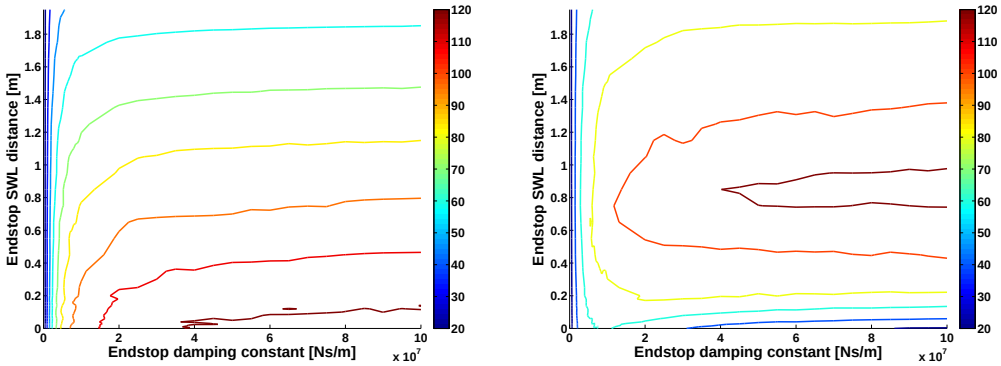

(a) Single damper. **(b)** Two dampers.

Figure 3.17: The average of the 1% highest accelerations , with endstop damper(s), with a linear damping and spring constant of 0.2 MNs/m and 0.4 MN/m respectively. The accelerations are represented by the colour of the lines and this scale is shown on the colour bar.

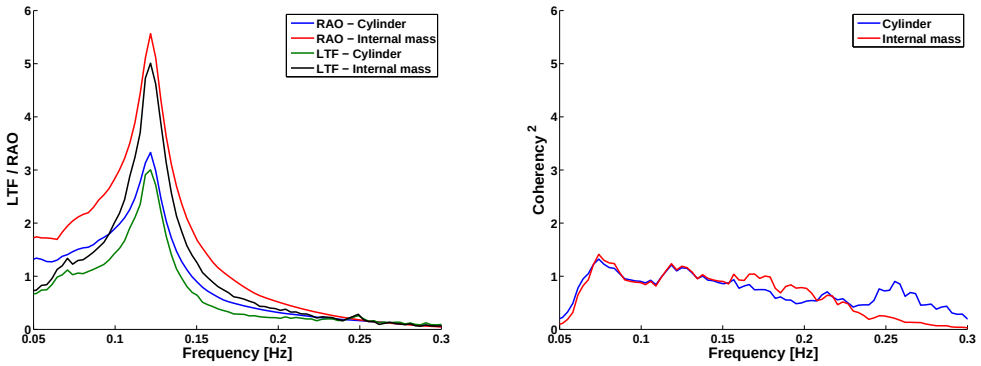

(a) LTF and RAO. **(b)** Coherency.

Figure 3.18: A comparison between the LTF and the RAO, with the LTF coherency, for a linear damper, with a linear spring of 0.4 MN/m and linear damper of 0.2 MNs/m.

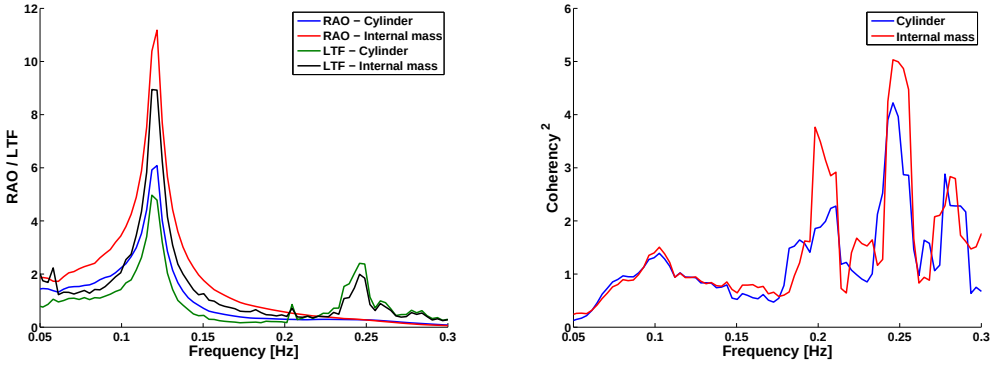

(a) LTF and RAO. **(b)** Coherency.

Figure 3.19: A comparison between the LTF and the RAO, with the LTF coherency, for a expansion mono-directional damper, with a linear spring of 0.4 MN/m and linear damper of 0.2 MNs^2/m^2.

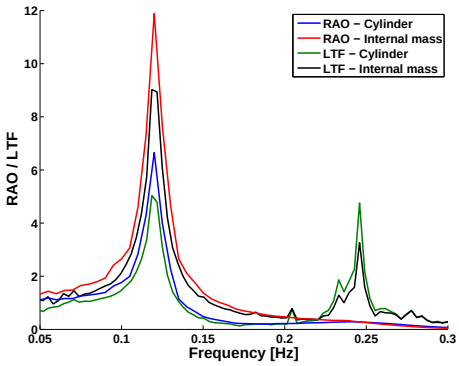

(a) LTF and RAO.

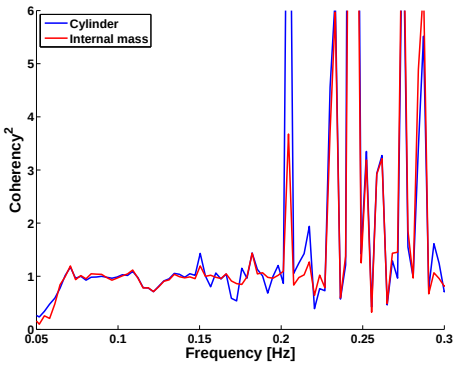

(b) Coherency.

Figure 3.20: A comparison between the LTF and the RAO, with the LTF coherency, for a compression mono-directional damper, with a linear spring of 0.4 MN/m and linear damper of 0.2 MNs^2/m^2.

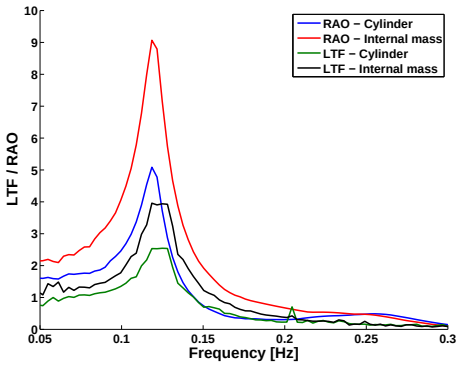

(a) LTF and RAO.

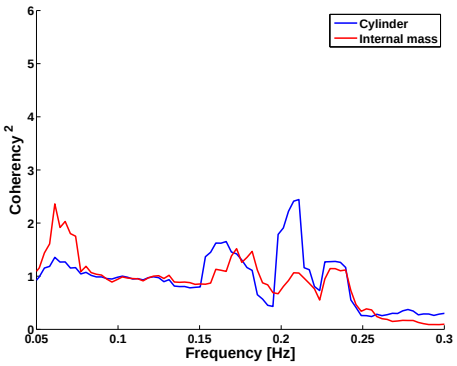

(b) Coherency.

Figure 3.21: A comparison between the LTF and the RAO, with the LTF coherency, for a quadratic damper, with a linear spring of 0.4 MN/m and quadratic damper of 0.2 MNs^2/m^2.

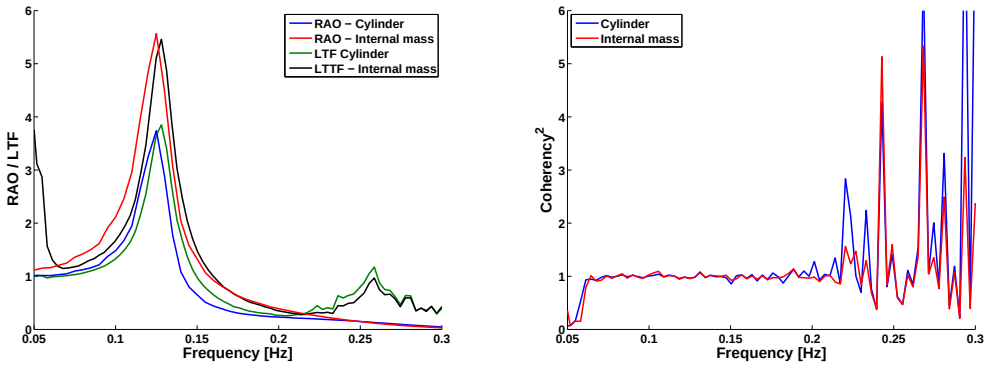

(a) LTF and RAO. **(b)** Coherency.

Figure 3.22: A comparison between the LTF and the RAO, with the LTF coherency, for a linear and an endstop damper, with a linear spring of 0.4 MN/m, a linear damper of 0.2 MNs/m, a SWL endstop distance of 0.2 m and an endstop damping constant of 2.0 MNs/m.

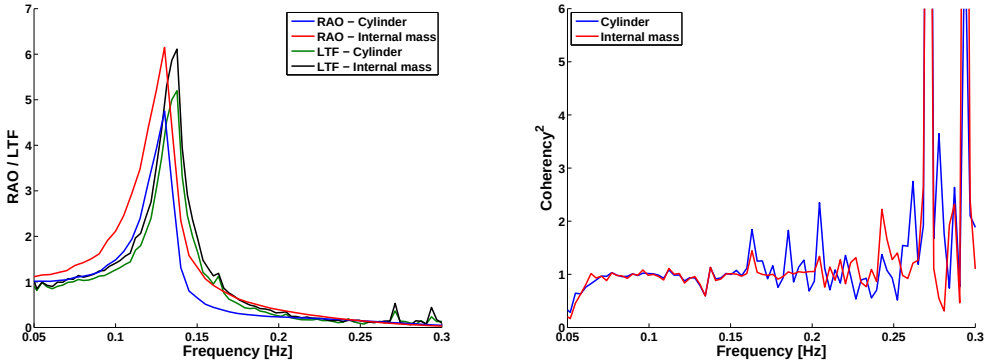

(a) LTF and RAO. **(b)** Coherency.

Figure 3.23: A comparison between the LTF and the RAO, with the LTF coherency, for a linear and two endstop dampers, with a linear spring of 0.4 MN/m, a linear damper of 0.2 MNs/m, a SWL endstop distance of 0.2 m and a endstop damping constants of 2.0 MNs/m.

Chapter 4

The experimental model

4.1 Summary

This chapter describes the physical model, the processes used to design the model and the different PTO systems and their calibrations. Parts of this chapter have been previously reproduced in Bailey and Bryden (2008).

Section 4.2 shows the use of linear wave theory to choose the parameters used in the model and the practical constraints considered. Section 4.3 looks at how the model is scaled, and the influence of the scaling factors on the wave tank model to full scale model, for different parameters of interest. Section 4.4 describes the Curved Wave Tank, that is used for the testing, and Section 4.5 looks at how the data to be collected was obtained and recorded. Section 4.6 describes how the physical model evolved from initial designs and preliminary testing and the changes and reasoning that occurred. The final physical model is described in Section 4.7, with detailed dimensions and descriptions given with drawings and photos of the model. The PTO system, especially the dampers are discussed in Section 4.8 where the methodology for the damper calibration is given.

4.2 Model parameters

4.2.1 Linear theory

The linear model is developed in the frequency domain, and is strongly based upon the two-body problem worked on by Falnes (1999), where the bodies considered are separate bodies that are linked together, although Falnes refers to the case where the second body is within the first. These equations have been reproduced in Bailey and Bryden (2008) and are based on linear wave theory, as discussed in Section 1.6.

The equations of motion for the external cylinder and internal mass, in the frequency domain, are

$$(M_e + m)i\omega\dot{x}_e + N\dot{x}_e + \frac{C\dot{x}_e}{i\omega} + Z_L(\dot{x}_e - \dot{x}_i) = F_{ex}, \quad (4.1)$$

$$M_i i\omega\dot{x}_i - Z_L(\dot{x}_e - \dot{x}_i) = 0, \quad (4.2)$$

where

$$Z_L = c + \frac{k}{i\omega},$$

and

M [kg] is the mass of the bodies;

m [kg] is the added mass of the external body;

i is $\sqrt{-1}$;

ω [1/s] is the incident wave angular frequency;

$\dot{x}$ [m/s] is the absolute velocity;

N [N] is the added damping of the external body;

C [N] is the buoyancy of the body;

F_{ex} [N] is the excitation force;

c [Ns/m] is the damping constant;

k [N/m] is the spring constant;

and the subscripts i and e refer to the internal and external bodies respectively.

By introducing mechanical impedances, the abbreviated form of Equations 4.1 and 4.2 becomes,

$$\begin{bmatrix} Z_e + Z_L & -Z_L \\ -Z_L & Z_i + Z_L \end{bmatrix} \begin{bmatrix} \dot{x}_e \\ \dot{x}_i \end{bmatrix} = \begin{bmatrix} F_e \\ 0 \end{bmatrix}, \quad (4.3)$$

where the impedances, Z_e and Z_i are

$$Z_e = N + i\omega\left(M_e + m - \frac{C}{\omega^2}\right),$$

$$Z_i = i\omega M_i.$$

Therefore, the solution to this equation is

$$\begin{bmatrix} \dot{x}_e \\ \dot{x}_i \end{bmatrix} = \frac{1}{D_{et}} \begin{bmatrix} Z_i + Z_L & Z_L \\ Z_L & Z_e + Z_L \end{bmatrix} \begin{bmatrix} F_e \\ 0 \end{bmatrix}, \quad (4.4)$$

with the determinant, D_{et}, being

$$D_{et} = Z_e Z_i + Z_L Z_e + Z_L Z_i. \quad (4.5)$$

The velocities of the internal mass and external cylinder are

$$\dot{x}_e = \frac{(Z_i + Z_L)F_e}{D_{et}}, \tag{4.6}$$

$$\dot{x}_i = \frac{Z_L F_e}{D_{et}}. \tag{4.7}$$

Therefore, the relative motion is

$$\dot{x}_r = \dot{x}_e - \dot{x}_i = \frac{Z_i F_e}{Z_e Z_i + Z_L(Z_e + Z_i)}. \tag{4.8}$$

The time averaged power produced from the relative motion between the internal mass and external shell is

$$P = \frac{1}{2} Re\{Z_L \dot{x}_r \dot{x}_r^*\} = \frac{1}{2} Re\{Z_L\} |\dot{x}_r|^2. \tag{4.9}$$

Equations 4.8 and 4.9 enable the power and relative motion to be determined for any set of mechanical impedances, with a known excitation force. The variables that need to be determined in this physical model, which affect the mechanical impedances, are the mass of the internal body, the spring constant and the damping constant. These can be chosen to maximize the power extracted and / or the relative motion, for a set size of model. Maximizing power extraction is an obvious goal for most devices. Having a large relative motion is also important for a tank scaled model for the internal mass to properly connect with the dampers and for the movement of the mass to be observed and recorded.

This frequency domain model is simulated to investigate the approximate values of the physical model parameters that will lead to both high power extraction and large amounts of relative motion. Since this simulation is developed in order to aid the design process of the physical model it is based on a physical model with a 0.115 m radius and an assumed smaller draft than the final model of 0.25 m.

4.2.2 The influence of the internal mass

The effect of the internal mass on the relative motion between it and the external cylinder and the power dissipated in the PTO can be seen in Figure 4.1, from using Equations 4.8 and 4.9. In this figure, a spring constant of 200 N/m and a damping constant of 50 Ns/m was used, with an incident wave frequency of 4 rad/s. The draft of the body remained at 0.25 m in still water, by decreasing the external body mass proportionally to the increase in the internal body mass. Figure 4.1 shows that to both maximize the power extracted in the PTO and the relative motion, the internal mass should be as large as possible. The effect of changing the spring and damping constants does not change the general trend of Figure 4.1.

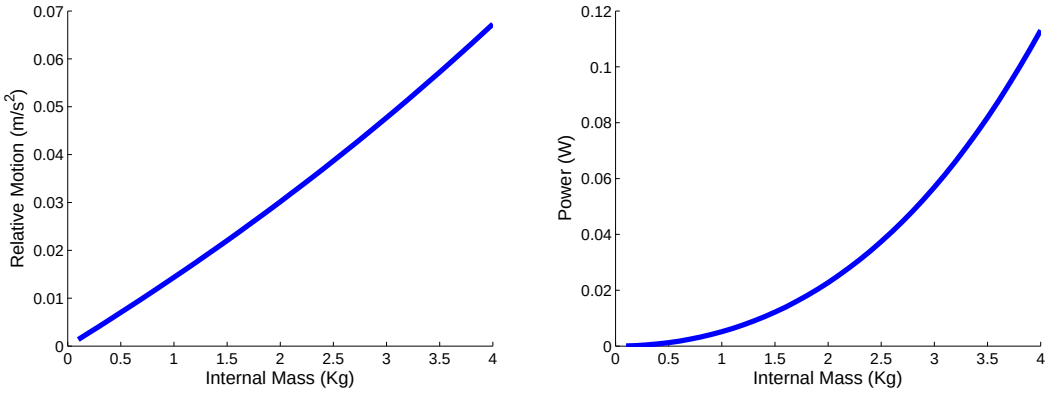

(a) Relative motion. **(b)** Power.

Figure 4.1: The influence of the internal mass on the relative motion and power.

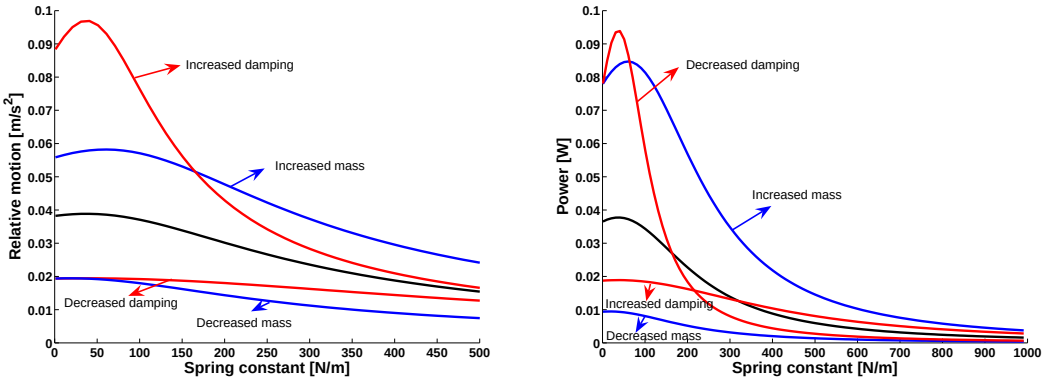

(a) Relative motion. **(b)** Power.

Figure 4.2: The influence of the spring constant on the relative motion and power.

4.2.3 The influence of the spring constant

Figure 4.2 displays the power extracted and the relative motion for a varying spring constant, this is also from Equations 4.8 and 4.9. The black line is for an internal mass of 2 kg and a damping constant of 50 Ns/m. The red lines show the effect of varying the damping constant, the upper red line had the increased damping constant of 100 Ns/m and the lower red line has a decreased damping constant of 20 Ns/m. The blue lines show the influence of the mass, with the upper blue line having an increased internal mass of 3 kg and the lower blue line a decreased internal mass of 1 kg. The incident wave frequency was 4 rad/s.

Both graphs show that the maximum power extracted and relative motion occur at a spring constant of between 40 N/m and 80 N/m, for these parameters. The exact values of the power and the relative motion at the maximum vary considerably, and the gradient away from the

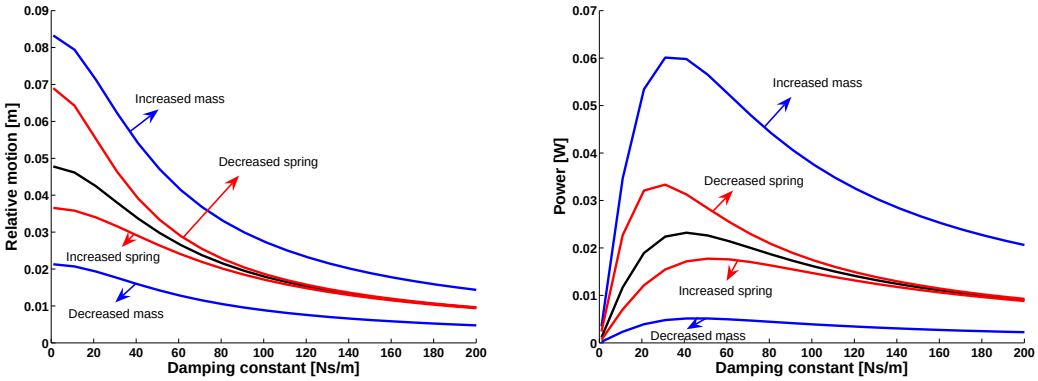

(a) Relative motion.

(b) Power.

Figure 4.3: The influence of the damping constant on the relative motion and power.

maximum varies but the spring constant that corresponds with the maximum values is relatively stable. This figure shows that the ideal value of the spring constant would be approximately between 40 – 80 N/m, depending on the other parameters chosen.

4.2.4 The influence of the damping constant

The amount of damping in the PTO will obviously affect both the amount of power produced and the relative motion. This is seen in Figure 4.3, where the black line corresponds to a spring constant of 200 N/m and an internal mass of 2 kg. The blue lines shows variations in the mass, with the upper blue line having an increased internal mass of 3 kg and the lower line a decreased internal mass of 1 kg. The red lines show the effect of the spring constant, with the upper red line having a spring constant of 150 N/m and the lower red line an increased spring constant of 250 N/m. The incident wave frequency was 4 rad/s.

As expected, the power extracted is zero when the damping constant is zero, and increases as the damping constant increases from zero until reaching a maximum and decreasing towards zero for higher values of damping constant. For maximum power extraction, the ideal damping constant is approximately 30 – 60 Ns/m, for these parameters. For maximum relative motion, the ideal damping constant would be zero - so a conflict is seen between these two criteria. However, since power extraction is a priority, an ideal damping constant would be between 30 - 60 Ns/m, for these parameters, especially since relative motion is not minimal. During tank experiments, this value will be adjusted to further look at this relationship, for both linear damping to confirm this result and for nonlinear damping to see what effect the nonlinearities have on the system.

4.2.5 Practical considerations

To conclude, from looking at the influences of the different parameters, the ideal system for the maximum power extraction and the relative position, for the parameters considerered, would be

1. the largest internal mass possible;
2. a spring constant of between 40 – 80 N/m;
3. a damping constant of 30 – 60 Ns/m for maximum power extraction.

However, to have a large mass and a small spring constant would require a very long, very weak spring. For example, a 50 N/m spring compressed by a 5 kg mass would reduce in length by 1 m, and further spring compression would occur when this mass is in motion due to the greater forces being applied. The solid height of the spring and not wanting to operate the spring near to its fully compressed solid state, due to unknown nonlinearities, needs to be considered. Therefore, in this example, a free length of at least 2 m would be required. Therefore, either a lighter internal mass or a higher spring constant would be needed.

The additional considerations related to the spring are: the wire diameter becoming excessively thin and liable to damage; the space restraints within the cylinder; the solid height of the spring; and the ability of the spring to be manufactured.

The damping constant suggested from the linear model would be larger than what is actually required due to power being dissipated in the dynamic and static friction between the internal mass and the central rod, as well as between the rod and the fixed bearings, this is especially problematic due to the scaled size of the model.

4.3 Scaling

As Hughes (1993) says,

> *The basis of all physical modeling is the idea that the model behaves in a manner similar to the prototype it is intended to emulate. Thus a properly validated physical model can be used to predict the prototype under a specified set of conditions.*

A properly validated model comprises a model where all the significant factors that affect the reactions and responses, are in proportion, between the experimental model and the full sized device, and all the factors that are not in proportion have a negligible effect on the model. To measure this proportionality between the physical tank tested model and the full sized model, scaling factors or ratios are used. This is measured as,

$$N_X = \frac{\text{Value of X in experimental model}}{\text{Value of X in full scale device}}. \tag{4.10}$$

The scale factors are linked for different model parameters such as the length, time, power, etc., depending on which scaling criterion is chosen.

Length	N_L
Area	N_L^2
Volume	N_L^3
Time	$N_L^{0.5}$
Frequency	$N_L^{-0.5}$
Velocity	$N_L^{0.5}$
Acceleration	N_L^1
Mass	N_L^3
Force	N_L^3
Energy	N_L^4
Power	$N_L^{3.5}$

Table 4.1: The scaling ratios for the experimental model to full size device.

In this work, the Froude criterion is used. The Froude number is the non-dimensional number that is most relevant when the inertial forces on the model are primarily balanced by the gravitational forces. This criterion is typically used for hydraulic models that have a free surface. The Froude number is based on the ratio,

$$Fr = \sqrt{\frac{\text{Inertial force}}{\text{Gravity force}}} = \sqrt{\frac{\rho L^2 V^2}{\rho L^3 g}} = \frac{V}{\sqrt{gL}}. \tag{4.11}$$

This assumes that the mass density of the water is the same for the experimental model and the full scale device [1]. The scaling ratios can be seen in Table 4.1 (Hughes, 1993).

These ratios are used to directly obtain the results for a full scale model from the experimental physical model. For example, using a 1:40 scale model, the power extracted would be multiplied by a factor of $40^{3.5}$, a factor of 404772.

The scale effects are the differences between the full and scaled model due to some physical properties of the system which change between the two sizes of model not being dependent on the Froude number. The model effects are the differences that occur due to the physical models

1. This is not accurate since the density of the fresh water in the wave tank is $\approx 1000\ kg/m^2$ and the density of sea water varies depending on the levels of salinity but on average is $1025\ kg/m^2$, however the difference is considered small enough to be neglected.

Figure 4.4: The Curved Wave Tank, (Taylor, 2002).

not being exactly the same due to the reduced size and power extraction. Both of these effects are ideally minimized for this work.

4.4 The Curved Wave Tank

The Curved Wave Tank at the University of Edinburgh is a unique facility. It is 1.2 m deep and it is shaped in an arc, with a radius of 9 m, which has an inclusive angle of just over 90^o. The arc section contains 48 wave maker paddles. Perpendicular to the main direction that the waves travel, along one side of the tank is a beach and parallel to the wave direction is an 8 m wide viewing glass wall. There are no parallel walls in the tank which helps reduce reflections.

The wave makers are of the flap type. They are 305 mm wide, constructed as an aluminum box with a rolling seal between the wave makers to prevent water getting behind their front face. They are force controlled, with strain gauges operating between the paddles and the drive system. The force control enables most wave reflections to be eliminated by the effective absorption of the wave, since the incident wave that is produced, in addition to being the required incident wave, cancels out the unwanted reflected wave.

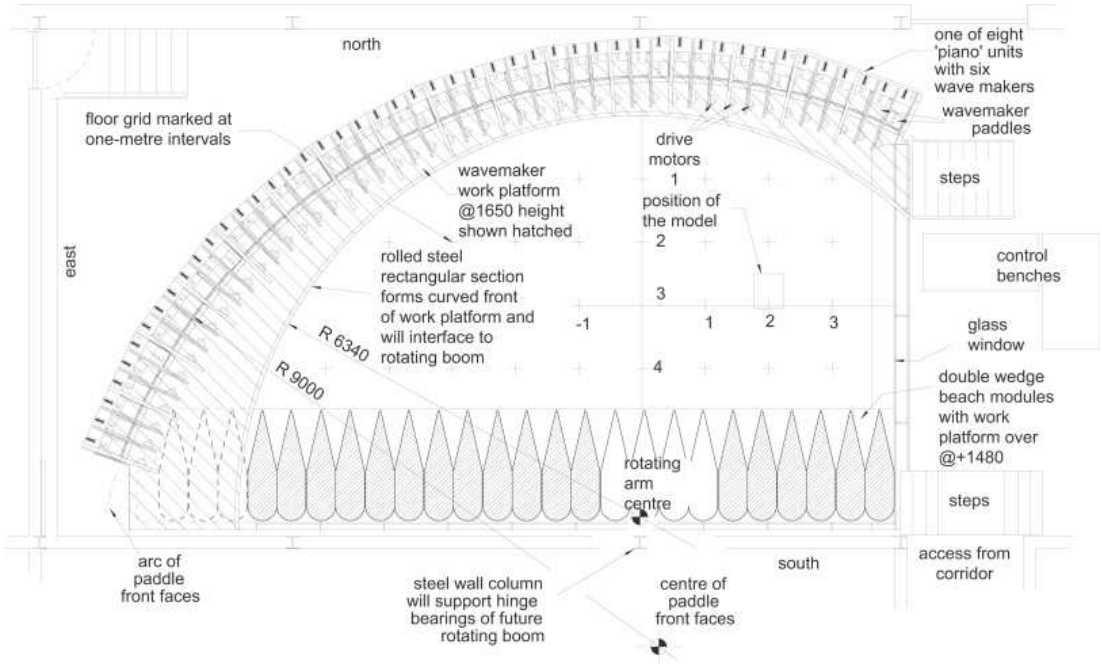

Figure 4.5: A schematic plan view of the Curved wave tank, by Jamie Taylor.

The beaches are wedge shaped and constructed of a mix of polyether skeleton foam and a three dimensional geo-textile material. The large number of sharp edges and constricted spaces within the material leads to the energy from the waves being effectively dissipated. The packing material has increased density further from the initial contact plane of the wave, to further eliminate reflections. The reduced reflections within the tank, from the beaches, the force control on the paddles and the geometry of the tank results in a facility with high repeatability, reliable wave climates and a short settling time.

The Curved Wave Tank is optimized to operate at 1 Hz. It can produce good waves between 0.5 Hz and 1.5 Hz, depending on the wave height that is required. The waves are produced at fixed frequencies of $n/64$ Hz, where n is a positive integer.

These and further details on the tank have been published by Taylor *et al.* (2003). A photograph of the tank is shown in Figure 4.4 and a drawing of the plan view of the tank is presented in Figure 4.5.

4.5 Measurements

4.5.1 Qualisys motion capture

The positions of the internal mass and the cylinder during experimental testing, and the positions of the calibration mass for the calibration of the dampers, was recorded using software and hardware from Qualisys Motion Capture Systems (Qualisys Motion Capture, 2009). The system works by having two infrared cameras which detect marker balls that are placed on the model. With four marker balls on a rigid body, motion in all six degrees of freedom can be recorded. This system enables non-intrusive measurements to be taken using the principles of triangulation, from multiple cameras. Two cameras, each with 250 infrared diodes, were rigidly positioned, with appropriate focus and aperture.

The markers used are spherically shaped with a diameter of 30 mm, painted in a reflective coating. The minimal marker size and circularity (as viewed and calculated by the cameras) is chosen to ensure that only the markers are detected by the system. The markers are attached to the structures with double sided adhesive tape, as the manufacturer recommends.

The cameras were initially calibrated following the manufacturers' suggested procedure. A fixed length "L-shaped" wand with four markers at fixed positions was used. The rod was manually moved around the testing area, covering the entire three dimensional area, for a set time period. This procedure was repeated several times and the run that resulted in the most accurate calibration, as determined from the provided software, was used as the final calibration. The cameras are locked in position, and after the initial calibration is completed, they are used for the entire experimental data collection time period.

The accuracy of the Qualisys Motion Capture System varies for different number of cameras, configurations and measuring rate. This has been estimated as 0.3 mm by Faber *et al.* (2001) for the measurement of the position of horses's spines, with 7 cameras recording at 240 Hz and 3600 Hz. An accuracy of 0.025 mm was found by Holt *et al.* (2005) for the measurement of intervertebral kinematics at 60 Hz, with an unstated number of cameras. Estimates for the camera accuracy as have been setup in the Curved Wave Tank is 0.1 mm (Payne *et al.*, 2008) at 32 Hz.

4.5.2 Wave gauges

The surface elevation of the water was measured with twin wire resistance wave gauges. These have two wires in parallel, connected at the bottom by a non-conductive material. A high frequency AC is passed though the wires and the resistance is calculated and is proportional to the length of the wire not in contact with the water. These have an accuracy of ± 0.1 mm (Hughes, 1993). An array of 4 wave gauges was calibrated by raising them vertically with an overhead crane at a known speed. These were positioned at the same location as the model

was tested to record all the different sea states used with the model absent. These are the same waves that the model would experience from the incident wave field, without any interference from the radiated waves that the model produces.

4.6 Model Evolution

The physical model went though a period of prelimary testing and redesign in order to enable the model to operate with

- minimal bearing friction;
- minimal unwanted damping;
- maximal relative motion between the internal mass and the cylinder;
- minimal non-heave motion.

4.6.1 Internal mass

The geometry of the mass affects both the contact area of its bearing and the potential for the centre of gravity to be non-centrally positioned. The final mass is thin and long, designed to have a long contact area with less potential to “twist” about a horizontal axis which would result in a significant amount of static friction. The obvious physical constraint of having to fit the mass and its potential range of movement within the cylinder is an additional constraint.

4.6.2 Bearings

The bearings in the model have PTFE in contact with stainless steel. PTFE was chosen due to its low coefficient of friction compared to most commercially available materials. Rolling bearings and HDPE contact bearings were considered but their coefficient of friction was deemed to be greater than PTFE. The upper and lower bearings, attaching the central rod to the fixed rig, are rod-end bearings. Rod-end bearings can rotate, in all directions, which allows limited non-heave movement and compensates for any misalignments of the cylinder, resulting in a lower friction in heave due to having less forces opposing the motion.

4.6.3 Central rod

The diameter of the central rod during the preliminary testing was 8 mm. This was seen to visually move in surge and rotate in pitch whilst experiencing incident waves. A high resistive force was felt to manual perturbations of the rod especially during incoming incident waves. This was partially due to the flexibility of the rod which resulted in additional friction at the external bearings when the waves exerted a force in surge and pitch on the cylinder. To counter this, a rod with a larger diameter was required. However, this would result in both an increase

Diameter (mm)	Deflection (mm)	End rotation (degrees)	Weight (kg)
8	83.3	9.54	0.59
10	34.1	3.90	0.94
12	16.4	1.88	1.33
14	8.87	1.02	1.81
16	5.20	0.60	2.36
18	3.25	0.37	2.99
20	2.13	0.24	3.69

Table 4.2: The deflections and rotations of the rod.

in the weight of the combined cylinder and rod, and have the potential to be influenced by the wave motions so would have to be included in the numerical simulation. The deflection and end rotation of a pinned rod (CUED, 1999) can be calculated from Equation 4.12 and 4.13.

$$\text{Deflection} = \frac{Fl^3}{48EI}, \tag{4.12}$$

$$\text{End rotation} = \frac{Fl^2}{16EI}, \tag{4.13}$$

where F is the force applied at the centre of the rod, l the length of the rod and E is Young's modulus. I is the second moment of area, equal to the product of the cross sectional area and the radius of gyration, $\pi r^2(\frac{r^2}{4})$, where r is the cross sectional radius of the rod.

The deflections and rotations are found for a force of 50 N (a not unreasonable amount for the cylinder to experience in surge), using a 1.5 m length rod. The Young's Modulus for steel is 210 MPa and its density is 7840 kg/m^2. The results for the varying rod diameter are presented in Table 4.2.

From this table, it was decided that a rod with a 16 mm diameter should be used, due to its low deflections with an acceptable weight penalty.

4.7 The experimental model

The final design of the experimental model has been used for all the experiments presented in this thesis. It comprises a 16 mm diameter, 2 m long, ground straight, stainless steel central rod that is held vertical and limited to move in heave by two rod-end stainless steel bearings with PTFE sleeves. The rod-end bearings are screwed into a support rig which is attached to the internal fixed platforms within the Curved Wave Tank. These bearings are connected to the rod at its upper and lower ends, and the central rod moves relative to them.

The internal platform that is used to hold the rig stationary is constructed of galvanised steel. It comprises a thin legged structure below the waterline and is fixed within the Curved Wave

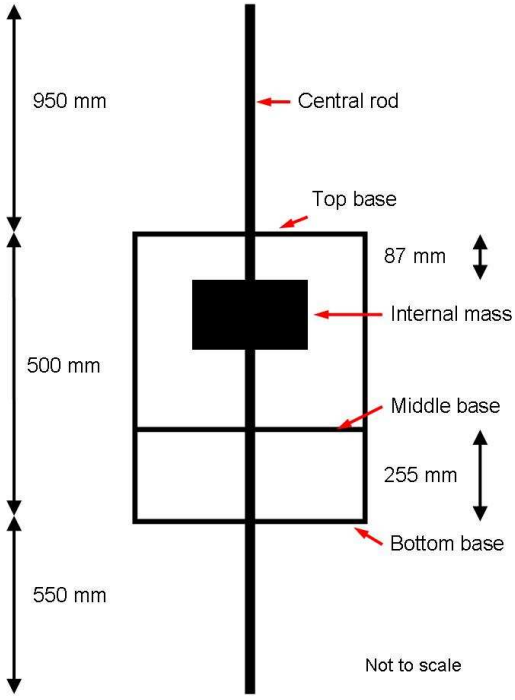

Figure 4.6: Dimensioned drawing of the model.

Tank. Above the waterline, there is an area suitable for attaching the rig, and it can be walked on to aid access.

The support rig is made of two bars, that protrude perpendicular to the Curved Wave Tank's fixed platforms, 1250 mm apart, with the lower bar underwater. These are supported by diagonal arms halfway along their length. The cylinder is held away from the platforms to minimise any interference to the wave climate that these thin-legged structures and the attached rig may have. The cylinder is held at approximately position "1", as shown in the plan view of the tank, in Figure 4.5.

Rigidly attached to the central rod is a clear plastic open ended axi-symmetric cylinder orientated so its axis of symmetry is aligned with the central rod. The radius of the cylinder is 115 mm and it has a depth of 0.5 m. Within the cylinder there are three plastic bases at its top, middle and bottom. The bottom base is fully sealed so no water enters the cylinder. There are circular cutouts in the top plastic base to allow the motion of the internal mass to be observed and to allow access and removal. The middle base's role is to provide a platform for the different dampers. The position of these bases and the cylinder with respect to the central rod is presented in Figure 4.6.

On the central rod, within the cylinder and between the middle and the top base, is the internal mass. The internal mass weighs 6.721 kg and has a radius of 30 mm and a depth of 101.5 mm. A central hole along its axis of symmetry, of radius 10 mm, is where a 3 mm thick, hollow

circular PTFE bearing sits. There is a small tapered hole where the dampers are attached.

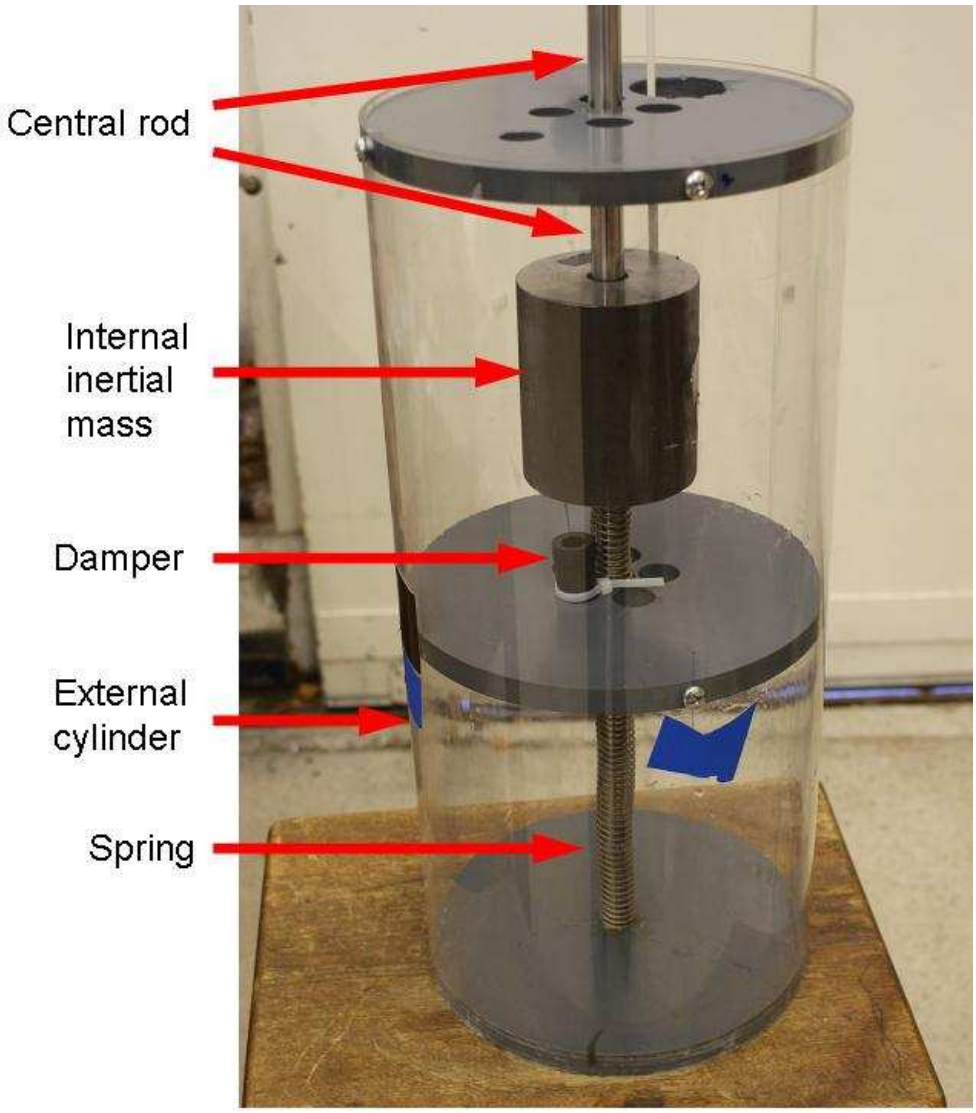

Figure 4.7: Photos of the experimental model (by the author): A close up shot of the model, out of the water.

Between the bottom base of the cylinder and the internal mass is a custom made spring, sitting freely on the rod with a spring stiffness of 200 N/m. The spring has a wire diameter of 1.64 mm, is made from stainless steel and has a free length of 600 mm.

Photos of the experimental model are presented. Figure 4.7 shows a close up photo of the cylinder containing the internal mass, spring and damper, shown out of the water. Figure 4.8 shows the entire setup, including the fixed platform, the support rig with the rod-end bearings, the cylinder and the markers used for data collection.

The entire body, when in the water, has a draft of 0.285 m on the cylinder, and the external

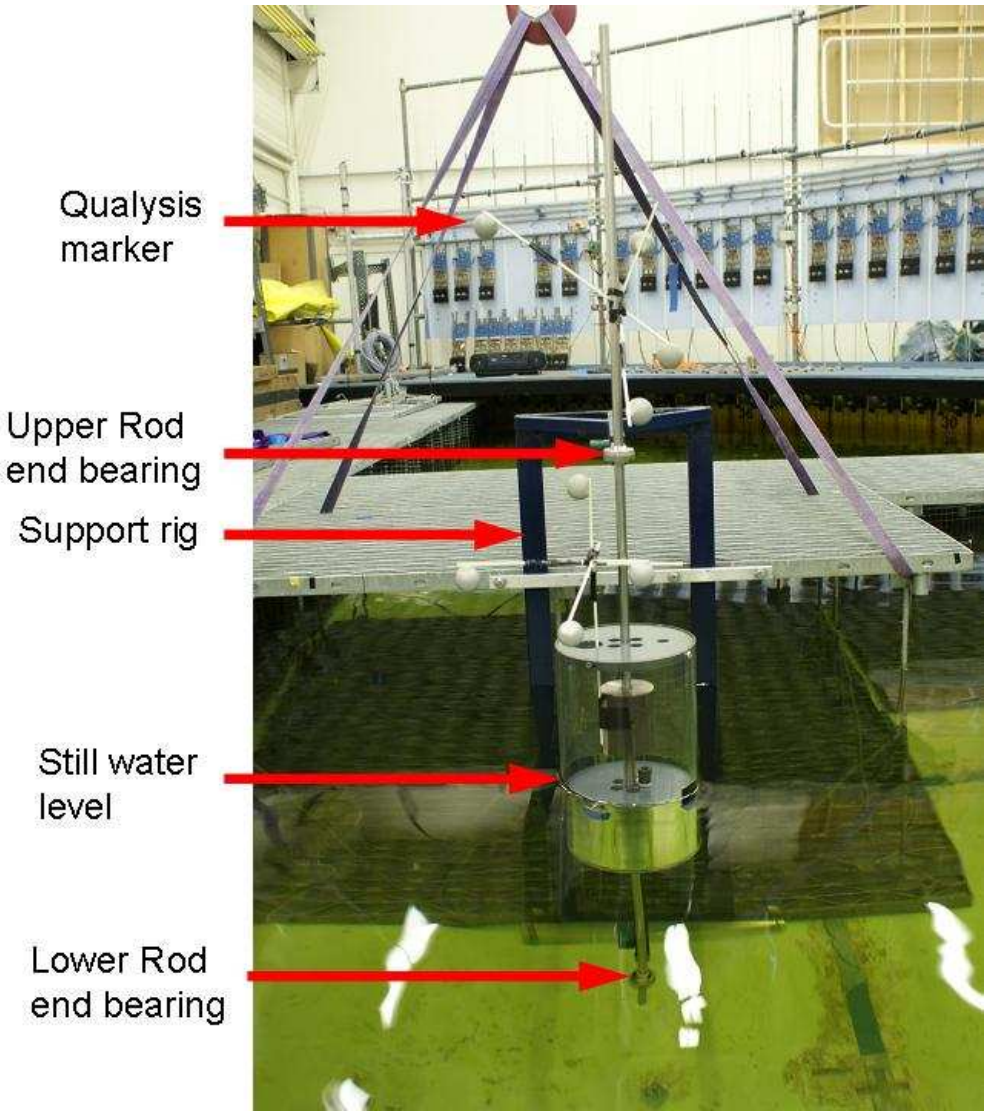

Figure 4.8: Photos of the experimental model (by the author): The experimental setup, along with the motion-detection markers.

body without the internal mass weighs 4.856 kg.

4.8 PTO

The different PTO setups used in the physical model are as follows.

- **Linear PTO**
  The linear PTO setup is tested to be able to compare with the nonlinear systems and with numerical simulations. Bi-directional dampers, as described in Section 4.8.1 where used with the 200 N/m spring. Also included in this section are the cases where there is no spring or damper present.
- **Mono-directional PTO**
  Mono-directional PTO comprises the 200 N/m spring and a mono-directional damper, as described in Section 4.8.1. Two different dampers were used, one that produces a force that was proportional to velocity in expansion, and negligible force in compression, referred to as an expansion mono-directional damper. The other damper produces a force in compression and negligible force in expansion, which is referred to as a compression mono-directional damper.
- **Endstop PTO**
  These use a 200 N/m spring and no main damper, but an endstop dampers is placed in known positions that contact the internal mass once it has moved away from its SWL position. No main damper is used to enable a larger range of motions and to allow the effects of the endstop dampers to be clearer within the results. Further descriptions of the endstop dampers are given in Section 4.8.3.

4.8.1 Main damper description

The main dampers used are pneumatic and designed to have a linear response. They have the brand name Airpot, (Airpot Corporation, 2008). Three types of dampers have been used: a compression damper, which provides a resisting force when the piston of the damper is compressed into the unit, and an expansion damper, which provides a resisting force when the piston is expanding from the unit and a linear damper which produces a resistive force in both directions. There is some friction when the motion should have no resisting forces but this is very small and is assumed to be zero in this work. The dampers are both adjustable via an attached screw to get a variety of different damping constants.

There is an air spring effect in the dampers. When the resistive force generated from the air moving from within the dampers, through the orifice and to the atmosphere is greater than the force required to compress the air, then the damper will compress the air in preference, acting like an air spring. For moderate damping constants the air spring effect affects the first 1-2 mm

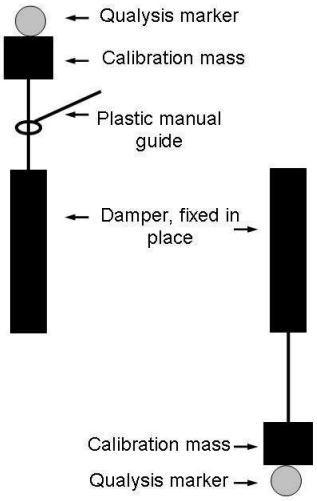

Figure 4.9: A schematic diagram of the calibration system for the dampers.

of motion from a stationary position, but higher damping constants has a greater influence. This allows a certain amount of relative movement that is not being damped to occur, and this amount of movement increases for higher damping constants. For this reason, the maximum value of the damping constants has been limited although theoretically the dampers could produce higher damping constants.

4.8.2 Calibration of the main dampers

The dampers are calibrated by rigidly attaching the damper to the fixed platform. The damper is orientated so that the weight of the calibration mass is opposed by the dampers resistive force. A 23 g and a 55 g calibration mass is screwed into the damper, in the same way that the internal mass is attached. A Qualisys marker weighing 7 g is attached to the calibration mass. The dampers are either manually extended or compressed (depending on which damper is being tested), released, and allowed to move under gravity due to the weight of the mass. The marker is tracked at 64 Hz or 128 Hz and the expansion / compression is repeated for a minimum of 128 s, until enough results have been obtained to be able to determine the damping constant. For the compression mono-directional damper, a plastic manual guide is used to keep the mass falling vertically, with as little interference to the motion as possible. A schematic diagram of the calibration process is presented in Figure 4.9.

The results are visually reviewed and individual results for which there has been difficulty obtaining a vertical descent are removed. When a slope has been deemed acceptable for use, it is split into exactly four sections and the velocity and acceleration calculated from the midpoint of each section. Having four sections results in a more consistent result that averages out any

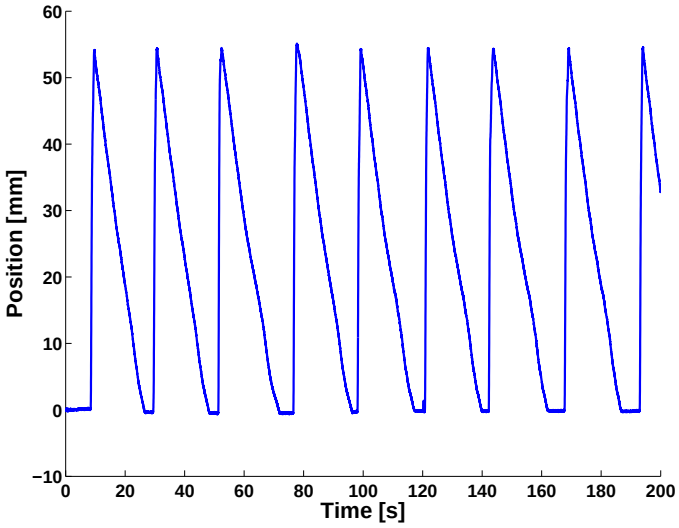

Figure 4.10: The expansion damper **E93** being calibrated.

swinging motion or other random small variations. A typical recorded example section of the position of the calibration mass is presented in Figure 4.10. Due to the manual input for the compression mono-directional dampers in keeping the mass moving vertically with the plastic guide, the reliability of the compression mono-directional damper constant is lower than the expansion mono-directional dampers.

This method obtains between 5 and 20 results for the different masses falling under gravity for each damping constant. The overall damping constant is calculated using Equation 4.14, which is then averaged.

$$c = \frac{m(g-a)}{v}, \tag{4.14}$$

where c [Ns/m] is the damping factor to be calculated, m [kg] the combined weight of the calibration mass and the marker, g [m/s^2] the acceleration due to gravity, a [m/s^2] the measured acceleration of the calibration mass and v [m/s] the measured velocity of the calibration mass.

To check that the dampers are linear as claimed by the manufacturer, Equation 4.14 has been used as a basis for a numerical simulation. The simulation uses the Runge–Kutta numerical method (see Section 2.4.1), to obtain the positions, starting from the same position as the experimental results. The numerical simulation does not model the damper reaching the end of its stroke. The numerical simulation is compared to experimental data and shows a good level of agreement. This is demonstrated by an example, presented in Figure 4.11.

In this figure, just after the damper is released from stationary, the experimental results show the mass descending faster than the numerical simulation. This could be due to the air spring effect or slight nonlinearities in the damper due to being close to the end of its stroke. During the central motion, the rate of the mass being lowered is very similar. At the end of the stroke

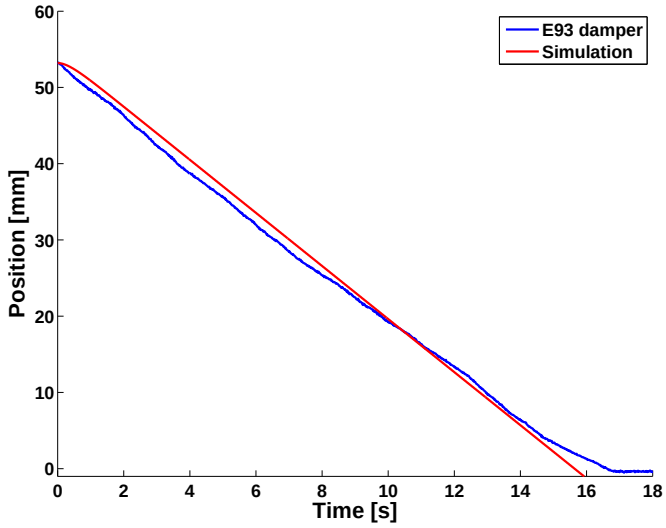

Figure 4.11: The expansion damper **E93** being compared to a numerical simulation of a linear damper.

for the experimental damper, the rate of descend decreases, this is due to the damper behaving with some nonlinear characteristics, which does not occur in the numerical simulation. This is not unexpected as the damper is nearly fully expanded, and the limited stroke is influencing the dampers motion. However, it can be confirmed that during the majority of the motion, the damper is behaving in a linear manner, as claimed by the manufacturer.

Random Errors in the calibration process

An indication of the random error in this method of testing the dampers would be the magnitude of the standard deviation. For 95% confidence that the mean is within the limits provided, two standard deviations away from the mean are used for the error bars.

Systematic error in the calibration process

Systematic errors are errors which are related to the testing procedure and as such would not be detected by multiple testing and the resulting variance. Such errors are,

- The effect of the air spring effect.
- If the mass has been weighed incorrectly, due for example if the scales have been calibrated incorrectly.
- For the expansion mono-directional damper, the plastic manual guide will reduce the velocity of the motion for all the results.

4.8.3 Endstop damper

The endstop dampers are also manufactured by Airpot, (Airpot Corporation, 2008). They comprise an internal pneumatic damper and an internal spring. The fully extended endstop damper has an axi-symmetric cylinder plunger made from a rubber based material which allows a small amount of movement in non-heave directions. This protrudes from the main body, and is compressed by the internal mass when in contact with the plunger. The internal damper is adjusted to vary the damping constant over a limited range. The spring has a spring constant of 27 N/m, which is used to return the dampers to the fully extended position after they have been compressed, and in the fully extended position the spring is compressed by 9.6 mm. Due to the spring the damper tends to stays in contact with the internal mass until the damper is fully extended. However, when the damper is returning to its fully extended state, it does not provide a damping force on the internal mass. The endstop dampers are attached to the top internal base at a known distance away from the SWL position of the internal mass.

4.8.4 Calibration of the endstop dampers

The endstop dampers are calibrated in a similar manner to the main dampers. Three different calibration masses can be used to increase the accuracy of the procedure. Each calibration mass is made of steel with a 5 mm radius hole where the plunger of the endstop damper sits, they have a constant external radius of 15 mm. Their heights are 22 mm, 30 mm and 50 mm, and the masses weigh 72 g, 103 g and 183 g, respectively. Typically two of the three masses are used to calibrate the endstop damper, which are chosen based on the approximate resistive force of the damper. If the endstop damping constant is high the smaller calibration mass will not cause much movement and for larger endstop damping constants the large mass may cause damage to the endstop damper.

A Qualysis marker was attached to the calibration masses and the position of the calibration mass was recorded, as the mass was lifted and held for approximately 1 s, where it just sat on top of the fully extended plunger and released; this was repeated for each damper for at least 128 s. Each time the calibration mass was released, the results were visually checked for obvious experimental error. The damping constant has been calculated based on the equation of motion for the calibration mass, from,

$$c_{endstop} = \frac{m(\ddot{x} - g) + k(x + x_{pd})}{\dot{x}}, \tag{4.15}$$

where m [kg] is the combined marker and calibration mass, x the position of the calibration mass, k the endstop damper spring constant and x_{pd} is the predetermined compression of the endstop damper spring, set at 9.6 mm.

The positions, velocities and accelerations of the calibration mass were calculated for the first 10 mm of motion, and this 10 mm was divided into two sections. The largest and smallest 10%

of the values of $c_{endstop}$ were removed due to potential experimental error associated with the position that the calibration mass was held before being released. The remaining values were averaged to find the value of $c_{endstop}$ and the associated standard deviation.

Chapter 5

Experimental results in regular waves

5.1 Summary

This chapter presents experimental results, analysis and discussion for the linear, mono-directional and endstop dampers, in regular sinusoidal waves. Parts of this chapter have been reproduced in Bailey and Bryden (2008) and Bailey and Bryden (2009).

Section 5.2 details the dampers used and their calibrated damping constants. Section 5.3 presents the RAO against frequency for the displacements of the cylinder, internal mass and the relative displacement between them, for each damper. It also presents the RAO against the damping constant, for predefined frequencies. In Section 5.4 the relative phase between the cylinder and the internal mass is presented and discussed for the different damper types. Section 5.5 presents calculations of the power extracted from the dampers. It compares the power extracted across the different damping constants for the same type of damper, and the power extracted for different dampers and discusses the implications of this. The chapter is concluded in Section 5.6. The figures for this chapter have been placed in Section 5.7, at the end of the chapter, for clarity.

5.2 The dampers tested

5.2.1 Linear dampers

The linear dampers are calibrated using the same method as the expansion mono-directional dampers (see Section 4.8.2). Their damping constant is obtained from an average value and the error is calculated as two standard deviations, which is the equivalent of placing 95% confidence limits on the mean value. The linear dampers and their respective damping constants and 95% confidences are presented in Table 5.1. The linear dampers, on average, have a 95% confidence value that is 8.6% of the damping constant.

Other linear setups that were tested have either no spring present or no damper present. These are shown in Table 5.2, with their equivalent damping constants.

Name	Damping constant [Nm/s]	95% confidence
L41	41.2	± 5.6
L85	85.1	± 6.9
L144	143.6	± 10.4
L229	288.6	± 24.3
L365	365.4	± 15.1
L699	698.7	± 69.0

Table 5.1: The values of damping for the linear bi-directional damper.

Name	Description	Equivalent damping constant [Nm/s]
ND	No damper present	0
NS	No spring present	∞

Table 5.2: The values of damping for other linear devices.

5.2.2 Mono-directional dampers

The mono-directional dampers have been calibrated using the methods described in Section 4.8.2, for both the expansion and compression mono-directional dampers. The range of the damping constants considered is designed to have a wide and even spread of the different damping constants. Some similar damping constants are included, in order to check for experimental repeatability and for experimental runs were there was a low confidence in the results.

The damping constants of the mono-directional dampers with their 95% confidence limits, are presented in Table 5.3 for the expansion mono-directional dampers and Table 5.4 for the compression mono-directional dampers. The 95% confidence interval is, on average, 8.0% for the expansion mono-directional damper constants and 47.4% for the compression mono-directional damper constants. This is as expected due to the method of the calibrating the compression mono-directional dampers, as discussed in Section 4.8.2.

Higher damping constants have been obtained for the expansion mono-directional dampers compared to the compression mono-directional dampers due to the ability to calibrate the expansion mono-directional dampers relatively accurately at high damping constants and because the dampers are less likely to be damaged by the calibration masses[1].

1. The calibration process for the compression damper involves attaching the calibration mass to the damper, as was presented in Figure 4.9. When the plastic manual guide is not being used, i.e. when active calibration is not occurring, the calibration mass causes a torsional moment about its attachment point, since it rests at an angle. This causes stress on the damper which potentially leads to failure.

Name	Damping constant [Nm/s]	95% confidence
E13	13.6	± 0.5
E14	14.0	± 3.5
E66	65.7	± 4.2
E93	93.0	± 3.3
E101	101.4	± 3.1
E176	175.6	± 10.4
E283	282.9	± 44.9
E334	333.7	± 20.9
E437	436.5	± 28.3
E686	686.3	± 44.5
E867	866.6	± 18.7
E872	871.8	± 97.3

Table 5.3: The values of damping for expansion mono-directional damping.

Name	Damping constant [Nm/s]	95% confidence
C26	26.4	± 8.8
C40	40.0	± 18.4
C113	113.2	± 33.6
C161	161.1	± 65.6
C178	177.9	± 79.6
C528	528.1	± 473.9

Table 5.4: The values of damping for compression mono-directional damping.

Name	Damping constant [Nm/s]	95% confidence
ES8	7.6	2.4
E21	20.6	2.9
E34	33.9	14.4
E44	44.2	27.7
E50	50.2	28.7
E55	54.5	24.7
E73	73.1	14.2
E78	78.2	12.7

Table 5.5: The values of damping for endstop damping.

5.2.3 Endstop dampers

The endstop damper were positioned 2 ± 1 mm above the SWL position of the internal mass. Due to the static friction between the internal mass and the central rod, the SWL position of the internal mass varied slightly, both within a test as well as between different tests. However, the position of the endstop damper and the other experimental parameters were kept constant.

The different endstop damping constants can be seen in Table 5.5. These were calculated from the calibration procedure discussed in Section 4.8.4, for the top 10 mm of compression from the plungers being fully extended. These constants are much lower than the constants for the main damper due to the first 10 mm of travel not being able to provide a high damping force.

The magnitude of the 95% confidence interval, on average, as a proportion of the damping constants is 36.1%. This shows that the calibration process is not as accurate as the linear dampers, since the calibration masses have to be placed on the fully extended damper's plunger and released cleanly.

5.3 Response Amplitude Operator

The RAO is the ratio of the magnitude of the body's response to the incoming wave, and the amplitude of the incoming wave. This measure is used to show how the device would move in any different sea state, if the incoming waves and the device were fully linear (see Section 3.2 for more details). The RAO emphasises the resonant peak(s) for the device and a wide resonant peak is considered ideal (Lin, 1999) for maximum power extraction from irregular waves. The RAO is used to directly compare different devices and different parameters within the same device.

These RAOs are later compared to the numerical simulation results in Section 7.3, which can also be used as a "sanity check" on the experimental results presented in this section.

5.3.1 Regular waves

The device was tested in regular sinusoidal waves for 64 s, with an additional 16 s used to allow the waves to reach steady state, i.e., all the transient waves had decayed. The data was recorded at 32 Hz and represented either the position of the bodies obtained from the markers using the Qualysis motion capture system, or the wave height from the wave gauges used when the model was not present. The frequencies being tested were in 0.05 Hz steps, from 0.50 Hz to 1.10 Hz. In addition, at the frequencies where the cylinder has a larger response, from 0.67 Hz to 0.81 Hz all possible frequencies that the Curved Wave Tank could produce were tested. The tests were at a nominal wave height of 20 mm, with the wave height measured using wave gauges and the actual wave height falling between 16 mm and 27 mm, for different wave frequencies.

5.3.2 RAO of the linear damper

The RAO for each of the linear dampers, for the cylinder, the internal mass and the relative position between them, is presented in Figure 5.1. The relative position between the two bodies is the difference between the cylinder RAO and the internal mass RAO; these are based on their individual maximum positions. Therefore, for the relative RAO the phases of the internal mass and the external cylinder are assumed to be the same.

These results show that there is a resonant peak with a maximum value at approximately 0.8 Hz, with frequencies between 0.75 Hz to 0.85 Hz having an increased response. The largest relative RAO occurred, as expected, when there was no damper present. The cylinder that has the largest RAO is when there was no spring (and damper) present.

The larger than expected relative RAO result for the damper **L699** is most likely due to the air spring effect of the damper.

Damper **L144** is seen to have a lower relative motion than dampers with similar damping constants. This difference is not simply explained but is potentially due to changing internal mass friction and damping from the spring interacting with the central rod. It is unlikely to be due to an interesting physical phenomena of the system since the device should have only linear components and the linear response would not involve a double peak for the relative motion RAO of this model.

To compare the effect of the linear damping directly to the RAO for the cylinder, the internal mass and the relative position between them, results are presented in Figures 5.2, 5.3 and 5.4. These plot the RAOs against the linear damping constants, for each of the frequencies at and around the resonant frequency of the body.

5.3.3 RAO of the expansion mono-directional dampers

The physical model with an expansion mono-directional damper was tested in regular waves and the RAO for the external cylinder, internal mass and the relative RAO between them are presented in Figures 5.5 and 5.6, for the different damping constants. The general shape of the RAO for the bodies and the relative motion between them is similar to the linear dampers.

Damper **E66** has a negative relative RAO, which is different from all the other linear and expansion mono-directional dampers (although it occurs once in the compression mono-directional dampers). The time series results for this damper are presented in Figure 5.7, which shows no distinct difference to the other time series results except that the cylinder moves more than the internal mass. There is no clear explanation why this occurs and whether it is due to an initial condition prevalent in this damper setup or an intrinsic quantity of this particular damping constant is not evident and would be hard to determine.

It was recorded during experimentation that damper **E176** was visually seen to have little motion compared to the other damper setups. Its RAO for both the external cylinder and the internal mass is much lower than similar damping constants. The time series results for 0.78 Hz regular waves are presented in Figure 5.8. This figure shows that the regular motion took longer to get established than for the other dampers and, as expected, the relative motion between the two bodies was small.

It is postulated that the central rod had twisted in pitch and the rod-end bearings were not allowing free movement of the central rod due to the undesirable position of the central rod. This has happened for other damper setups, were the lack of motion had been noted and the central rod was physically felt to resist motion. This was remedied by forcing the central rod to move in large motions, which realigned the system and resulted in *normal* motions of the system. The experiments were then re-ran for this damping constant.

The different damping constants have been plotted with the RAO of the cylinder, internal mass and the relative position between them, for defined frequencies. These are presented for the expansion mono-directional damper in Figures 5.9, 5.10 and 5.11.

From viewing the data points, although not statistically valid, a general trend can clearly be seen, with the value of the RAO reducing for increased damping constant.

5.3.4 RAO of the compression mono-directional damper

For compression mono-directional dampers, the RAO for the cylinder, internal mass and the relative position between them, is presented in Figure 5.12. The RAOs of which are generally similar to the linear and expansion mono-directional dampers. The exception to this is damper **C178**, were the majority of the relative RAO between the cylinder and the internal mass is negative. The relative RAO results have a high variability between the frequencies of 0.65 Hz and 0.75 Hz.

The influence of the different damping constants of the compression mono-directional damper, on the RAO for different wave frequencies, is presented in Figures 5.13, 5.14 and 5.15.

5.3.5 RAO for endstop dampers

The response of the internal mass, the cylinder and the relative position between these bodies can be seen for the endstop dampers, in Figure 5.16, which shows each of the individual dampers. These are of the same general shape as the linear and mono-directional dampers, with the relative RAO between the cylinder and mass, remaining positive for all of the significant responses.

Figure 5.17 shows the RAO for the relative motion between the cylinder and mass, for all the endstop dampers on one graph. It can be seen (and is emphasised on the graph) that there are two distinct responses. The upper response is a broader banded spectrum, with, at its highest response, a RAO of between 0.30 – 0.55, and a lower narrower banded response, which at its highest response has a RAO of between 0.1 – 0.2. The endstop dampers **ES8, ES21, ES34,** and **ES50** are in the upper response and these dampers tend to have the lowest damping constant of those tested. Endstop dampers **ES44, ES55, ES73** and **ES78** are in the lower response category, and these dampers tend to have the higher damping constant of those tested.

Figures 5.18, 5.19 and 5.20 show the RAO of the internal mass, cylinder and the relative position, against the endstop damping constant, for each frequency.

From the RAO it shows that the absolute position of the cylinder and internal mass are not significantly affected by the variation in the endstop damper constant. For frequencies nearer the resonance frequency of the cylinder, the influence of the endstop damping constant on the overall motions of the cylinder and internal mass is higher. This is as expected since frequencies nearer to resonance result in larger motions, where the relative motion of the internal mass is more likely to contact with and stay in contact with the endstop damper for a greater proportion of the time. There is a slight trend for the motion of the cylinder and the internal mass to generally increase after the lowest damping constant (**ES8**), and then start to decrease again by **E34**. For the frequencies that are close to the resonant frequency, in this case for frequencies 0.77 Hz – 0.81 Hz inclusive, the higher two endstop damping constants have

an increased absolute RAO compared to their neighbours, whilst outside of this range, they decrease compared to their neighbours.

5.3.6 Comparison and further discussions of the RAO

Linear and mono-directional dampers

The RAOs for the linear and mono-directional dampers are compared in order to see what effect having a nonlinear mono-directional damper has on the resulting RAOs. There are difficulties in comparing the results due to some dampers having lower or higher results than expected and compared to similar damping constants, and because exactly the same damping constants were not used for the different types of dampers.

In order to aid the comparison between the dampers, Figure 5.21 presents the average and the average plus and minus the standard deviation, for the different damper types. This figure shows the RAO separately for the cylinder, internal mass and the relative position between them, over the frequency range of interest.

The RAOs for the position of the cylinder are largest for the linear damper and the compression mono-directional damper. These are, on average, significantly higher than for the expansion mono-directional damper. However, there is less variation in the RAO for different damping constants, for the linear damper than for both the mono-directional dampers.

From the numerical simulations in Chapters 3 and 7 the mono-directional dampers are shown to have a very similar response to the waves. The compression mono-directional damper has a higher proportion of low damping constants compared to the other dampers, and a smaller overall sample size. This would potentially explain why the compression mono-directional dampers' cylinder RAO is higher than the expansion mono-directional dampers.

The RAO of the internal mass is, on average, highest for the linear damper with the expansion mono-directional damper having the lowest response. Therefore, the relative RAO is highest for the compression mono-directional damper, with the linear damper having the lowest response. The expansion mono-directional damper is between the two other damper types. The variability in the mono-directional dampers is significant, with the compression mono-directional damper having a slightly higher standard deviation than the expansion mono-directional damper. The linear damper's standard deviation is much lower than the mono-directional dampers.

An additional uncertainty in the results occurs for the compression mono-directional damper, because its damping constants have a significantly greater error in their calibration (two standard deviations were 47% of the damping constant as opposed to 8% and 9% for the expansion mono-directional and linear dampers).

Having a higher relative RAO is desirable because it implies that the power extracted will be greater. For regular waves, the mono-directional dampers have a higher relative RAO than the

linear damper. This is not highly influenced by the exact damping constant that is chosen.

Linear and endstop dampers

The linear and the endstop damper are compared to see what influence having an endstop damper has on the resulting RAOs. The average response and the RAO plus and minus the standard deviation, for the different bodies and their relative motion, are presented in Figure 5.22.

The RAO of the cylinder shows that the linear damper and the endstop dampers have a similar response to the waves at nearly all frequencies. At frequencies that are very close to resonance, the endstop damper has a slightly lower response. This difference in response occurs because at these incoming frequencies, the cylinder has larger amplitudes of motion. Therefore, the endstop damper is likely to have more of an influence on the motions.

The standard deviation of the linear damper is much greater than the endstop damper. This is to be expected since the linear damping that occurs in the endstop damper is the same for the different endstop damping constants.

The difference RAO is lower for the endstop damper for most frequencies except the resonant frequencies. At the resonant frequencies, the endstop damper has a higher relative RAO, compared to the linear damper. The difference for the lower response away from the resonant frequency is due to the linear damping aspect of the endstop damper setuponly having an effect. Since this linear damping component is at a low damping constant, the relative motion is, on average, higher for higher damping constants.

5.4 Relative phase

The relative phase is the phase difference between the external cylinder with respect to the internal mass. This varies according to the PTO damper used. This is calculated in the time series results (for both the experimental and numerical simulation results) from obtaining the highest values of the position of the internal mass and cylinder, for each wave cycle and observing the time at which these occur. The average time difference between them is the relative phase used.

	Relative phase [Rad]				
Damper	Zero	$< \|0.2\|$	> 0 and < 0.2	> -0.2 and < 0	≤ 0
Linear	53%	86%	9%	23%	88%
Expansion mono-dir'	38%	75%	11%	27%	86%
Compression mono-dir'	32%	67%	11%	24%	82%
Endstop	49%	83%	11%	23%	79%

Table 5.6: The percentage of dampers with zero and small relative phase.

5.4.1 Relative phase of the linear and mono-directional dampers

The relative phase for the linear and mono-directional dampers are presented in Figure 5.23. These contour plots show the different relative phases, for the different frequencies of the incoming waves. They show the number of times each phase occurs in 0.1 radian bins. These have been normalised by dividing the number of times each phase occurs in each radian bin by the number of dampers tested, to allow a comparison between the different damper types. The normalised occurrence of each phase is shown on the colour bar in the figure presented.

These figures show that there is a general trend for the linear damper to have a relative phase nearer to zero than for the mono-directional dampers. The relative phase of the mono-directional dampers tends to be further from zero for frequencies around where the cylinder has the greatest response. All the dampers have both a positive and a negative phase difference.

The relative phase is presented for linear, compression and expansion mono-directional dampers, for set frequencies, showing the phase against the damping constants in Figures 5.24 and 5.25. These show a general trend for an increased relative phase of the cylinder to the internal mass, whether lagging or leading, from a damping factor around of 100 – 150 Ns/m to approximately 400 Ns/m.

The proportion of individual experimental runs when there is no relative phase difference and when there is a less than $\pm$ 0.2 rads relative phase difference are presented in Table 5.6. This shows that the linear damper has more experimental runs with no relative phase or with a small relative phase compared to both mono-directional dampers. The ratio of the positive to negative relative phase is approximately the same (between 28% and 31% of non-zero values were postive) for the different damper types.

5.4.2 Relative phase of the endstop damper

The relative phase between the cylinder and the internal mass has been calculated for the endstop damper. These are also presented in the normalised contour plot in Figure 5.23, alongside the linear and mono-directional dampers. This figure shows that the relative phase when there is an endstop damper was generally greater than with a linear damper but less than with a mono-directional damper.

Zero relative phase and a small relative phase of less than 0.2 rads occur in a proportion of the results, as presented in Table 5.6. This shows that the endstop dampers have a percentage of zero and small relative runs between the percentages of the linear damper and both mono-directional dampers.

The different frequencies are considered separately in Figure 5.26, were there is no clear pattern between the value of the relative phase, the frequency at which it occurs or the damping constant.

5.4.3 Discussions of the relative phase

There is no obvious indicators of whether a damper type, frequency or damping constant, will result in the relative phase, if it is not zero, being either positive or negative. All the dampers have a similar proportion of positive or negative relative phase. It could be speculated that whether the relative motion is lagging or leading is a factor of the spring and internal mass and not directly associated with the type of damper or damping constant used. The exact initial conditions of the spring and internal mass for each run would then determine the positive or negative nature of the relative phase, if there was to be a relative phase. Whether there was any relative phase is influenced by the type of damper used and the its damping constant.

The reason for interest in the relative phase is that it allows a greater relative motion between the internal mass and the cylinder, without the need for a spring with a lower spring constant or a heavier internal mass. Since the amount of relative motion is a determining component in the amount of power extracted, having a larger relative phase, regardless of whether it is lagging or leading is beneficial.

5.5 Regular wave power extraction

The power extracted from the waves is calculated from the product of the square of the relative velocity and the damping constant. The different damper types extract the power at different positions in the wave cycle.

For this calculation, the positions of the cylinder and mass are centered on zero by subtracting their average value. Due to high frequency vibrations, the original signal for the positions

for both the cylinder and internal mass is smoothed by passing a moving average filter over the signal. This finite impulse response filter [2] takes 10 data points to determine the moving average. The velocity is then obtained from the signal differences and this signal is also smoothed, using the same procedure. The power is then calculated from this signal squared and multiplied by the damping constant. Due to some occasional remaining spikes in what should be an approximately regular signal since it is from a sinusoidal input, any data point that has a value of four times the average is replaced with the average. This is justified because of the sinusoidal nature of the signal, therefore the power extracted would have a smooth cyclic pattern. The spikes are not repeating in a regular manner confirming that they are spurious data points. This occurs for approximately between 0% and 10% of the signal in the most extreme example. The extreme examples occur when it has been noted that there were issues with the light rod that carries the markers colliding with the top base, and hence causing oscillations in the markers. The power extraction for the signal without smoothing and filtering for damper **E437**, and the same signals which have been smoothed but not filtered, with the final smoothed and filtered signal are presented in Figure 5.27.

A more useful measure than the power extracted for different wave frequencies (especially as the amplitude of the waves varied slightly for different frequencies) is to use the power capture efficiency or ratio. This is the power extracted by the damper, divided by the power that is in the waves that contact along the front length of the WEC. The power in the waves for the front length of the device, assuming deep water, was calculated using Equation 5.1, from Falnes (2002).

$$\text{Power in the incident waves on the front of the device} = \frac{a\rho g^2 A^2}{16 f}, \tag{5.1}$$

where a [m] is the radius of the device, and A [m] is the wave height.

The ratio of the power captured from the waves to the power in the incident waves is the power capture efficiency, which is used to present results in this chapter. This is a fraction where a unity ratio would mean that the same amount of power is captured as was in the incident wave on the front of the device.

5.5.1 Power extraction from a linear damper

The time averaged power capture from a linear damper is obtained by recording the power captured over a number of entire representative wave cycle and an average is obtained.

The power capture efficiency of the linear damper, for different damping constants, against the wave frequency, is presented in Figure 5.28.

Damper **L699**'s power capture efficiency is considerably higher than the other damping constants. This damper has a much higher damping constant than the other dampers and it is

2. A filter that results in the signal becoming zero for a finite number of passes.

assumed that the “high power extraction” is actually due to the extra relative motion occurring due to the air spring effect.

The power capture efficiency against the damping constant is shown in Figure 5.29, for the individual frequencies. It is observed that at the frequencies where the cylinder has a higher response to the waves, there is more power capture.

5.5.2 Power extraction from an expansion mono-directional damper

The power capture from an expansion mono-directional damper is obtained when the relative velocity of the cylinder to the internal mass is negative. During these periods of the wave cycle, the power captured is calculated, otherwise the power capture is zero. The time averaged power capture is obtained from the average for the entire time period.

The power captured from the expansion mono-directional dampers is presented in Figures 5.30 and 5.31, for each individual damping constant.

As stated previously, since damper **E176** did not appear to have much movement of the external cylinder, as discussed in Section 5.3.3, then this damper has a low time averaged power compared to its neighbours. The three larger damping constants all appear to have a higher than expected power capture, which is due to the air spring effect.

The individual frequencies are presented for the power capture efficiency against the damping constant in Figure 5.32.

5.5.3 Power extraction with a compression mono-directional damper

The power extraction from a compression mono-directional damper occurs when the relative velocity of the external cylinder to the internal mass is positive. During these periods, the power is captured using the same method as in the linear bi-directional dampers, and outside these periods it is zero.

The power capture efficiency for the compression mono-directional damper, for each different damping constants, for all frequencies is presented in Figure 5.33.

In this figure the damper **C178** has significantly higher power extraction than the other dampers and notably than damper **C161** which has a similar damping constant. The reason for this is unclear, but it is likely to be due to either experimental errors in the results or the value of the damping constant is inaccurate due to the large standard deviation for the compression dampers.

The power capture is viewed against the damping constants, for predefined frequencies, in Figure 5.34.

5.5.4 Power extracted from an endstop damper

The time averaged power extracted from the endstop damper is calculated for the linear internal frictional damping force, for the power extracted from the endstop damper and for these two power extraction mechanisms combined. The power from the frictional damping is calculated as a bi-directional linear damper, with a damping constant of 24 Ns/m, as found in Section 2.6.3. The time averaged power extracted from the endstop is calculated from when the relative position of the internal mass is greater than $+2$ mm from its SWL position and when the relative velocity is positive, otherwise the power extracted is zero. The power capture efficiency is calculated and presented in Figure 5.35, for the individual dampers over the frequency range, for the endstop damping power, the linear frictional damping power and both the damping powers combined.

The power extraction for each damper shows high variations in the power capture over the frequency range for the different damping constants. The proportion of the different types of damping in the combined power capture varies between the different damping constants, but within the same damping constant, the proportion is similar across the frequency range.

The effect of the power capture efficiency for the individual frequencies can be seen in Figure 5.36, for the endstop, linear and combined power capture efficiencies.

5.5.5 Discussion of power extracted

There is high variability in the power capture efficiency results both within the different damping constants and in the different damping types. Part of this variability is due to the small values of the relative velocity between the internal mass and the cylinder. Since the relative velocity is small, than any errors due to any slight changes in the experimental setup are a significant proportion of the relative velocity. The power is a product of the relative velocity squared and the damping constant, so these errors in the relative velocity are squared to obtain the power capture efficiency. Hence the large error values presented in these results. Therefore, the results should be treated as a general indication of the trends and as qualitative results as opposed to quantitative and exact conclusions. The occasionally small sample size, and the variable power extraction results, produces relationships that do not allow a high statistical confidence, although visual interpretation and awareness of the potentially spurious results does allow some conclusions to be reached.

As an aid for comparison between the linear and mono-directional dampers, the average power capture efficiency and the error for this based on the mean plus and minus one standard deviation are presented in Figures 5.37 and 5.38 .

These figures shows that the average power extraction is greatest when an expansion mono-directional damper is used compared to when a linear damper is used. There are similar standard deviations on these two dampers.

The average power capture efficiency is slightly less when a compression damper is used as opposed to a linear damper. However, there is a larger standard deviation for the compression mono-directional damper, implying a certain amount of uncertainty in this result, possibly from the smaller sample size of this damper compared to the expansion mono-directional damper.

Reasons for the difference in power extraction are due to the difference in the relative value of the RAO, which results in the differences in the relative velocities of the internal mass. The relative phase between the internal mass and external cylinder, also influences the amount of power extracted.

The reason for the difference between the two mono-directional dampers is not clear or expected. Numerical simulations of the mono-directional dampers (Section 7.5) show these values should be similar. The difference could be due to the lower confidence in the value of the damping constant for the compression damper as opposed to the expansion mono-directional damper. This could result in the compression mono-directional dampers consistently under or over estimating their damping constant.

The power captured from the linear damper is also compared to the endstop damper setup. The endstop damping constant tends to be much lower than the linear damping constant, and the linear component of the endstop damper is also present for the linear damper. The power captured from the linear damper and from the endstop damper alone, from the linear frictional damper component of the endstop damper setup and from their combined power extraction is presented in Figures 5.39 and 5.40.

The linear damper has a higher power extraction over nearly all the frequencies to any of the endstop dampers, although the linear damper also has a higher standard deviation. The power extraction generally has the same shape regardless of which damper or combination of dampers is viewed.

5.6 Conclusions of chapter

This chapter has shown that the relative RAO is higher for the mono-directional dampers than for the linear dampers. The endstop damper has slightly lower values of the relative RAO than the linear damper, except at the resonance frequencies.

The relative phase between the internal mass and the cylinder is generally greatest (in both lag and lead) for the mono-directional dampers, with the endstop dampers having a smaller relative phase and the linear dampers an even smaller relative phase. Having a larger relative phase and a greater relative RAO is an indicator that more power can be extracted.

The power extracted was generally greater for the compression mono-directional damper than for the linear and expansion mono-directional dampers, which had similar values. The lower

power extracted from the expansion mono-directional dampers compared to the compression mono-directional damper was not expected, and probably due to a combination of the sample size, the range of the damping constants and experimental errors.

The next chapter considers the motions and power extracted from the same dampers, in irregular waves.

5.7 Figures

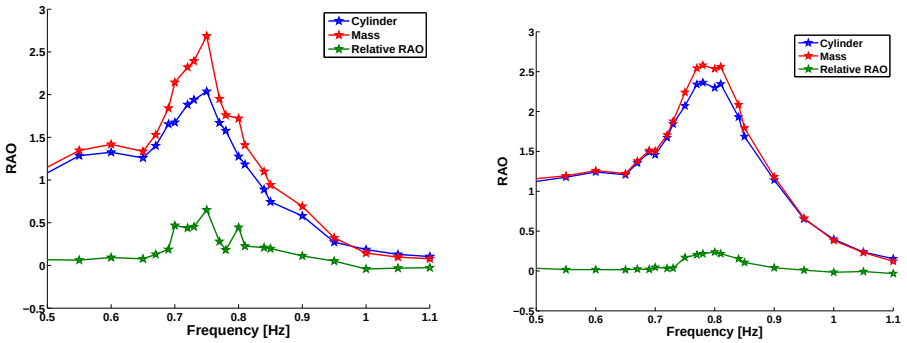

(a) ND **(b)** L41

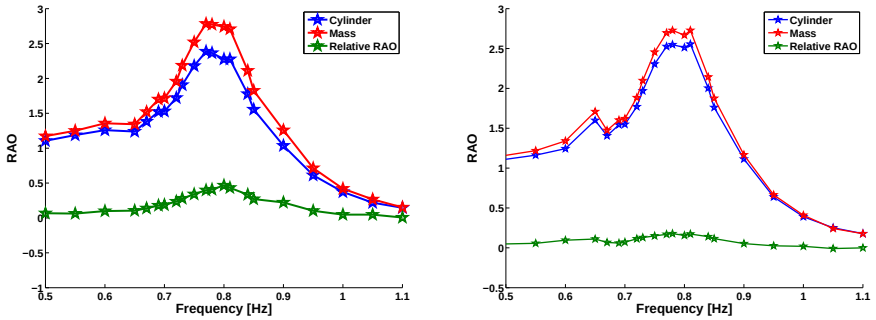

(c) L85 **(d)** L144

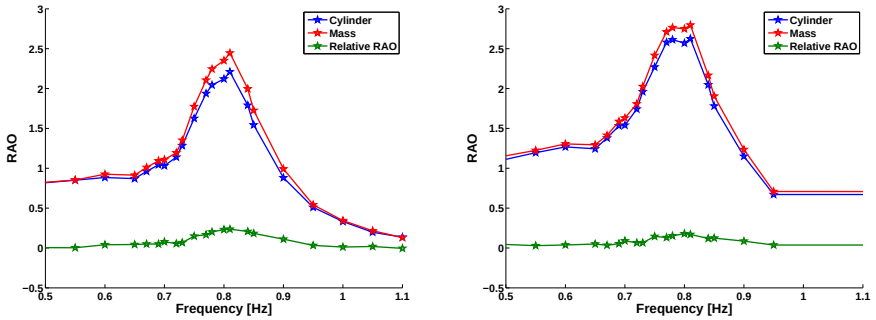

(e) L229 **(f)** L365

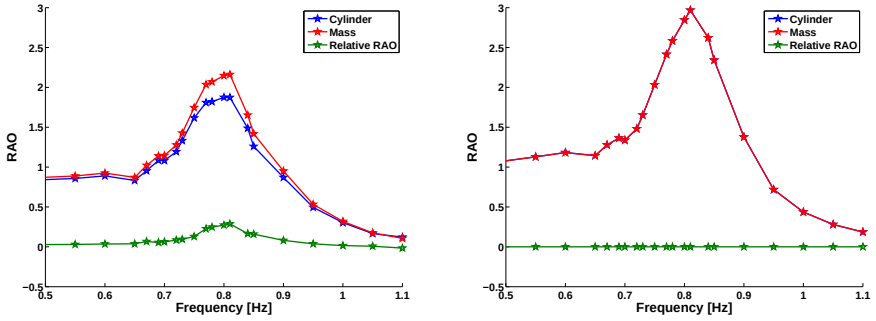

(g) L699 **(h)** NS

Figure 5.1: The RAO for the cylinder, the internal mass and the relative position between them, for a linear damper.

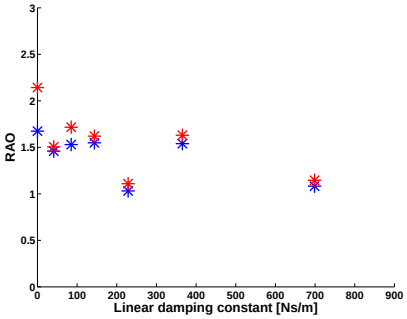

(a) 0.703 Hz, cylinder and mass.

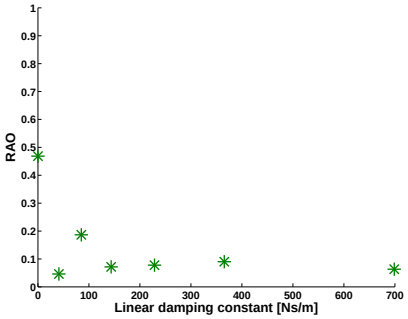

(b) 0.703 Hz, relative position.

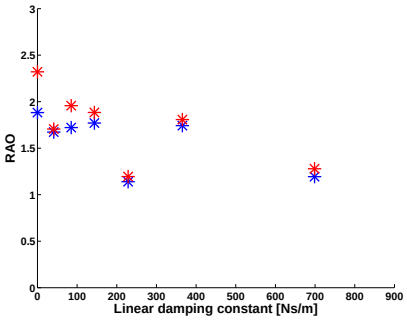

(c) 0.719 Hz, cylinder and mass.

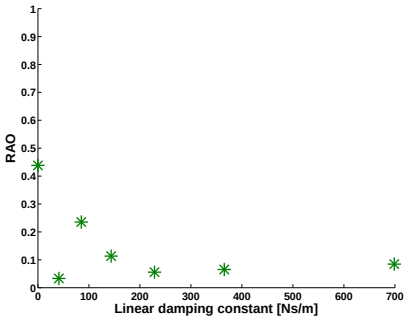

(d) 0.719 Hz, relative position.

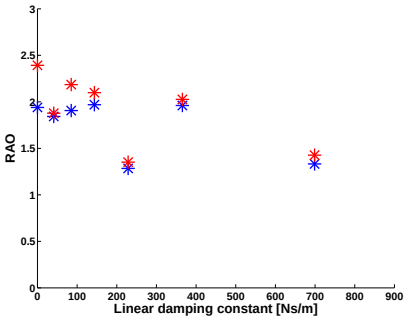

(e) 0.734 Hz, cylinder and mass.

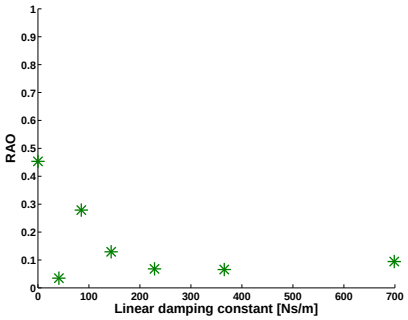

(f) 0.734 Hz, relative position.

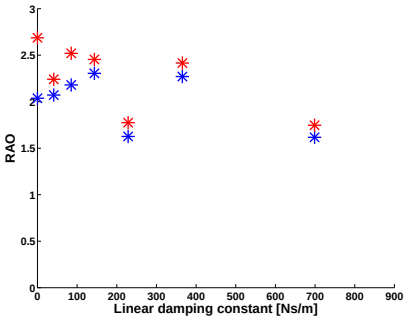

(g) 0.750 Hz, cylinder and mass.

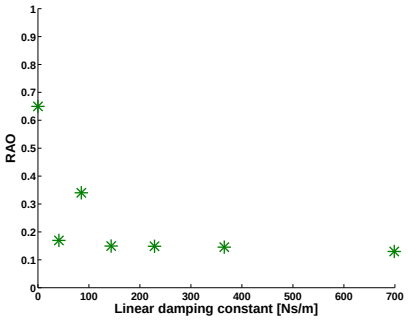

(h) 0.750 Hz, relative position.

Figure 5.2: RAO of the cylinder (blue), mass (red) and their relative motion (green), with a linear damper, for frequencies 0.703 Hz to 0.750 Hz.

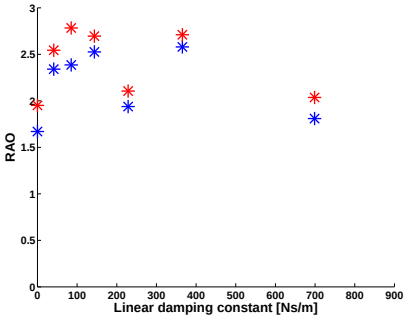

(a) 0.766 Hz, cylinder and mass.

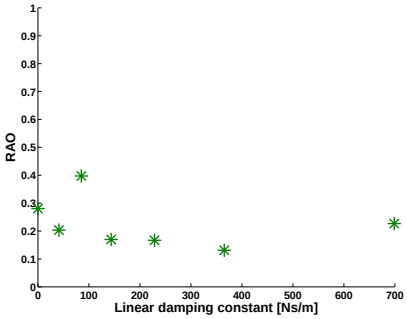

(b) 0.766 Hz, relative position.

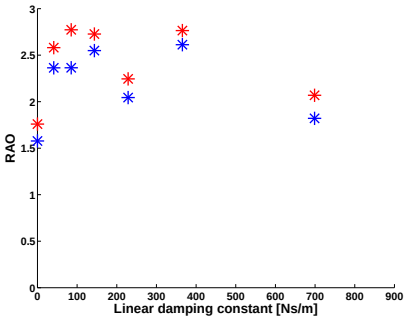

(c) 0.781 Hz, cylinder and mass.

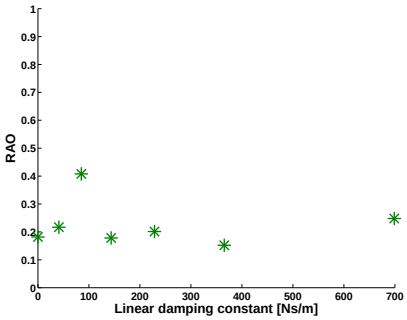

(d) 0.781 Hz, relative position.

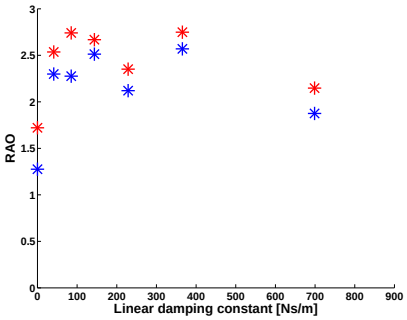

(e) 0.797 Hz, cylinder and mass.

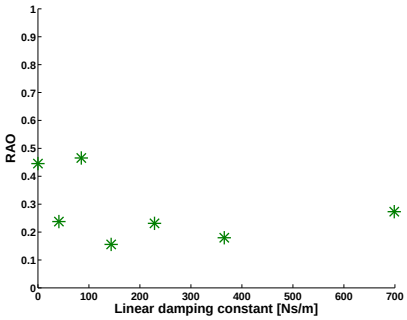

(f) 0.797 Hz, relative position.

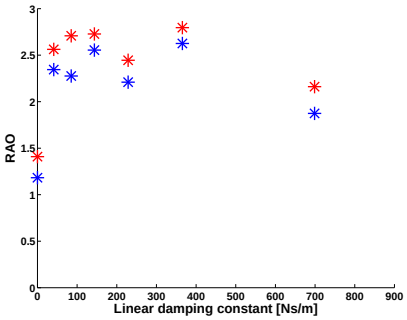

(g) 0.812 Hz, cylinder and mass.

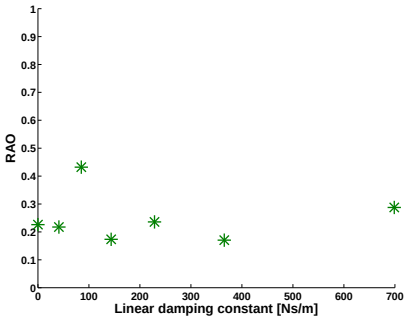

(h) 0.812 Hz, relative position.

Figure 5.3: RAO of the cylinder (blue), mass (red) and their relative motion (green), with a linear damper, for frequencies 0.766 Hz to 0.812 Hz.

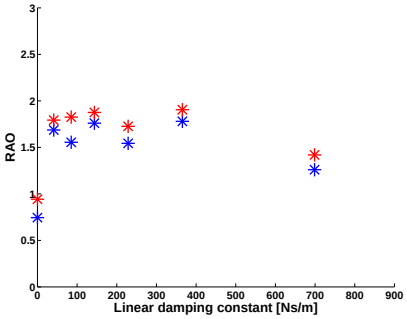

(a) 0.844 Hz, cylinder and mass.

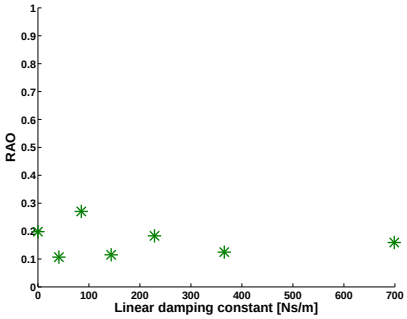

(b) 0.844 Hz, relative position.

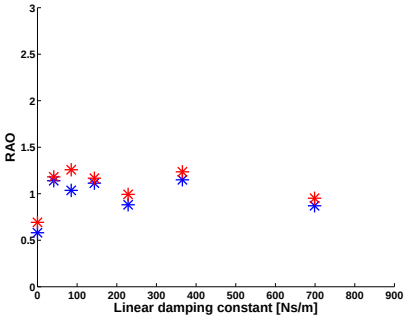

(c) 0.906 Hz, cylinder and mass.

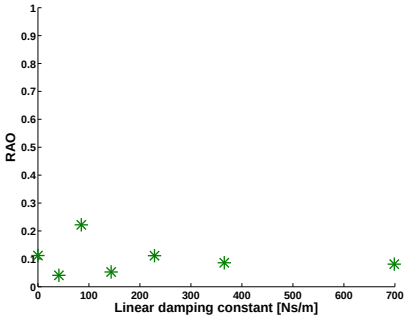

(d) 0.906 Hz, relative position.

Figure 5.4: RAO of the cylinder (blue), mass (red) and their relative motion (green), with a linear damper, for frequencies 0.844 Hz to 0.906 Hz.

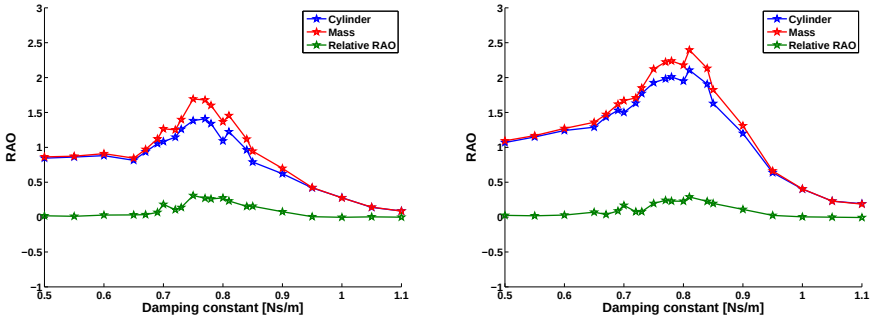

(a) E13

(b) E14

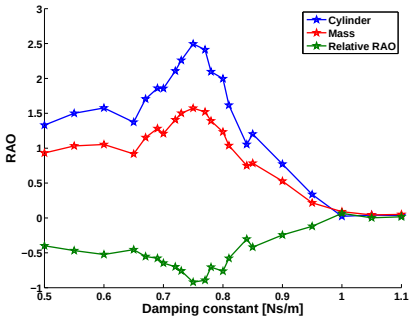

(c) E66

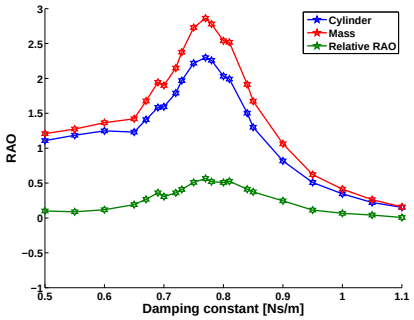

(d) E93

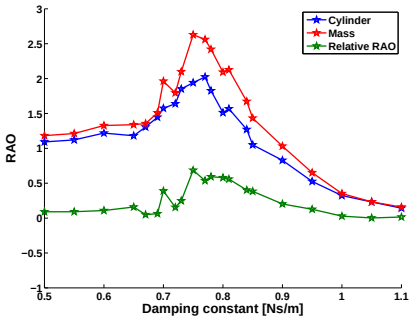

(e) E101

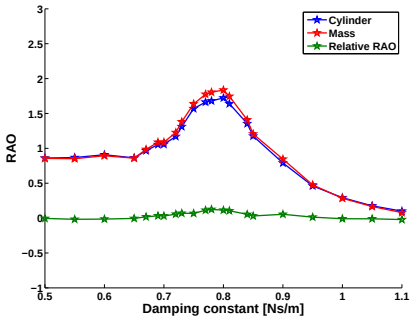

(f) E176

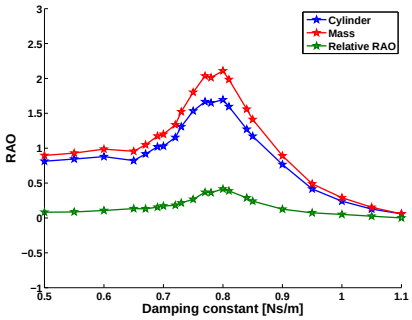

(g) E283

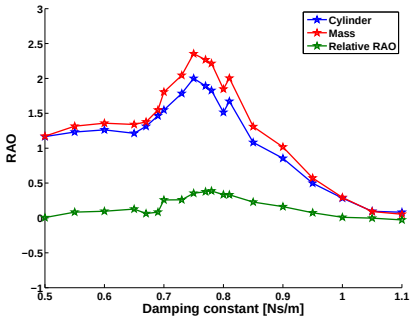

(h) E334

Figure 5.5: The RAO for the cylinder, mass and relative position, with an expansion mono-directional damper, for dampers E13 to E334.

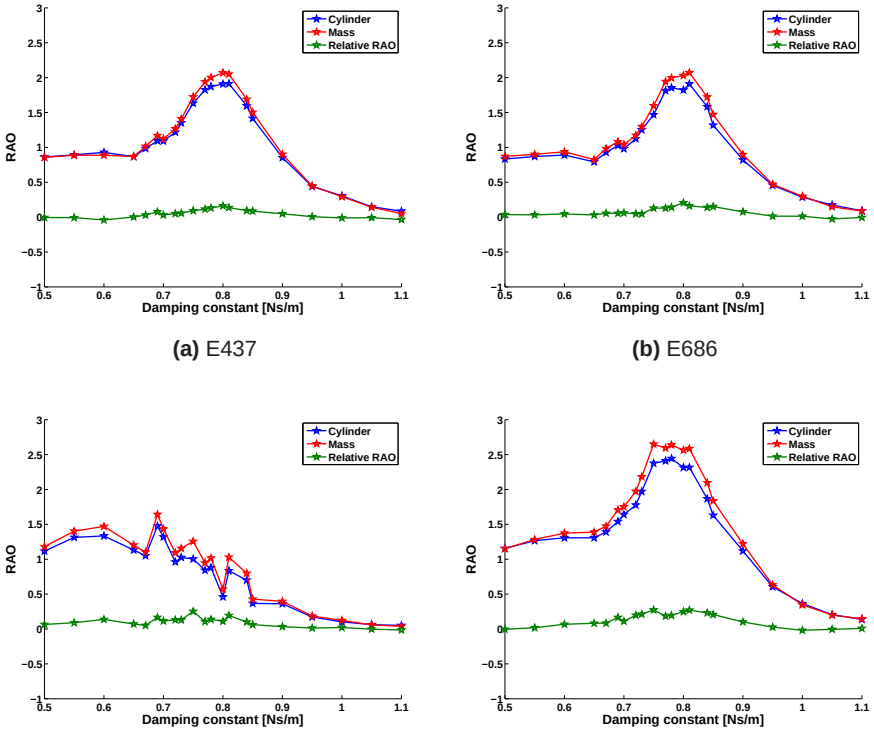

(a) E437 **(b)** E686

(c) E867 **(d)** E872

Figure 5.6: The RAO for the cylinder, mass and relative position, with an expansion mono-directional damper, for dampers E437 to E872.

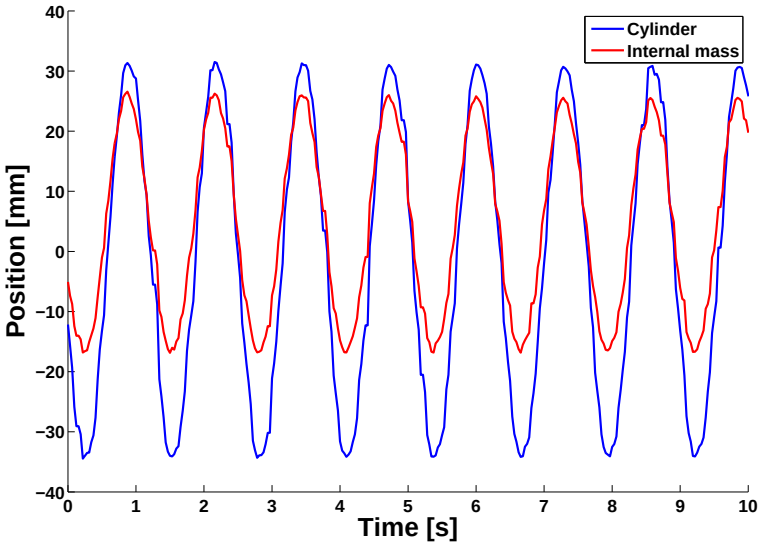

Figure 5.7: The time series of **E66**, for 0.78 Hz regular waves.

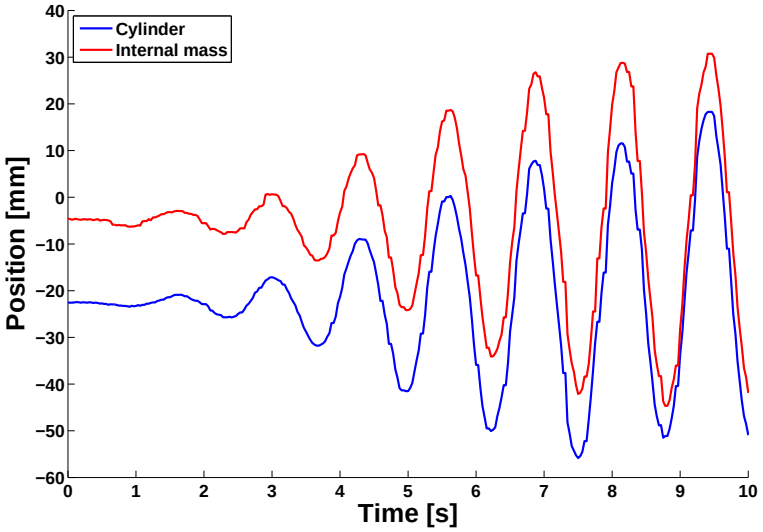

Figure 5.8: The time series of **E176**, for 0.78 Hz regular waves.

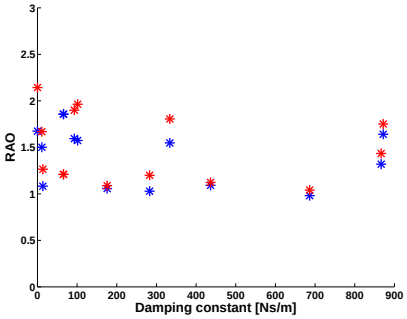

(a) 0.703 Hz, cylinder and mass.

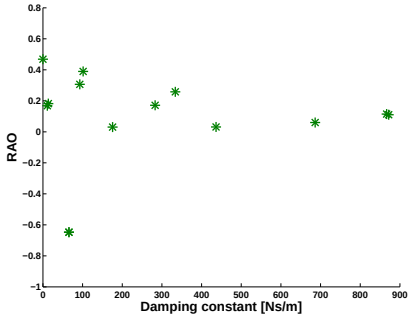

(b) 0.703 Hz, relative position.

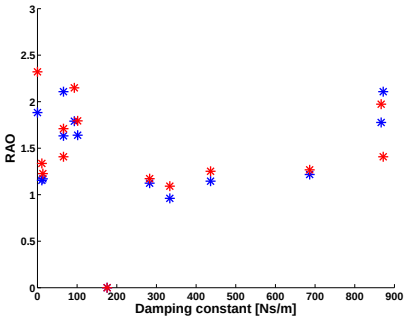

(c) 0.719 Hz, cylinder and mass.

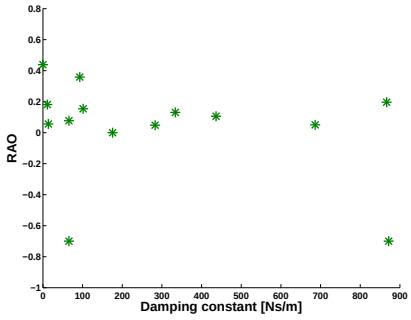

(d) 0.719 Hz, relative position.

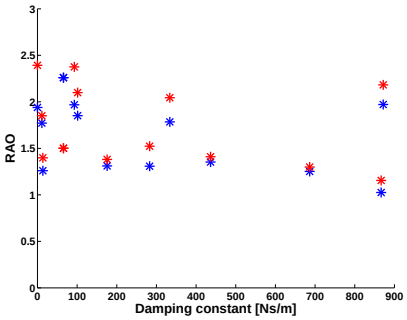

(e) 0.734 Hz, cylinder and mass.

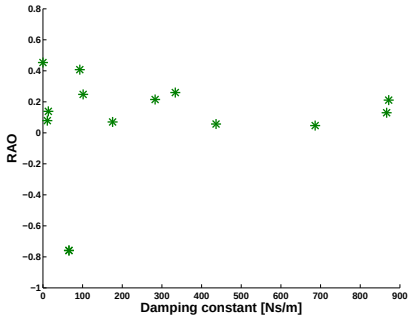

(f) 0.734 Hz, relative position.

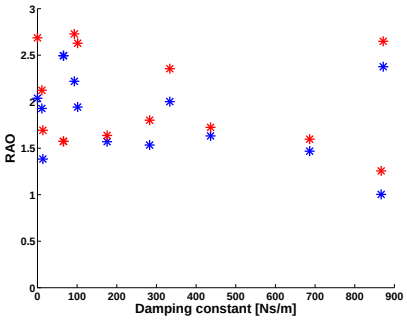

(g) 0.750 Hz, cylinder and mass.

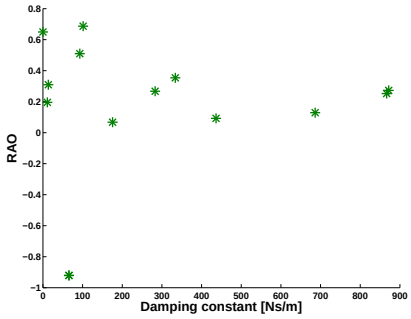

(h) 0.750 Hz, relative position.

Figure 5.9: RAO of the cylinder (blue), mass (red) and the relative motion (green), with an expansion mono-directional damper, for frequencies 0.703 Hz to 0.750 Hz.

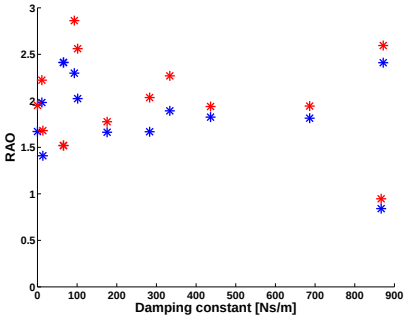

(a) 0.766 Hz, cylinder and mass.

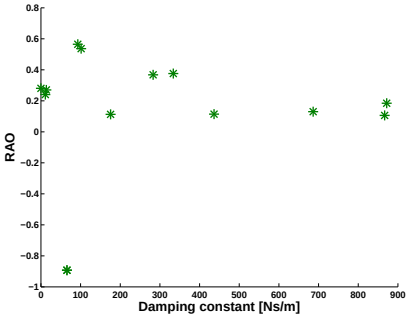

(b) 0.766 Hz, relative position.

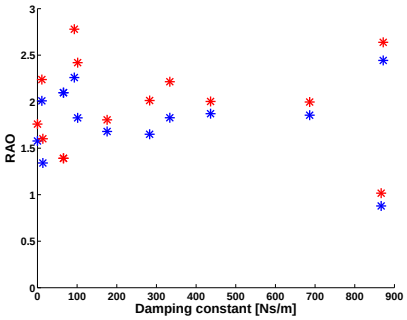

(c) 0.781 Hz, cylinder and mass.

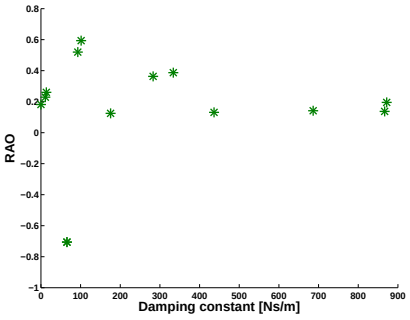

(d) 0.781 Hz, relative position.

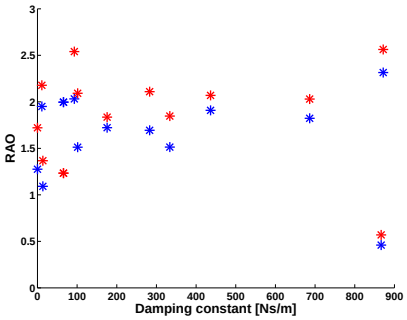

(e) 0.797 Hz, cylinder and mass.

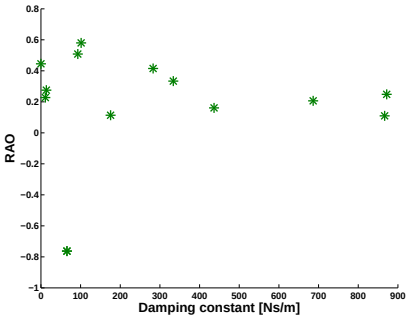

(f) 0.797 Hz, relative position.

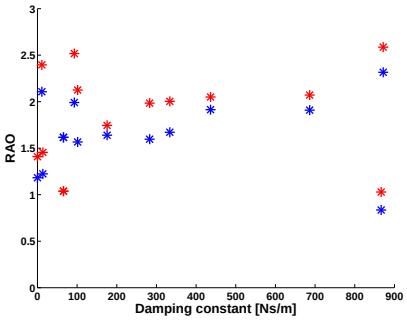

(g) 0.812 Hz, cylinder and mass.

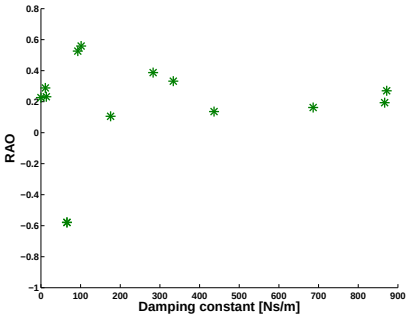

(h) 0.812 Hz, relative position.

Figure 5.10: RAO of the cylinder, mass and the relative motion, with an expansion mono-directional damper, for frequencies 0.766 Hz to 0.812 Hz.

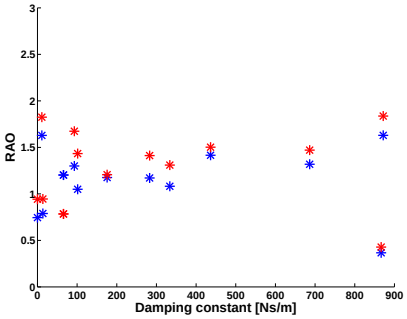

(a) 0.844 Hz, cylinder and mass.

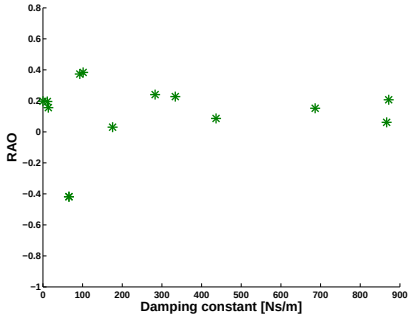

(b) 0.844 Hz, relative position.

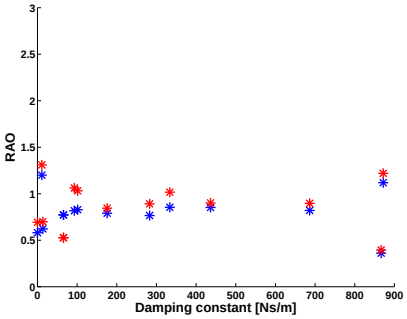

(c) 0.906 Hz, cylinder and mass.

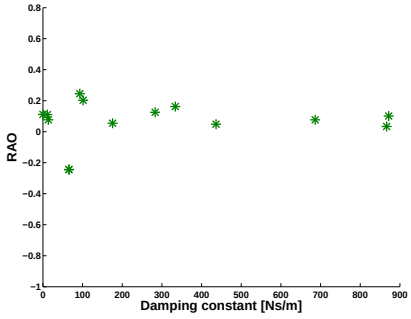

(d) 0.906 Hz, relative position.

Figure 5.11: RAO of the cylinder, mass and the relative motion, with an expansion mono-directional damper, for the frequencies 0.844 Hz to 0.906 Hz.

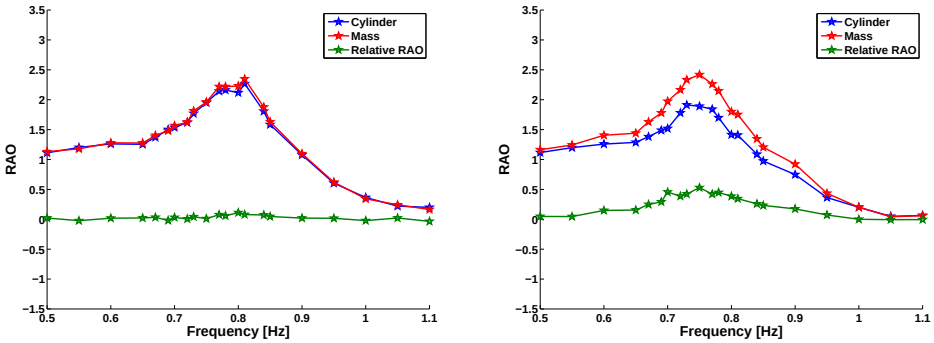

(a) C26

(b) C40

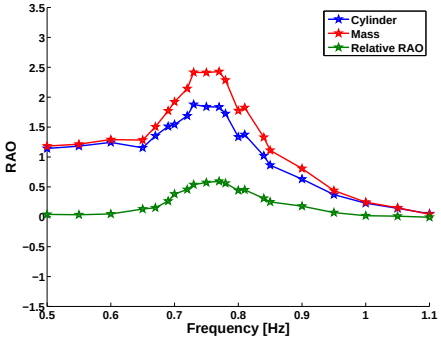

(c) C113

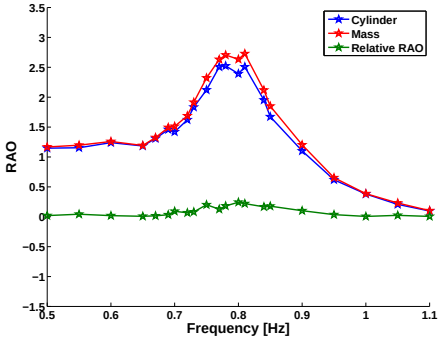

(d) C161

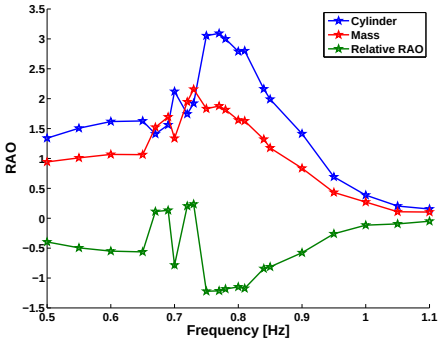

(e) C178

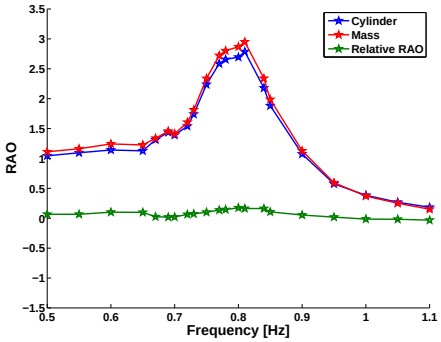

(f) C528

Figure 5.12: RAO of the cylinder, mass and the relative position between them, for each compression mono-directional damper.

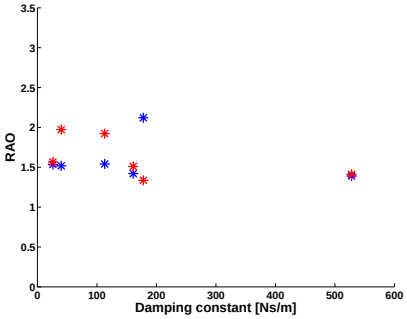

(a) 0.703 Hz, cylinder and mass.

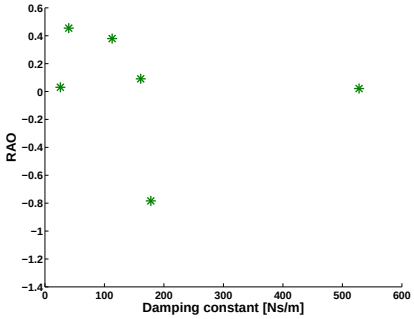

(b) 0.703 Hz, relative position.

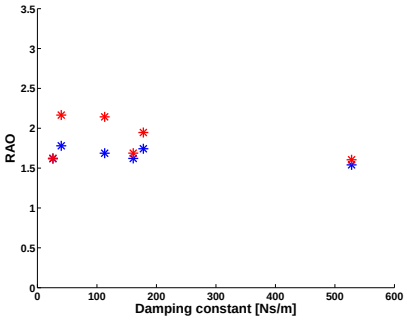

(c) 0.719 Hz, cylinder and mass.

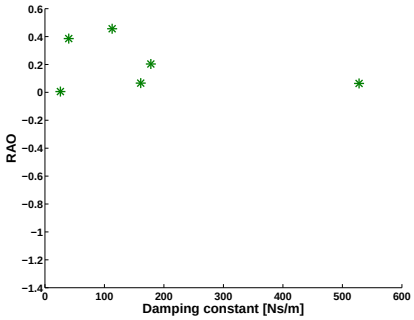

(d) 0.719 Hz, relative position.

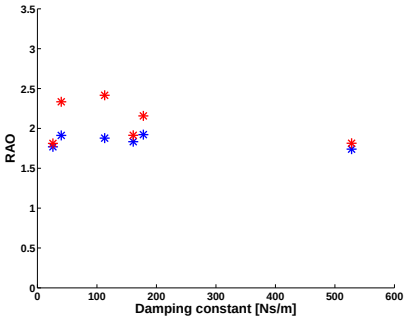

(e) 0.734 Hz, cylinder and mass.

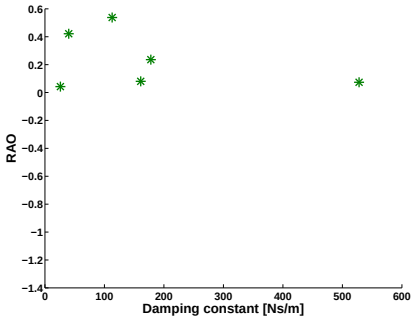

(f) 0.734 Hz, relative position.

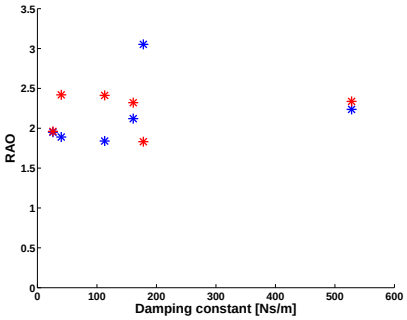

(g) 0.750 Hz, cylinder and mass.

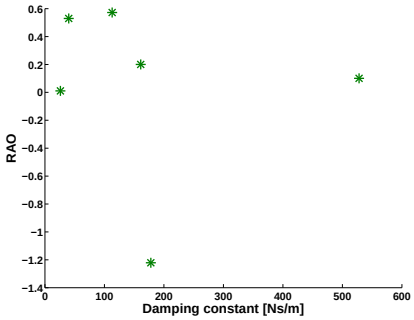

(h) 0.750 Hz, relative position.

Figure 5.13: RAO of the cylinder (blue), mass (red) and the relative position between them (green), with the compression mono-directional dampers, for frequencies 0.703 Hz to 0.750 Hz.

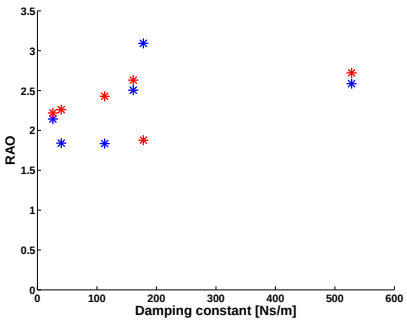

(a) 0.766 Hz, cylinder and mass.

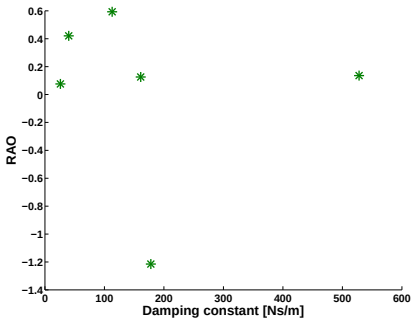

(b) 0.766 Hz, relative position.

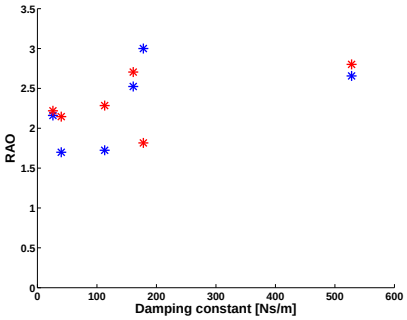

(c) 0.781 Hz, cylinder and mass.

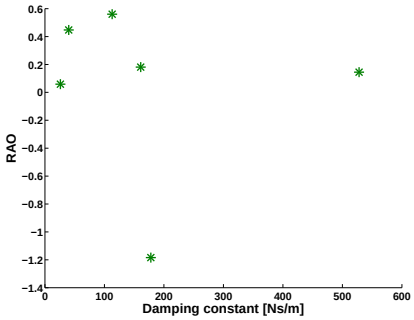

(d) 0.781 Hz, relative position.

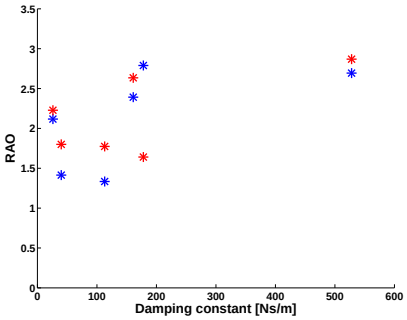

(e) 0.797 Hz, cylinder and mass.

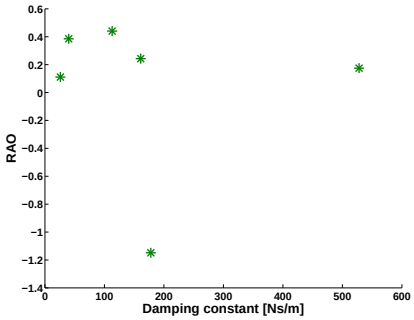

(f) 0.797 Hz, relative position.

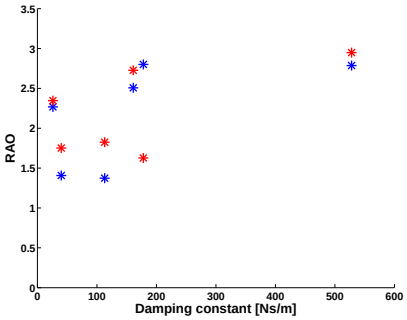

(g) 0.812 Hz, cylinder and mass.

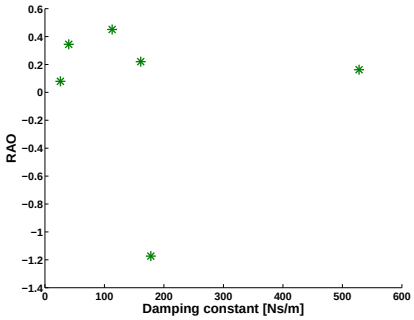

(h) 0.812 Hz, relative position.

Figure 5.14: RAO of the cylinder (blue), mass (red) and the relative position between them (green), with the compression mono-directional dampers, for frequencies 0.766 Hz to 0.812 Hz.

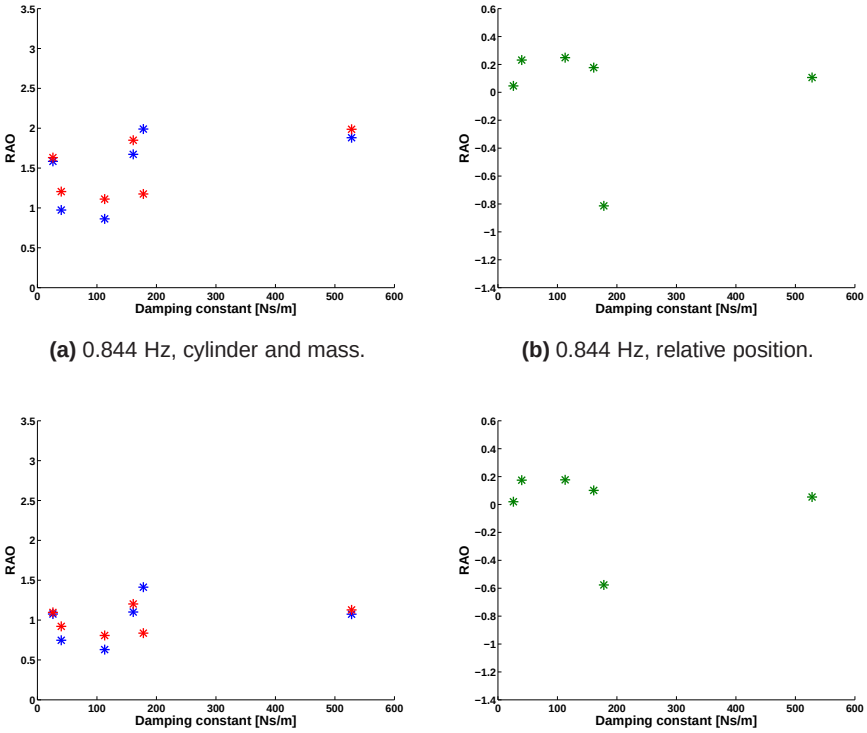

(a) 0.844 Hz, cylinder and mass.

(b) 0.844 Hz, relative position.

(c) 0.906 Hz, cylinder and mass.

(d) 0.906 Hz, relative position.

Figure 5.15: RAO of the cylinder (blue), mass (red) and the relative position between them (green), with the compression mono-directional dampers, for frequencies 0.844 Hz to 0.906 Hz.

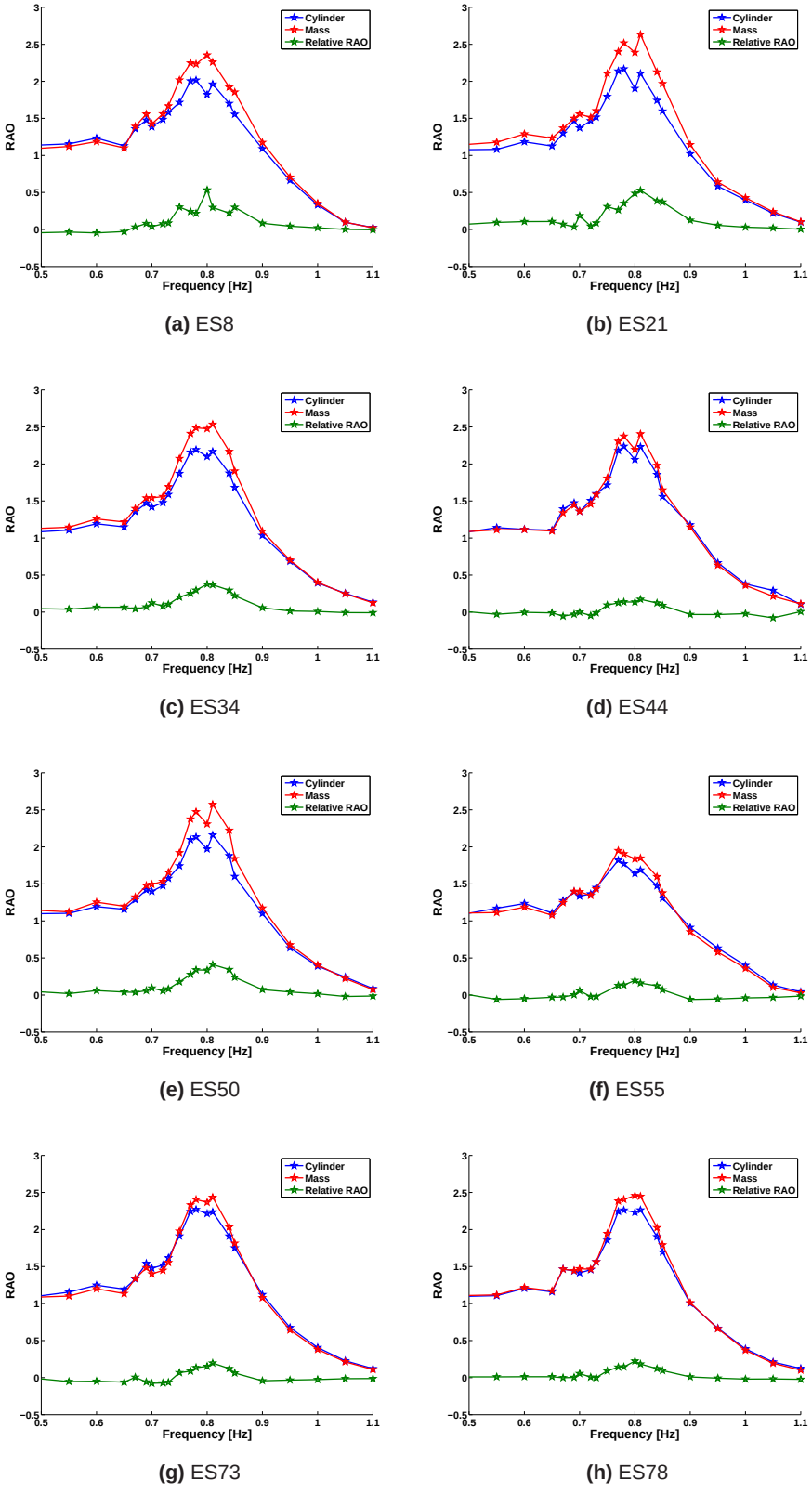

(a) ES8 **(b)** ES21

(c) ES34 **(d)** ES44

(e) ES50 **(f)** ES55

(g) ES73 **(h)** ES78

Figure 5.16: The RAO for the cylinder, mass and the relative position between them, for the endstop dampers.

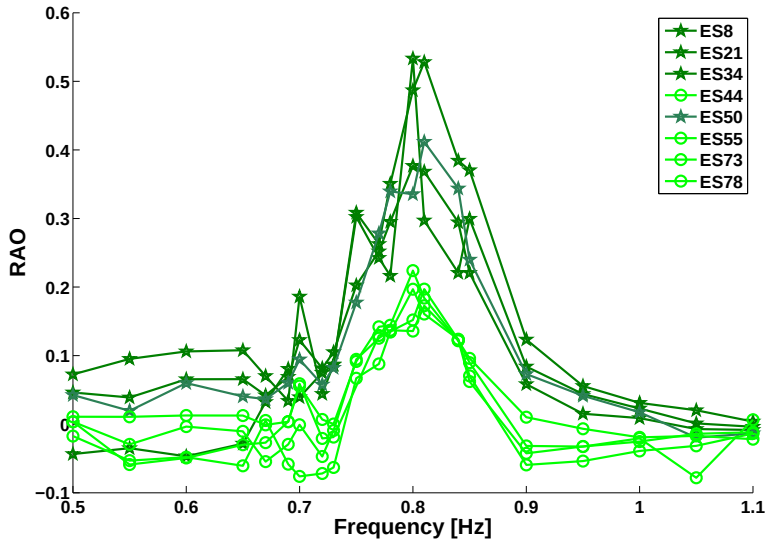

Figure 5.17: The RAO of the relative motion between the mass and cylinder, with endstop dampers, with the two different responses emphasised.

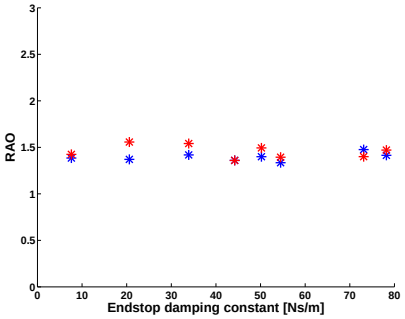

(a) 0.703 Hz, cylinder and mass.

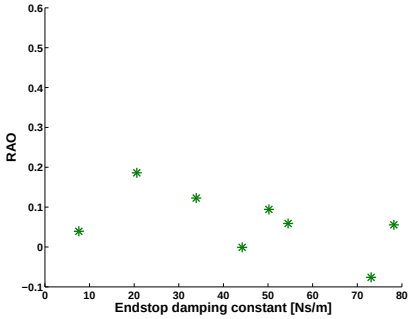

(b) 0.703 Hz, relative position.

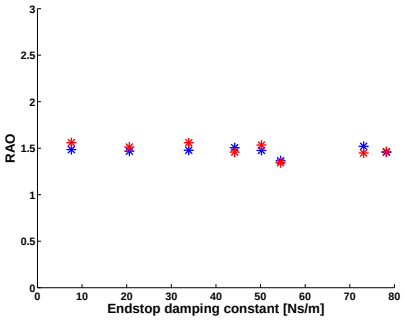

(c) 0.719 Hz, cylinder and mass.

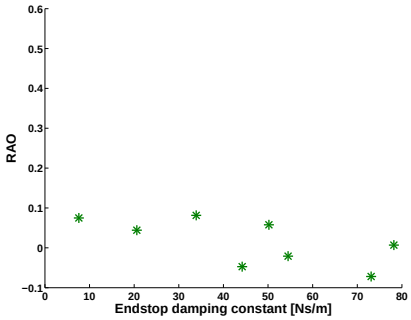

(d) 0.719 Hz, relative position.

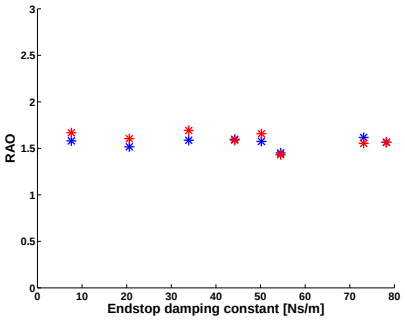

(e) 0.734 Hz, cylinder and mass .

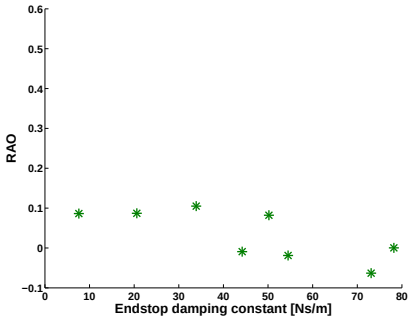

(f) 0.734 Hz, relative position.

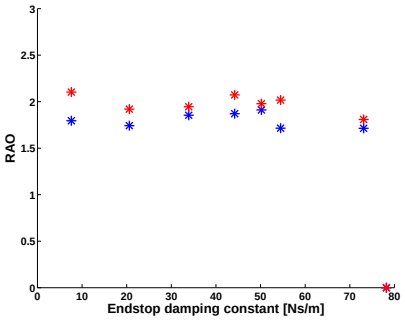

(g) 0.750 Hz, cylinder and mass.

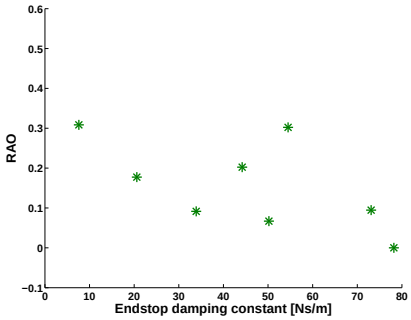

(h) 0.750 Hz, relative position.

Figure 5.18: RAO of the cylinder (blue), mass (red) and the relative position between them (green), with endstop dampers, for frequencies 0.703 Hz to 0.750 Hz.

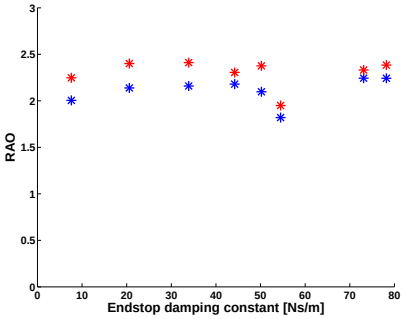

(a) 0.766 Hz, cylinder and mass.

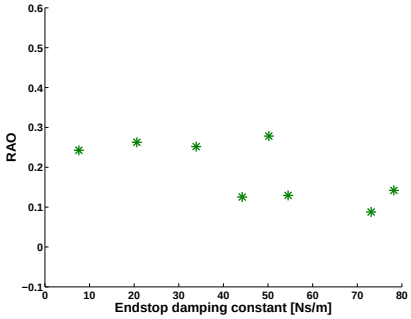

(b) 0.766 Hz, relative position.

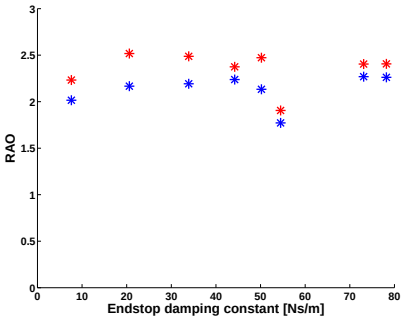

(c) 0.781 Hz, cylinder and mass.

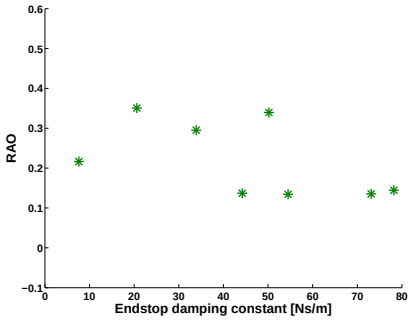

(d) 0.781 Hz, relative position.

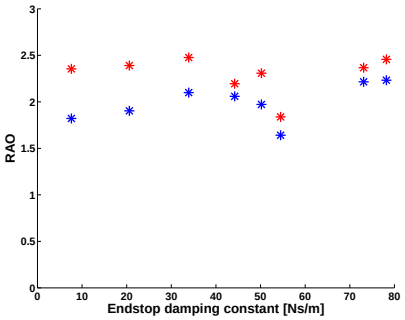

(e) 0.797 Hz, cylinder and mass.

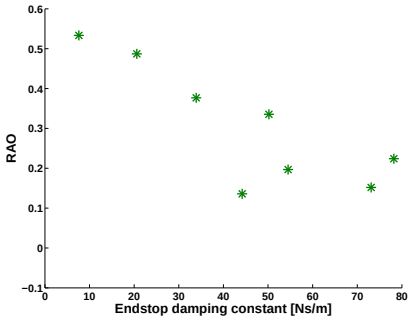

(f) 0.797 Hz, relative position.

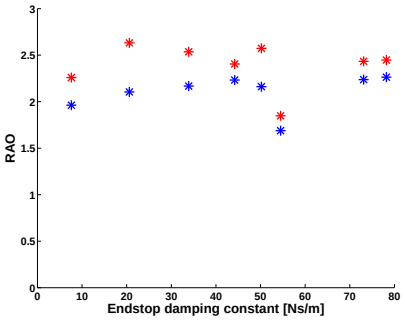

(g) 0.812 Hz, cylinder and mass.

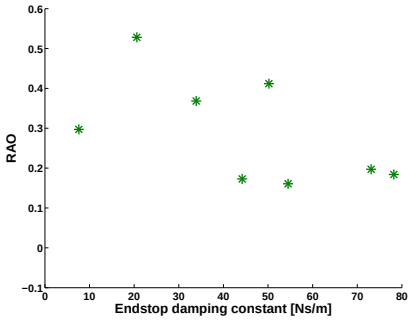

(h) 0.812 Hz, relative position.

Figure 5.19: RAO of the cylinder (blue), mass (red) and the relative position between them (green), for frequencies 0.766 Hz to 0.812 Hz.

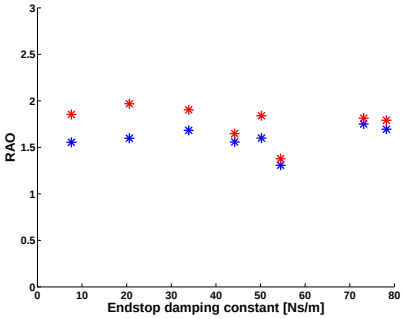

(a) 0.844 Hz, cylinder and mass.

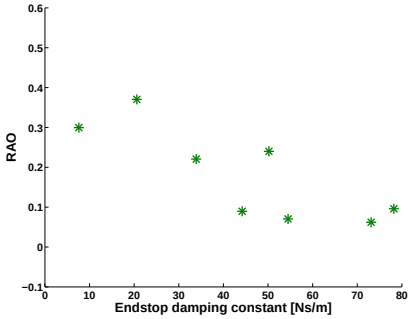

(b) 0.844 Hz, relative position.

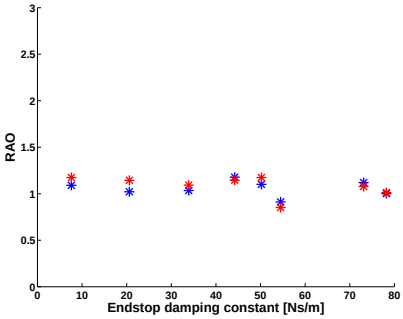

(c) 0.906 Hz, cylinder and mass.

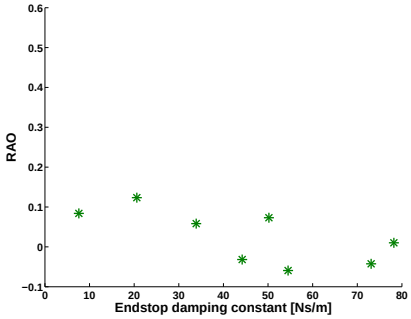

(d) 0.906 Hz, relative position.

Figure 5.20: RAO of the cylinder (blue), mass (red) and the relative position between them (green), for frequencies 0.844 Hz to 0.906Hz.

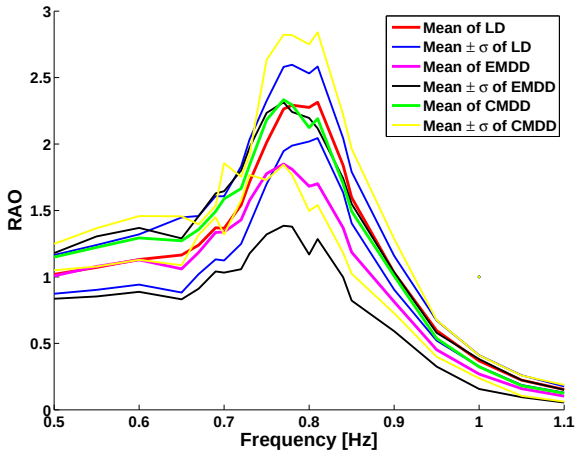

(a) External cylinder.

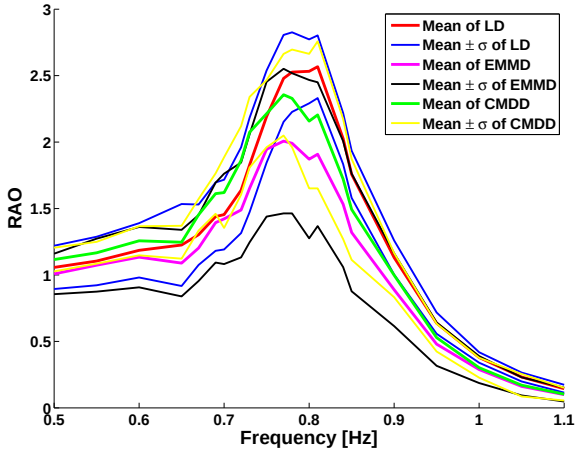

(b) Internal mass.

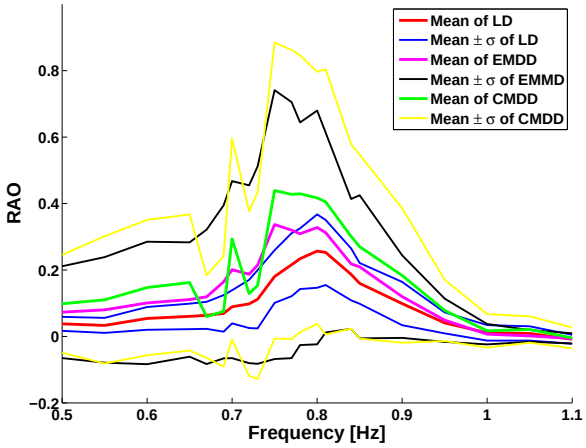

(c) Relative RAO.

Figure 5.21: The average and errors of the cylinder, mass and difference, for the linear and both mono-directional dampers.

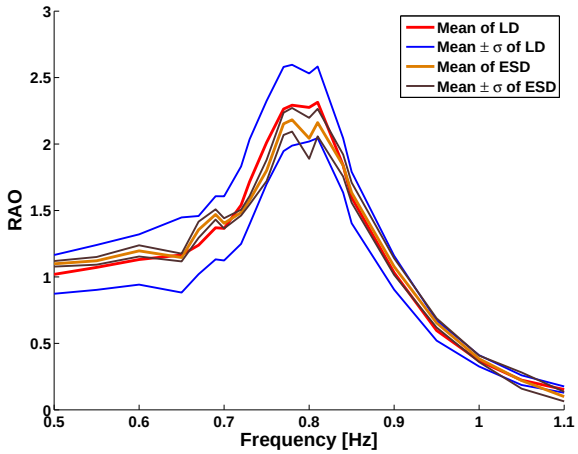

(a) External cylinder.

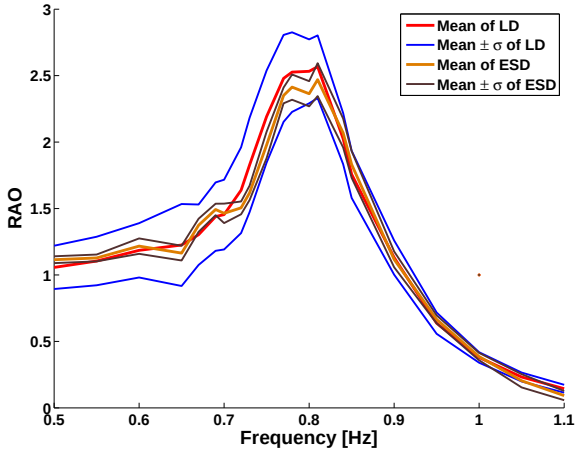

(b) Internal mass.

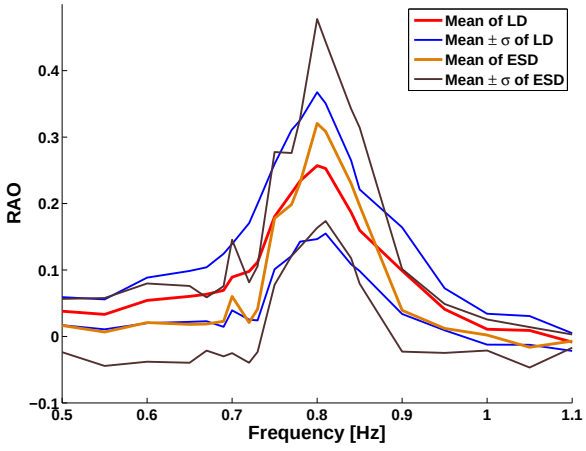

(c) Relative RAO.

Figure 5.22: The average and errors of the cylinder, mass and difference, for the linear and endstop dampers.

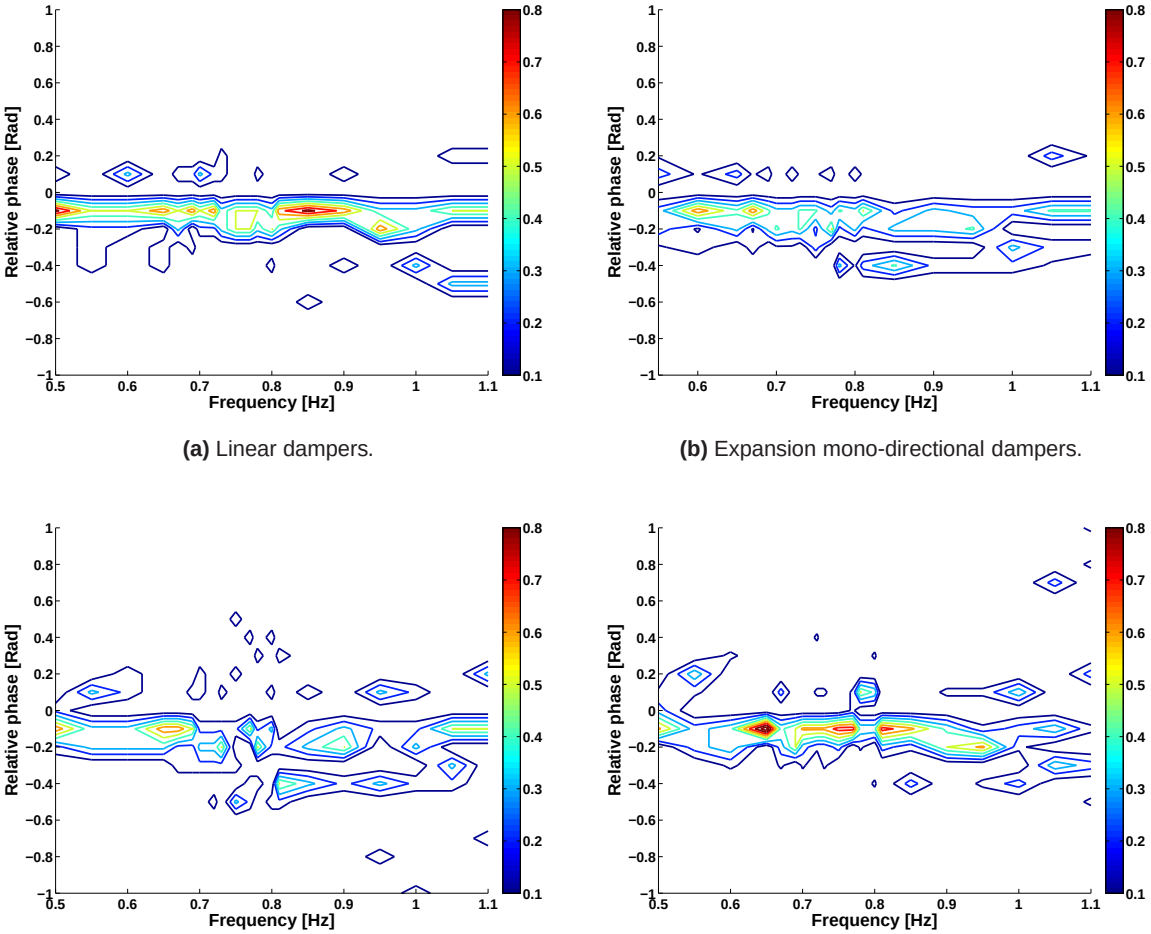

(a) Linear dampers.

(b) Expansion mono-directional dampers.

(c) Compression mono-directional dampers.

(d) Endstop dampers.

Figure 5.23: The relative normalised phase between the cylinder and mass, for all the damper types.

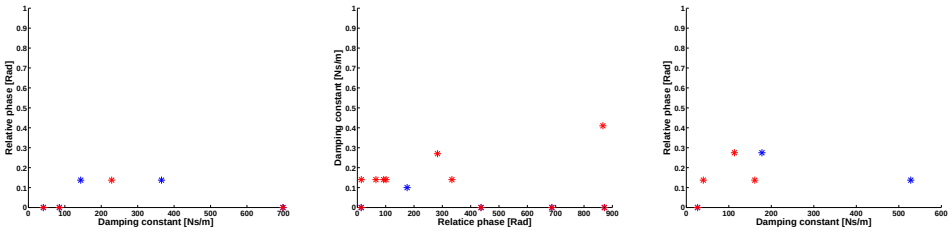

(a) LD, 0.70 Hz

(b) EMDD, 0.70 Hz

(c) CMDD, 0.70 Hz

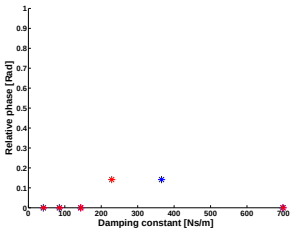

(d) LD, 0.72 Hz

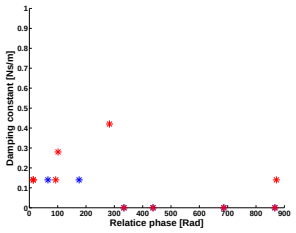

(e) EMDD, 0.72 Hz

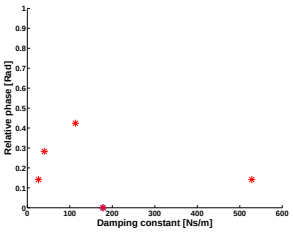

(f) CMDD, 0.72 Hz

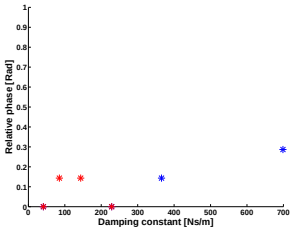

(g) LD, 0.73 Hz

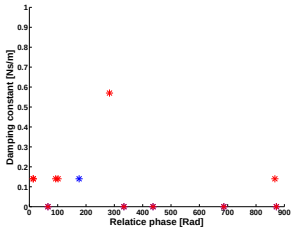

(h) EMDD, 0.73 Hz

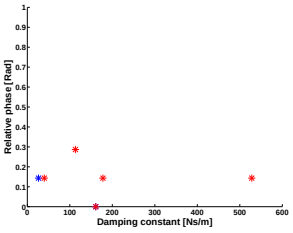

(i) CMDD, 0.73 Hz

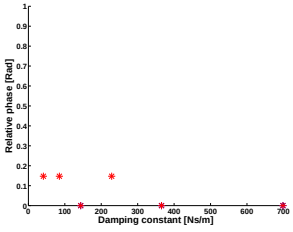

(j) LD, 0.75 Hz

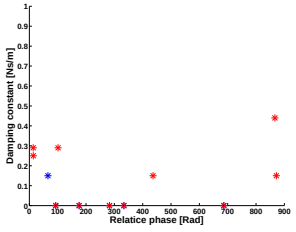

(k) EMDD, 0.75 Hz

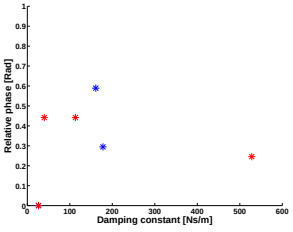

(l) CMDD, 0.75 Hz

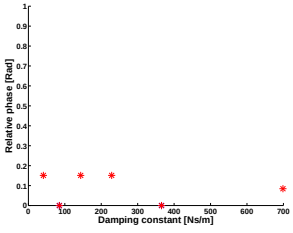

(m) LD, 0.77 Hz

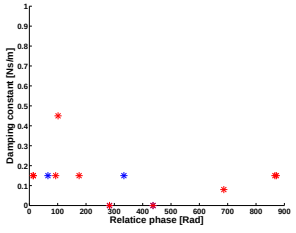

(n) EMDD, 0.77 Hz

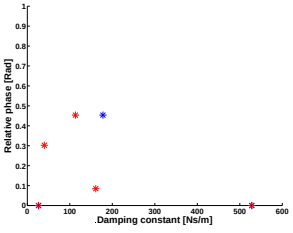

(o) CMDD, 0.77 Hz

Figure 5.24: The relative positive (blue) and negative (red) phase between the cylinder and mass, with the linear damper (LD), expansion mono-directional damper (EMDD) and compression mono-directional damper (CMDD), for frequencies 0.70 Hz to 0.77 Hz.

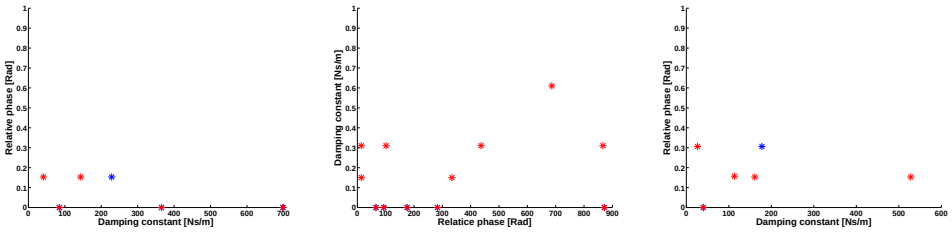

(a) LD, 0.78 Hz

(b) EMDD, 0.78 Hz

(c) CMDD, 0.78 Hz

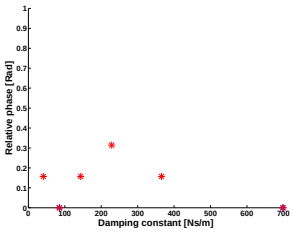

(d) LD, 0.80 Hz

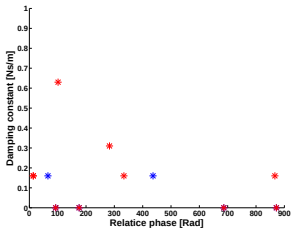

(e) EMDD, 0.80 Hz

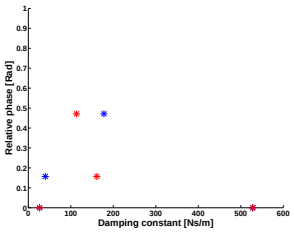

(f) CMDD, 0.80 Hz

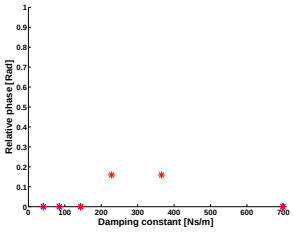

(g) LD, 0.81 Hz

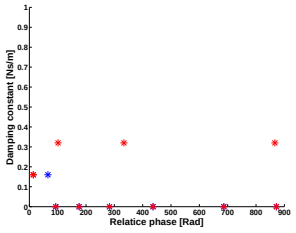

(h) EMDD, 0.81 Hz

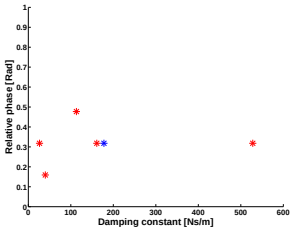

(i) CMDD, 0.81 Hz

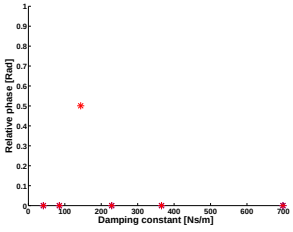

(j) LD, 0.85 Hz

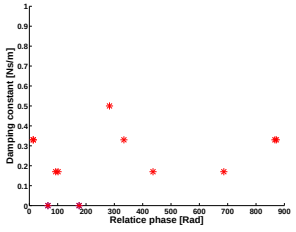

(k) EMDD, 0.85 Hz

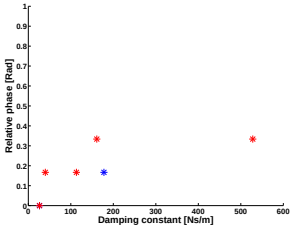

(l) CMDD, 0.85 Hz

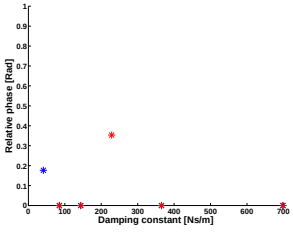

(m) LD, 0.90 Hz

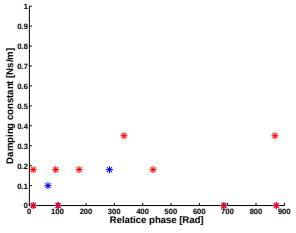

(n) EMDD, 0.90 Hz

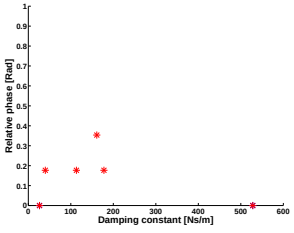

(o) CMDD, 0.90 Hz

Figure 5.25: The relative positive (blue) and negative (red) phase between the cylinder and mass, with the linear damper (LD), expansion mono-directional damper (EMDD) and compression mono-directional damper (CMDD), for frequencies 0.78 Hz to 0.90 Hz.

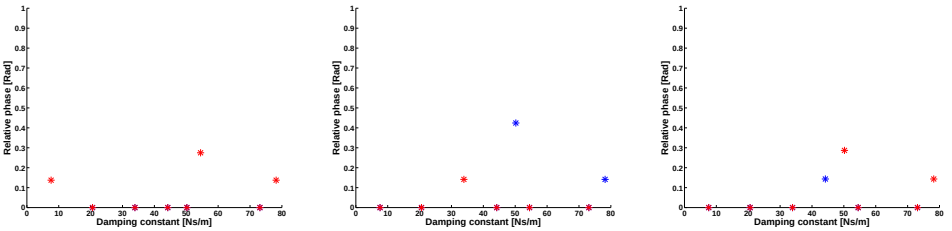

(a) 0.70 Hz **(b)** 0.72 Hz **(c)** 0.73 Hz

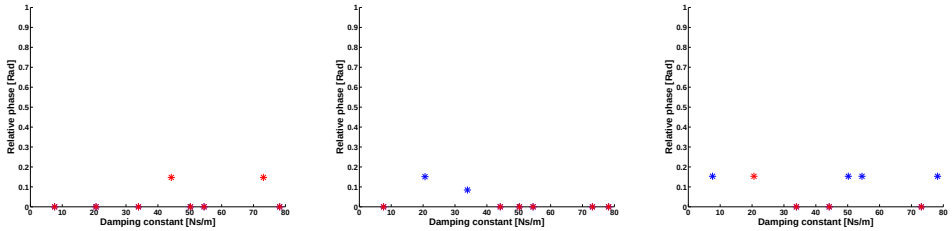

(d) 0.75 Hz **(e)** 0.77 Hz **(f)** 0.78 Hz

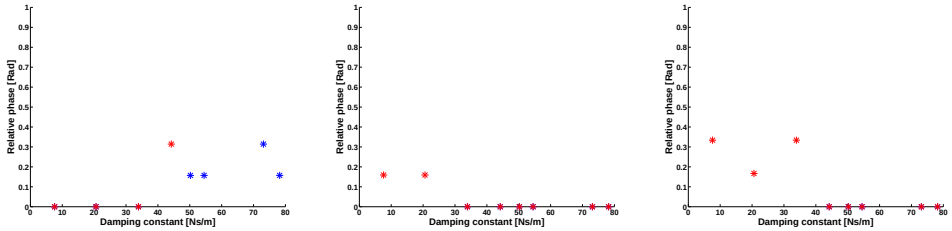

(g) 0.80 Hz **(h)** 0.81 Hz **(i)** 0.85 Hz

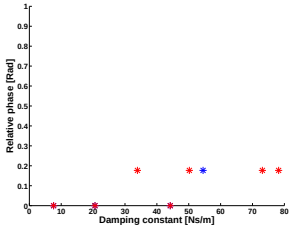

(j) 0.90 Hz

Figure 5.26: The relative positive (blue) and negative (red) phase between the cylinder and mass, with the endstop dampers.

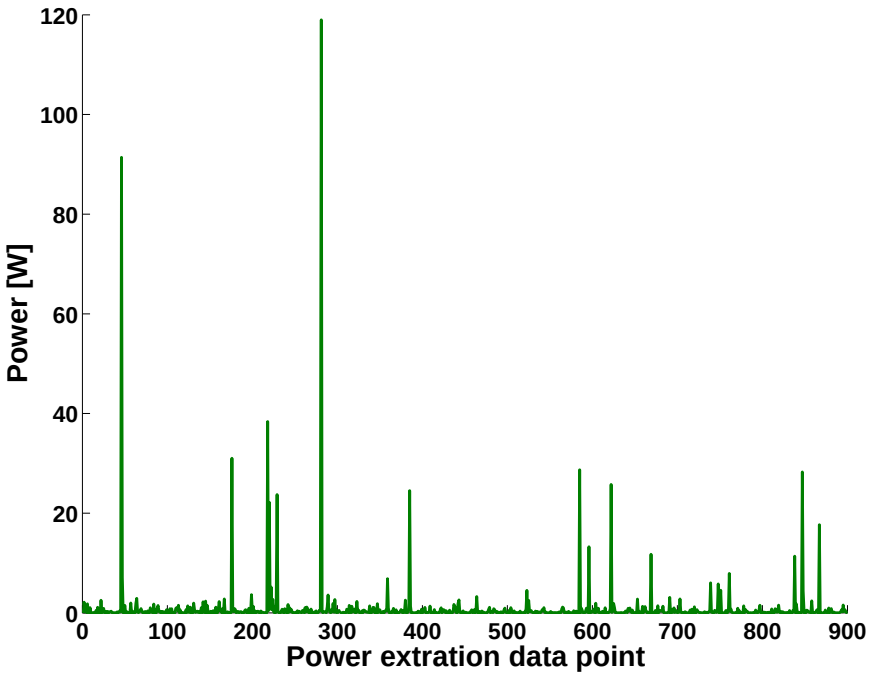

(a) Original signal with no smoothing or filtering

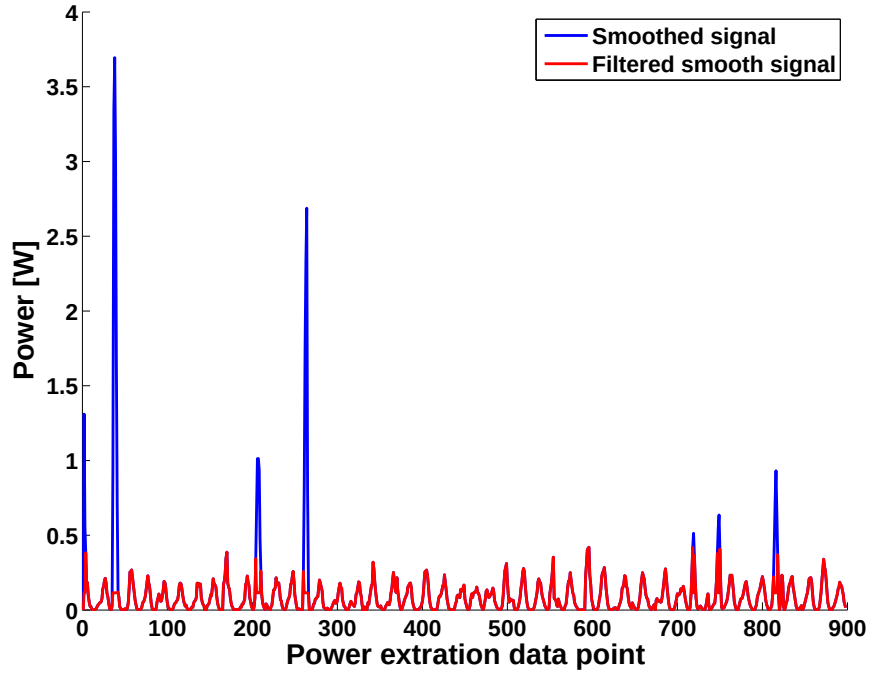

(b) The power signal with only smoothing and with smoothing and filtering

Figure 5.27: The power extraction for a linear damper, showing the influence of smoothing and filtering the signal.

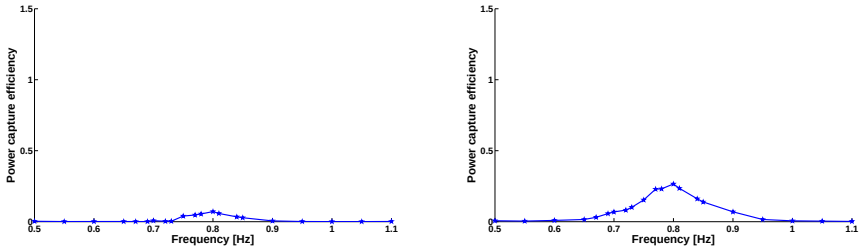

(a) L41

(b) L85

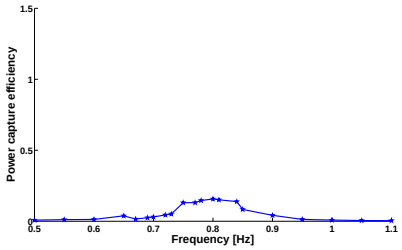

(c) L144

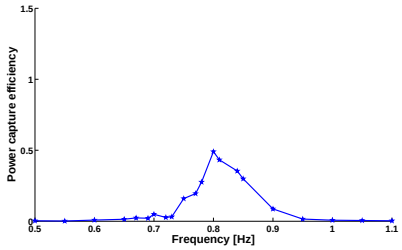

(d) L229

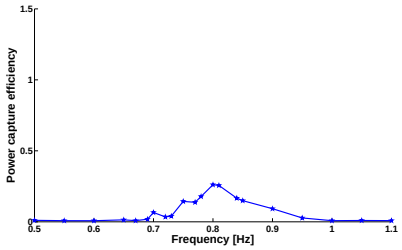

(e) L365

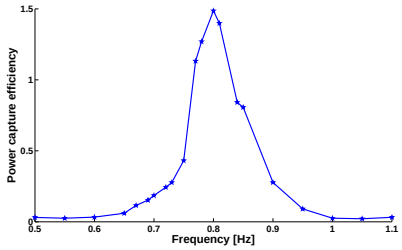

(f) L699

Figure 5.28: The power capture efficiency (fraction) of the linear damper, for different damping constants.

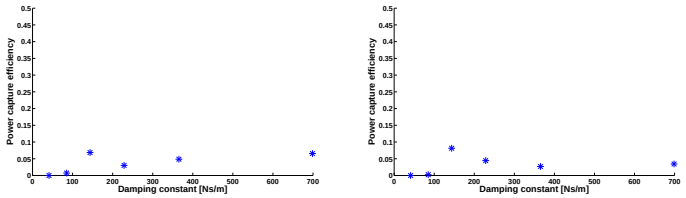

(a) 0.703 Hz **(b)** 0.719 Hz

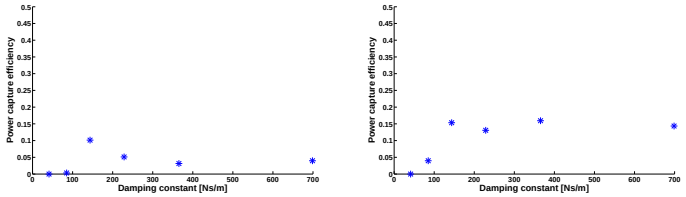

(c) 0.734 Hz **(d)** 0.750 Hz

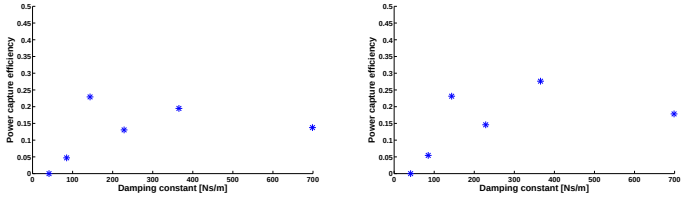

(e) 0.766 Hz **(f)** 0.781 Hz

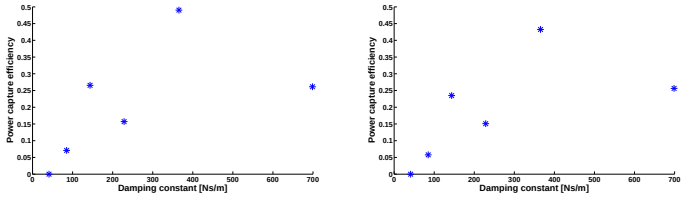

(g) 0.797 Hz **(h)** 0.813 Hz

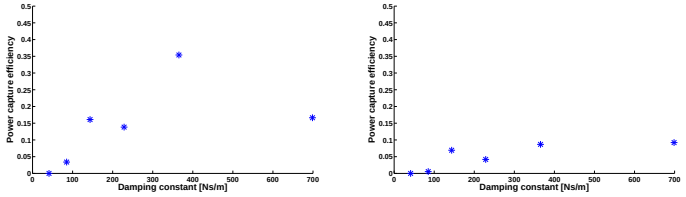

(i) 0.844 Hz **(j)** 0.910 Hz

Figure 5.29: The power capture efficiency (fraction) of the linear damper, for different frequencies.

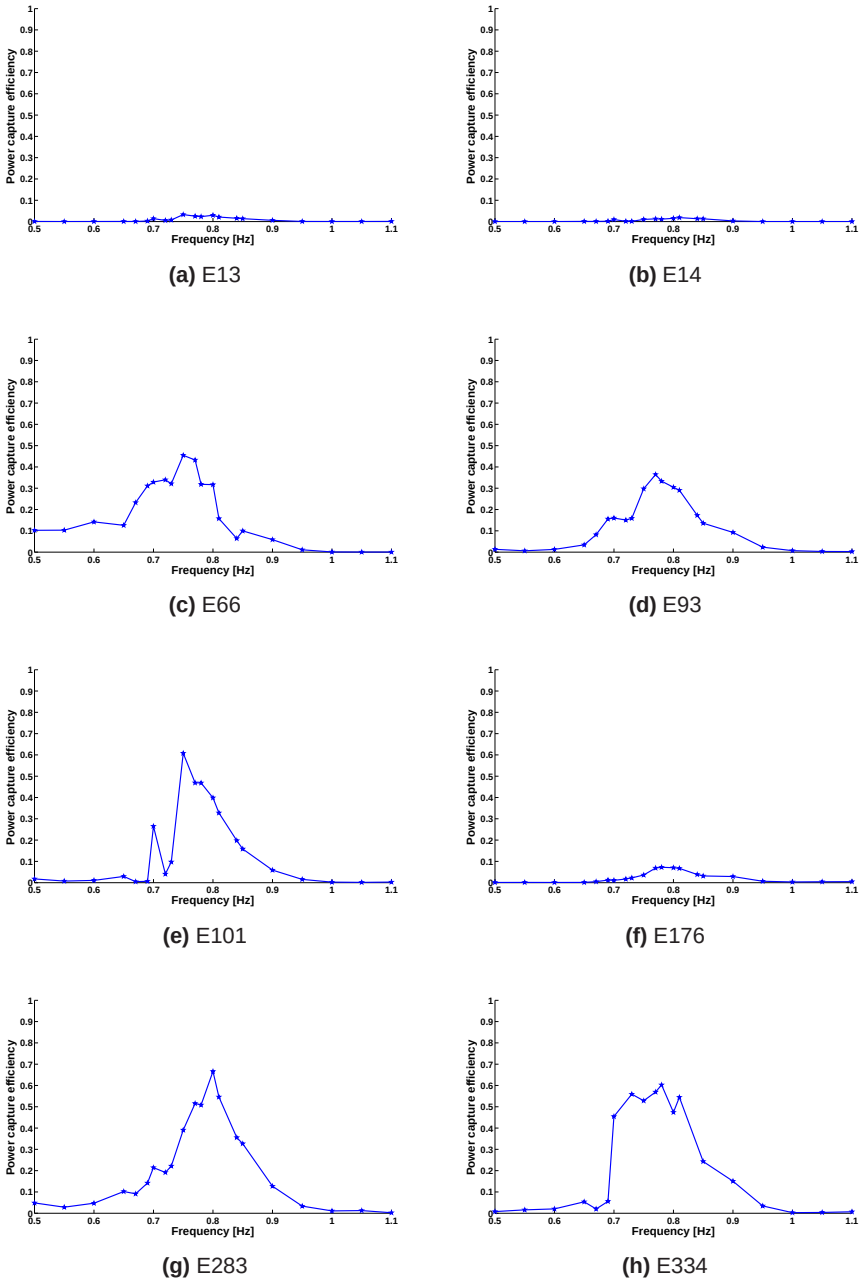

(a) E13 **(b)** E14

(c) E66 **(d)** E93

(e) E101 **(f)** E176

(g) E283 **(h)** E334

Figure 5.30: The power capture efficiency (fraction), for expansion mono-directional dampers, for dampers E13 to E283.

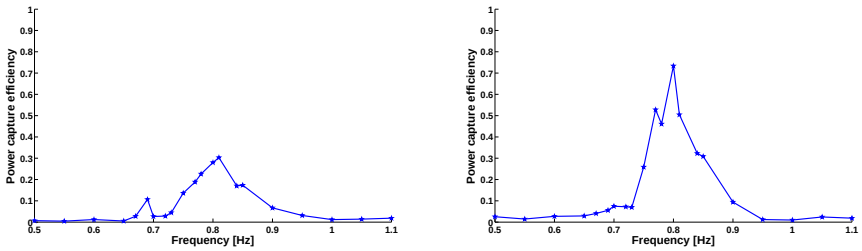

(a) E437

(b) E686

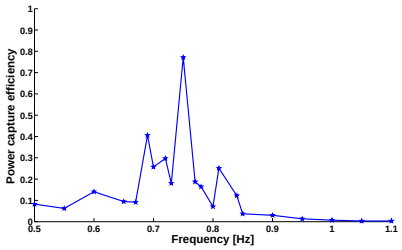

(c) E867

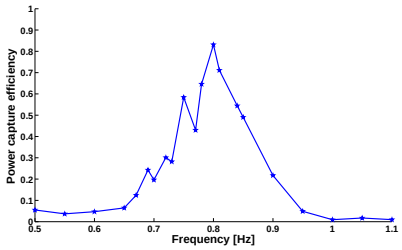

(d) E872

Figure 5.31: The power capture efficiency (fraction), for expansion mono-directional dampers, for dampers E437 to E872.

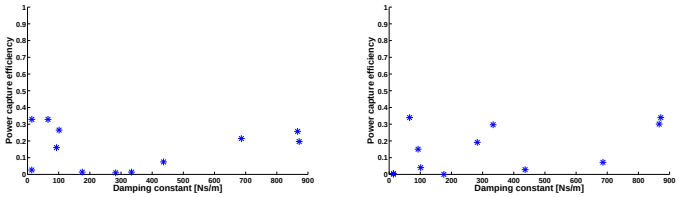

(a) 0.703 Hz

(b) 0.719 Hz

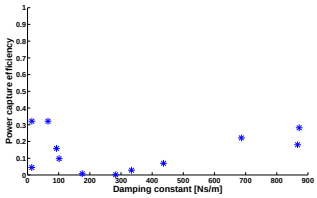

(c) 0.734 Hz

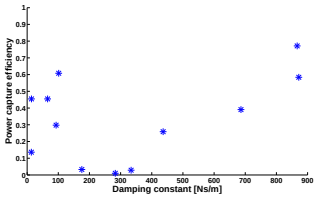

(d) 0.750 Hz

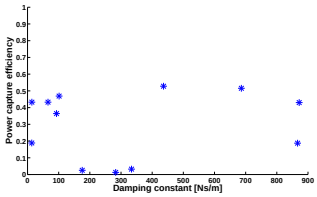

(e) 0.766 Hz

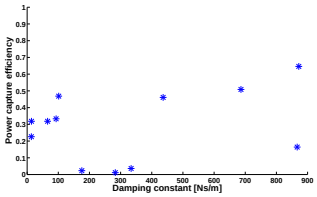

(f) 0.781 Hz

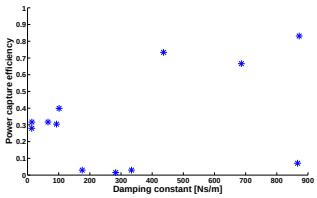

(g) 0.797 Hz

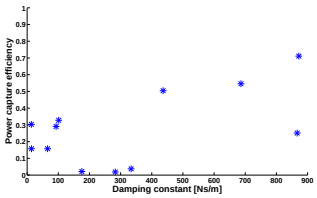

(h) 0.813 Hz

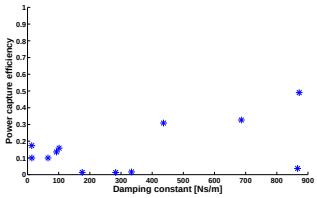

(i) 0.844 Hz

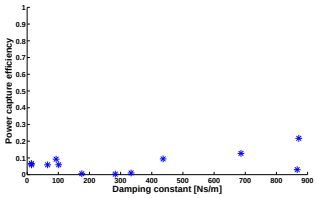

(j) 0.910 Hz

Figure 5.32: The power capture efficiency (fraction) for expansion mono-directional dampers.

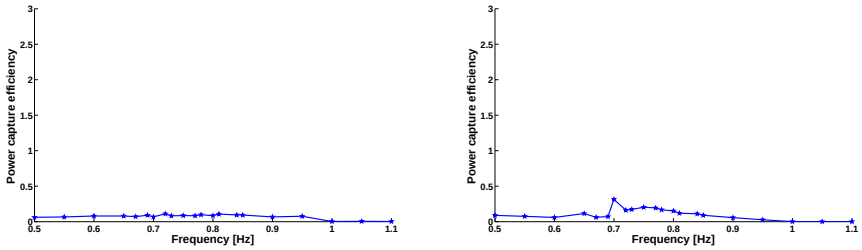

(a) C26

(b) C40

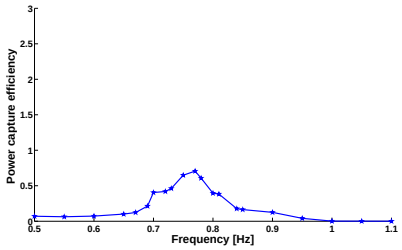

(c) C113

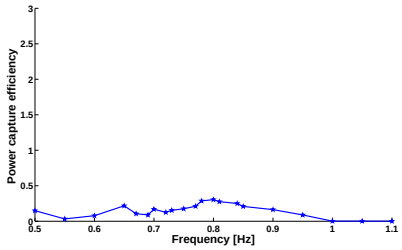

(d) C161

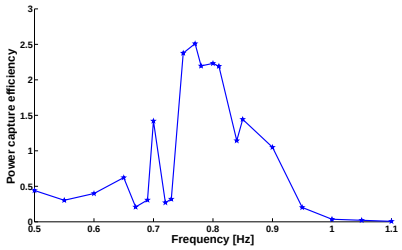

(e) C178

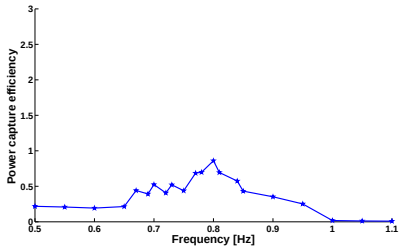

(f) C528

Figure 5.33: The power capture efficiency (fraction) for a compression mono-directional damper.

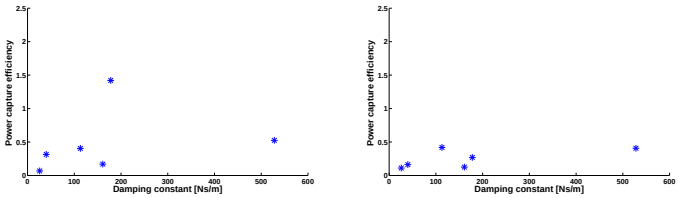

(a) 0.703 Hz

(b) 0.719 Hz

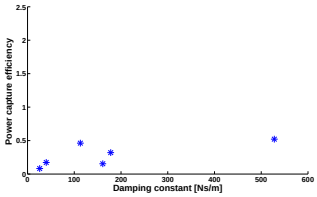

(c) 0.734 Hz

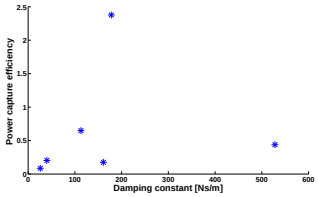

(d) 0.750 Hz

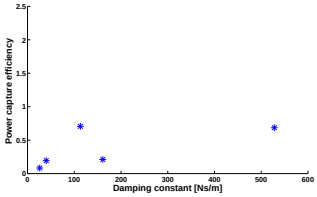

(e) 0.766 Hz

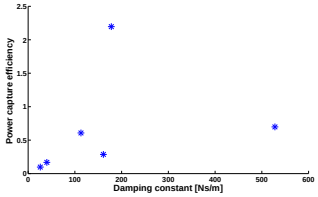

(f) 0.781 Hz

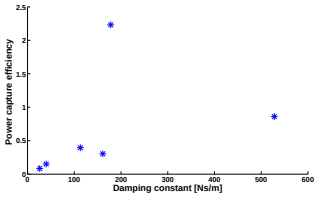

(g) 0.797 Hz

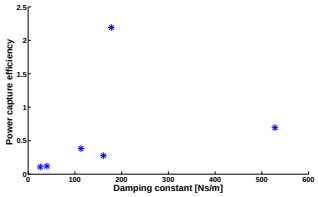

(h) 0.813 Hz

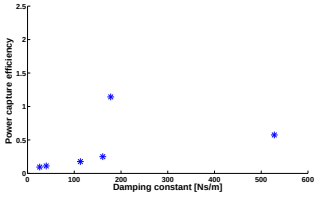

(i) 0.844 Hz

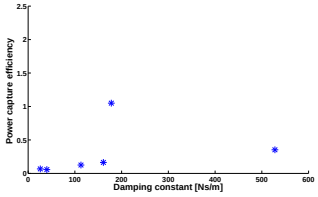

(j) 0.910 Hz

Figure 5.34: The power capture efficiency (fraction) for compression mono-directional dampers.

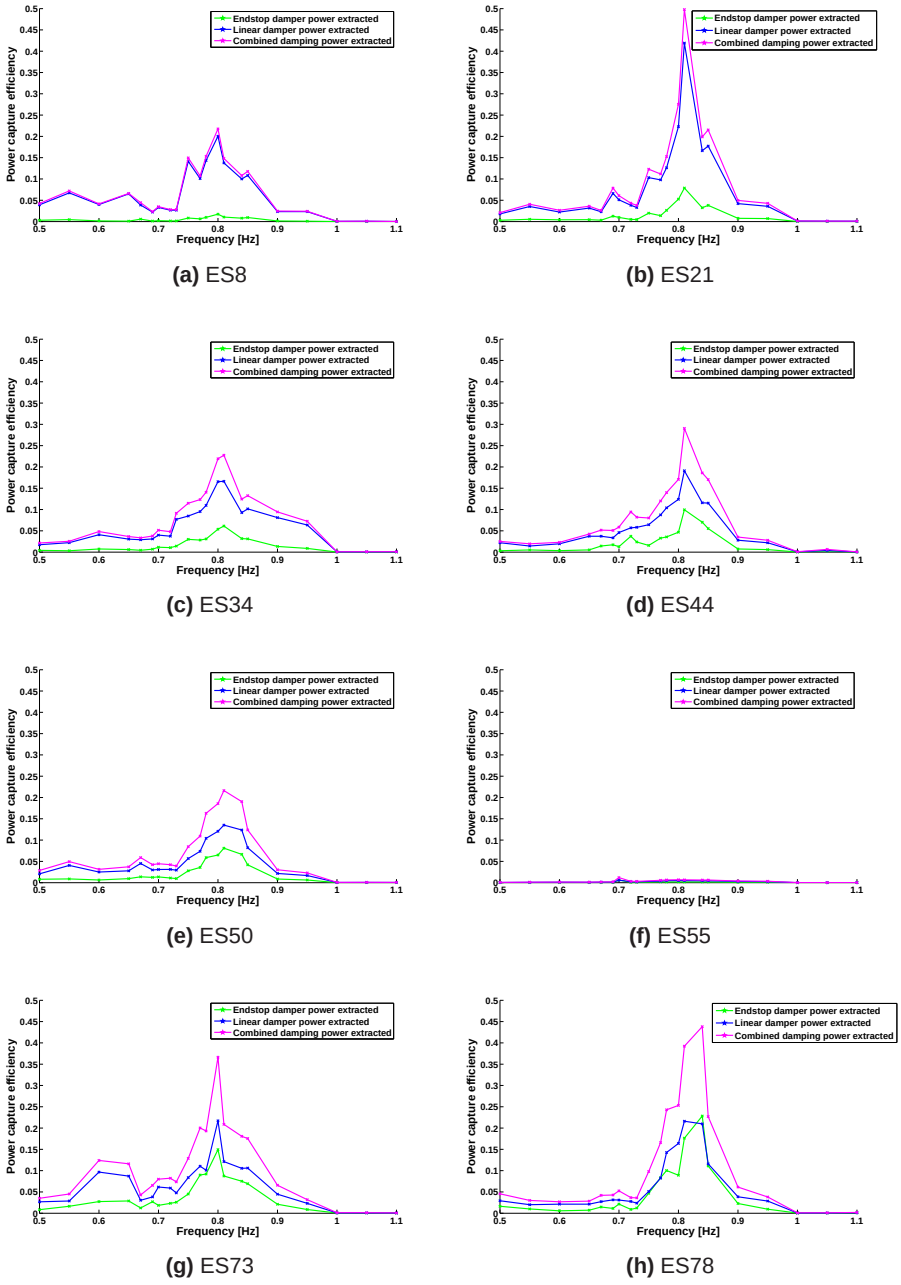

(a) ES8 **(b)** ES21

(c) ES34 **(d)** ES44

(e) ES50 **(f)** ES55

(g) ES73 **(h)** ES78

Figure 5.35: The power capture efficiency (fraction) of the endstop damper, and the power extracted from the linear frictional damping, and the combined power extracted.

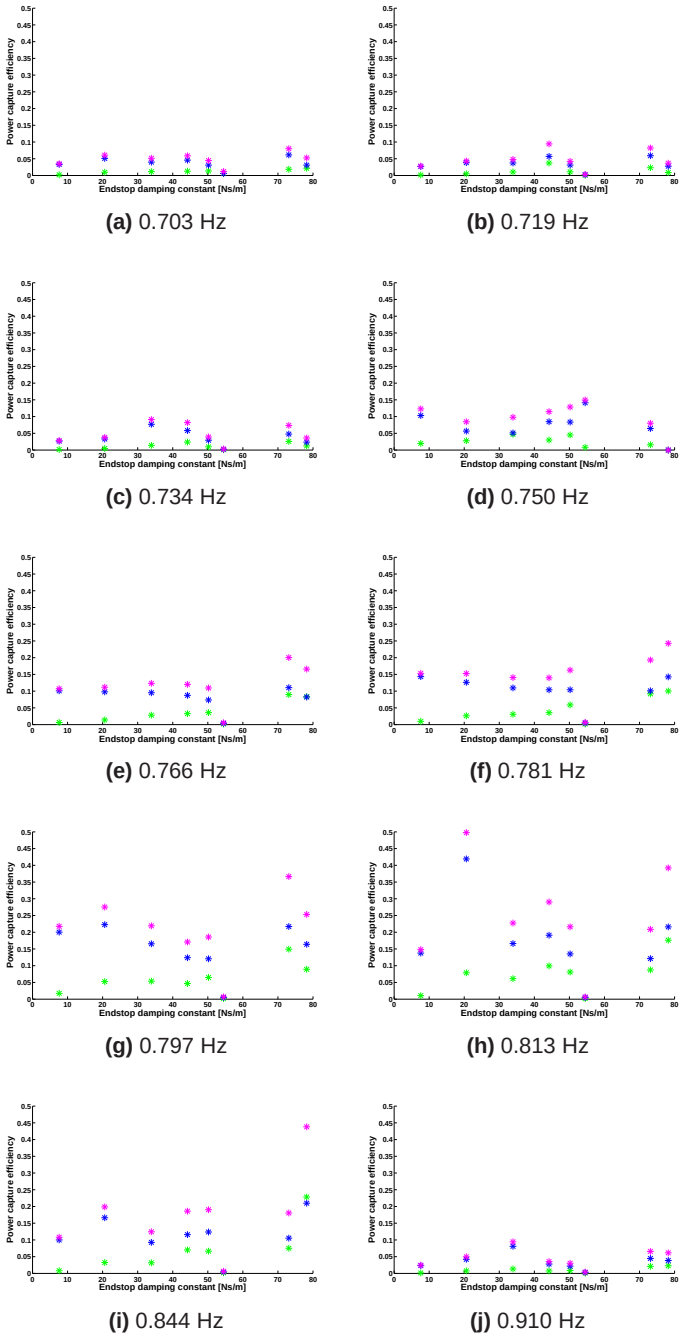

(a) 0.703 Hz **(b)** 0.719 Hz

(c) 0.734 Hz **(d)** 0.750 Hz

(e) 0.766 Hz **(f)** 0.781 Hz

(g) 0.797 Hz **(h)** 0.813 Hz

(i) 0.844 Hz **(j)** 0.910 Hz

Figure 5.36: The power capture efficiency (fraction) for endstop dampers (green), linear frictional dampers (blue) and combined damping (pink).

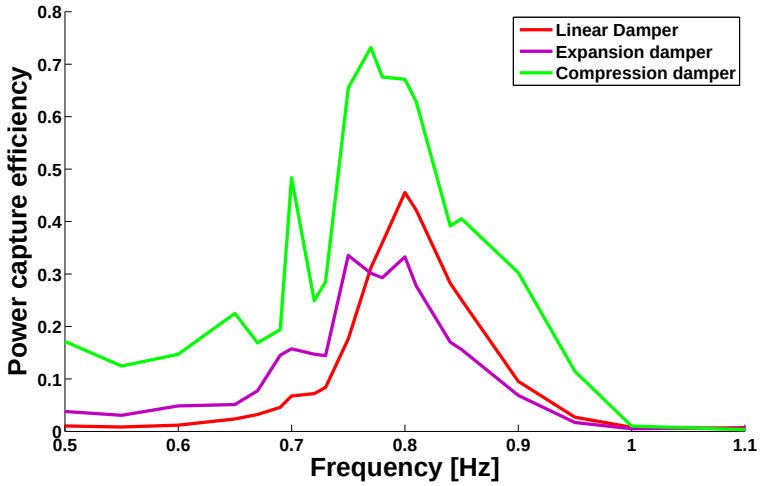

Figure 5.37: Comparing the average power capture efficiency (fraction) for the linear and both mono-directional dampers.

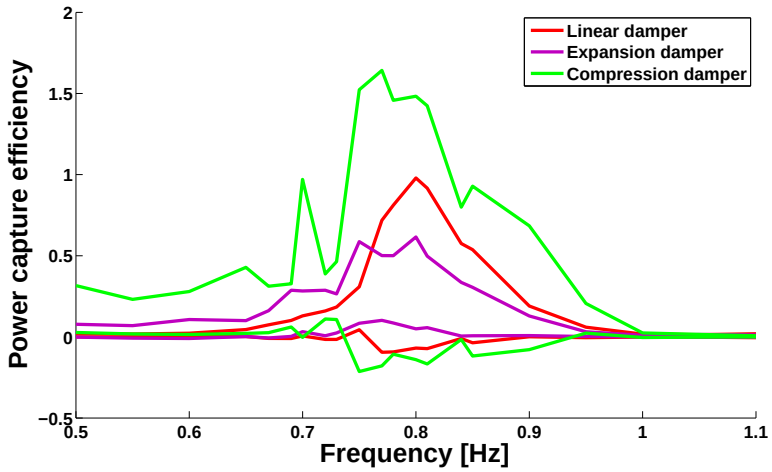

Figure 5.38: Comparing the average power capture efficiency (fraction) $\pm$ their standard deviations, for the linear and both mono-directional dampers.

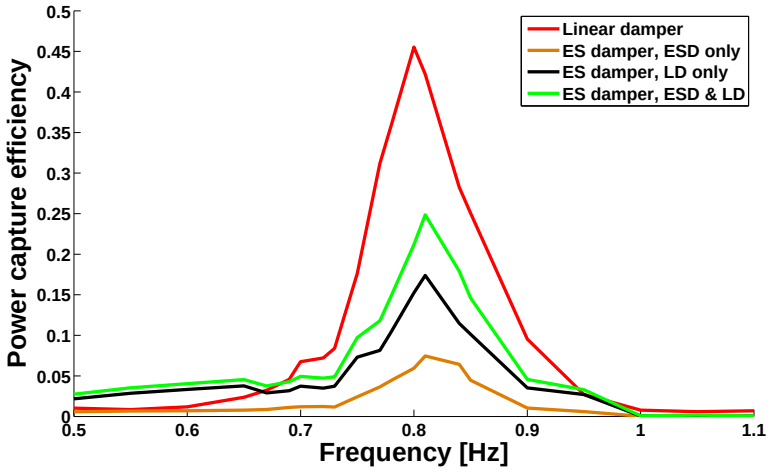

Figure 5.39: Comparing the average power capture efficiency (fraction) for the linear and endstop dampers.

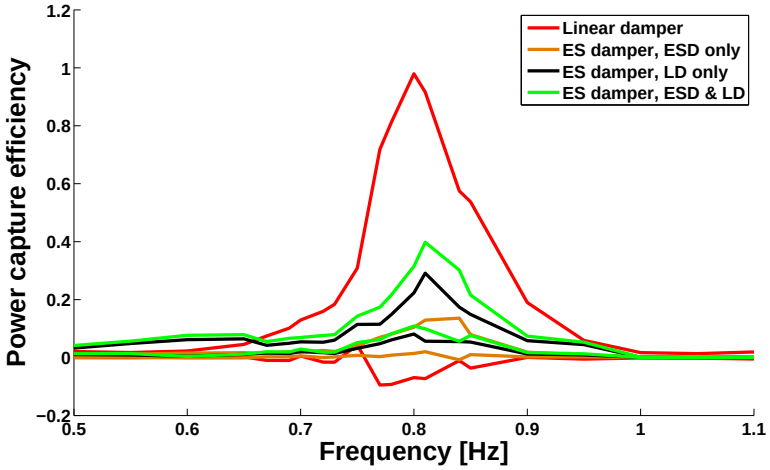

Figure 5.40: Comparing the average power capture efficiency (fraction) $\pm$ their standard deviations, for the linear and endstop dampers.

Chapter 6

Experimental results in irregular waves

6.1 Summary

In this chapter results are presented, analysed and discussed for the experimental model in irregular waves, looking at the positions of the cylinder, the internal mass and the relative position between them and the power extracted.

Section 6.2 considers the repeatability of the experimental setup in irregular seas. Section 6.3 presents a time series analysis of the device, using examples to demonstrate the typical response of the bodies to the waves, for different damper types. In Section 6.4 a comparison is made between the RAO and the LTF, which gives an indication of the amount of nonlinearities present in the experimental model. Section 6.5 presents the results showing the power extracted from the physical model with different PM spectrum seas, for all the damper types. Section 6.6 briefly concludes the chapter. The figures for this chapter are placed in Section 6.7 to increase the readability of the chapter.

6.2 Experimental accuracy and repeatability

In order to have confidence in the physical model results, it is necessary to have high levels of repeatability within the experimental setup. The Curved Wave Tank paddles has previously been shown to have high levels of repeatability by Bryden (1983). To test the repeatability and accuracy of the experimental model, a PM spectrum sea with a peak frequency of 0.90 Hz was used for 128 s to look at the correlation for 5 runs with identical sea states, with damper **C26**. The runs were taken in succession with no physical interference to the model occurring between the runs. The time series of these runs is presented in Figure 6.1, which shows different length time sections of the runs.

The data sets were used to find the R correlation, which is a linear measure of the normalized strengths of the relationships between two data sets, where an outcome of 1 implies *identical*

data sets. The R correlation is calculated from Equation 6.1, where the values already have their mean value subtracted from them.

$$R = \sum_{n=1}^{N} \left(\frac{(y_{1,n}\, y_{2,n})}{\sqrt{(y_{1,n}\, y_{1,n})(y_{2,n}\, y_{2,n})}} \right), \tag{6.1}$$

where $y_{1,n}$ and $y_{2,n}$ are the equivalent data points from the two different data sets, of length N.

The R correlation for the cylinder were always above 0.985, with an average of 0.989. For tests with the internal mass, the R values were above 0.975 with an average of 0.986. This shows that the repeatability of the model is high, although not exact. This is further confirmed by visual inspection of the time series.

A statistical test is applied to this data to see if there is a random chance that we got the level of correlation we observed. The hypothesis was tested that the data was not correlated to a confidence level of 6 sigmas, or 0.999999998027% confidence. This showed that at this confidence level there was a 0.000 % chance that the data was not correlated.

6.3 Time domain analysis with PM spectrum seas

A series of tests of the physical model in an irregular PM spectrum sea state were developed to see how the model responds to a more realistic wave climate. The time series results and analysis of the model's response is presented in this section.

6.3.1 Linear damper example

The time series for the damper **L41** is presented as an example of the changing positions, velocities and power captured over time, for the linear damper. The motions of the device as it experiences a PM spectrum sea, with a peak frequency of 0.90 Hz, for an arbitrary 20 s section are recorded, where the experimental run lasted for 384 s. As the repeat period of the waves in the Curved Wave Tank is 64 s, so these experimental runs last for 6 repeat periods. The same time section is used for the different types of dampers, so that an approximate comparison can be made of the effect of the different damping types.

In Figure 6.2 the height of the waves is presented, that the device with this damper (and all the other types of dampers) is subjected to. The wave height is the measured height of the waves at the same position as the device is located, without the device present. This figure also presents the absolute positions of the cylinder and the internal mass and the relative position between them. The absolute velocities of the internal mass and the cylinder are presented, without any smoothing or filtering.

Figure 6.3 shows the relative velocity between the two bodies, presented as the exact difference of the relative position data and also when these values have been smoothed and filtered. They

are filtered by comparing the values at each recorded time and at that recorded time plus the repeat period of the sea state. The smallest absolute value is then used as the filtered value. This helps eliminate large spurious results from the data set. The data is then smoothed using a low pass filter, in this case a 10 point moving average filter, and presented in this figure.

The power captured from the relative motion of the internal mass and the cylinder is calculated from the smoothed and filtered relative velocity. This is also presented in this Figure 6.3.

The difference between the smoothed and filtered relative velocity and the unaltered signal is significant. The unaltered signal has a number of much larger data points which, from considering the position data, seem spurious. The removal of these points allows the velocity signal to be a more accurate representation of the actual relative velocities. For this reason, for the other damper types, only the smoothed and filtered signal is presented.

The device with the linear damper shows that a significant amount of the power extraction occurs during small time sections. Hence the time averaged power extraction can be highly influenced by these occurrences of higher relative motion.

6.3.2 Mono-directional dampers example

Figure 6.4 shows the typical time series results for an expansion mono-directional damper, using damper **E93** as an example. It shows the positions of the cylinder and the internal mass and the relative position between them. The smoothed and filtered relative velocity of the internal mass is presented, and the power extracted using this relative velocity and considering when the expansion mono-directional damper would be providing a damping force is also presented.

The equivalent results are presented for the compression mono-directional damper, using damper **C113** as an example, in Figure 6.5.

The relative velocity of the expansion mono-directional damper, compared to the linear example, is generally larger and there is a slight tendency for the positive values to be larger than the negative values. Since power is only extracted from the relative velocity when the motion is negative, therefore during the positive relative velocity the increased relative internal mass motion results in additional potential energy stored in the compression of the spring.

The power extracted for the expansion mono-directional damper has significantly higher peaks (0.05 W for the linear damper compared to 0.2 W for the expansion mono-directional damper, although it should be noted that the damping constants were different, 41 Ns/m to 93 Ns/m). However, the amount of time that the linear damper generates a relatively substantial amount of power is higher.

The compression mono-directional damper has values of relative velocity similar to the expansion mono-directional damper, and therefore greater than the linear damper. The compression

damper has a slight tendency for the negative relative velocities to be larger than the positive values. Which, as expected, is the opposite of the expansion mono-directional damper.

The compression mono-directional damper has a slightly higher relative velocity than the expansion mono-directional damper, probably due to the difference in the damping constants of these examples, which is the reason that the power extraction peak values are greater (power extraction maximum peaks of c. 0.5 W) than the expansion mono-directional dampers. As with the expansion mono-directional damper, the time when a significant amount of power is being extracted is much lower than for the linear damper.

6.3.3 Endstop dampers example

An example time series of the endstop damper, using damper **ES34**, is presented in Figure 6.6, showing the position of the internal mass and the cylinder, the relative position between them, and the smoothed and filtered relative velocity. The power extracted is presented in Figure 6.7, which shows the power extracted from the endstop damper alone, the power from the linear frictional losses and the combined power that is extracted.

The relative velocity of this damper setup is slightly higher than but much closer to the linear damper than the mono-directional dampers, for most values. When the endstop damper collides with the internal mass the relative velocity is higher.

The power extracted from the endstop damper alone shows a distinct spike where the internal mass has contacted with the endstop damper and is zero elsewhere.

As the amount of damping from the endstop damper was small, the combined damping instantaneous power is very similar to the linear damper (0.04 W compared to 0.05 W peak power).

6.4 LTF and RAO comparison

The LTF is a measure of the frequency domain transform between the input signal (the waves) and the output (the motion of the bodies). It is related to the RAO, and for a fully linear system (including both the waves and the model) it would be expected that the RAO and the LTF are identical. More details are given in Section 3.2.

The LTF is obtained from the wave height and the position of the cylinder and mass in a PM spectrum sea with a peak frequency of 0.75 Hz. Where this signal is unavailable[1], a peak frequency of 0.80 Hz is used. The Fast Fourier Transform was used on 2048 data points and was completed twice for each data series of 4096 data values or 128 s of data, collected at 32 Hz, therefore the FFT was calculated on a complete repeat period. The final values used was an average of the two intermediate values.

1. This data was not recorded for **E334** and **E283** due to error.

This analysis was not completed on the endstop damper, since it was deemed in Section 5.3.5 that the endstop damper did not have a significant influence on the motion of the cylinder.

6.4.1 Linear damper

The LTF and the RAO are presented, for the linear dampers, with the difference between the LTF and the RAO shown for both the internal mass and external cylinder, in Figure 6.8.

All the linear dampers have good agreement between the LTF and the RAO away from the resonant peak frequency. At and near the resonant peak frequency, one third of the sample still have a high agreement while the remaining two thirds of the sample the LTFs were lower than the RAOs. This implies there was some nonlinearities in the system, either in the waves and / or the physical model.

6.4.2 Mono-directional dampers

The LTF and the RAO for the mono-directional dampers are presented in Figures 6.9 and 6.10 for the expansion mono-directional dampers and in Figure 6.11 for the compression mono-directional dampers.

A comparison between the LTF and the RAO shows a good agreement away from the resonant peak frequency and less agreement nearer the resonant frequency. Half of the mono-directional expansion dampers sample have a relatively good agreement near or at the resonant peak frequency, with the remaining dampers tending to have a lower LTF than the RAO at resonant frequencies. For the compression mono-directional dampers none of the dampers had a good agreement at the resonant frequencies for both the internal mass and the cylinder, although they all had good agreement away from the resonant frequencies.

6.4.3 Discussion

The RAO and the LTF are compared for the different damper types. This is initially presented using visual observations and is later presented using a statistically measure.

The difference in the RAO and the LTF from visual observations, is relatively consistent across the different damper types and the general trend is that the values are similar for frequencies that are not at the resonance of the system. For the frequencies from approximately 0.73 Hz to 0.85 Hz the RAO is tends to be significantly larger than the LTF, often by around 50%. As previously discussed, according to linear theory these values should be identical if the model and the water waves were fully linear. An explanation of the difference is particially due to nonlinearities in the water resulting in turbulance and friction from the water affecting the motion of the larger amplitude resonace frequency responses, espeically as the waves for the PM spectrum sea were often higher than the c. 20 mm wave for the regular waves. Another

component of the difference between the LTF and the RAO would be the nonlinearities in the model, and when the nonlinear dampers are used, these would contribute to this nonlinearity.

A statistical measure that has been used to judge the relative error between the different damping types is the Root Mean Square Error (RMSE), (Montgomery and Runger, 1994). This is also referred to as the *standard error of the regression* or as the *fit standard error*. It measures the square of the error between the numerical simulation and the experimental results, and takes the square root of the mean of this value.

$$RMSE = \sqrt{\frac{SSE}{N}}, \tag{6.2}$$

where

$$SSE = \sum_{i=1}^{N} (y_i - \widehat{y}_i)^2, \tag{6.3}$$

and N is the number of data points, y_i is the data value and $\widehat{y}_i$ is the predicted data value. In this work, the LTF data points are y_i and the equivalent RAO data points are $\widehat{y}_i$.

This statistical measure can indicate the relative error, with smaller values indicating increased goodness of fit. It does not provide information about whether the experimental results are generally higher or lower than the experimental results or are approximately equally spread, but only how close they are to the experimental results.

The RMSE has been used to compare the linear and mono-directional dampers, and the results are presented in Table 6.1. The resulting RMSE values show that the expansion mono-directional damper has a greater difference between the LTF and the RAO than the linear damper. The compression mono-directional damper has RMSE values that are approximately equal to the linear damper values. Although the sample size is small and the variation in the results significant, these results imply that the model with the expansion mono-directional damper has more nonlinearity than with the linear damper, i.e. having a nonlinear damper is resulting in nonlinear absolute cylinder and internal mass motions, as expected. The result of the compression mono-directional damper having a mean value of RMSE similar to the linear damper is unexpected and probably connected to the sample size, the high variability in the LTF and RAO results and in the different damping constants used.

6.4.4 The influence of the amplitude

In order to help understand which component of the nonlinearities is due to nonlinear water effects as opposed to nonlinear effects in the physical model, the wave amplitude was reduced to limit the nonlinearities from the waves and the associated LTF is studied. This was completed by testing some of the dampers with a PM spectrum sea with a peak frequency of 0.75 Hz but

Linear			Expansion MD			Compression MD		
	RMSE			RMSE			RMSE	
	Mass	Cylinder		Mass	Cylinder		Mass	Cylinder
L41	0.586	0.510	E13	0.373	0.242	C26	0.335	0.309
L85	0.441	0.345	E14	0.435	0.334	C40	0.543	0.398
L144	0.414	0.385	E66	0.315	0.560	C113	0.396	0.252
L229	0.417	0.385	E93	0.486	0.342	C161	0.385	0.327
L365	0.325	0.275	E101	0.473	0.280	C178	0.264	0.621
L699	0.309	0.286	E176	0.325	0.285	C528	0.462	0.423
			E283	0.465	0.359			
			E334	0.824	0.509			
			E437	0.387	0.372			
			E686	0.342	0.309			
			E867	0.476	0.438			
			E872	0.564	0.465			
Average	0.415	0.364		0.456	0.375		0.398	0.388
σ	0.099	0.086		0.139	0.098		0.097	0.130

Table 6.1: The RMSE for the linear and mono-directional dampers, for the comparison between the LTF and the RAO.

with a reduced amplitude of waves[2]. Dampers **L229** and **C528** had a PM spectrum sea with 50%, 70% and 100% wave height of the original PM spectrum sea with a peak frequency of 0.75 Hz and damper **E867** has 50% and 70% of a PM spectrum sea with a peak frequency of 0.75 Hz and 100% of a PM sea with a peak frequency of 0.80 Hz. This was only recorded in these limited cases since these tests were not originally planned.

These results are presented in Figure 6.12. In these cases, it is seen that the changing amplitude results in the value of the LTF changing in a consistent manner. Whether it is increasing or decreasing varied and with the sample size that is presented, there is no consistent pattern that can be identified. However none of the LTFs have a strong agreement to their corresponding RAO's. This implies that although there is some effect from the changing amplitudes, probably due to nonlinear water motions, this is not the only nonlinear influence on the external cylinder and the internal mass.

2. Technically this would mean the seas were not PM, but a different spectrum, however since the identical seas have been used except that the amplitude has been proportional reduced, we are going to continue referring to them as PM spectrum seas.

6.5 Power extracted

The power from different peak frequency PM spectrum seas was obtained using the same smoothing as occurred with the relative velocity time series (see Section 6.3). The power extracted is obtained for the entire time period and the data has been filtered by collecting the data for 128 s and because the waves and hence output data should repeat every 64 s the two values of data at n and $n+64s$ are compared and the lowest value used. The minimum value from the two repeated wave cycles is used to get the power extraction over the 64 s repeat period as any errors were deemed more likely to increase the value than decrease it. This is done to help eliminate any spurious vibrations. The power has been obtained from PM spectrum seas with peak frequencies of 0.75 Hz, 0.80 Hz, 0.85 Hz, 0.90 Hz, 0.95 Hz and 1.00 Hz. Not all the different PM spectrum seas have been obtained for all the different damper types, but a representative sample was obtained.

6.5.1 Linear dampers

The linear dampers response to the different PM spectrum seas for the time averaged power extraction is presented in Figure 6.13.

As expected, the PM seas which have the most energy (with the lower peak frequencies) result in higher amounts of power captured compared to seas with less energy. The large time averaged power extraction of the the **L699** damper would be due to inaccurate calculations of the power extraction due to the air spring effect, as previouisly discussed. Although the sample size is small, and variations are high, there is a general trend for an increase in the power extracted for increasing damping constant up to a maximum and then a decrease. However the exact maximum value and the steepness of the slopes are hard to accurately ascertain.

6.5.2 Mono-directional dampers

The power extracted from the expansion mono-directional damper is presented in Figure 6.14 and for the compression mono-directional damper is presented in Figure 6.15, for the different peak frequency PM spectrum seas.

The average power extracted for each of the different PM spectrum seas is higher with the expansion mono-directional damper than with the linear damper. The maximum power captured for the expansion mono-directional damper is at a lower damping constant than for the linear damper.

For the compression mono-directional damper, the average power extracted for the different PM spectrum seas is slightly higher than the linear damper, however since the damping constants at which these are compared are not the same, this is extrapolated based upon the damping constants where the power is known. As for the expansion mono-directional damper, the damping constant that has the maximum power extraction is lower than the linear damper.

6.5.3 Endstop dampers

The time averaged power extracted from the endstop dampers has been separated into different components. The power extracted directly from the endstop damper, the power extracted from the linear frictional damping and a combination of these. These are presented in Figures 6.16, 6.17 and 6.18, respectively.

The power extracted from the linear frictional damper is higher than the power extracted from the endstop damper alone (maximum value of 0.017 W compared to 0.003 W).

The power extracted from the endstop damper directly has a maximum power extraction for these experimental results at a damping constant of c. 50 Ns/m, while for the linear frictional damping, the power extracted is greater for smaller or zero damping constants.

6.5.4 Discussion of the power extracted from the PM spectrum sea

Linear and mono-directional dampers

The results of the power extraction for both regular waves and irregular PM spectrum seas, for the experimental model, show that the amount of power extracted from a device can be equal to and is often higher when a mono-directional damper is used compared to a bi-directional linear damper. This has some interesting implications for this type of WEC.

It may be beneficial for a WEC to have a mono-directional PTO as opposed to a bi-directional PTO, especially if a bi-directional damper is more expensive than a mono-directional damper. It is also relevant, for example, for a design where the PTO is intended to be bi-directional but at the prototype stage has been made mono-directional for ease, and the developer has to determine what the power output would be for the final design from the prototype results.

Endstop dampers

The combination of the two sources of power extraction shows that for maximum power extraction, when compared to the linear damper **L41**, extracts more total power than without an endstop damper present. However, when you include the additional damping constant from the linear frictional damping as additional to the linear damping constant the values are much closer. Due to the different damping constants and the experimental variability that occurs, it is thought that having the endstop damper does produce more power but there is not enough information from these experimental results alone for a high confidence in this result. The numerical simulations agree with the prediction that having an endstop damper does result in more power extraction, as presented and discussed further in Chapters 3 and 7.

6.6 Conclusions of chapter

This chapter has demonstrated that the time series of the positions, velocities and the power extracted are influenced by whether a mono-directional or linear damper is used. In some cases, more overall power was extracted from the mono-directional dampers than the linear dampers, although the experimental errors need more analysis to confirm this.

The endstop dampers have less obvious influences in affecting the motions of the cylinder and the internal mass. When the total power extraction is considered they have a greater time averaged power extraction than just having a linear damper.

The LTF and the RAO are similar away from the resonant frequency of the physical model, but close to the resonant frequencies the LTF tends to be significantly lower than the RAO. This occurs for all damper types to some extent.

The next chapter will compare the physical model results with the numerical simulation and look at the similarities and differences that occur.

6.7 Figures

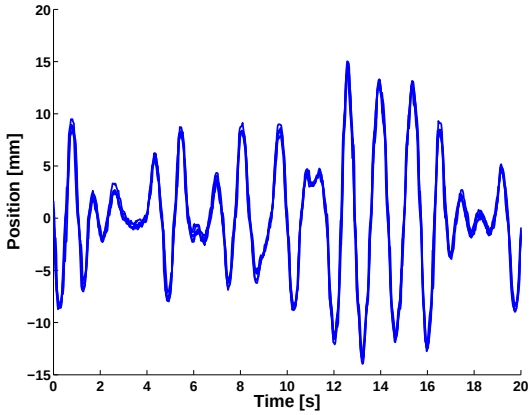

(a) 20 s of data.

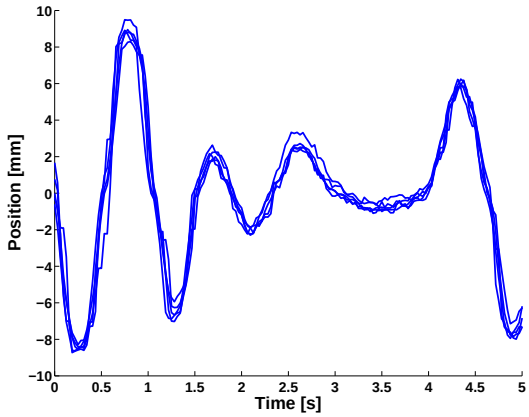

(b) 5 s of data.

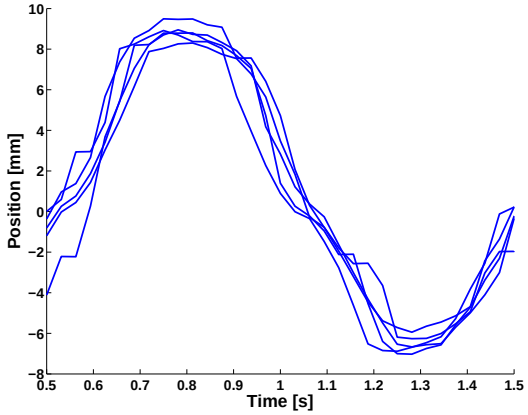

(c) 1 s of data.

Figure 6.1: Five *identical* PM sea test runs with damper C26, showing the high repeatability of the results.

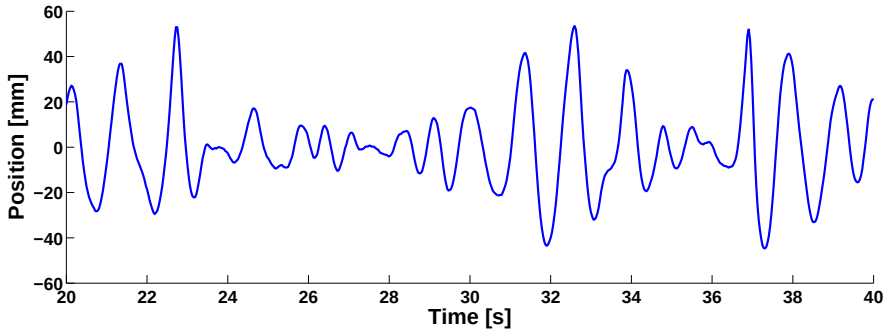

(a) Wave height.

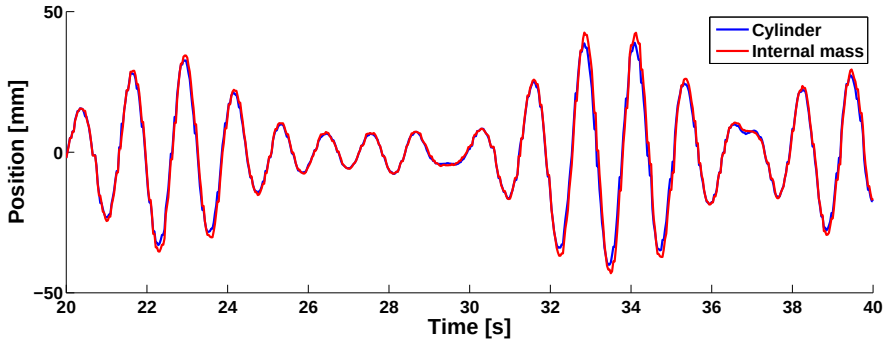

(b) Position of cylinder and internal mass.

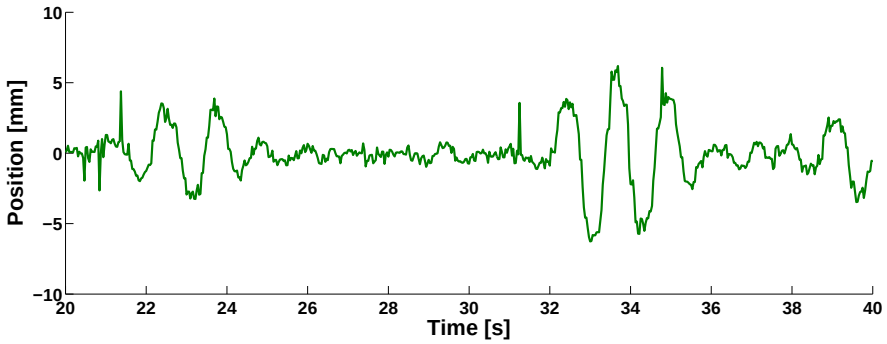

(c) Relative position.

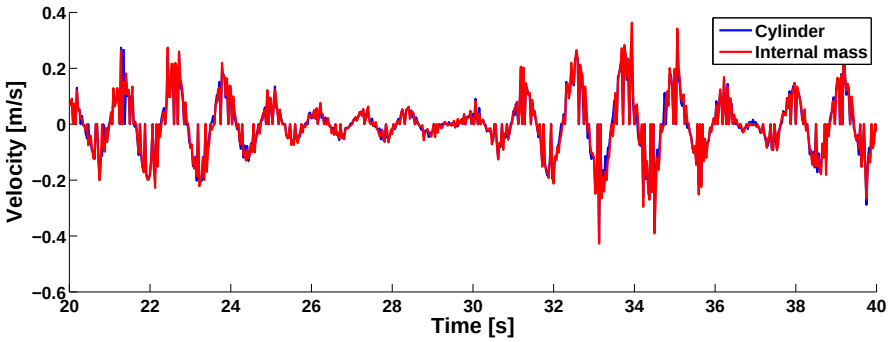

(d) Velocities of the cylinder and internal mass.

Figure 6.2: Time series for L41.

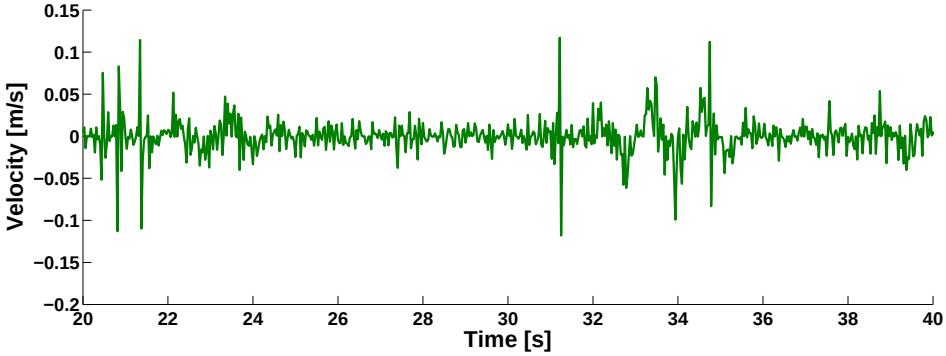

(a) Relative velocity - unaltered.

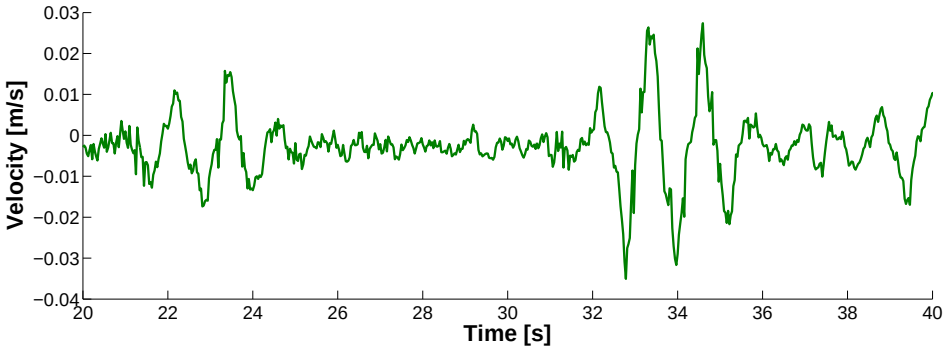

(b) Relative velocity - Smoothed and filtered, as discussed in Section 6.5.

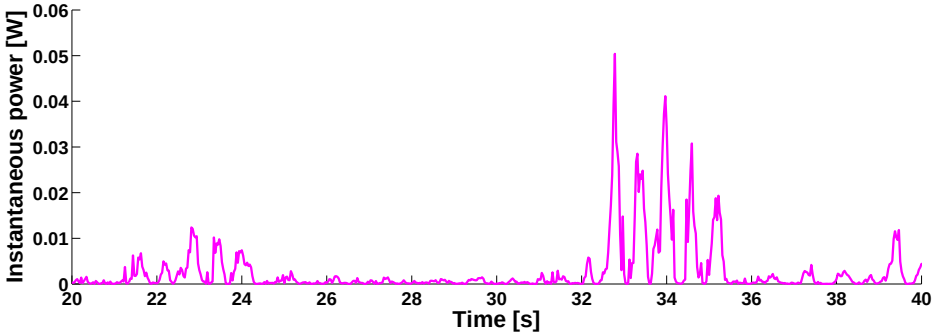

(c) Instantaneous power capture.

Figure 6.3: Velocity time series for L41.

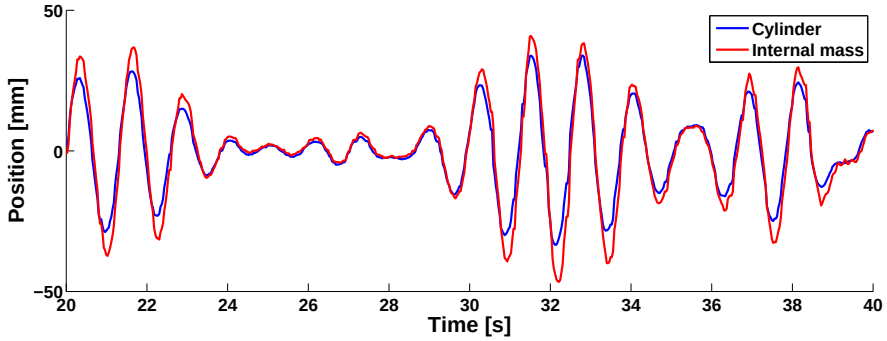

(a) Positions of the cylinder and internal mass.

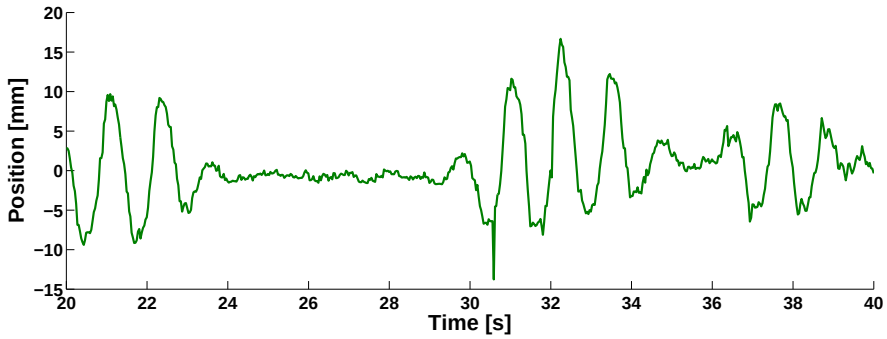

(b) Relative position.

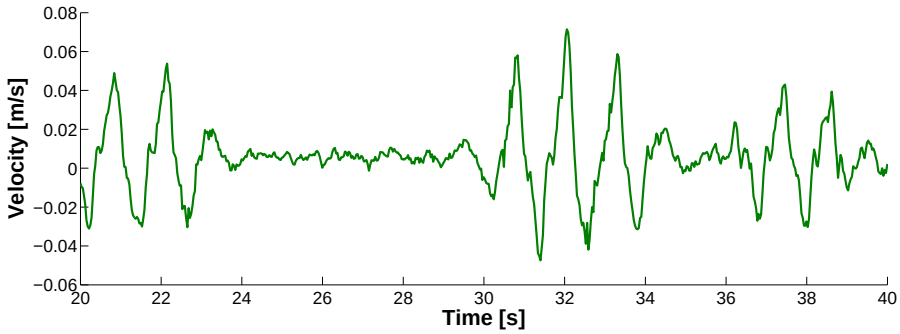

(c) Relative velocity - smoothed and filtered, as discussed in Section 6.5.

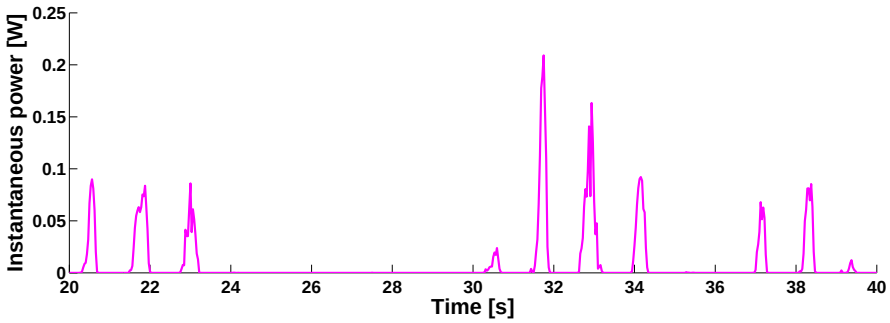

(d) Instantaneous power captured.

Figure 6.4: Time series for E93.

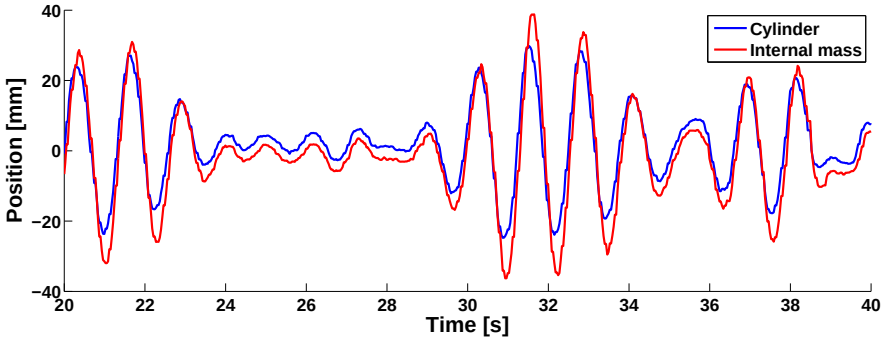

(a) Positions of the cylinder and internal mass.

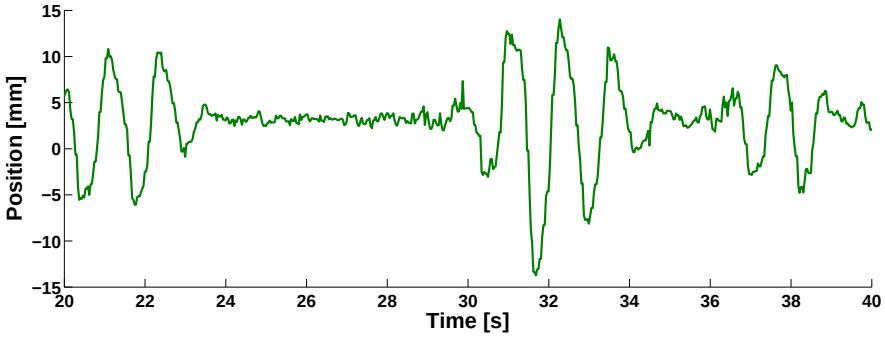

(b) Relative position.

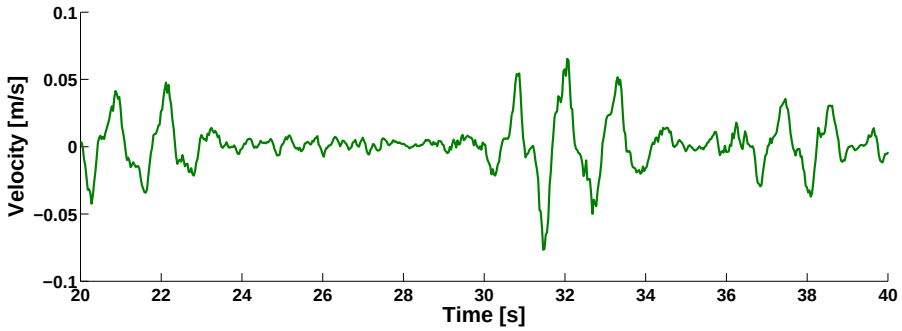

(c) Relative velocity - smoothed and filtered, as discussed in Section 6.5.

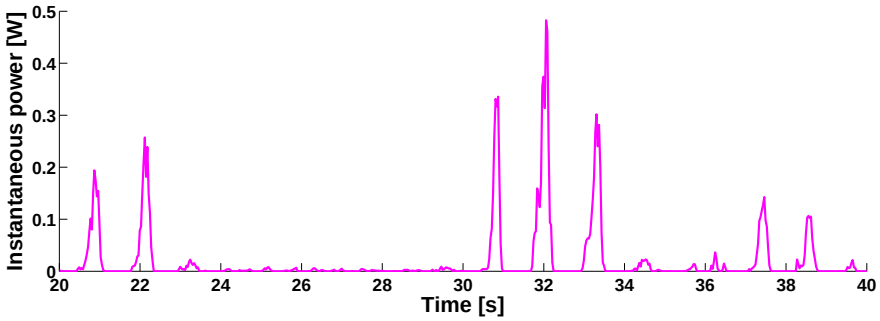

(d) Instantaneous power captured.

Figure 6.5: Time series for C113.

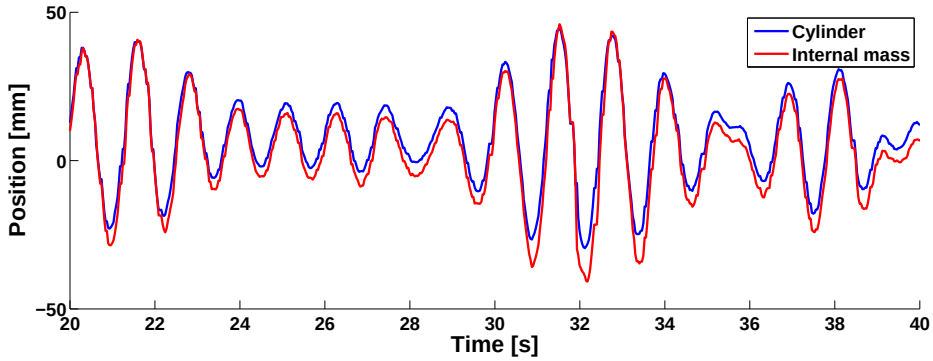

(a) Positions of the cylinder and internal mass.

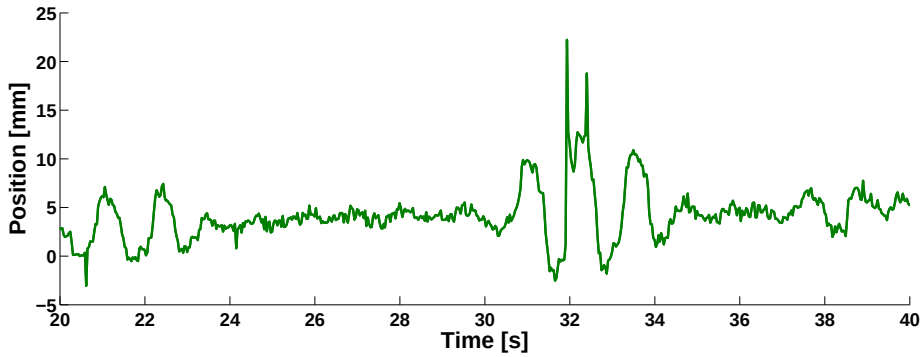

(b) Relative position.

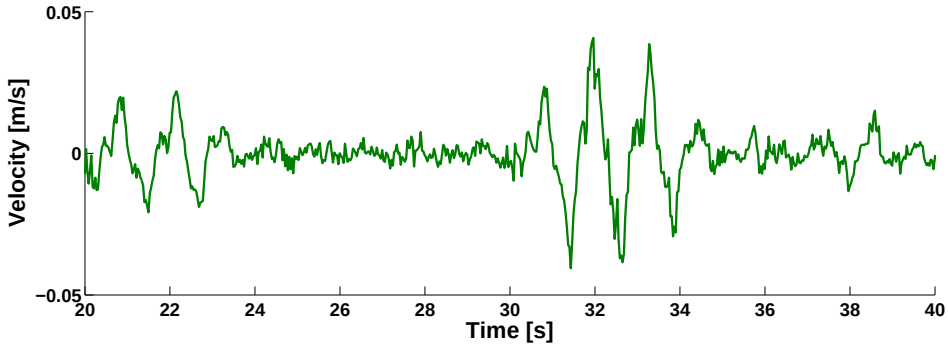

(c) Relative velocity - smoothed and filtered, as discussed in Section 6.5.

Figure 6.6: Time series for ES34.

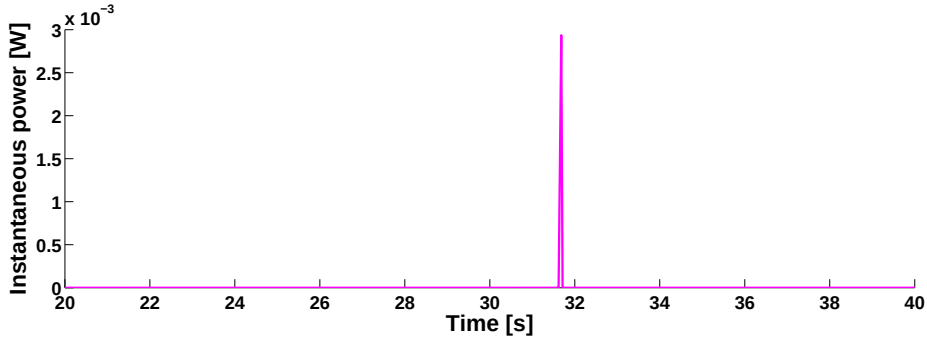

(a) Power extracted from endstop damper only.

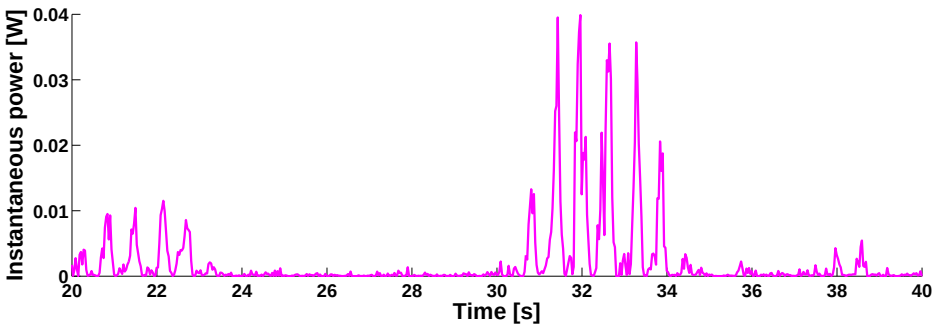

(b) Power extracted from linear frictional damping.

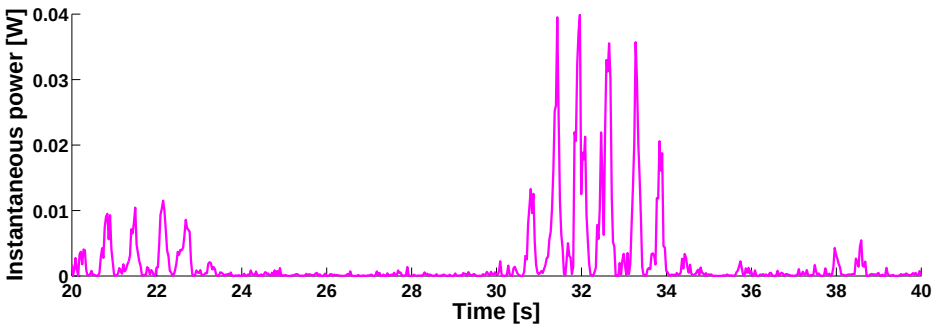

(c) Combined power extraction.

Figure 6.7: Time series showing power extraction for ES34.

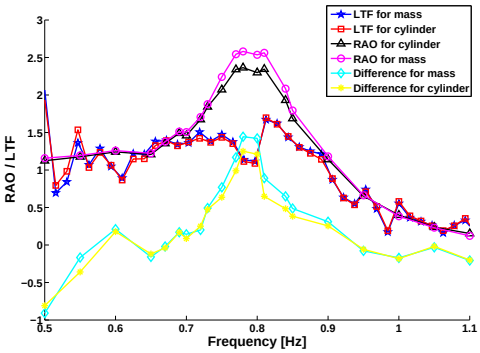

(a) L41.

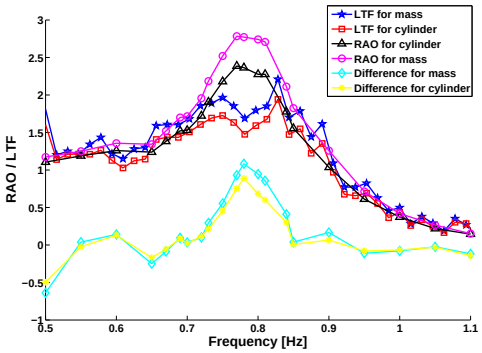

(b) L85.

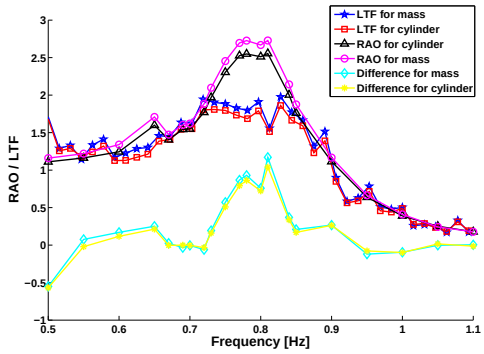

(c) L144.

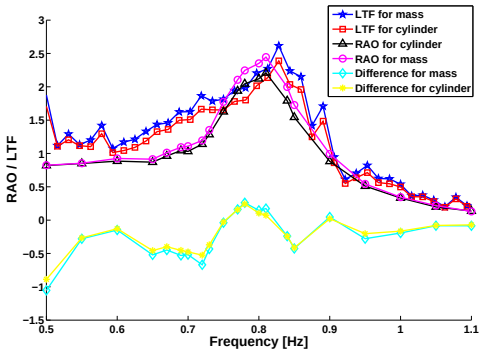

(d) L229.

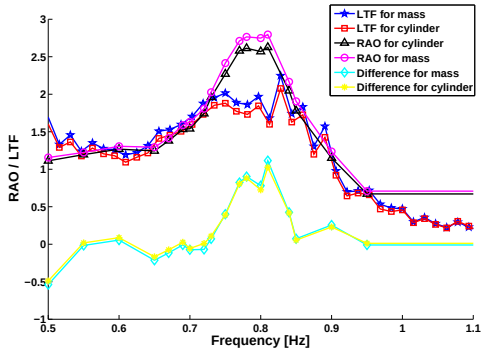

(e) L365.

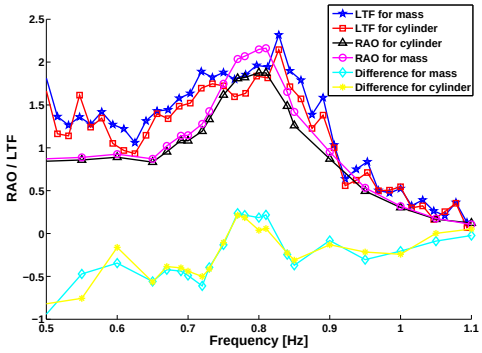

(f) L699.

Figure 6.8: LTF and RAO of the linear damper, and the difference between them for the external cylinder and the internal mass.

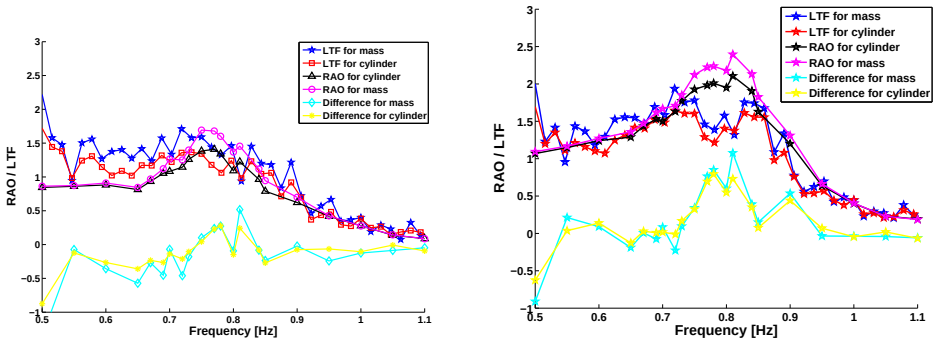

(a) E13. **(b)** E14.

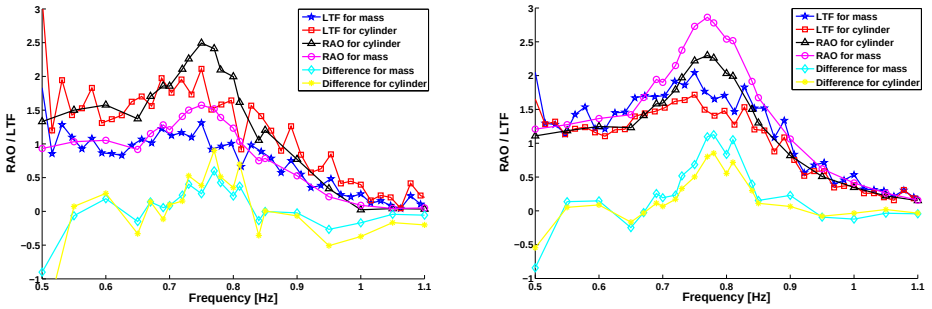

(c) E66. **(d)** E93.

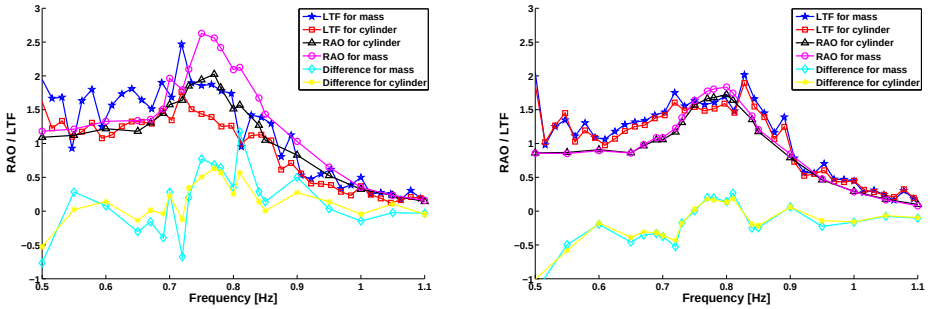

(e) E101. **(f)** E176.

Figure 6.9: LTF and RAO of the expansion mono-directional damper, and the difference between them for the external cylinder and the internal mass, for E13 to E176.

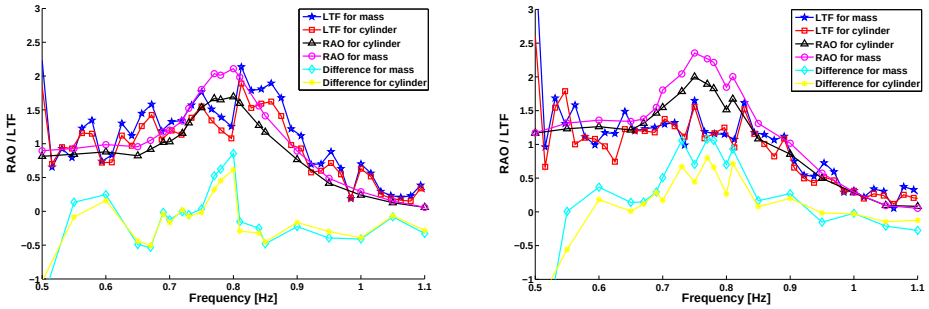

(a) E283. **(b)** E334.

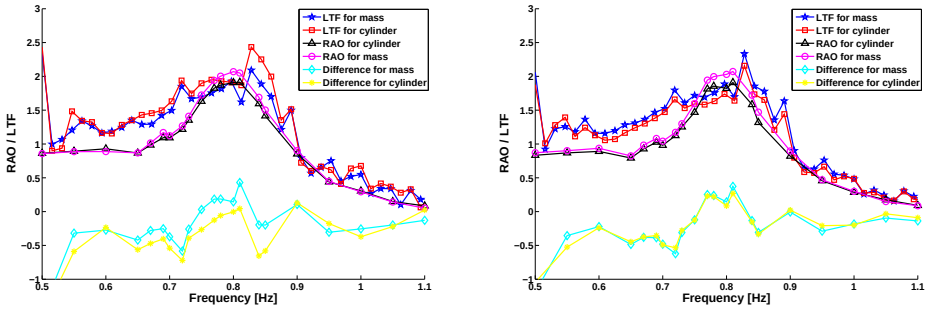

(c) E437. **(d)** E686.

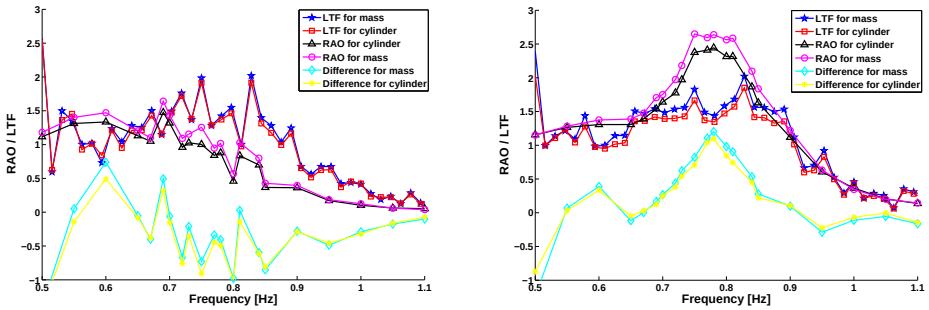

(e) E867. **(f)** E872.

Figure 6.10: LTF and RAO of the expansion mono-directional damper, and the difference between them for the external cylinder and the internal mass, E283 to E872.

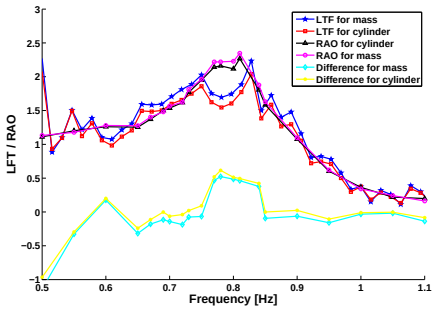

(a) C26.

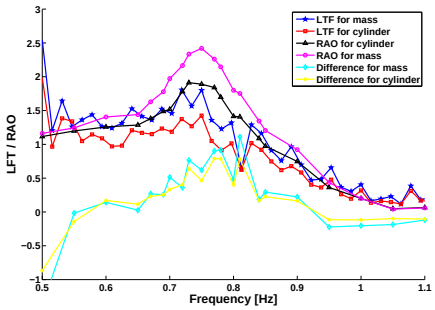

(b) C40.

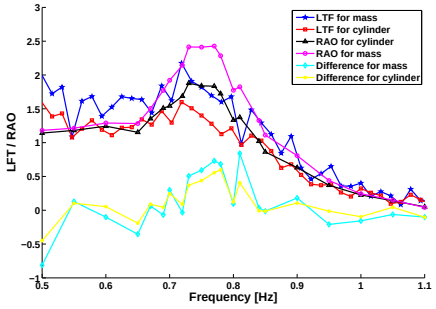

(c) C113.

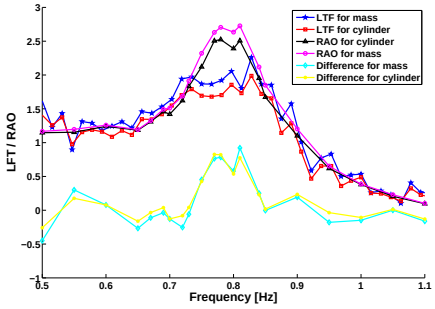

(d) C161.

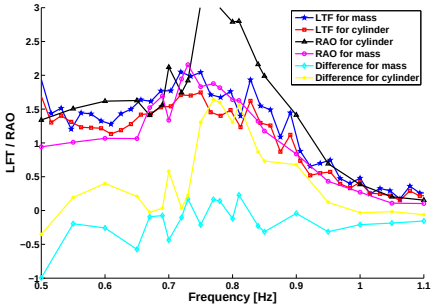

(e) C178.

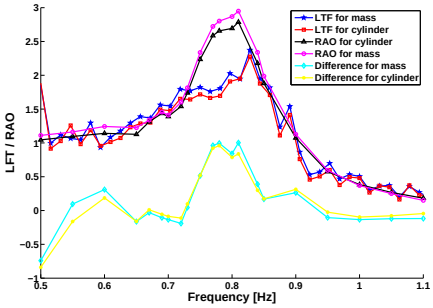

(f) C528.

Figure 6.11: LTF and RAO of the compression mono-directional damper, and the difference between them for the external cylinder and the internal mass.

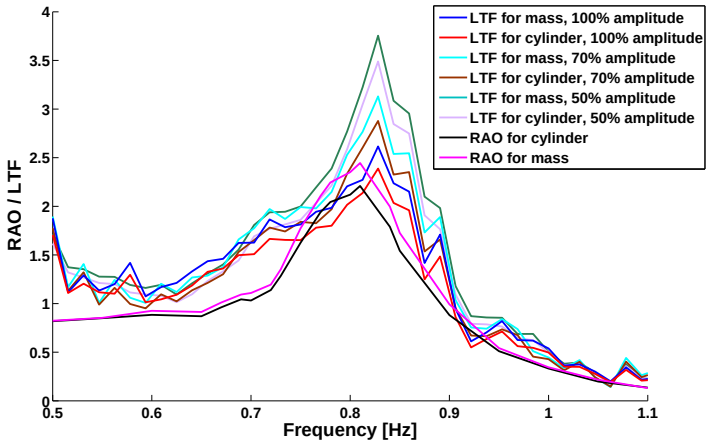

(a) L229.

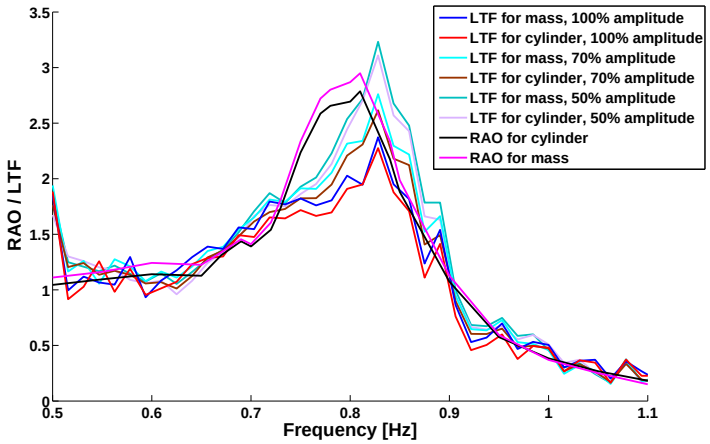

(b) C528.

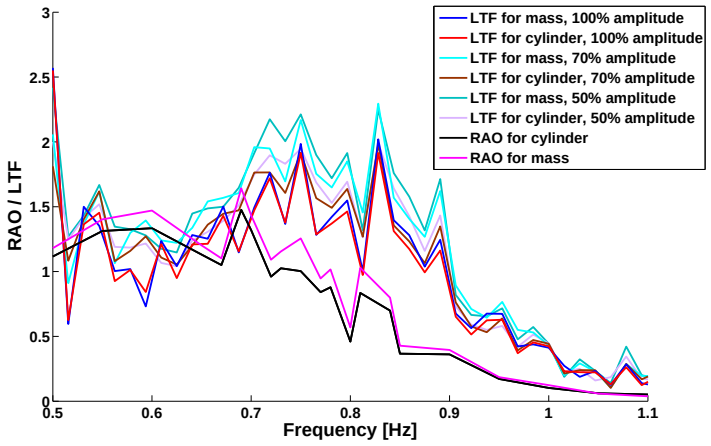

(c) E867.

Figure 6.12: LTF and RAO for the external cylinder and the internal mass for PM seas of peak frequency 0.75 Hz with varying amplitude, for dampers L229, C528 and E867.

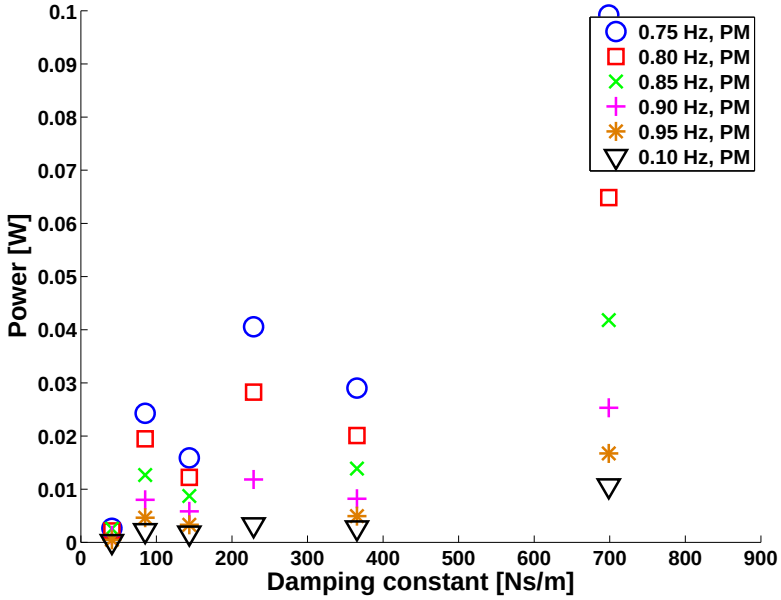

Figure 6.13: The power from different PM spectrum seas, for the linear damper.

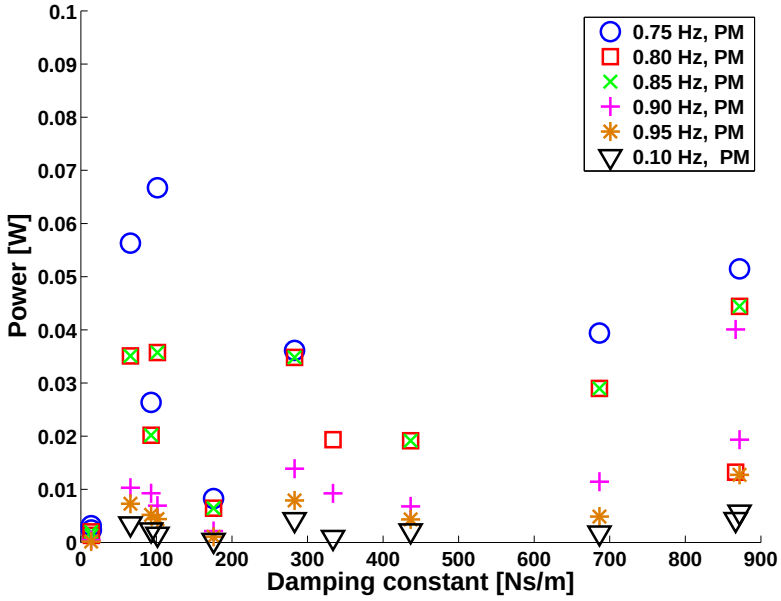

Figure 6.14: The power from different PM spectrum seas, for the expansion mono-directional damper.

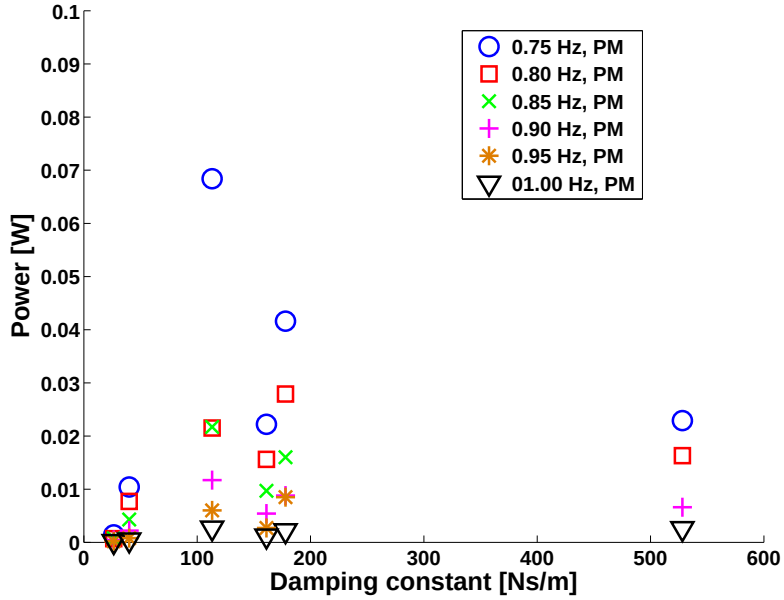

Figure 6.15: The power from different PM spectrum seas, for the compression mono-directional dampers.

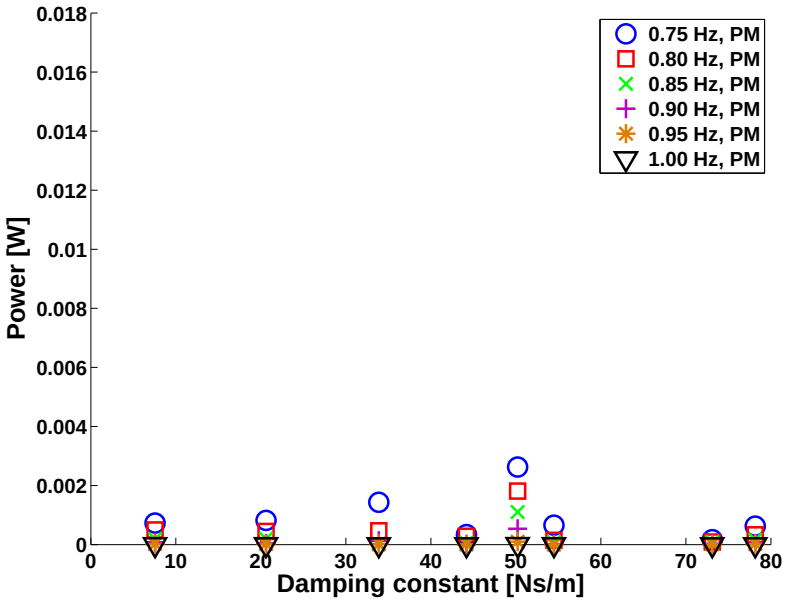

Figure 6.16: The power from different PM spectrum seas, for the endstop damping only.

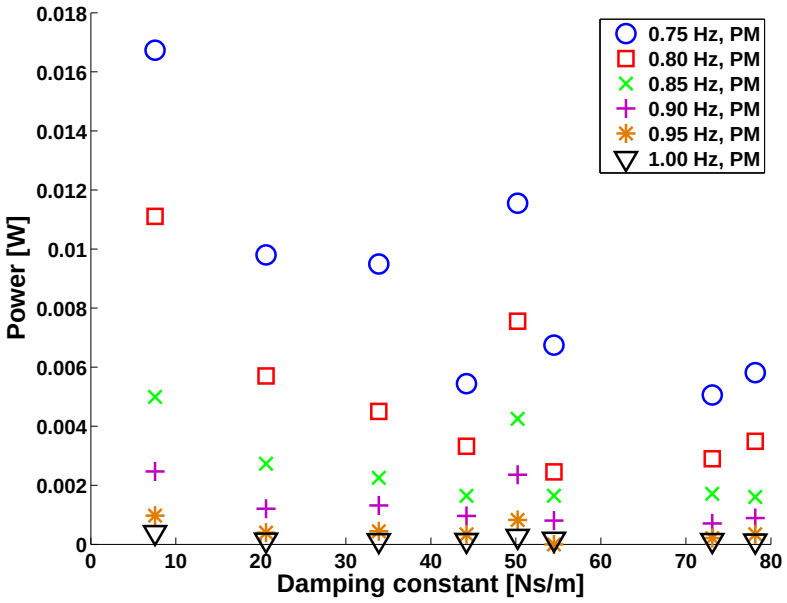

Figure 6.17: The power from different PM spectrum seas, for the linear frictional damping with the endstop damper.

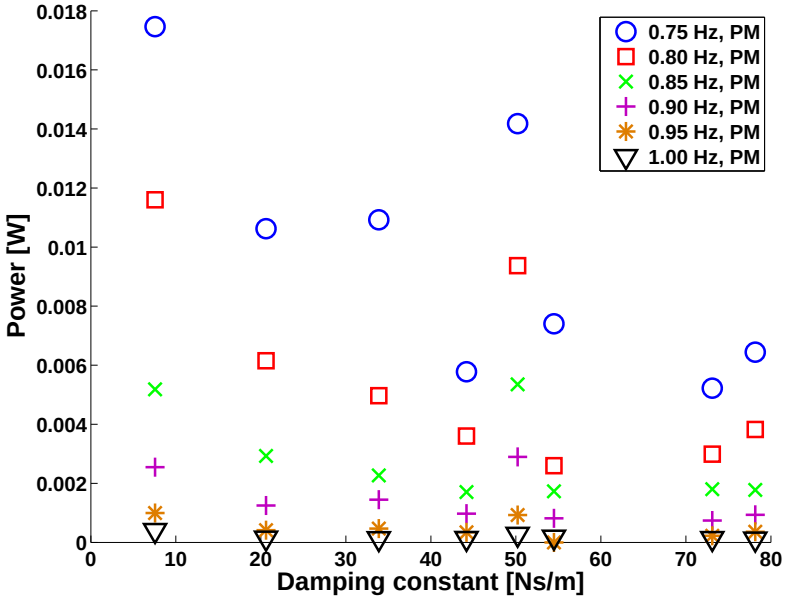

Figure 6.18: The power from different PM spectrum seas, for the combined endstop and linear frictional damping with the endstop damper.

Chapter 7

Comparison between experimental and numerical models

7.1 Summary

In this chapter the differences between the numerical simulation and the experimental results in the Curved Wave Tank will be presented. The results of the numerical simulation for the tank scaled model will be presented, analysed and discussed. These will then be compared to the experimental results that have previously been presented in Chapters 5 and 6.

Section 7.2 of this chapter presents details of the parameters used in the numerical simulation. Section 7.3 presents results for the RAO in regular waves, for the experimental and numerical models, for both bodies and the relative RAO between them. In Section 7.4, the relative phase between the cylinder and internal mass will be presented and discussed for the numerical and experimental results. Results for the power extraction efficiency in regular waves will be presented and discussed in Section 7.5. The power extraction in irregular seas is presented in Section 7.6, where the numerical simulation is discussed and compared to the experimental results. This chapter is briefly concluded in Section 7.7. The figures for this chapter are all located in Section 7.8, to aid clarity.

7.2 Numerical simulation of the tank scaled model

The numerical simulation was run to replicate the experimental results from Chapters 5 and 6. The numerical setup used was as described in Section 2.2.2. The numerical simulation included the terms to calculate the friction between the central rod and the external bearings, and the friction and damping between the internal mass bearing and the central rod.

For regular wave testing, waves were used of the same frequency as in the experimental model testing. Some additional frequencies were included (in some of the results) to allow more data points in areas of interest. All the different frequency waves in the regular wave tests had a wave height of 0.2 m and zero phase. There were no reflections or any additional waves with

different directionality and the waves were exact sinusoidal shapes. In the same manner as in the experimental tank testing, the waves were initially run for 16 s and this data was discarded to obtain the regular waves in a steady state. A further 32 s of waves were used for the comparison work, with the data being calculated at 32 Hz.

For irregular wave testing, the numerical simulation was run with a Pierson Moskowitz sea spectrum, using 201 different regular wave frequencies combined together, with a frequency spacing of 0.05 rad/s (0.008 Hz) and a range from $\frac{\sqrt{6}}{10}$ rads to $10+\frac{\sqrt{6}}{10}$ rads (0.04 Hz to 1.63 Hz). A uniformly distributed randomly generated phase between 0 and 2π was used.

7.3 Regular wave RAOs

To find the RAO of the cylinder and the internal mass in the numerical simulation the difference in the average of the highest 10 data values and the average of the lowest 10 data values was calculated. The relative RAO between the internal mass and the cylinder has been calculated from these RAOs assuming that there was no phase difference. This is the same procedure as for the experimental results.

The maximum numerical damping constant used is 500 Ns/m, because above this value the response is approximately constant for higher damping constants.

7.3.1 RAO for linear damping

The numerical simulation and experimental runs are compared for the linear damping constant. Experimental results of the RAO at each damper constant are presented with the equivalent numerical simulation result, in Figure 7.1, for the internal mass, cylinder and the relative position between them. These results show the influence of the different frequencies on the predefined damping constants.

The numerical simulation shows an increase in the frequency of the resonant peak as the damping constant is increased. This shows how the relative motion of the internal mass is coupled to the motion of the overall body. This change in frequency of the resonant peak was not seen in the experimental model.

The relative motion between the cylinder and the internal mass becomes very small for values of damping of 230 Ns/m and above, in the numerical simulation. This is because the numerical dampers are exactly proportional to the relative velocity and they do not have any air spring effect.

At lower damping constants, the experimental results are generally higher than the numerical simulation results. As the damping constants increases, the numerical simulation absolute values become higher than the experimental results, but the relative motion is negligible. At

the higher damping constants there is limited motion between the cylinder and internal mass in the numerical simulation and the two bodies act as a single body, which has a large resonant response. The physical phenomena of the turbulence in the water from large responses which would cause damping of the cylinder is not represented in the numerical simulation, so a numerical simulation that included these phenomena would not have such a large response.

The numerical simulation and the experimental results are the most similar when a damping constant of 140 Ns/m is used. At this value, the damping from between the internal mass and the central rod is small compared with the damping from the PTO damper, but there are limited effects from the air spring effect in the experimental model.

The effect of the different damping constants on the RAOs, for predefined frequencies are presented in Figures 7.2, 7.3 and 7.4, for the numerical simulation and the experimental results. This shows the RAO for the cylinder and the internal mass, and also the relative position between them.

The numerical simulation has significant changes in the RAO of the absolute internal mass, at low damping constants. The internal mass RAO changes as the frequency of the waves increase. It goes from having a higher RAO for lower damping constants compared to the average RAO value for that frequency, to a lower RAO than the average RAO value, for lower damping constants. This change is due to the coupled motion of the cylinder and internal mass. Since the cylinder responds differently to different frequency waves, and the relative motion between the two bodies results in damping forces and power extraction, then the RAO of the internal mass responds to these connected influences.

The cylinder and internal mass of the numerical simulation have a large resonant response at 0.81 Hz and 0.84 Hz, which as was previously discussed, would be unlikely to be as large in an actual device.

Comparing the numerical and experimental results shows that there is some general agreement in the shape of the RAO of the internal mass and the cylinder, in the majority of cases. This is especially noted at frequencies of 0.80 Hz and lower.

The relative RAO show a generally good agreement between the experimental and numerical results. The experimental results tend to be higher at all damping constants except very low damping constants, where the numerical results are consistently higher. This could be due to larger relative motion resulting in additional damping in the experimental model which is not represented well in the numerical simulation.

The RMSE is a statistical measure, as discussed in Section 6.4, with smaller values indicating increased goodness of fit. It does not provide information about whether the experimental results are generally higher or lower than the experimental results or are approximately equally spread, but only how close they are to the experimental results. As such, these results should be considered in parallel with visual inspection of the figures provided.

	Linear RMSE		
Freq. [Hz]	**Cylinder**	**Mass**	**Relative**
0.703	0.201	0.218	0.116
0.719	0.259	0.278	0.128
0.734	0.327	0.350	0.139
0.750	0.448	0.523	0.144
0.766	0.554	0.645	0.159
0.781	0.481	0.553	0.170
0.797	0.484	0.486	0.193
0.812	0.780	0.713	0.181
0.844	1.856	1.773	0.113
0.906	0.543	0.483	0.097
Average	0.593	0.602	0.144
σ	0.471	0.439	0.032

Table 7.1: The RMSE for the RAO of the linear damper, comparing the experimental and numerical results.

The RMSE for the numerical and experimental results are presented in Table 7.1, for the linear damper. These are for the cylinder, internal mass and for the relative RAO between them, for different frequencies.

The RMSE values show that the RAO of the relative motion was the most consistent in producing similar experimental and numerical simulation data, then the absolute RAOs bodies, across the frequency range.

7.3.2 RAO for an expansion mono-directional damper

The RAO results for the expansion mono-directional damper, comparing the numerical to the experimental results, are presented in Figure 7.5, for the different damping constants tested. Again, the higher damping constants have not been included, due to a lack of confidence in these experimental results because of the air spring effect.

The numerical simulation of the expansion mono-directional damper has similar properties in the position of the resonant peak, and the RAO values, to the linear damper simulation.

Comparing the damper **E14** and the numerical simulation of 10 Ns/m, shows that although the resonant peak is at a different frequency, if the relative peak was shifted to the same frequency the RAO values would be very similar.

At 100 Ns/m, the experimental results have much higher values than the numerical simulation, although the resonant peak is at a similar frequency.

The numerical and experimental results have high agreement at 180 Ns/m, and quite high agreement at 280 Ns/m. These damping constants are likely to have close agreement due to the

	Expansion MD RMSE		
Freq. [Hz]	**Cylinder**	**Mass**	**Relative**
0.703	0.312	0.527	0.374
0.719	0.366	0.451	0.394
0.734	0.446	0.374	0.369
0.750	0.578	0.477	0.361
0.766	0.629	0.531	0.335
0.781	0.611	0.534	0.296
0.797	0.604	0.495	0.307
0.812	0.728	0.676	0.267
0.844	0.877	0.800	0.187
0.906	0.471	0.423	0.119
Average	0.562	0.529	0.301
σ	0.169	0.125	0.089

Table 7.2: The RMSE of the RAO for the expansion mono-directional damper, comparing the experimental and numerical results.

smaller relative damping effect from between the internal mass and cylinder and the reduced air spring effect in the experimental model – as discussed for the linear model.

For a selection of predefined frequencies of interest, the numerical and experimental results are presented for all the different damping constants, in Figures 7.6, 7.7 and 7.8; for both the external cylinder and the internal mass, and separately for the relative RAO between them.

The experimental results for 0.75 Hz and below show relatively high agreement with the numerical results. Above this frequency, the agreement is less precise due to the numerical simulation predicting large resonant responses. These do not occur in the experimental model since there would be additional damping from the water for large displacements which is not accounted for in the numerical simulation (as previously discussed). The agreement between the numerical simulations and the experimental results is described by the RMSE statistic. This is presented in Table 7.2, for the cylinder, internal mass and the relative RAO between them. These RMSE results confirm and backup the previous comments.

7.3.3 RAO for a compression mono-directional damper

The RAO against the different frequencies, for the numerical and the experimental results for the compression mono-directional damper are presented in Figure 7.9. This is for the RAO of the cylinder and the internal mass, and also for the RAO of the relative position between them.

The experimental results have a general higher value of the RAO than the numerical results, except for damper **C528**. There is a notable difference in the RAO of the cylinder and hence the relative RAO between the dampers **C113** and **C161**, where the resonant peak is at a similar frequency. The numerical damper at 500 Ns/m has virtually zero relative motion, while the

experimental model shows considerably more relative motion, which is due to the air spring effect.

The relative RAO for the numerical simulation is always positive. This is the same as the majority of damping constants except for damper **C178** where the relative RAO is negative.

The RAO against the different damping constants for both the experimental results and the numerical model is presented in Figures 7.10, 7.11 and 7.12, for the external cylinder, internal mass and the relative displacement between them.

The numerical simulation results for the compression mono-directional damper is nearly identical to the expansion mono-directional damper.

At low frequencies of 0.70 Hz – 0.72 Hz inclusive and at high frequencies of 0.84 Hz – 0.91 Hz inclusive, the experimental results of the cylinder and internal mass tend to be around the values of the numerical results, however with a lot of variability. Between these frequency ranges, the experimental results tend to be higher than the numerical results, partially due to the disparity in the resonant peak frequency.

The experimental results for the relative RAO is more evenly spread about the numerical simulation results at the lower frequencies of 0.70 Hz – 0.80 Hz, while above these frequencies the experimental results tend to be higher than the numerical results for higher damping and lower for lower damping.

All the very low damping constant numerical results are considerably higher than the equivalent experimental results. This is because it is thought that there could be a higher frictional damping component in the experimental model for large relative motions due to the spring coils coming into contact and rubbing on the central rod during these large motions.

The RMSE values for the results for the cylinder, internal mass and the relative RAO between them is presented in Table 7.3, which agrees with the points already discussed.

The RMSE values show less confidence in the relative RAO proportionally to the absolute values of RAO compared with other damper types. This is due to the compression mono-directional damper having a higher error in the prediction of the damping constants, so the experimental and numerical simulations are likely to be not comparing exactly the same damping constants.

	Compression MD RMSE		
Freq. [Hz]	**Cylinder**	**Mass**	**Relative**
0.703	0.296	0.265	0.386
0.719	0.237	0.292	0.294
0.734	0.38	0.400	0.280
0.750	0.752	0.489	0.532
0.766	0.853	0.616	0.517
0.781	0.801	0.601	0.502
0.797	0.684	0.524	0.471
0.812	0.766	0.613	0.480
0.844	0.772	0.710	0.333
0.906	0.400	0.334	0.246
Average	0.590	0.484	0.404
σ	0.237	0.155	0.109

Table 7.3: The RMSE of the RAO for the compression mono-directional damper, comparing the experimental and numerical results.

7.3.4 RAO for the endstop damper

The RAO for the cylinder and internal mass, and the difference between them is presented in Figure 7.13, for the numerical simulation and experimental results, for the endstop damper.

The numerical simulations shows that the different endstop damping constants appear to have only a small influence on the RAO.

The peak of the resonant frequency for the numerical results tends to be at c.0.65 Hz, while for the experimental results it is c.0.80 Hz. This is postulated to be due to the higher relative motion of the numerical simulation, which would result in the coupled system behaving differently and hence affecting the resonant frequency. If the results were shifted to allow the resonant peaks frequency to match, the magnitude of the cylinder and internal mass RAO would be very similar.

The relative RAO for the experimental results is always lower than the numerical simulation. This is different from all the other damper types.

The RAO is presented for the different frequencies, showing the RAO against the damping constant, in Figures 7.14, 7.15 and 7.16. This is for the RAO of the internal mass, external cylinder and the relative displacement between them.

The consistent nature of the RAO of the cylinder and the internal mass for varying damping constants, is shown for both the numerical results and the experimental model. For lower frequencies the experimental model cylinder and internal mass RAOs are lower than the numerical model, but these gradually become higher than the numerical model as the frequency increases, due to differences in the position of the resonant peak.

The relative RAO is fairly consistent for both the experimental and numerical results, with the

	Endstop RMSE		
Freq. [Hz]	**Cylinder**	**Mass**	**Relative**
0.703	0.226	1.072	1.000
0.719	0.141	0.946	0.946
0.734	0.188	0.713	0.911
0.750	0.523	0.212	0.972
0.766	0.967	0.475	0.903
0.781	1.122	0.728	0.859
0.797	1.111	0.872	0.881
0.812	1.324	1.130	0.802
0.844	0.996	0.804	0.583
0.906	0.668	0.467	0.301
Average	0.727	0.742	0.816
σ	0.437	0.289	0.215

Table 7.4: The RMSE for the endstop damper, comparing the experimental and numerical results.

experimental results always lower than the numerical simulation.

The RMSE values for the numerical and experimental results, for all the bodies and their relative RAO is presented in Table 7.4. These show a relatively high disparity between the experimental and the numerical results.

7.3.5 Comparison and further discussions

Linear and mono-directional dampers

The numerical simulations for the RAO of the expansion and compression mono-directional dampers were very similar to each other.

The displacement RAO for the cylinder and internal mass, as found by the numerical simulations, was higher for the linear damper model than for the mono-directional dampers.

The relative motion for the mono-directional damper is slightly greater than for the equivalent linear damper. It would be expected that the mono-directional dampers have a greater relative motion than the linear dampers, since they only experience a damping force over approximately half of their expansion and compression cycle. The reason for higher relative motion is that the velocity is higher for the mono-directional dampers than for the linear dampers, due to having the expansion or compression of the damper free from damping forces. This is illustrated in Figure 7.17.

The average RMSE can be used as an indicator of which damper were best represented by the numerical simulation; this showed that the mono-directional dampers had slightly lower average RMSE values for the cylinder and the internal mass than the other damper types. However, for the relative RAO, the linear damper had a significantly lower average RMSE

than the mono-directional dampers. The expansion mono-directional damper, had a slightly lower average RMSE than the compression mono-directional damper. The compression mono-directional damping constants have the largest error associated with them, so this larger experimental and numerical difference can be expected. As the RMSE statistic can be used to give an indication if the numerical simulations are accurately fitting the experimental data, alongside visual inspection, therefore, it implies that the linear damper is most accurately represented by the numerical simulation.

The numerical simulations for different frequencies have different resonant peaks, especially at the low frequencies. This occurred for both the linear and mono-directional dampers. The reason for this is postulated that the coupled effect of the cylinder and the internal mass results in changing the frequency of the resonant peak. This was much less prevalent, although there was some small variations, in the experimental model.

Endstop damper

The endstop damper does not seem to have a significant effect on the displacement of the cylinder or the internal mass, and only a limited effect on the relative displacement between them. This could be due to the wave height not being high enough to allow the endstop damper to have a lot of contact and therefore influence on the internal mass and hence the cylinder.

The endstop damper RMSE are much lower than for the other types of dampers, due to the large but constant difference in the RAOs.

7.4 Relative phase in regular seas

The relative phase is the angular position between the cylinder and the internal mass, and in theory, could be between $-\pi$ and π. The relative phase is a property of interest, since according to linear theory (Falnes, 1999), when the relative velocity and acceleration are in phase the optimal power extraction occurs.

The relative phase potentially increases the power extracted from the device, because with larger relative phases, the model has larger relative velocities between the internal mass and the cylinder.

The relative phase was calculated by finding the maximum positions for both the cylinder and the internal mass. The time difference between these maximum positions was then recorded for each wave cycle, after the initial transients had decayed. These values were then averaged for each experimental run.

7.4.1 Linear and mono-directional dampers

The relative phase between the cylinder and the internal mass has been calculated. This has been presented in Figures 7.18 and 7.19, for the linear and mono-directional dampers, for the predefined frequencies.

There are jumps between discrete values in the relative phase, for both the experimental model and the numerical simulation, because the results were recorded at 32 Hz, so the jumps are due to the positions of the bodies only being recorded every $\frac{1}{32}$ seconds. This discretization of the data results in errors in the analysis since the size of the time step between data points is a similar magnitude to the maximum relative phase time difference between the different damper types. This means that the maximum error for each relative phase presented is $\frac{1}{16}$ seconds and this should be considered in the following analysis and comparison.

All the results for the numerical calculation of the relative phase are negative or zero, this means that the internal mass is always leading (or equal to) the cylinder . This is in comparison to the experimental results, where the mass is leading or equal to the cylinder for between 82% and 88% of the time (see Table 5.6).

The numerical results show that across the frequency range of interest, the linear damper generally has the lowest magnitude of relative phase, with the mono-directional dampers having a higher magnitude relative phase. The compression mono-directional damper has a higher relative phase than the expansion mono-directional damper.

Comparing the linear dampers numerical simulation and experimental results shows that between 100 Ns/m and 500 Ns/m there is reasonable agreement, across the frequency range. For the lower damping constants, the numerical simulations has a higher relative phase than the experimental results. The exceptions to this, are the higher frequency results, 0.85 Hz and 0.90 Hz were the experimental results are mainly zero while the numerical simulation are non-zero relative phase.

The numerical simulation and the experimental results for the expansion mono-directional damper are closest for a damping constant of between 200 Ns/m and 500 Ns/m, and within this range the tendency of the experimental results are to be lower than the numerical simulation. Lower damping constants result in a bigger disparity, with the experimental simulation predicting a higher relative phase than the experimental results. These results were approximately constant over the entire frequency range.

The compression mono-directional damper's numerical simulation was generally higher than the experimental results. This was most significant for lower frequencies (less than 0.75 Hz) and higher frequencies (greater than 0.81 Hz). The central frequencies, although on average slightly lower than the numerical simulation results, were closer particularly in the range of 150 Ns/m to 500 Ns/m, and noticeably lower outside this range. Outside this central frequency range, the experimental results were considerably lower than the numerical simulation. Generally, the

	Damper type			
Freq. [Hz]	**Linear**	**Expansion MD**	**Compression MD**	**Endstop**
0.703	0.261	0.429	0.544	0.379
0.719	0.241	0.465	1.034	0.304
0.734	0.323	0.472	0.568	0.370
0.750	0.342	0.506	0.676	0.354
0.766	0.363	0.500	0.663	0.292
0.781	0.363	0.534	0.691	0.359
0.797	0.434	0.583	0.631	0.415
0.812	0.317	0.550	0.833	0.488
0.844	0.448	0.695	0.808	0.662
0.906	0.344	0.620	0.879	1.058
Average	0.343	0.535	0.733	0.468
σ	0.065	0.080	0.153	0.219

Table 7.5: The RMSE for the relative phase, for all damper types.

compression mono-directional damper performed the worse of the three dampers in matching the experimental model to the numerical simulation results, although the errors in the damping constant are highest for this damper type.

There is a difference between the numerical and experimental results for the three damper types, particularly at the lower damping constants when the numerical simulation predicted a relative phase that is much larger than the experimental model. This could be due to additional damping in the experimental model when large differences in the displacement of the internal mass and the cylinder occur.

The RSME for the relative phase for all the types of damping is presented in Table 7.5. When only the magnitudes of the relative phase are considered, the RMSE results are presented in Table 7.6. The reason why this table presents results from the magnitude only without consideration to the sign, is that the power captured is not directly affected by the sign of the relative phase. These results shows that the linear damper had the closest agreement between the experimental and numerical results. The endstop damper also have a high agreement. The mono-directional dampers, although not as high a level of agreement as the linear and endstop dampers, still have a good level of agreement, with the expansion mono-directional damper performing better than the compression mono-directional damper.

	Damper type			
Freq. [Hz]	**Linear**	**Expansion MD**	**Compression MD**	**Endstop**
0.703	0.231	0.256	0.329	0.270
0.719	0.205	0.256	0.538	0.251
0.734	0.222	0.284	0.352	0.326
0.750	0.156	0.249	0.278	0.288
0.766	0.212	0.264	0.381	0.292
0.781	0.200	0.295	0.429	0.296
0.797	0.236	0.340	0.448	0.351
0.812	0.244	0.358	0.365	0.401
0.844	0.304	0.333	0.516	0.438
0.906	0.260	0.450	0.596	0.895
Average	0.227	0.309	0.423	0.381
σ	0.039	0.063	0.101	0.190

Table 7.6: The RMSE for the magnitude of the relative phase, for all damper types.

7.4.2 Endstop dampers

The relative phase for the endstop dampers, for the numerical simulation and the experimental results is presented in Figure 7.20.

The relative phase of the endstop dampers for the numerical simulation was always zero or negative, the internal mass was either in phase with the external cylinder or leading it.

The numerical simulation had a larger relative phase for the lower damping constants compared to the higher damping constants. Higher frequency waves resulted in higher relative phase and especially at low damping constant.

Comparing the numerical simulation and the experimental results shows that the experimental results consistently are lower than the numerical simulation. They are closer for the central frequencies and for higher damping constants, but the agreement is worse for low damping constants.

7.5 Power extraction in regular waves

The power extracted for the numerical simulation is calculated for the different damper types and the power capture ratio or efficiency is obtained. The wave height in the numerical simulation for the different frequency waves is 0.2 m.

The predicted power extraction from the numerical simulation was generally greater than the experimental model, so the following figures only include the numerical simulations. The discussion considers both the numerical simulation and associated experimental results.

The difference between the experimental and numerical simulation results are due to the relative velocity being greater for the numerical simulation, and since the power is proportional to the square of this value, the power is much greater. The reasons why the relative velocity is greater are due to a combination of:

- The experimental model velocities were obtained from the displacement position data. Within this data there were also vibrations, uncertainty and error, which were amplified when the difference of the data points was used to calculate the velocities. A significant source of these variations were from the light rod that attaches the marker balls to the internal mass would sometimes interact with the upper base of the cylinder. This is demonstrated in Figure 7.21, were the impacts with the cylinder are clearly seen at 11 and 17 seconds. The variations resulted in large jumps and significant variation in the velocity data, which had considerable variation in both magnitude and sign.
- The relative displacements are small, so errors are a more significant proportion of the results than if the displacements were larger.
- The velocities were smoothed with a low pass filter, a 10 point moving average filter was used. This attempted to remove some of the error and fluctuations from the signal. However, it also decreased the average velocity.
- There could also be inaccuracies in calculating when the mono-directional dampers are producing a damping effect or not, in the experimental model.

7.5.1 Linear and mono-directional dampers

The power extracted efficiency against the damping constant, for the linear, and both mono-directional dampers is presented in Figure 7.22, for the numerical simulation.

The numerical simulations show that the mono-directional dampers extract approximately the same power regardless of the direction that they operate. This may not originally have been expected, since the RAOs are very nearly identical and the relative phase difference although small is not negligible.

For low damping constants, the linear damper extracts more power, while for higher damping constants, the mono-directional dampers extract more. The absolute maximum power extracted is slightly higher for the linear damper than the mono-directional dampers, across the frequency range. As was discussed in Section 7.3.5, the power extracted from the mono-directional dampers is comparable to the linear damper, and greater for some damping constants, since although the mono-directional dampers do not extract energy over the entire time period, they do allow the relative velocity of the internal mass compared to the cylinder to be higher, leading to a greater power extraction when the damper is extracting power.

In comparison to the experimental results, the power extracted is higher, therefore a direct comparison with the power capture efficiency would be difficult to justify. However, it is

	Linear		Expansion MD		Compression MD	
Freq. [Hz]	Damping constant [Nm/s]	Power capture ratio	Damping constant [Nm/s]	Power capture ratio	Damping constant [Nm/s]	Power capture ratio
0.703	30	1.07	60	1.00	60	1.01
0.719	35	1.31	90	1.20	90	1.22
0.734	45	1.50	90	1.40	90	1.37
0.750	50	1.74	120	1.62	120	1.60
0.766	60	2.09	150	1.89	150	1.90
0.781	90	2.48	180	2.22	210	2.22
0.797	120	3.21	270	2.82	270	2.83
0.813	180	4.25	450	3.72	450	3.76
0.844	600	8.88	100	7.94	1000	7.76
0.910	150	2.12	420	2.21	390	2.15

Table 7.7: The values of maximal damping for the linear and mono-directional dampers, from the numerical simulation.

interesting to compare the relative magnitude of the power extraction with respect to the different damping constants, although there would be some uncertainty in this analysis.

There is some similarity in the shape of the experimental and numerical power extraction, considering the experimental data points from Chapter 5. There are indications in the experimental results of an initial increase in the power for increased damping and a gradual decline in the power as the damping constant increases further, as seen in the numerical simulation.

The damping constants at the maximum power extraction, and the associated power extraction efficiency, for the numerical simulations, are presented in Table 7.7, for the linear and mono-directional dampers.

7.5.2 Endstop dampers

The power is extracted when using the endstop damper setup from both the endstop damper and the linear frictional damping. In this section these are presented both separately and combined together.

These results for the power capture efficiency against the endstop damping constant, for the different frequencies, are presented in Figure 7.23.

For all the frequencies in the numerical simulation, the endstop damper power extraction shows a rapid increase in the power extracted for increasing damping constant up to a maximum value and than a gradual decline for further increases of the damping constant.

The power extracted from the linear damping in the numerical simulation within the endstop damping setup is very frequency dependent. This frequencies dependency is related to the amplitude of the cylinder motion, so when the cylinder has a high RAO due to being at or near

resonance, then the relative RAO tends to be higher, therefore the internal mass is more likely to be in contact and influenced by the endstop damper. For low frequencies (0.70 Hz & 0.72 Hz) the power extracted reduces as the damping constant increases, at 0.73 Hz and 0.90 Hz it stays approximately constant. All the other frequencies experience an increase in the power captured for increasing damping constant.

The linear damping component of the combined power extraction contributes at least two thirds of the combined power extraction, in the numerical simulation. All, but the 0.70 Hz frequency waves, have an increase in power extraction for larger damping constants.

Comparing the shape of the numerical and experimental results shows that there are some similarities. The proportion of the linear and the endstop damping within the combined power extraction tends to be quite similar. The experimental model is also not highly influenced by the changing damping constant.

7.6 Power extraction in irregular waves

The results for the PM spectrum sea, from both the numerical simulation and the experimental model are presented in this section. The phases, magnitudes and the frequency range of the sea spectrum, for the experimental and numerical models are not the same, but they both produce a PM spectrum sea. Therefore over the repeat period of the waves, the power output can be compared.

The power captured is calculated in the numerical simulation for damping constants of 0 – 200 Ns/m in 30 Ns/m intervals, and 260 – 1000 Ns/m in 60 Ns/m intervals.

7.6.1 Linear dampers

The power captured from the numerical simulation and the experimental results are presented in Figure 7.24 for the linear damper.

The numerical simulation shows that the power extracted, for all the different peak frequencies, show a similar pattern. It increases from zero power capture at zero damping constant, increases rapidly towards a maximum and then reduces in a steady decline.

The numerical simulations are a similar shape although slightly larger in magnitude to the experimental results. This allows us to have a high confidence in the changing effect of the variable damping constant on the power extracted.

7.6.2 Mono-directional dampers

The power capture for the expansion mono-directional damper is presented in Figure 7.25, and in Figure 7.26 for the compression mono-directional damper. These are for both the numerical simulations and the experimental model.

The numerical simulation of the expansion and compression mono-directional dampers have a virtually identical power capture for the same damping constants.

The experimental results variation with the damping constant is in a similar pattern to the numerical simulation, with the exception being the large damping constants on the experimental model, where the air spring effect is prevalent.

The approximate agreement of the experimental and numerical allows us to have some confidence in both models and therefore can use a combination of the two different types of model to predict the behavior and power extraction of a full scale device.

7.6.3 Endstop dampers

The power captured from the endstop damper setup in the numerical simulation is much higher than the equivalent experimental model, therefore the experimental results have not been presented in this chapter, but have previously been presented in Chapter 6. This is probably due to the increased inaccuracies in the power captured due to the small motions of the internal mass when it was in contact with the endstop damper and not knowing in the experimental setup the exact SWL position of the internal mass within the cylinder.

The power captured in Watts for the numerical simulation, for the PM spectrum seas with variably peak frequency, is presented in Figure 7.27 for the power extracted only from the endstop damper, in Figure 7.28 for the power extracted only from the linear frictional damping and in Figure 7.29 for these two damping components combined. They are presented in seperate figures for clarity.

The power captured from the endstop damper increases from zero for zero damping, to a gradual increase for higher damping constants. The changing PM spectrum sea peak frequencies affects the size but not the shape of the variations of power extracted with the damping constant.

The power captured from the linear component of the endstop damper setup, has a finite value for zero endstop damping and reduces slowly for increased endstop damping constant. This is the same across the range of peak frequencies of the PM spectrum sea.

The endstop damper power extraction contributes less total power extracted compared to the linear damper. The combination of the two methods of power extraction results in a total power capture being slightly increased by the increasing endstop damping constant.

7.6.4 Discussions

The linear damper has been shown to have the greatest absolute power extraction in a variety of different peak frequency PM spectrum seas for the same spring constant. However, the mono-directional dampers have a higher power extraction than the linear damper for a wider range of damping constants and the decline in the power extraction for changing damping constant is less.

The similarities in the power extracted from the linear and the mono-directional dampers implies that the most effective way for a device developer to obtain power from their WEC is not necessarily by extracting power over the entire time period, especially if a mono-directional device is cheaper.

How a WEC responds in a PM spectrum sea is a more realistic measure of how a full sized WEC would respond in the real ocean. Therefore the power extracted from this PM spectrum sea is a more likely indicator of the potential power of a full scale device, than monochromatic wave testing.

The endstop damper, a damper which only extracts energy at the peripherals of the relative motion has advantages for obtaining extra power from the device. Having this supplementary damper of any damping constant was seen to increase the overall power extraction. Additional advantages are that the endstop damper could be connected to the survivability strategies of the WEC and the power rating on the linear damper could also potentially be lower, which would reduce the costs, in both the damper and associated power electronics. Although the disadvantages of such a system would be the costs and weight of the additional endstop dampers.

7.7 Conclusions of chapter

In this chapter results are presented and experimental and numerical results for the RAO, relative phase and power extraction are compared in both regular and irregular waves.

The RAO for the cylinder, internal mass the relative displacement between them has some agreement between the experimental results and the numerical simulation, shown in Figures 7.1 – 7.12. This agreement was reduced in instances when the resonant peak of the numerical simulation was influenced by the damping constant of the linear or mono-directional damper, which the experimental model was less affected by. The linear dampers tended to have a slightly higher relative RAO than the mono-directional dampers. The mono-directional dampers had virtually the same RAO regardless of the direction that they operated.

The RAOs when the endstop damper was used were not highly affected by the endstop damping constant, and the agreement between the numerical and experimental results was not very strong. Although the RAOs results were consistent for all the bodies for the numerical and experimental models.

The relative phase of the internal mass and the cylinder is linked to the potential power extracted. For the numerical simulation, for the linear and mono-directional dampers, the internal mass was always the same as or leading the cylinder. In the experimental results the internal mass was zero or leading in the majority of instances. There was a relatively close agreement in the magnitude of this phase, although the numerical simulation always predicted greater relative phase for low damping constants.

The relative phase for the endstop dampers was either zero or the internal mass was leading the cylinder for the numerical simulation and the majority of the experimental model. The numerical simulation tended to predict a larger relative phase than the experimental results, especially at low damping constants.

The power captured in regular waves from the linear and mono-directional dampers for the numerical simulation was considerably higher than for the experimental model. This was mainly due to errors and fluctuations in the experimental model in the displacements due to the small relative motions which became amplified in obtaining the relative velocity and further increased when the relative velocity was squared to obtain the power. However, the general trend of the power extraction compared with the damping constant showed some similarities between the experimental and numerical results. The maximum power extracted was higher for the linear damper than the mono-directional dampers, although the mono-directional dampers had a higher power extraction over a large range of damping constants. This is due to the mono-directional dampers allowing the relative velocities to increase during non-damped motion.

The power captured in regular waves from the endstop damper was split into the power from the linear frictional component, the endstop damper directly and a combination of these two power extraction mechanisms. These showed that although by having the endstop damper present, the linear power extraction sometimes decreased in certain frequency waves, the overall power extraction was higher in all frequency waves.

In PM spectrum seas, the power extracted tended to have the maximum power extraction for the optimal damping constant for the linear damper compared to the mono-directional dampers. However, over the majority of the damping constants tested, the mono-directional dampers had a greater power extraction.

The power extracted from the endstop damper setup in PM spectrum seas showed an optimal damping constant for power extraction, from the numerical results, if the endstop damper was the only method of obtaining power. The linear frictional damping component was the most significant contribution to the amount of power extracted and as such had the most influence on the overall power extraction, however, in all seas, the power extracted was increased with having an endstop damper present. This could be considered to be a peripheral damper to aid power extraction in higher energy sea states, whilst allowing a low rated power extraction method for lower energy sea states. It could potentially also be incorporated into the survival

strategy for very high energy sea states.

7.8 Figures

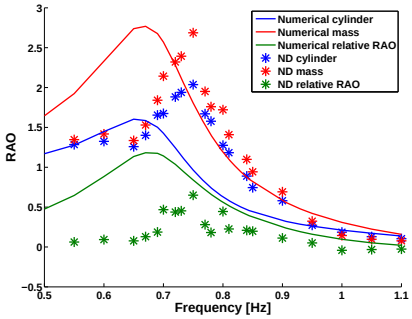

(a) 0 Ns/m

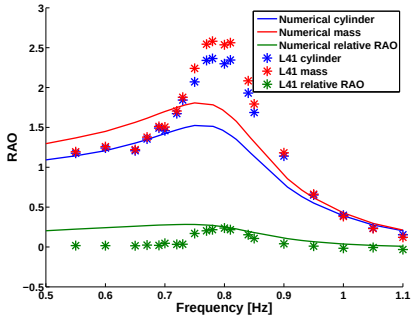

(b) 40 Ns/m

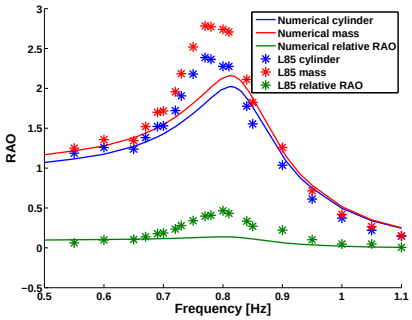

(c) 80 Ns/m

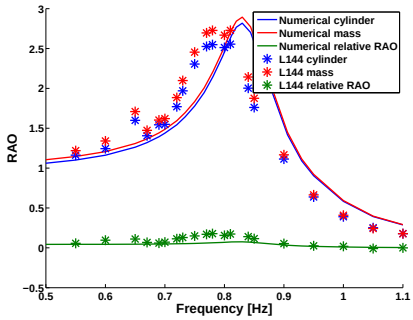

(d) 140 Ns/m

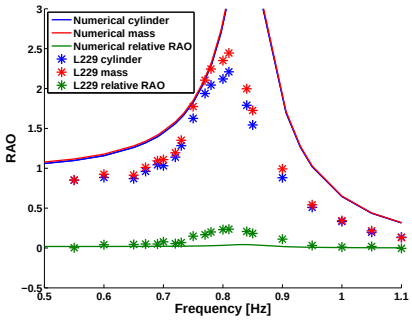

(e) 230 Ns/m

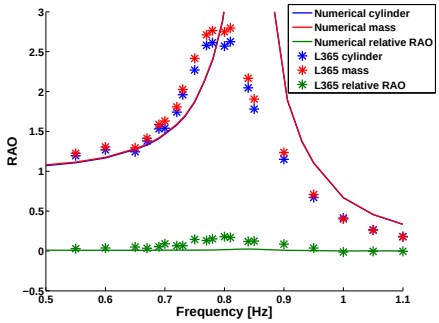

(f) 360 Ns/m

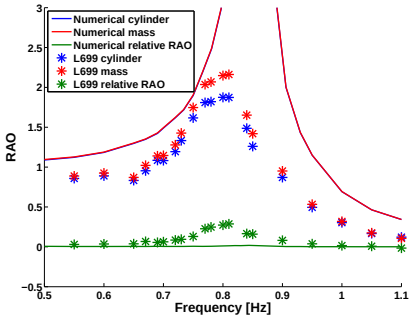

(g) 500 Ns/m

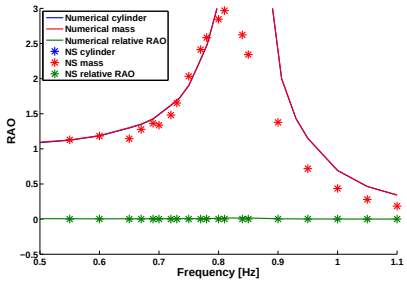

(h) 500 Ns/m

Figure 7.1: The RAO for both the numerical simulation and the experimental model, for linear dampers.

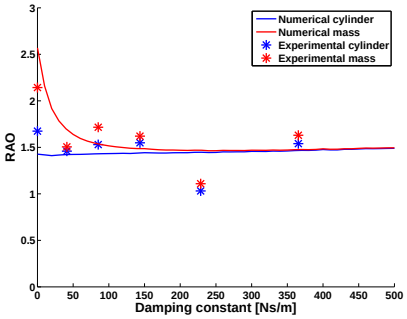

(a) 0.703 Hz, cylinder and mass.

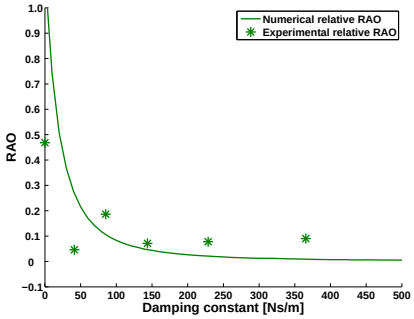

(b) 0.703 Hz, relative position.

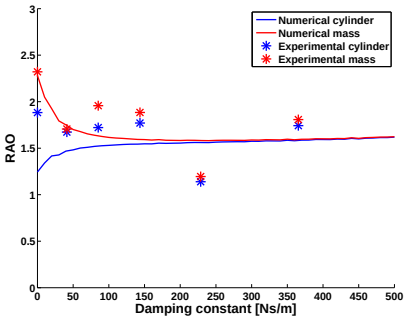

(c) 0.719 Hz, cylinder and mass.

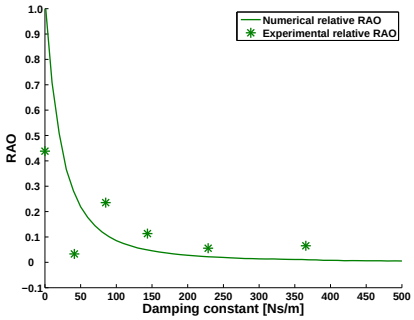

(d) 0.719 Hz, relative position.

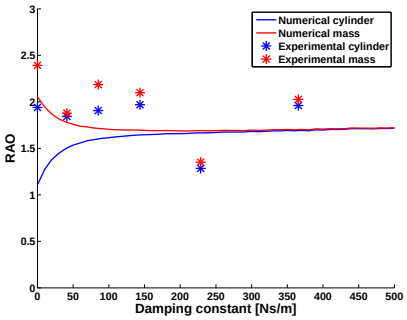

(e) 0.734 Hz, cylinder and mass.

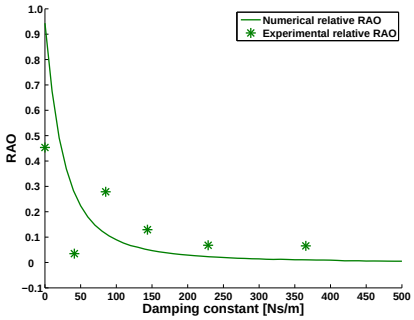

(f) 0.734 Hz, relative position.

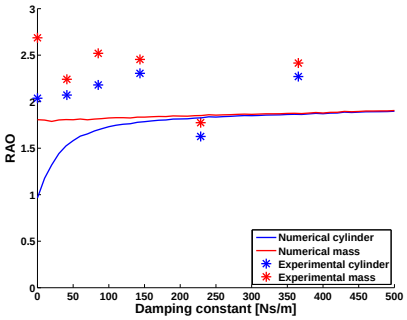

(g) 0.750 Hz, cylinder and mass.

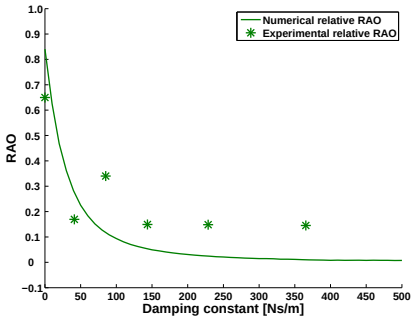

(h) 0.750 Hz, relative position.

Figure 7.2: Numerical and experimental RAO of the cylinder, mass and their relative motion, with a linear damper: 0.703 Hz to 0.750 Hz.

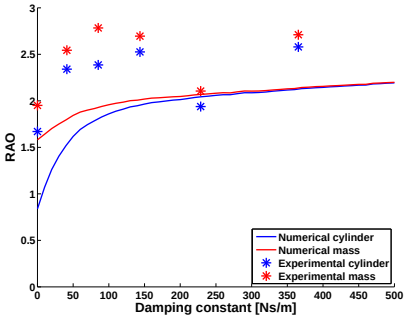

(a) 0.766 Hz, cylinder and mass.

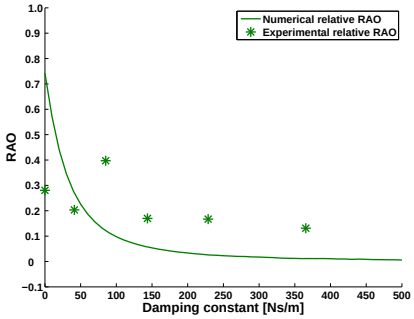

(b) 0.766 Hz, relative position.

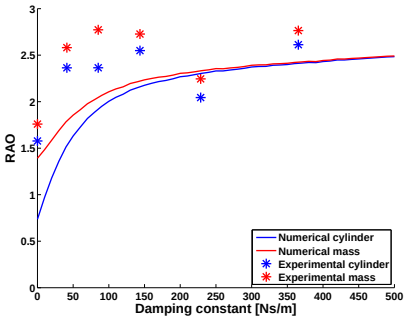

(c) 0.781 Hz, cylinder and mass.

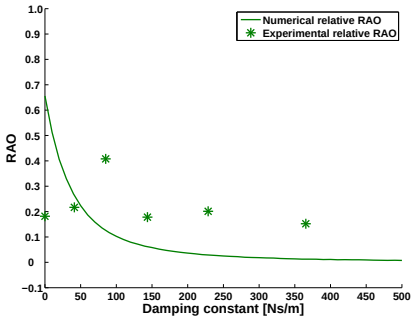

(d) 0.781 Hz, relative position.

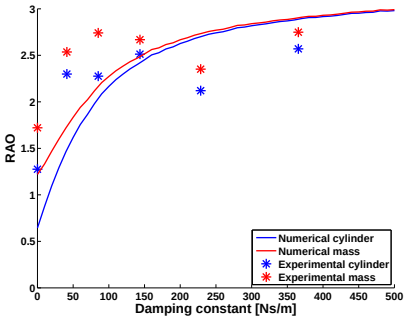

(e) 0.797 Hz, cylinder and mass.

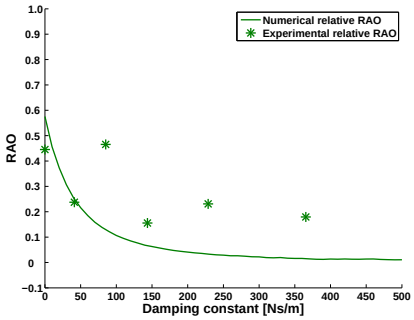

(f) 0.797 Hz, relative position.

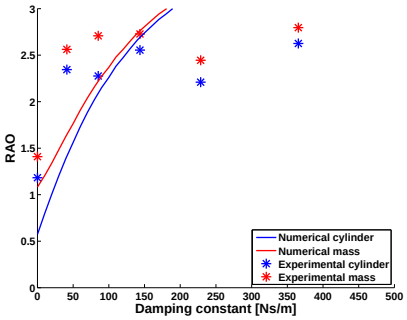

(g) 0.812 Hz, cylinder and mass.

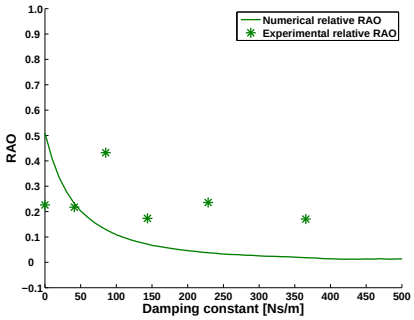

(h) 0.812 Hz, relative position.

Figure 7.3: Numerical and experimental RAO of the cylinder, mass and their relative motion, with a linear damper: 0.766 Hz to 0.812 Hz.

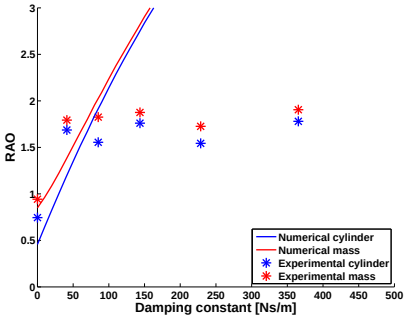

(a) 0.844 Hz, cylinder and mass.

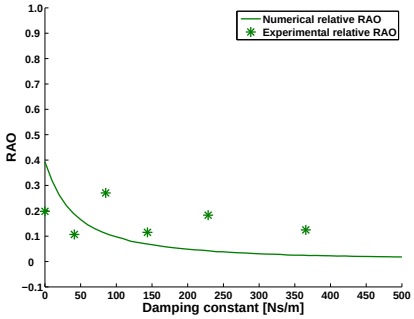

(b) 0.844 Hz, relative position.

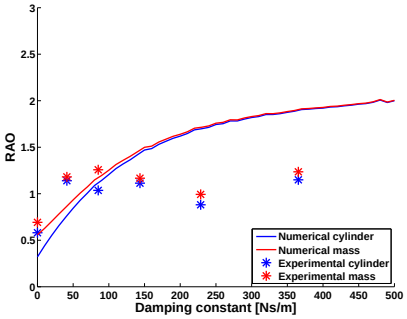

(c) 0.906 Hz, cylinder and mass.

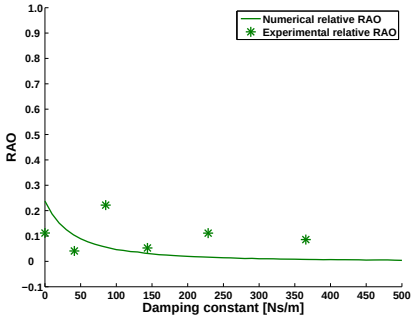

(d) 0.906 Hz, relative position.

Figure 7.4: Numerical and experimental RAO of the cylinder, mass and their relative motion, with a linear damper: 0.844 Hz to 0.906 Hz.

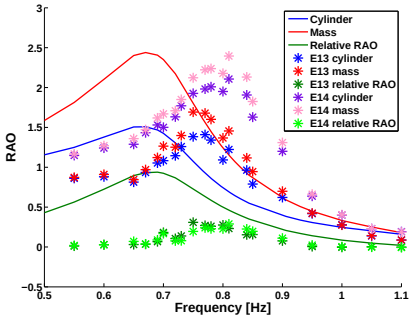

(a) 10 Ns/m

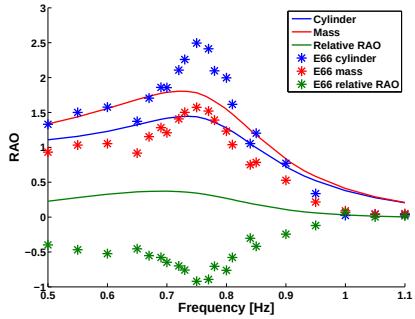

(b) 70 Ns/m

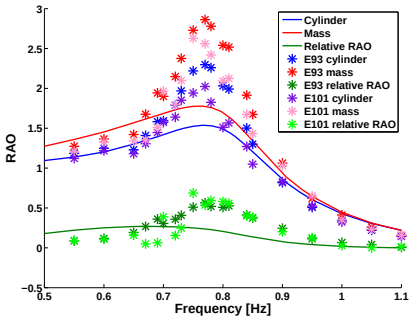

(c) 100 Ns/m

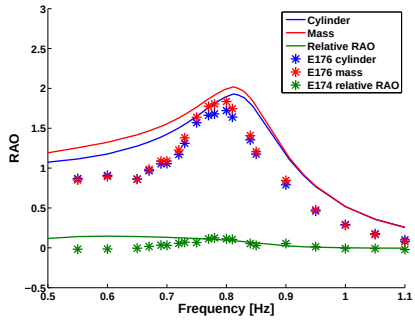

(d) 180 Ns/m

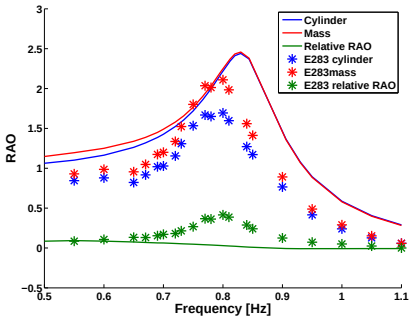

(e) 280 Ns/m

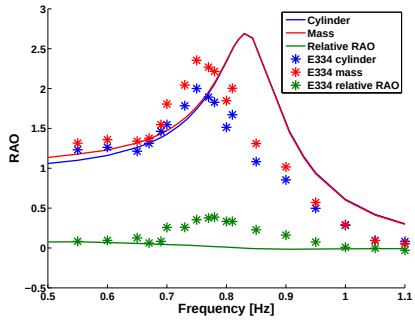

(f) 330 Ns/m

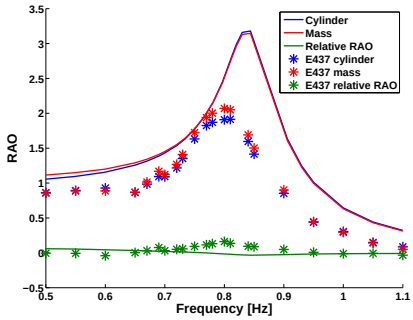

(g) 440 Ns/m

Figure 7.5: The RAO for both the numerical simulation and the experimental model, for an expansion mono-directional dampers.

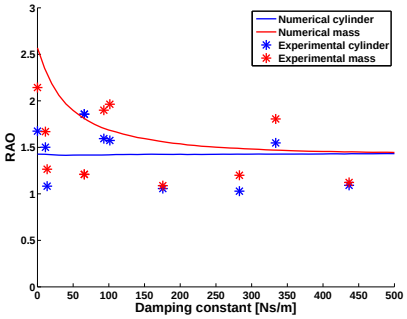

(a) 0.703 Hz, cylinder and mass.

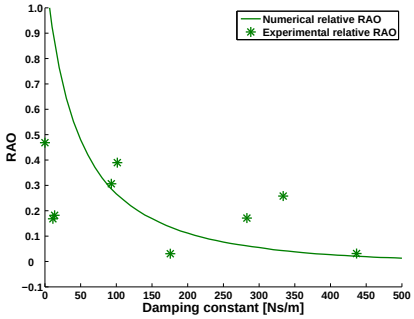

(b) 0.703 Hz, relative position.

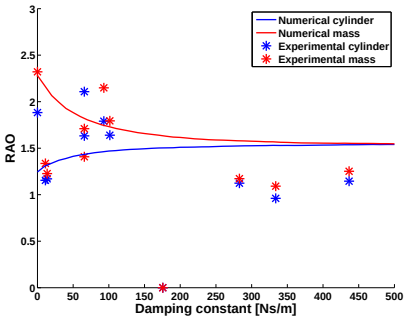

(c) 0.719 Hz, cylinder and mass.

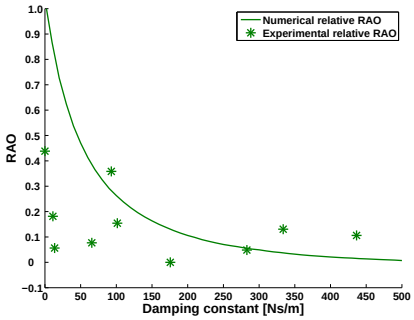

(d) 0.719 Hz, relative position.

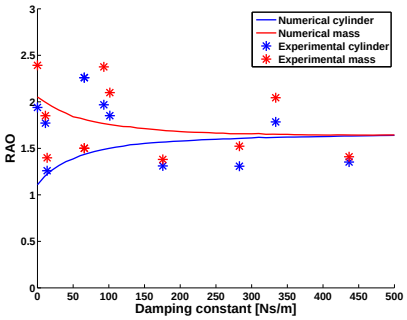

(e) 0.734 Hz, cylinder and mass.

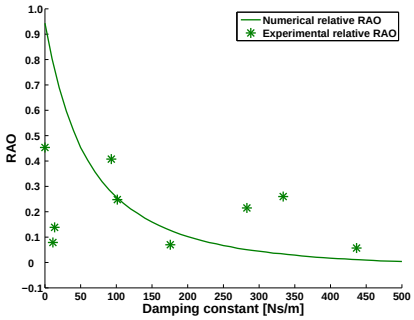

(f) 0.734 Hz, relative position.

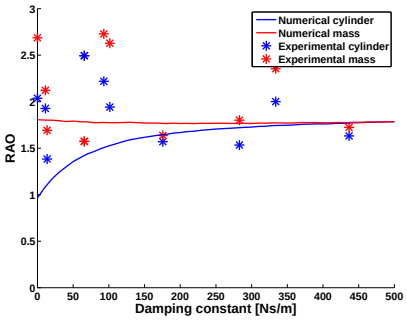

(g) 0.750 Hz, cylinder and mass.

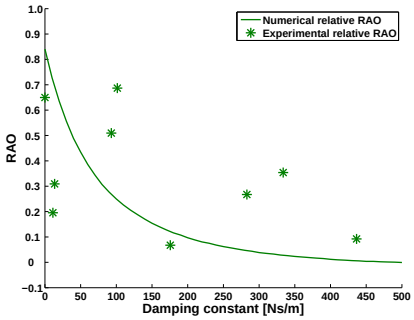

(h) 0.750 Hz, relative position.

Figure 7.6: Numerical and experimental RAO of the cylinder, mass and their relative motion, with an expansion mono-directional damper: 0.703 Hz to 0.750 Hz.

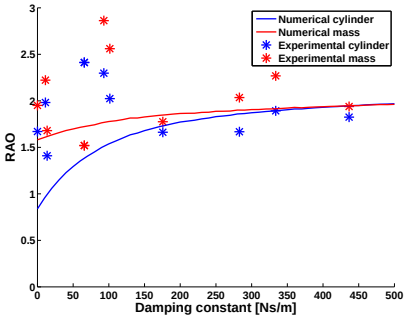

(a) 0.766 Hz, cylinder and mass.

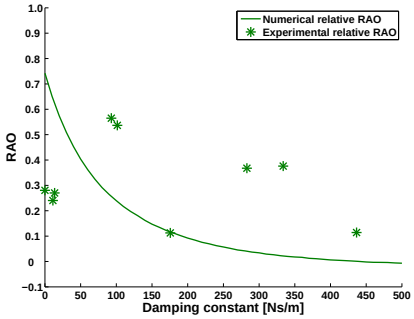

(b) 0.766 Hz, relative position.

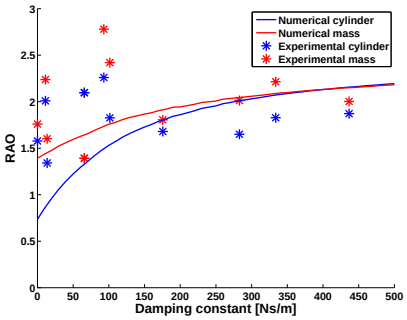

(c) 0.781 Hz, cylinder and mass.

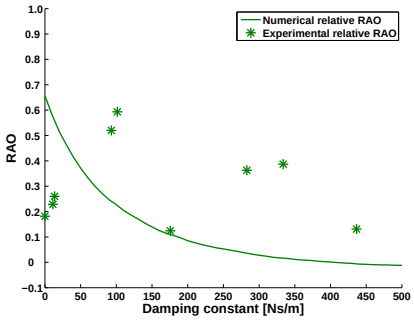

(d) 0.781 Hz, relative position.

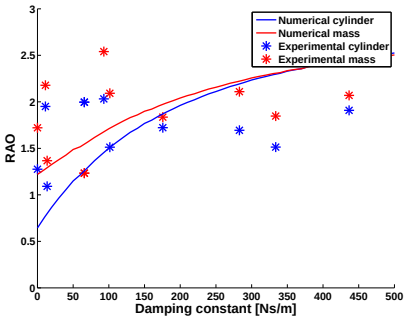

(e) 0.797 Hz, cylinder and mass.

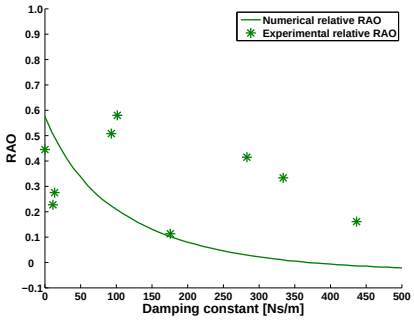

(f) 0.797 Hz, relative position.

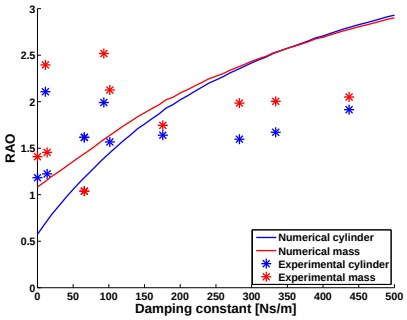

(g) 0.812 Hz, cylinder and mass.

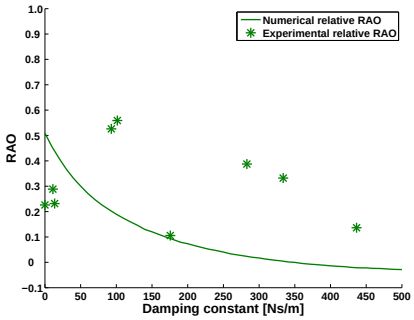

(h) 0.812 Hz, relative position.

Figure 7.7: Numerical and experimental RAO of the cylinder, mass and their relative motion, with an expansion mono-directional damper: 0.766 Hz to 0.812 Hz.

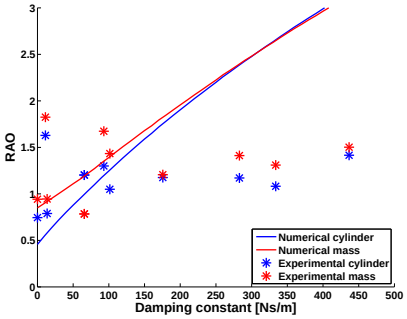

(a) 0.844 Hz, cylinder and mass.

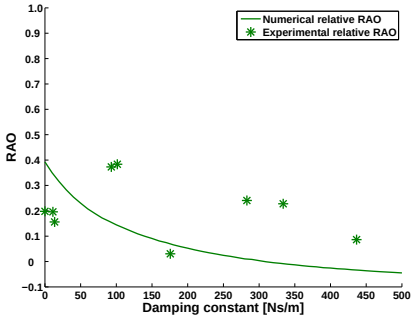

(b) 0.844 Hz, relative position.

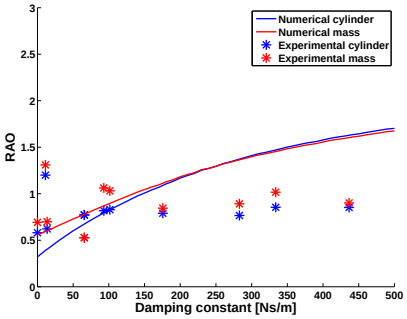

(c) 0.906 Hz, cylinder and mass.

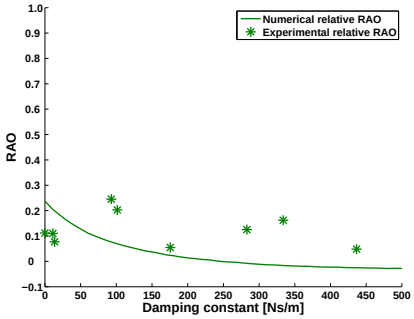

(d) 0.906 Hz, relative position.

Figure 7.8: Numerical and experimental RAO of the cylinder, mass and their relative motion, with an expansion mono-directional damper: 0.844 Hz to 0.906 Hz.

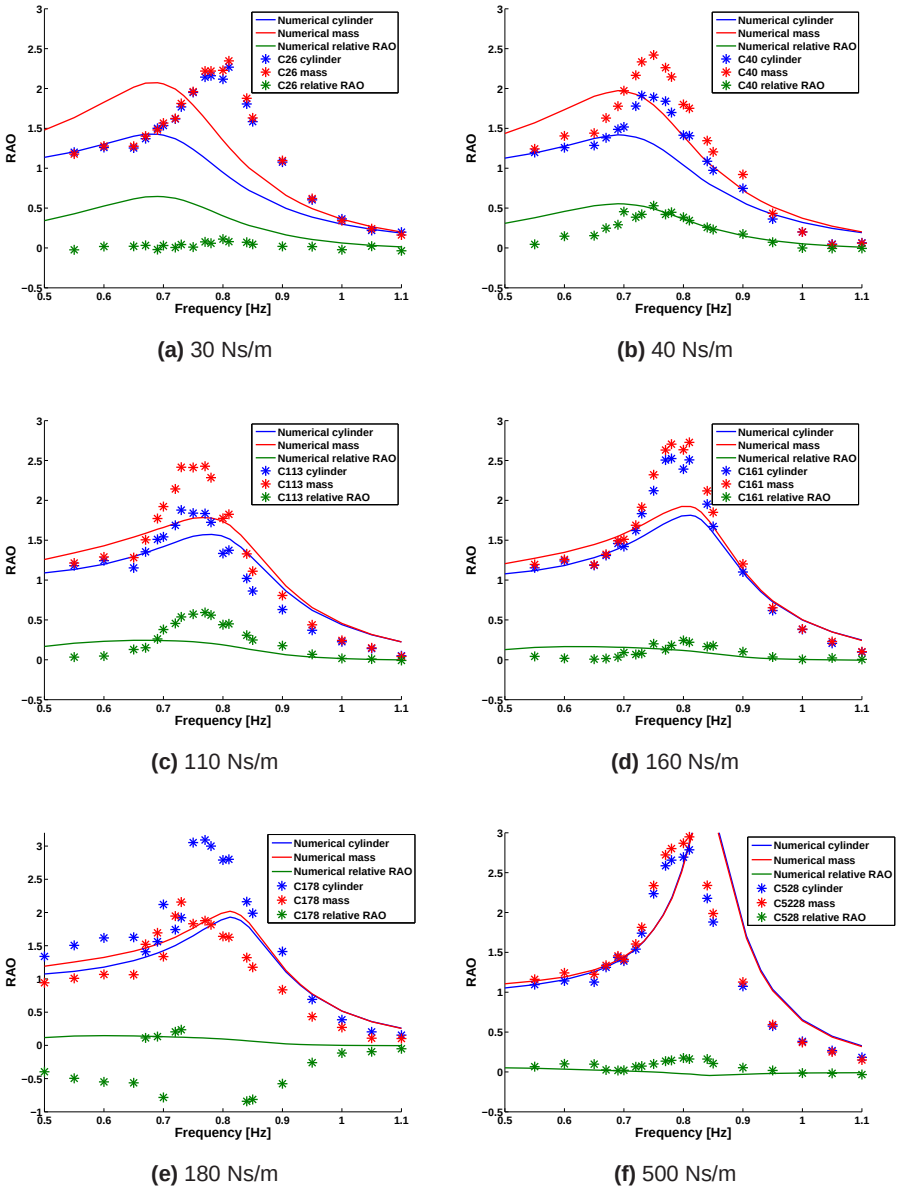

(a) 30 Ns/m **(b)** 40 Ns/m

(c) 110 Ns/m **(d)** 160 Ns/m

(e) 180 Ns/m **(f)** 500 Ns/m

Figure 7.9: The RAO for both the numerical simulation and the experimental model, for a compression mono-directional dampers.

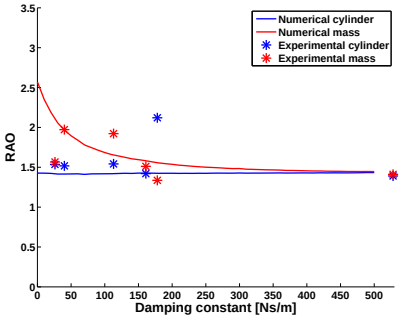

(a) 0.703 Hz, cylinder and mass.

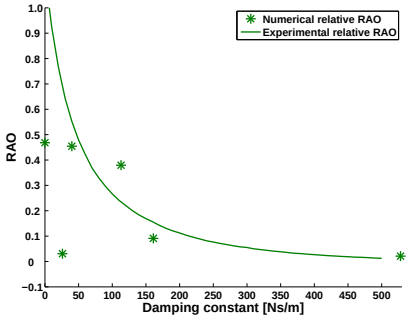

(b) 0.703 Hz, relative position.

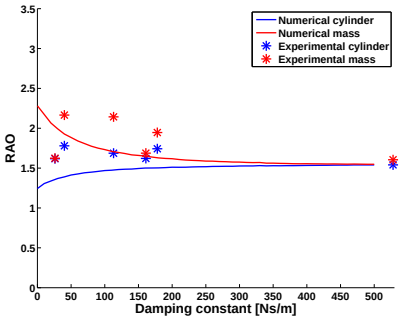

(c) 0.719 Hz, cylinder and mass.

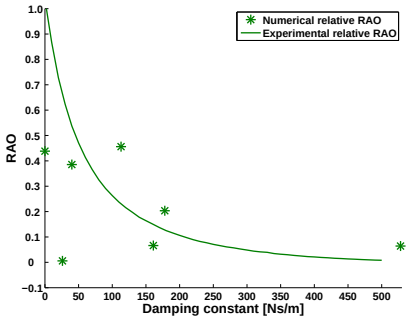

(d) 0.719 Hz, relative position.

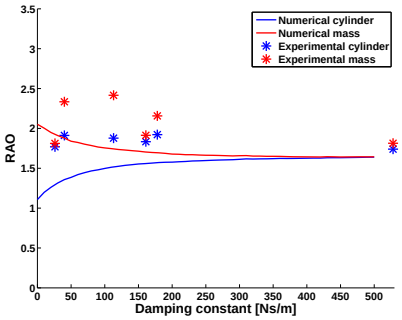

(e) 0.734 Hz, cylinder and mass.

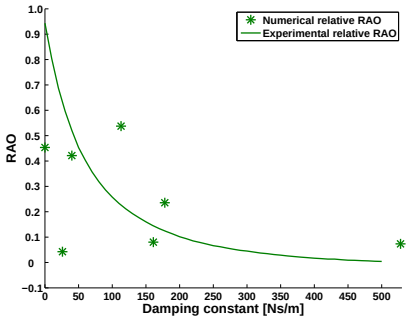

(f) 0.734 Hz, relative position.

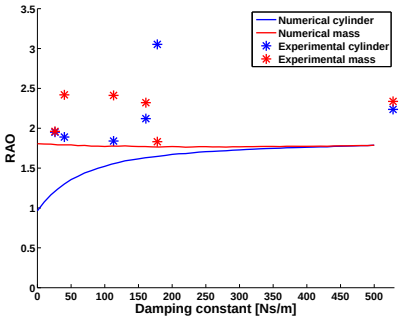

(g) 0.750 Hz, cylinder and mass.

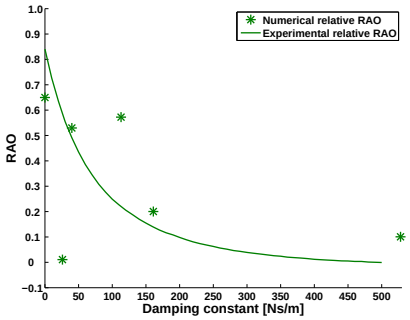

(h) 0.750 Hz, relative position.

Figure 7.10: Numerical and experimental RAO of the cylinder, mass and their relative motion, with a compression mono-directional damper: 0.703 Hz to 0.750 Hz.

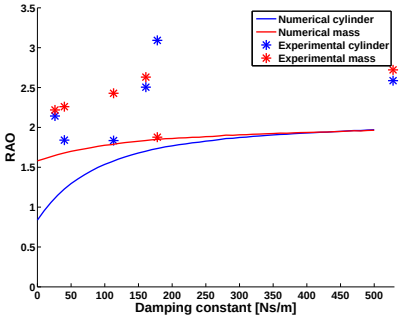

(a) 0.766 Hz, cylinder and mass.

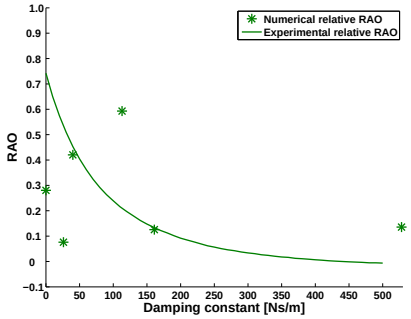

(b) 0.766 Hz, relative position.

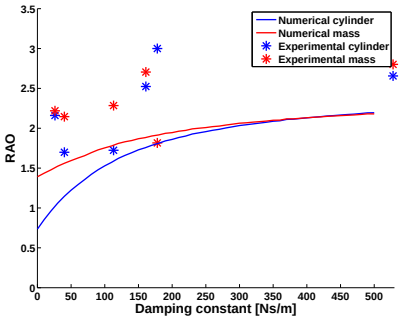

(c) 0.781 Hz, cylinder and mass.

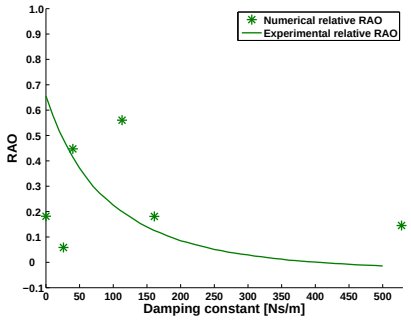

(d) 0.781 Hz, relative position.

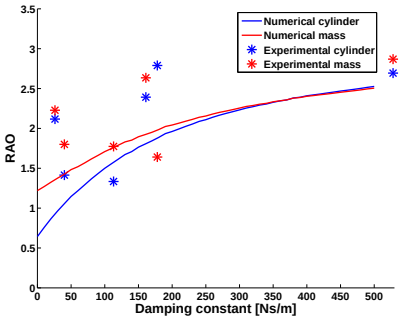

(e) 0.797 Hz, cylinder and mass.

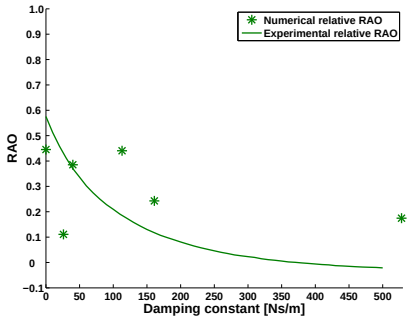

(f) 0.797 Hz, relative position.

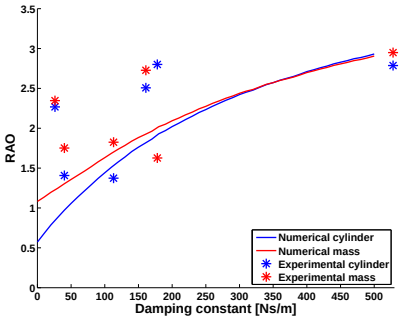

(g) 0.812 Hz, cylinder and mass.

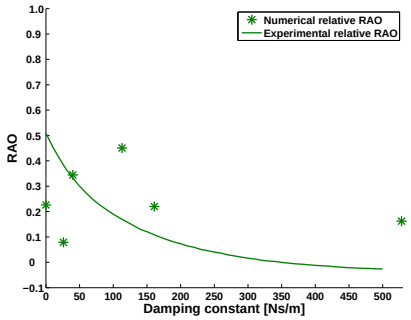

(h) 0.812 Hz, relative position.

Figure 7.11: Numerical and experimental RAO of the cylinder, mass and their relative motion, with a compression mono-directional damper: 0.766 Hz to 0.812 Hz.

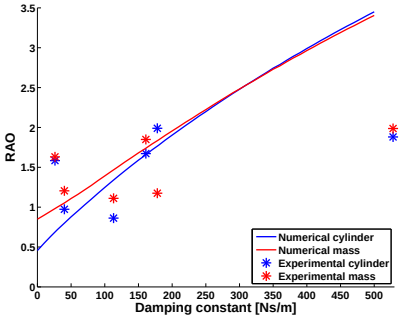

(a) 0.844 Hz, cylinder and mass.

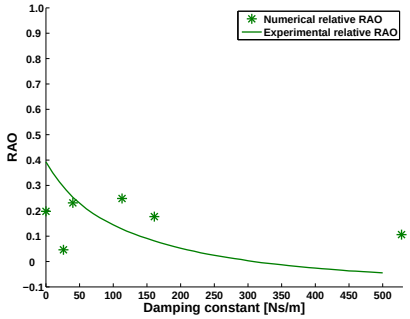

(b) 0.844 Hz, relative position.

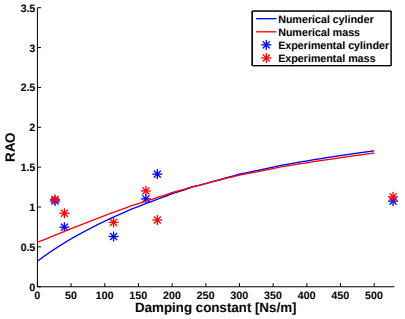

(c) 0.906 Hz, cylinder and mass.

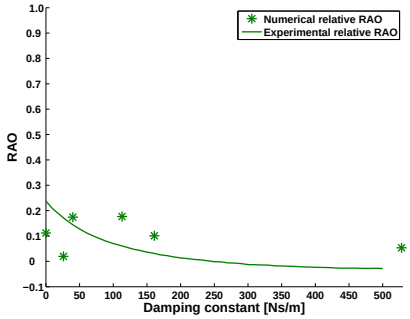

(d) 0.906 Hz, relative position.

Figure 7.12: Numerical and experimental RAO of the cylinder, mass and their relative motion, with a compression mono-directional damper: 0.844 Hz to 0.906 Hz.

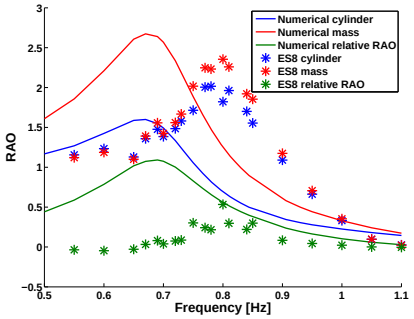

(a) 10 Ns/m

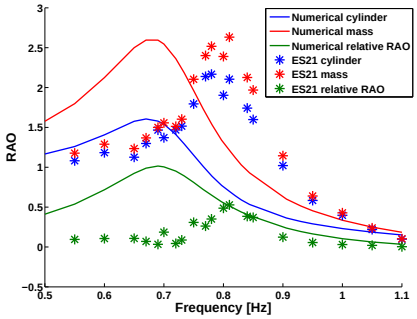

(b) 20 Ns/m

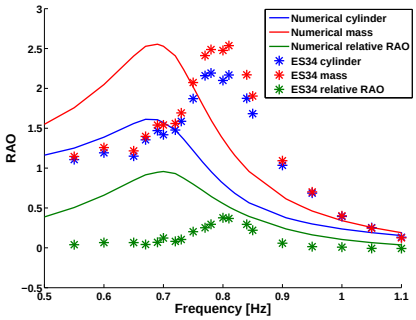

(c) 30 Ns/m

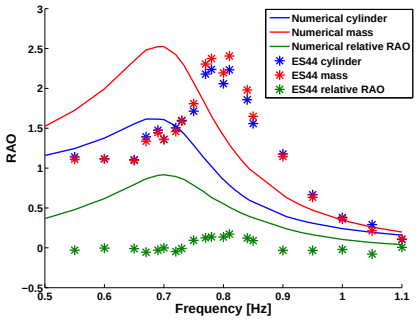

(d) 40 Ns/m

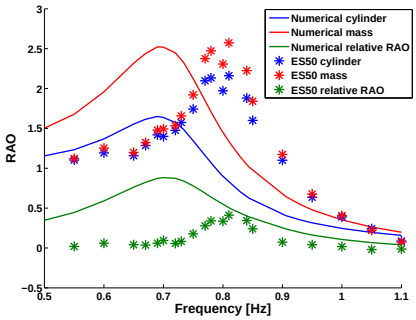

(e) 50 Ns/m

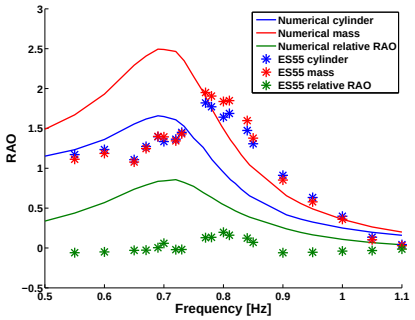

(f) 60 Ns/m

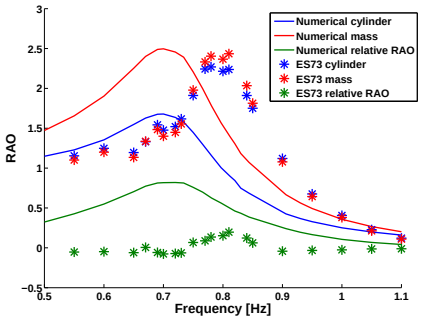

(g) 70 Ns/m

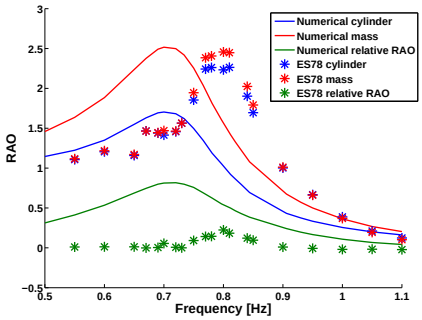

(h) 80 Ns/m

Figure 7.13: The RAO for both the numerical simulation and the experimental model, for an endstop damper.

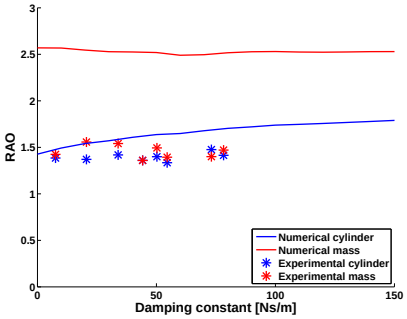

(a) 0.703 Hz, cylinder and mass.

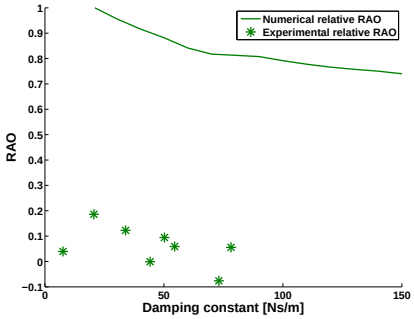

(b) 0.703 Hz, relative position.

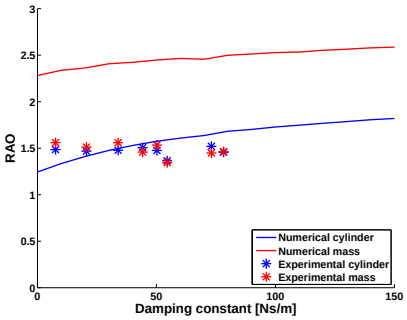

(c) 0.719 Hz, cylinder and mass.

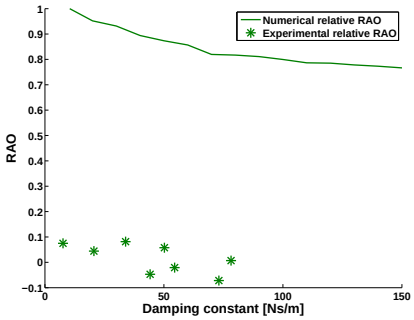

(d) 0.719 Hz, relative position.

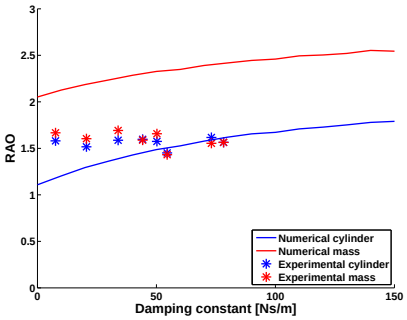

(e) 0.734 Hz, cylinder and mass.

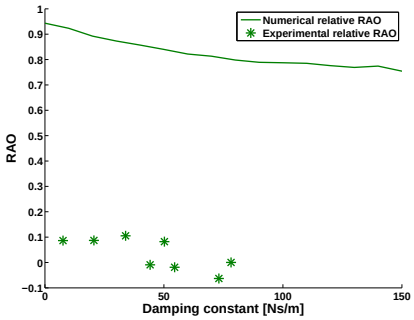

(f) 0.734 Hz, relative position.

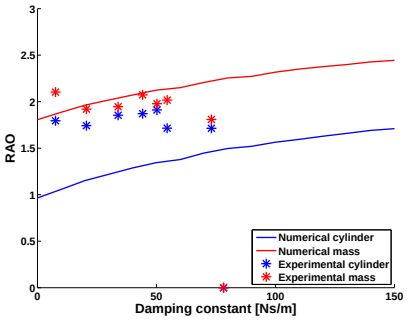

(g) 0.750 Hz, cylinder and mass.

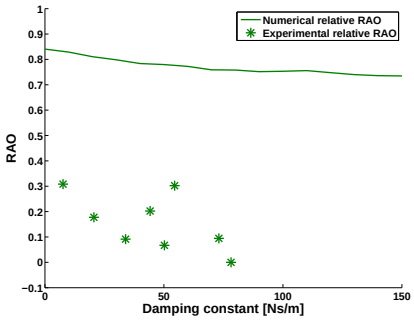

(h) 0.750 Hz, relative position.

Figure 7.14: Numerical and experimental RAO of the cylinder, mass and their relative motion, with an endstop damper: 0.703 Hz to 0.750 Hz.

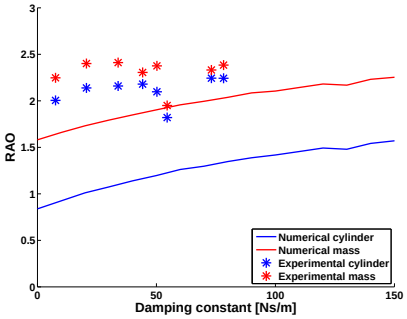

(a) 0.766 Hz, cylinder and mass.

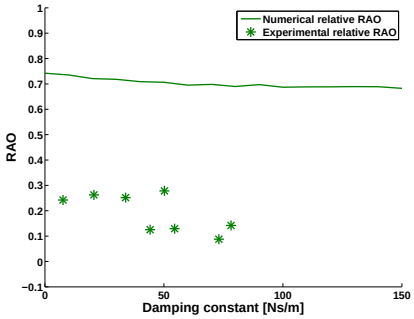

(b) 0.766 Hz, relative position.

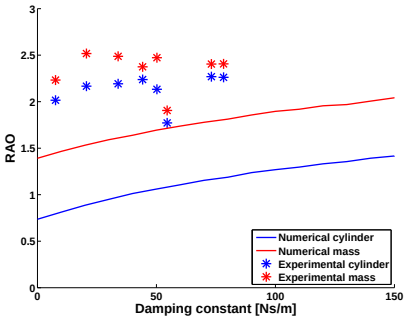

(c) 0.781 Hz, cylinder and mass.

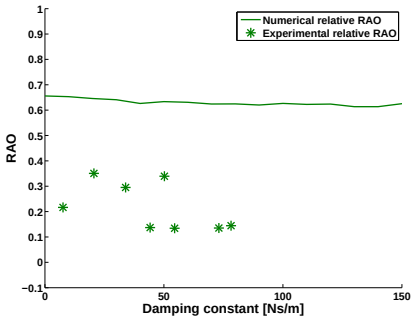

(d) 0.781 Hz, relative position.

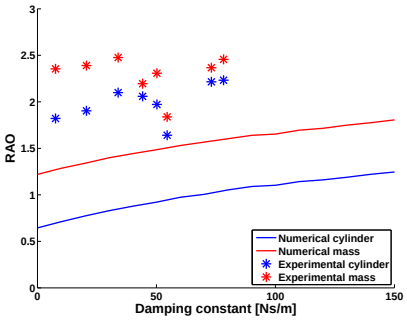

(e) 0.797 Hz, cylinder and mass.

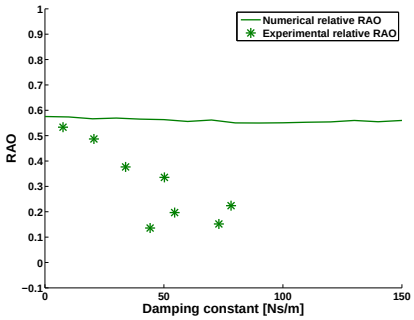

(f) 0.797 Hz, relative position.

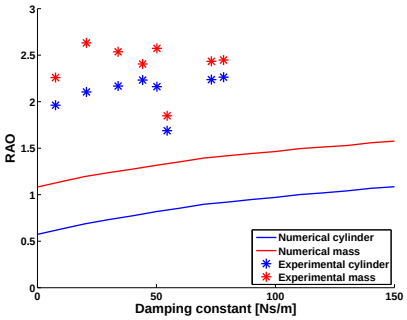

(g) 0.812 Hz, cylinder and mass.

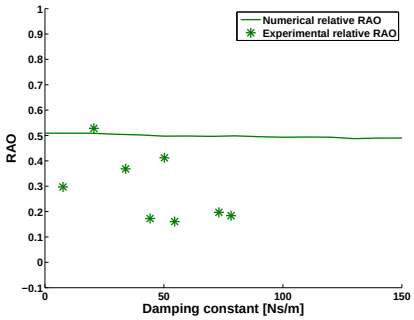

(h) 0.812 Hz, relative position.

Figure 7.15: Numerical and experimental RAO of the cylinder, mass and their relative motion, with an endstop damper: 0.766 Hz to 0.812 Hz.

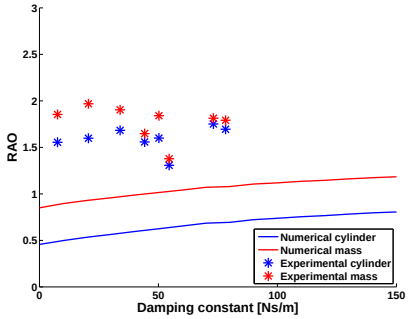

(a) 0.844 Hz, cylinder and mass.

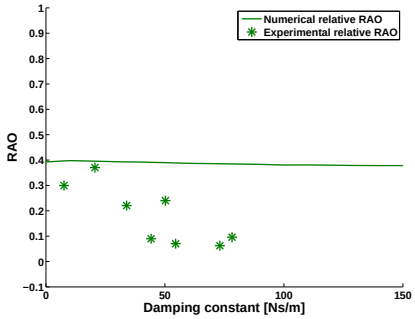

(b) 0.844 Hz, relative position.

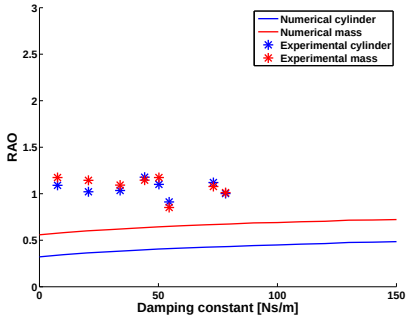

(c) 0.906 Hz, cylinder and mass.

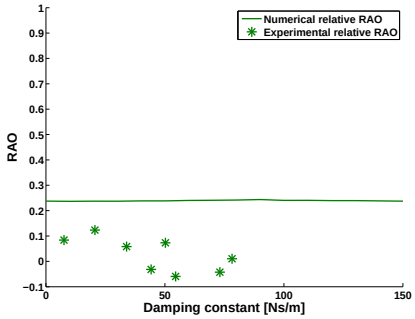

(d) 0.906 Hz, relative position.

Figure 7.16: Numerical and experimental RAO of the cylinder, mass and their relative motion, with an endstop damper: 0.844 Hz to 0.906 Hz.

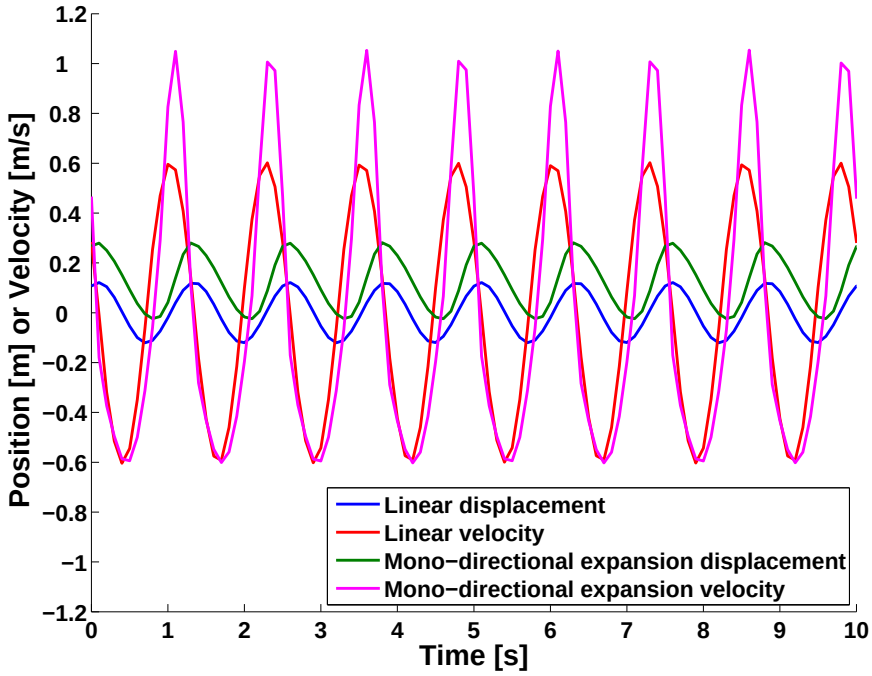

Figure 7.17: The time series of the linear and expansion mono-directional dampers, showing the displacement and velocities, in 0.80 Hz regular waves with 0.2 m wave height.

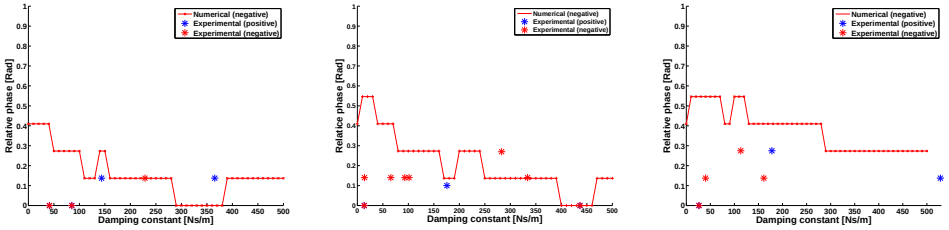

(a) LD, 0.70 Hz **(b)** EMDD, 0.70 Hz **(c)** CMDD, 0.70 Hz

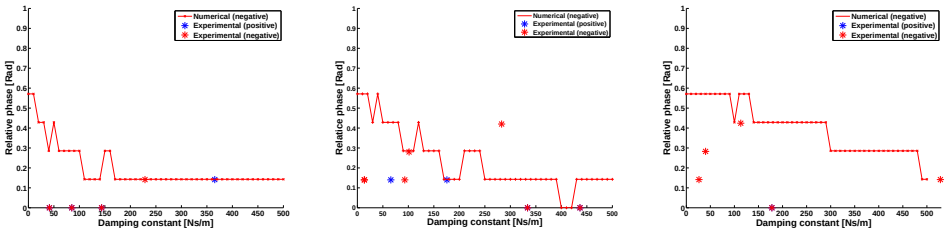

(d) LD, 0.72 Hz **(e)** EMDD, 0.72 Hz **(f)** CMDD, 0.72 Hz

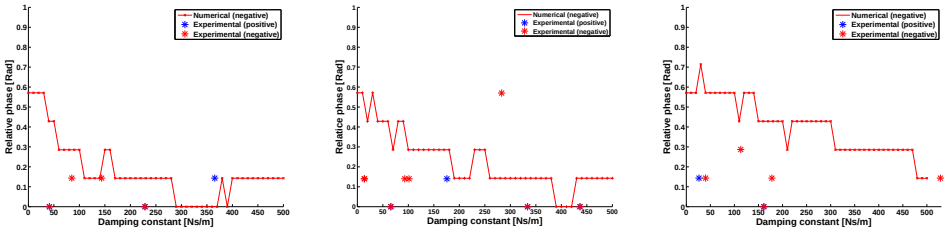

(g) LD, 0.73 Hz **(h)** EMDD, 0.73 Hz **(i)** CMDD, 0.73 Hz

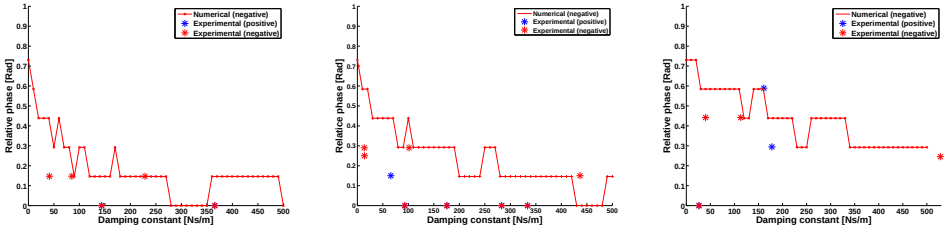

(j) LD, 0.75 Hz **(k)** EMDD, 0.75 Hz **(l)** CMDD, 0.75 Hz

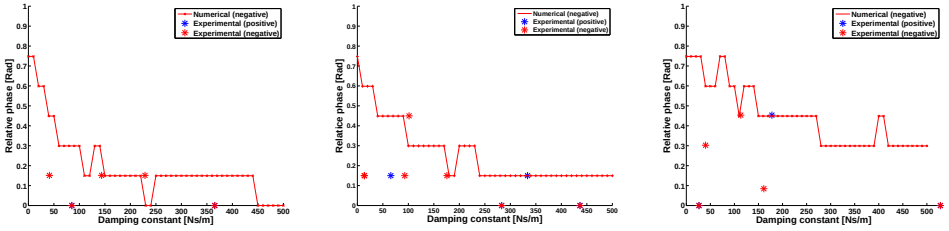

(m) LD, 0.77 Hz **(n)** EMDD, 0.77 Hz **(o)** CMDD, 0.77 Hz

Figure 7.18: The relative phase between the cylinder and mass, with the linear damper (LD), expansion mono-directional damper (EMDD) and compression mono-directional damper (CMDD), for frequencies 0.70 Hz to 0.77 Hz.

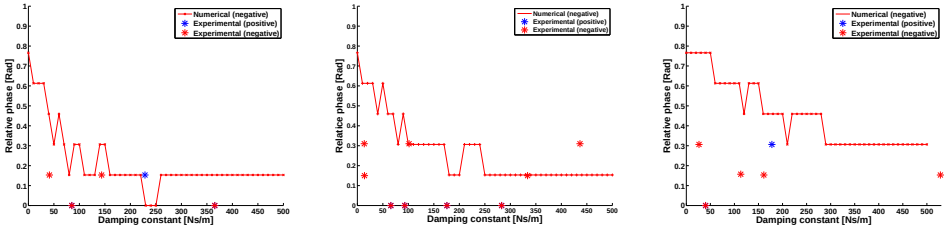

(a) LD, 0.78 Hz **(b)** EMDD, 0.78 Hz **(c)** CMDD, 0.78 Hz

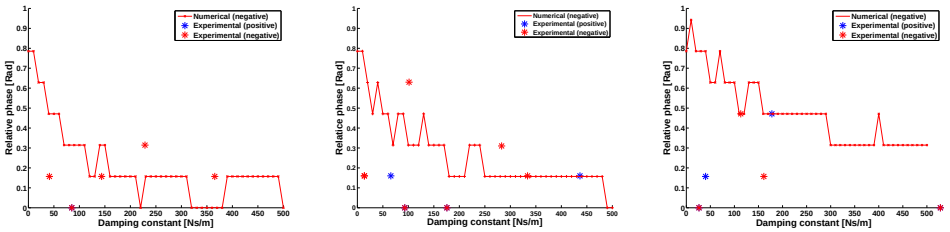

(d) LD, 0.80 Hz **(e)** EMDD, 0.80 Hz **(f)** CMDD, 0.80 Hz

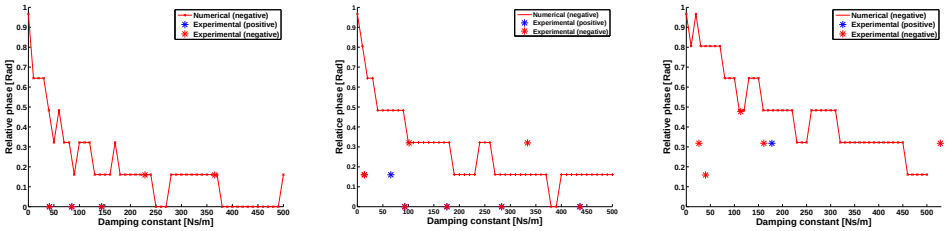

(g) LD, 0.81 Hz **(h)** EMDD, 0.81 Hz **(i)** CMDD, 0.81 Hz

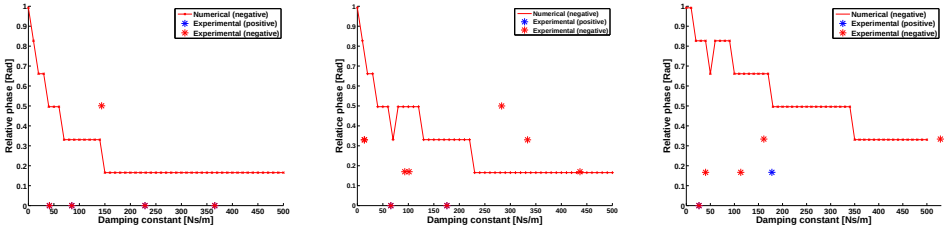

(j) LD, 0.85 Hz **(k)** EMDD, 0.85 Hz **(l)** CMDD, 0.85 Hz

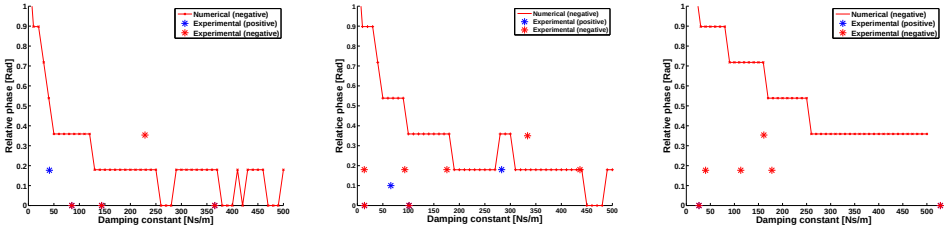

(m) LD, 0.90 Hz **(n)** EMDD, 0.90 Hz **(o)** CMDD, 0.90 Hz

Figure 7.19: The relative phase between the cylinder and mass, with the linear damper (LD), expansion mono-directional damper (EMDD) and compression mono-directional damper (CMDD), for frequencies 0.78 Hz to 0.90 Hz.

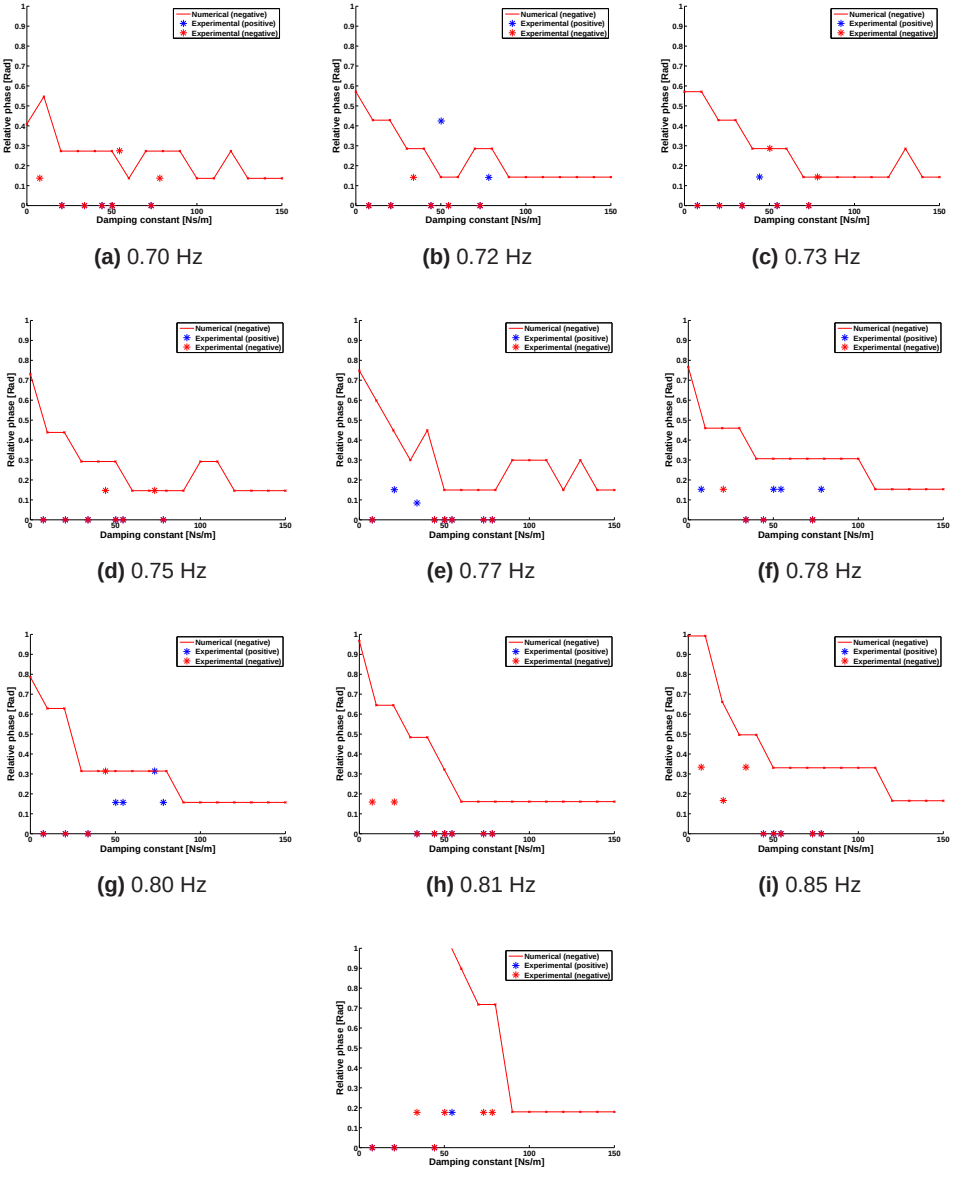

(a) 0.70 Hz **(b)** 0.72 Hz **(c)** 0.73 Hz

(d) 0.75 Hz **(e)** 0.77 Hz **(f)** 0.78 Hz

(g) 0.80 Hz **(h)** 0.81 Hz **(i)** 0.85 Hz

(j) 0.90 Hz

Figure 7.20: The relative positive (blue) and negative (red) phase between the cylinder and mass, with the endstop dampers.

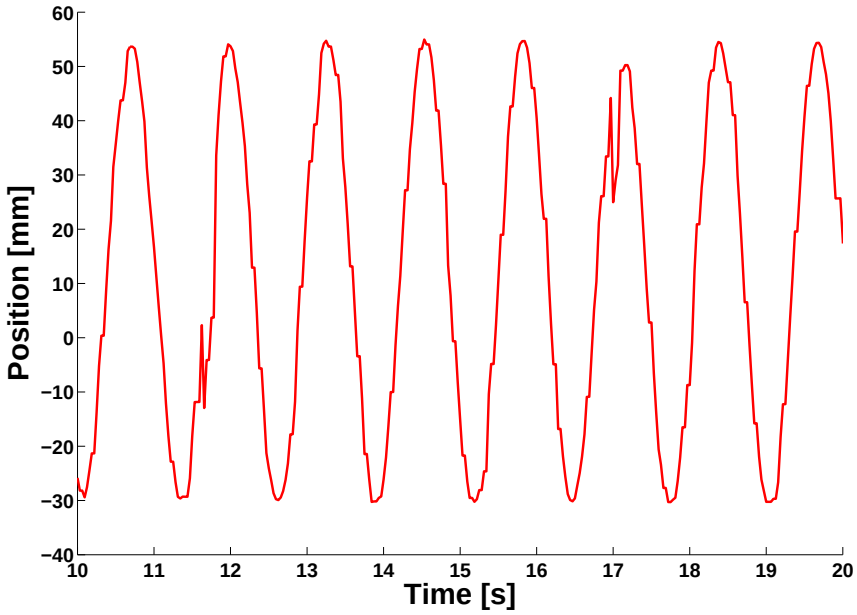

Figure 7.21: The measured position of the internal mass, showing signs of the light rod interacting with the upper cylinder base, in regular waves

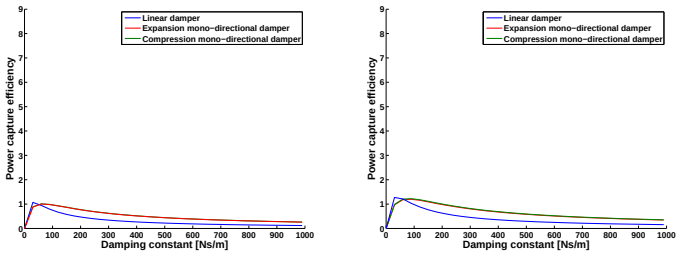

(a) 0.703 Hz **(b)** 0.719 Hz

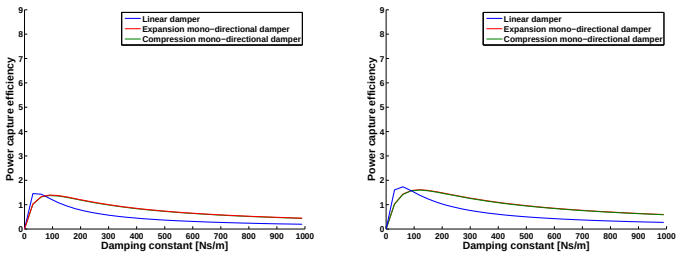

(c) 0.734 Hz **(d)** 0.750 Hz

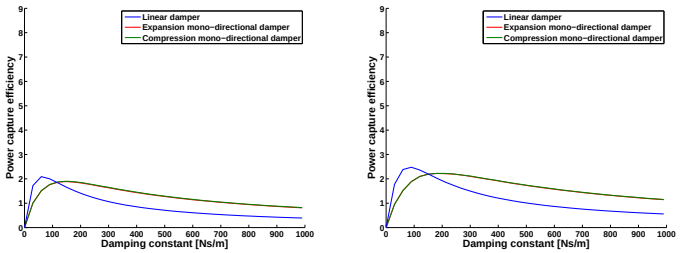

(e) 0.766 Hz **(f)** 0.781 Hz

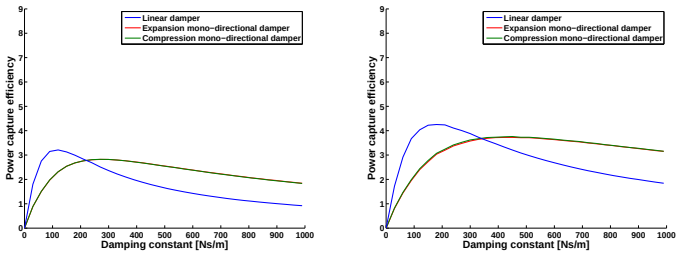

(g) 0.797 Hz **(h)** 0.813 Hz

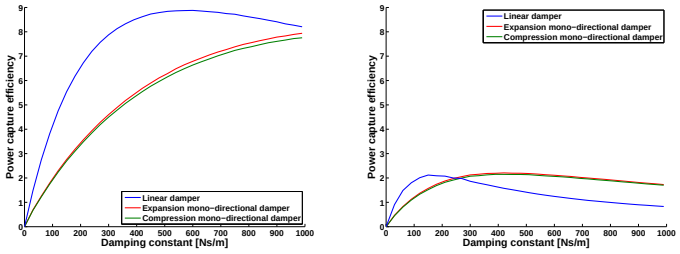

(i) 0.844 Hz **(j)** 0.910 Hz

Figure 7.22: The power capture efficiency from the numerical simulations, for a linear damper and an expansion and compression mono-directional dampers.

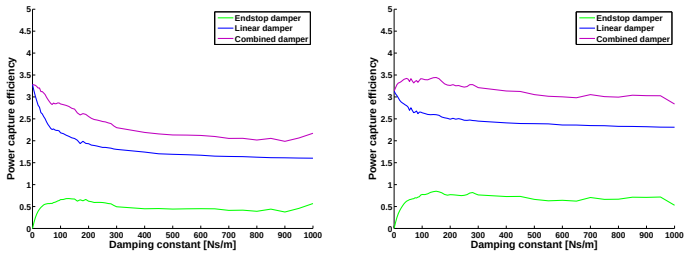

(a) 0.703 Hz **(b)** 0.719 Hz

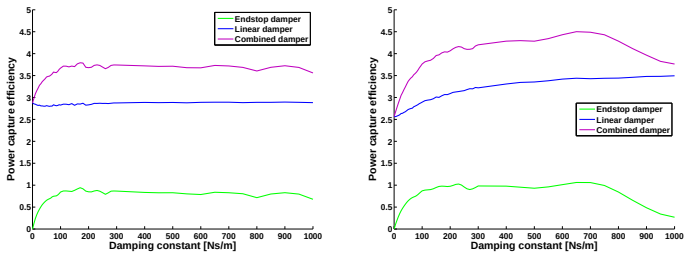

(c) 0.734 Hz **(d)** 0.750 Hz

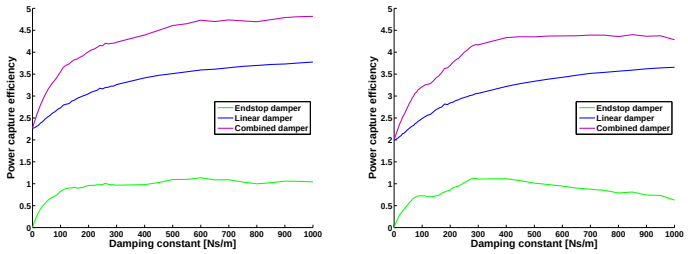

(e) 0.766 Hz **(f)** 0.781 Hz

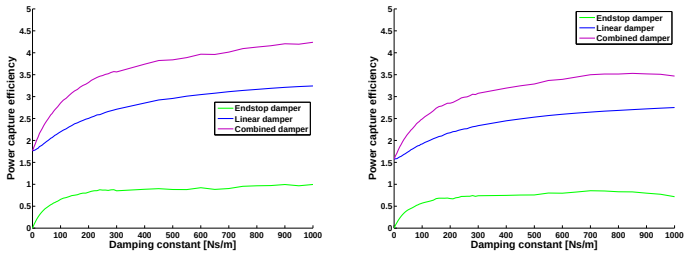

(g) 0.797 Hz **(h)** 0.813 Hz

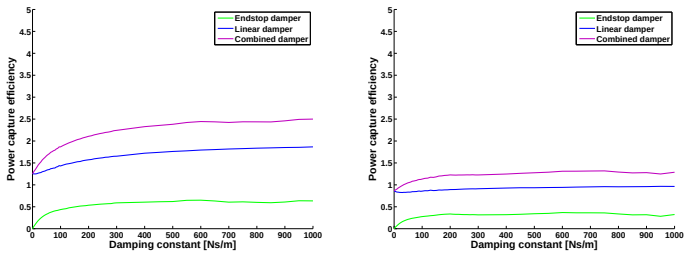

(i) 0.844 Hz **(j)** 0.910 Hz

Figure 7.23: The power capture efficiency from the numerical simulations, for an endstop damper setup, showing the power from the endstop, its linear damper and combined.

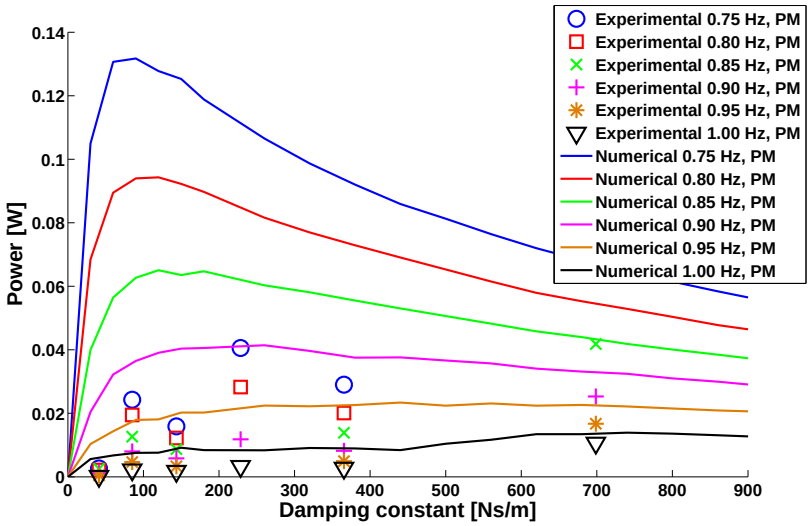

Figure 7.24: The power captured from PM spectrum seas, for the numerical simulation and experimental results, for the linear damper.

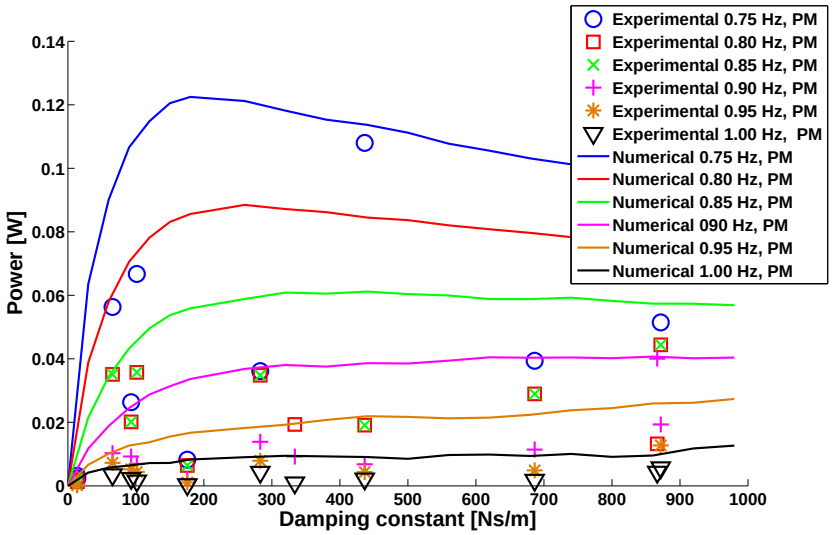

Figure 7.25: The power captured from PM spectrum seas, for the numerical simulation and experimental results, for the expansion mono-directional damper.

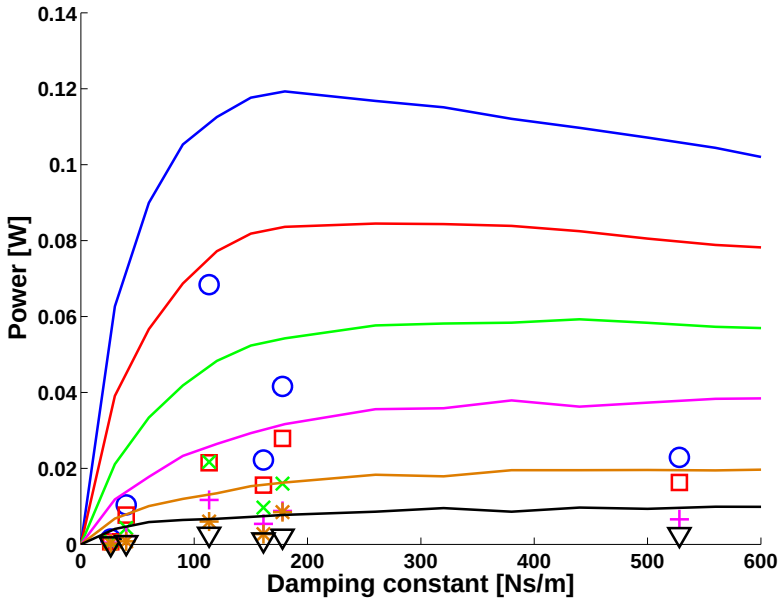

Figure 7.26: The power captured from PM spectrum seas, for the numerical simulation and experimental results, for the compression mono-directional damper.

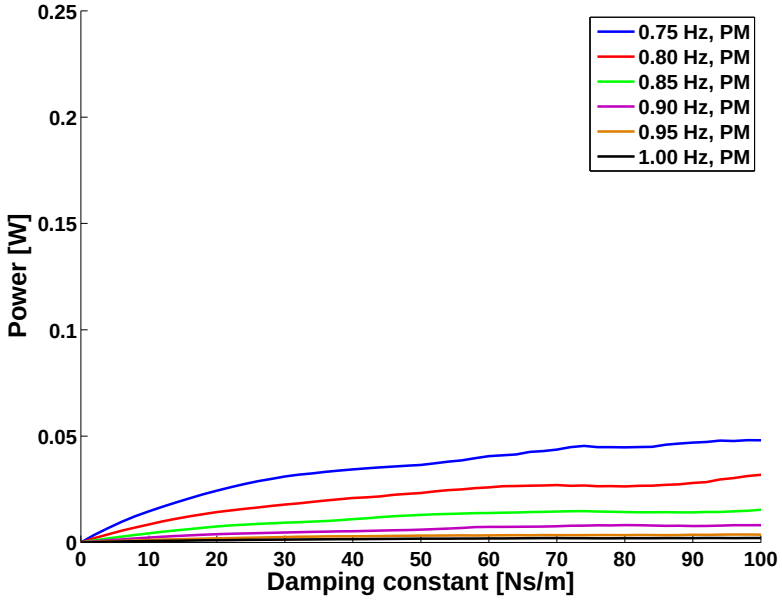

Figure 7.27: The power captured from PM spectrum seas, for the numerical simulation, for endstop damping setup with the endstop damper.

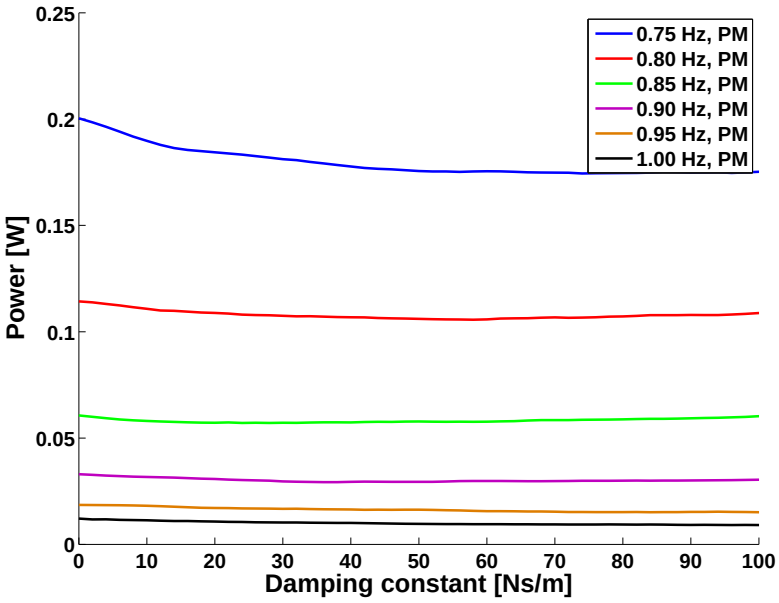

Figure 7.28: The power captured from PM spectrum seas, for the numerical simulation, for linear damping with the endstop damper setup.

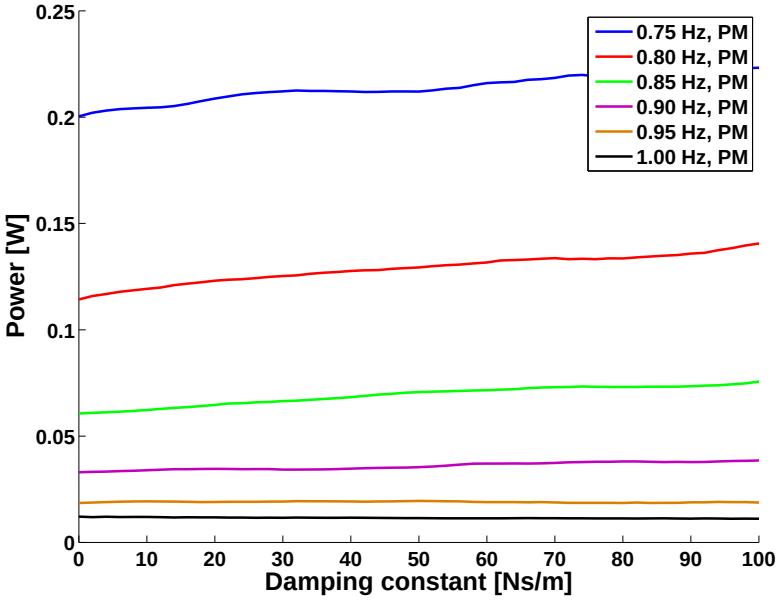

Figure 7.29: The power captured from PM spectrum seas, for the numerical simulation, for the linear and endstop damping with the endstop damper setup.

Chapter 8

Conclusions

An experimental model and a numerical simulation have been presented in this thesis to demonstrate the influence that a nonlinear PTO has on the motions and power extraction of a slack moored, self-referenced, point absorber, WEC. From this work, the following conclusions have been drawn:

Mono-directional PTO

- The power extracted from the experimental model and the numerical simulation can be larger for mono-directional dampers than for a linear bi-directional dampers over a range of frequencies in regular waves. In irregular waves, if the optimal PTO parameters are used, the mono-directional dampers can extract more power than the linear dampers. This is due to the increased relative velocities that are experienced in the mono-directional damper setup. This was shown in Sections 3.4, 3.7, 5.5, 6.5, 7.5 and 7.6.
- The LTF and the RAO differ considerably for both the experimental model and the numerical simulation, with the RAO being higher than the LTF at resonant frequencies. For the numerical simulation, a secondary peak occurred in the LTF but not the RAO. These are all indicators of the effect of the nonlinear PTO. This was presented in Section 7.3.
- The relative phase between the internal mass and the external cylinder in the experimental and numerical models, shows that the average relative phase is larger for mono-directional dampers than for linear bi-directional dampers. A larger relative phase implies there is more potential for power extraction. This was demonstrated in Sections 5.4 and 7.4.
- For the full sized model, the ideal PTO parameters for the mono-directional dampers, for a maximum power extraction of 0.27 MW, are spring and damping constants of 3.5 MN/m and 4.0 MNs/m, respectively. These are calculated for a 0.1 Hz peak frequency PM spectrum sea. This was shown in Section 3.4.
- The compression and expansion mono-directional dampers have very similar responses to the waves and extracted similar amounts of power. This was presented in Sections 3.4, 5.2, 5.3, 5.4, 6.3, 6.5 7.3, 7.4, 7.5 and 7.6.

- The numerical simulation and the experimental model have similar results for the RAOs, the relative phase between the bodies and the time series analysis. The estimates for the power extraction differ due to the difficulties in accurately obtaining the relative velocities in the experimental model. These difficulties arise from the small relative motion that occurs and the high frequency fluctuations in the markers used to determine the body positions. This was demonstrated in Sections 7.5 and 7.6.

Quadratic PTO

- For the parameters tested in this thesis, the ideal linear spring and quadratic damping constants, for a full scale device, are 4.5 MN/m and 2.5 MNs^2/m^2, respectively. These consider both the power extracted and indicators of reliability. The time averaged power extracted for these parameters, in a 0.1 Hz peak frequency PM spectrum sea, is 0.28 MW. This was presented in Section 3.5.
- The nonlinear influence of the PTO affects the absolute motions of both bodies, this results in differences between the LTF and the RAO and is further emphasized by having a coherency function that is not close to unity. This was demonstrated in Section 3.5.

Endstop dampers

- Having endstop dampers tends to increase the power extracted, especially when power could be extracted from the linear damper and additionally from the endstop dampers. This was shown in Sections 3.6, 5.5, 6.5, 7.5 and 7.6.
- Using two endstop dampers to limit the amplitude of the relative motion can result in a higher power extraction than from the linear damper alone or from just one endstop damper. This was presented in Sections 3.6, 7.5 and 7.6.
- The optimal endstop damping constant and distance from the SWL position of the internal mass to the endstop damper, when the linear spring and damping constant are 0.4 MN/m and 0.2 MNs/m, are 2.5 MNs/m and zero distance for a single endstop damper and 100 MNs/m and 0.75 m for two endstop dampers. These result in 0.75 MW and 1.94 MW of power extracted, respectively, for a PM spectrum sea state with a peak frequency of 0.1 Hz. This assumes that the linear dampers are capable of extracting the power, over all time, as proportional to the relative velocity. This was shown in Section 3.6.

Nonlinear systems

- Nonlinear PTO systems in WECs have differences in the RAO and the LTF and therefore, the RAO can not be used to estimate the response and the power extraction from mixed frequency seas. This was demonstrated in Sections 3.4, 3.5, 3.6 and 6.4.
- Significant responses can occur at frequencies in irregular waves were there is a very limited response at that frequency in regular waves. This was presented in Section 6.4.

These results show that for a WEC with a nonlinear PTO, experimental modelling and time domain numerical simulations are needed to accurately understand the motions, choose the optimal parameters and predict the power extracted from the waves.

Having a linear and additional endstop dampers can dramatically increase the power extracted, provided that the linear damper can extract the energy as required. A mono-directional damper extracts more power than a linear damper at its optimal PTO parameters. A quadratic damper has the potential to extract more power than both the linear and mono-directional dampers, with optimal PTO parameters.

Further work

Additional work based on the concepts and results from this thesis could be completed to further the understanding of WECs with nonlinear PTOs and their interactions with the marine environment. Specifically, further work could concentrate on:

- Looking at the effect of nonlinearities on different generic types of WEC.
- Looking at the nonlinear effects from the waves through either experimental modelling or numerical simulations with large wave heights, to see how the nonlinearities of the model and of the waves influence and interact with each other.
- Further experimental testing with a larger physical model in a bigger wave tank, to allow the power extraction from the dampers to be more accurately known.
- Experimental testing of two endstop dampers and of endstop damper(s) with varying distances to the SWL position of the internal mass.
- Investigations based on combining quadratic or mono-directional dampers with additional endstop dampers.

Bibliography

Airpot Corporation. Airpot's website and product information. http://www.airpot.com, Nov 2008.

AWS Ocean energy Ltd. Waveswing. http://www.awsocean.com, Nov 2008.

Babarit A., Clement A. H., and Gilloteaux J. C. Optimization and time-domain simulation of the searev wave energy converter. *Proceedings of the 24th International Conference on Offshore Mechanics and Arctic Engineering*, 2:703–712 1003, 2005.

Babarit A., Clement A. H., Ruer J., and Tartivel C. Searev: a fully integrated wave energy converter. In *OWEMES Conference*, Rome, 2006.

Bailey H. and Bryden I. Influence of a quadratic power take off on the behaviour of a self contained inertial referenced wave energy converter. In *Proceedings of the Institution of Mechanical Engineers, Part M, Journal of Engineering for the Maritime Environment*, 2011. Accepted for publication.

Bailey H. and Bryden I. Experimental testing on the effect of nonlinear power take off on the motions of wave energy converters. In *2nd International Conference on Ocean Energy*, Brest, France, 2008.

Bailey H. and Bryden I. The influence of a mono-directional pto on a self-contained inertial wec. In *8th Europeon Wave and Tidal Energy Conference*, Uppsala, Sweden, 2009.

Beatty S., Buckham B., and Wild P. Modeling, design and testing of a two-body heaving wave energy converter. In *ISOPE-2007: Seventeenth International Offshore and Offshore and Polar Engineering Conference Proceedings*, pages 380–387, 2007.

Bendat J. *Nonlinear system techniques and applications.* Wiley, New York ; Chichester, 1998.

Bhatta D. and Rahman M. On scattering and radiation problem for a cylinder in water of finite depth. *International Journal of Engineering Science*, 41(9):931–967, 2003.

Boyle G. *Renewable energy : power for a sustainable future.* Oxford University Press in association with the Open University, Oxford, 1996.

Bryden I. *Long floating cylinders in three-dimensional random seas.* PhD thesis, University of Edinburgh., 1983.

Budal K. and Falnes J. Resonant point absorber of ocean-wave power. *Nature*, 256(5517): 478–479, 1975.

Checkmate. Anaconda. http://www.checkmateuk.com/seaenergy, Sept 2009.

Chung T. *Computational fluid dynamics*. Cambridge University Press, Cambridge, 2002.

CUED. *Structures Date Book*. Cambridge University Engineering Department, 1999.

Dean R. and Dalrymple R. *Water wave mechanics for engineers and scientists*. Advanced series on ocean engineering ; v.2. World Scientific, Singapore ; London, 1992.

Department of Energy and Climate Change. http://www.decc.gov.uk, Nov 2009.

Duclos G., Clement A., and Chatry G. Absorption of outgoing waves in a numerical wave tank using a self-adaptive boundary condition. *International Journal of Offshore and Polar Engineering*, 11(3):168–175, 2001.

Faber M., Johnston C., Schamhardt H., van Weeren R., Roepstorff L., and Barneveld A. Basic three-dimensional kinematics of the vertebral column of horses trotting on a treadmill. *American Journal of Veterinary Research*, 62(5):757–764, 2001.

Falcao A. Modelling and control of oscillating-body wave energy converters with hydraulic power take-off and gas accumulator. *Ocean Engineering*, 34(14-15):2021–2032, 2007.

Falcao A. Phase control through load control of oscillating-body wave energy converters with hydraulic pto system. *Ocean Engineering*, 35(3-4):358–366, 2008.

Falnes J. Wave-energy conversion through relative motion between two single-mode oscillating bodies. *Journal of Offshore Mechanics and Arctic Engineering-Transactions of the Asme*, 121(1):32–38, 1999.

Falnes J. *Ocean waves and oscillating systems : linear interactions including wave-energy extraction*. Cambridge University Press, Cambridge, 2002.

Falnes J. A review of wave-energy extraction. *Marine Structures*, 20(4):185–201, 2007.

Finavera Renewables. Aquabuoy. http://www.finavera.com, June 2009.

FREDS Marine Energy Group. Marine energy road map. Technical report, The Scottish Government, 2009. URL `http://www.scotland.gov.uk/Resource/Doc/281865/0085187.pdf`.

French M. and Bracewell R. Heaving point absorbers reacting against an internal mass. In Springer B. ., editor, *IUTAM symposium*, page pp. 247ï£¡255, lisbon, 1985.

Greenberg M. *Advanced engineering mathematics*. Prentice Hall, 2nd ed. edition, 1998.

Greenhow M. Approximate models of a heaving sphere with linear and non-linear power take-off mechanisms. *Applied Ocean Research*, 4(3):160–164, 1982.

Hall M. *Identification of motions and mooring loads in sea-cage systems.* PhD thesis, Heriot-Watt University, 1991.

Henderson R. Design, simulation, and testing of a novel hydraulic power take-off system for the pelamis wave energy converter. *Renewable Energy*, 31(2):271–283, 2006.

Holt C., Evans S., Dillon D., and Ahuja S. Three-dimensional measurement of intervertebral kinematics in vitro using optical motion analysis. *Proceedings of the Institution of Mechanical Engineers Part H-Journal of Engineering in Medicine*, 219(H6):393–399, 2005.

Hughes S. *Physical models and laboratory techniques in coastal engineering.* Advanced series on ocean engineering ; v.7. World Scientific, Singapore ; River Edge, NJ, 1993.

Jefferys E. Simulation of wave power devices. *Applied Ocean Research*, 6(1):31–39, 1984.

Korde U. On providing a reaction for efficient wave energy absorption by floating devices. *Applied Ocean Research*, 21(5):235–248, 1999.

Korde U. Latching control of deep water wave energy devices using an active reference. *Ocean Engineering*, 29(11):1343–1355, 2002.

Kugi A. *Non-linear control based on physical models : electrical, mechanical and hydraulic systems.* Lecture notes in control and information sciences ; 260. Springer, London, 2001.

Lewis A. Hydrodynamic modelling of a floating oscillating water column system. In *Fifth European Wave Energy Conference*, Cork, Ireland, 2003.

Lin C. *Experimental studies of the hydrodynamic characteristics of a sloped wave energy device.* PhD thesis, University of Edinburgh, 1999.

Lucas J., Cruz J., Salter S., Taylor J., and Bryden I. Update on the design of a 1:33 scale model of a modified edinburgh duck wec. *Proceedings of the 27th International Conference on Offshore Mechanics and Arctic Engineering*, 6:605–615, 2008.

McCabe A., Aggidis G., and Stallard T. A time-varying parameter model of a body oscillating in pitch. *Applied Ocean Research*, 28(6):359–370, 2006.

Montgomery D. and Runger G. *Applied statistics and probability for engineers.* Wiley, New York ; Chichester, 1994.

Mueller M., Polinder H., and Baker N. Current and novel electrical generator technology for wave energy converters. In *IEEE International Electric Machines & Drives Conference*, volume 1, pages 1401–1406, 2007.

Newman J. *Marine hydrodynamics.* MIT Press, Cambridge, Mass., 1977.

Nikias C. and Petropulu A. *Higher-order spectra analysis : a nonlinear signal processing framework*. Prentice Hall signal processing series. PTR Prentice Hall, Englewood Cliffs, N.J., 1993.

OceanEnergy. Oe buoy. http://www.oceanenergy.ie, Sept 2009.

Panicker N. Power resource potential of ocean surface waves. In *Proceedings of the Wave and Salinity Gradient Workshop*, pages J1–J48, Newark, Delaware, USA, 1976.

Parker R., Harrison G., and Chick J. Energy and carbon audit of an offshore wave energy converter. *Proceedings of the Institution of Mechanical Engineers Part a-Journal of Power and Energy*, 221(A8):1119–1130, 2007.

Payne G. *Numerical modelling of a sloped wave energy device*. PhD thesis, University of Edinburgh, 2006.

Payne G., Taylor J., Bruce T., and Parkin P. Assessment of boundary-element method for modelling a free-floating sloped wave energy device. part 2: Experimental validation. *Ocean Engineering*, 35(3-4):342–357, 2008.

Pierson W. and Moskowitz L. A proposed spectral form for fully developed wind seas based on the similarity theory of SA Kitaigorodskii. *Journal of Geophysical Research*, 69(24): 5181–5190, 1964.

Qualisys Motion Capture. Qualisys product information. http://www.qualisys.com, Feb 2009.

Rogers D. and King G. *Wave generation using Ocean and wave,*. Edinburgh Designs Ltd., 1997.

Ross D. *Energy from the waves : the first-ever book on a revolution in technology*. Pergamon international library. Pergamon, Oxford, 1979.

Sa da Costa J., Sarmento A., Gardner F., Beirao P., and Brito-Melo A. Time domain model of the archimedes wave swing wave energy converter. In 9 S., editor, *6th European Wave and Tidal Energy Conference*, page pp. 91ï£¡97, Glasgow, UK, 2005.

Schetzen M. *Volterra and Wiener theories of nonlinear systems*. Robert E. Krieger, 1989.

Seabased AB. Seabased. http://www.seabased.com, Nov 2008.

Solomon S. *Climate change 2007 : the physical science basis : contribution of Working Group I to the fourth assessment report of the Intergovernamental Panel on Climate Change*. Cambridge University Press, Cambridge, 2007.

Taghipour R., Perez T., and Moan T. Hybrid frequency-time domain models for dynamic response analysis of marine structures. *Ocean Engineering*, 35(7):685–705, 2008.

Taylor J., Rea M., and Rogers D. The edinburgh curved tank. In *5th European Wave Energy Conference*, Cork, Ireland, 2003.

Tick L. The estimation of "transfer functions" of quadratic systems. *Technometrics*, 3(4): 563–567, 1961.

Trinnaman J. and Clarke A. *2004 survey of energy resources.* Elsevier, Amsterdam ; London, 2004.

Tyrberg S., Stalberg M., Bostrom C., Waters R., Svensson O., Stromstedt E., Savin A., Engstrom J., Langhamer O., Gravrakmo H., Haikonen K., Tedelid J., Sundberg J., and Leijon M. The lysekil wave power project: Status update. In *WREC X*, Glasgow, UK, 2008.

WAMIT I. Wamit user manual version 6.0, 6.0pc, 5.3s., 2000.

Wang J., Yan F., and Xue Q. Tribological behavior of PTFE sliding against steel in sea water. *Wear*, 267:1634–1641, 2009.

Wavebob Ltd. Wavebob. http://www.wavebob.com, Sept 2009.

Weinstein A., Nielsen K., Zandiyeh K., and Bensted J. The aquabuoy hose-pump ï£¡ theory and experimental results. In *7th European Wave Energy Conference*, Porto, Portugal, 2007.

Worden K. and Tomlinson G. Nonlinearity in experimental modal analysis. *Philosophical Transactions of the Royal Society of London Series a-Mathematical Physical and Engineering Sciences*, 359(1778):113–130, 2001.

Appendices

Appendix A

Copies of Publications

The influence of a mono-directional PTO on a self-contained inertial WEC

H. Bailey[1] and I.G. Bryden[2]

[1]Institute for Energy Systems,
University of Edinburgh,
EH9 3JL, UK
E-mail: Helen.Bailey@ed.ac.uk

[2] E-mail: Ian.Bryden@ed.ac.uk

Abstract

This paper looks at the effect that a mono-directional Power Take Off (PTO) has on the motions and power extraction of a Wave Energy Converter (WEC). A mono-directional damper is one where the resisting force only operates in one direction. The model comprises of a cylinder that is restrained to move in heave, reacting against an internal mass (also limited to move in heave) that is connected to the cylinder by a spring and mono-directional damper in parallel.

This paper presents results for a variety of different damping constants for mono-directional dampers which operate in both in expansion and compression. The response amplitude operators to monochromatic waves for both the cylinder, the internal mass and the relative motion between them are presented. A Pierson Moskowitz spectrum is used to look at the effect of an irregular sea state and the power extraction is calculated from this spectrum. The results show a greater response of the cylinder, but also in certain cases the internal mass and relative motion, when a mono-directional damper is present than when there is no damper. It is postulated by the authors that this is due to a "latching" effect. This increase in motion results in a greater than expected power extraction.

Keywords: Experimental wave tank testing, Nonlinear Power Take Off, Inertial point absorber, Wave Energy Converters (WECs)

1 Introduction

A wave energy converter's (WEC's) motion is influenced by its Power Take Off (PTO) system, which in turn affects the potential power extraction of the device. The experimental results from using a mono-directional damper are presented, where a mono-directional damper is a damper that only provides a resisting force when the damper is moving in one direction.

Having a mono-directional PTO will have advantages in terms of cost and potential simplicity of design, although the disadvantages are that it may reduce the power captured and it could limit the possible control strategies that may need to be implemented. A number of WECs which currently use a mono-directional PTO system are in various stages of development including the Manchester Bobber [1] and the Langlee Wave Power [2].

The type of device being presented is a self-contained inertial slack moored point absorber. The entire structure of the device, including the PTO system is encased in a watertight shell and the moorings are slack and are not connected to the PTO system. This means that this type of device is highly deployable. The PTO operates by having a large inertial mass that reacts against the rest of the body [3]. This mass resides within the device and is connected to the main body by a spring and damper in parallel. Both the internal mass and the overall device are limited to move in heave only. The relative motion between the external shell and internal mass is used by the damper to extract energy.

This device is generic, and is not meant to replicate or become a commercial device but to be used to further understand how having a nonlinear PTO influences both the overall motions of the device and the power extraction.

The device is at a 1:40 scale and has been tested in the University of Edinburgh's curved tank [4] in both regular waves and irregular sea states. Different damping constants are tested, for dampers that provide a resisting force in both expansion and compression.

In this paper the detailed experimental setup will be given in section 2, including photos of the device and details of how the dampers were calibrated. The results are presented and discussed in the third section, which contains the response amplitude operator graphs obtained from a regular sea for the overall body of the device, the internal mass and the relative motion. This section also shows the motion of the device in a PM sea for the different bodies and the power extracted from the system

for a variety of different sea states.

2 Experimental Setup

2.1 The model

The model comprises a 16 mm diameter, 1.5 m long ground stainless steel rod that is held vertical and limited to move in heave by two rod-end bearings with PTFE (polytetrafluoroethylene) sleeves attached at its upper and lower ends. The rod-end bearings are fixed to a rig attached to the internal platforms within the wave tank. Rigidly attached near the center of the rod is a clear plastic cylinder with plastic bases at the top, middle and bottom. The bottom is fully sealed but there are circular cutouts in the top plastic base to allow the motion of the internal mass to be observed and to allow access and removal. The middle base's role is to provide a platform for the damper to be located. On the rod between the bottom of the cylinder and the internal mass is a custom made spring, sitting freely on the rod with a spring stiffness of 200 N/m. A close up view of the cylinder containing the internal mass, spring and damper is given in Fig. 1, which is shown out of the water. The entire setup, including the fixed platform, the rig with the rod-end bearings, the cylinder and the markers used for data collection can be seen in Fig. 2.

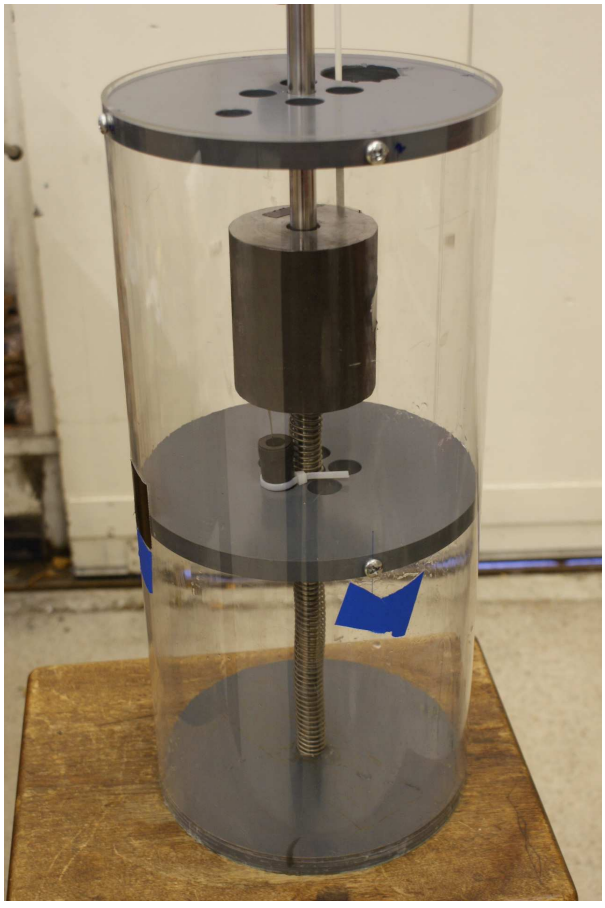

Figure 1: The experimental model, out of the water.

The radius of the cylinder is 115 mm and it has a depth of 0.5 m with a draft of 0.285 m. The internal mass

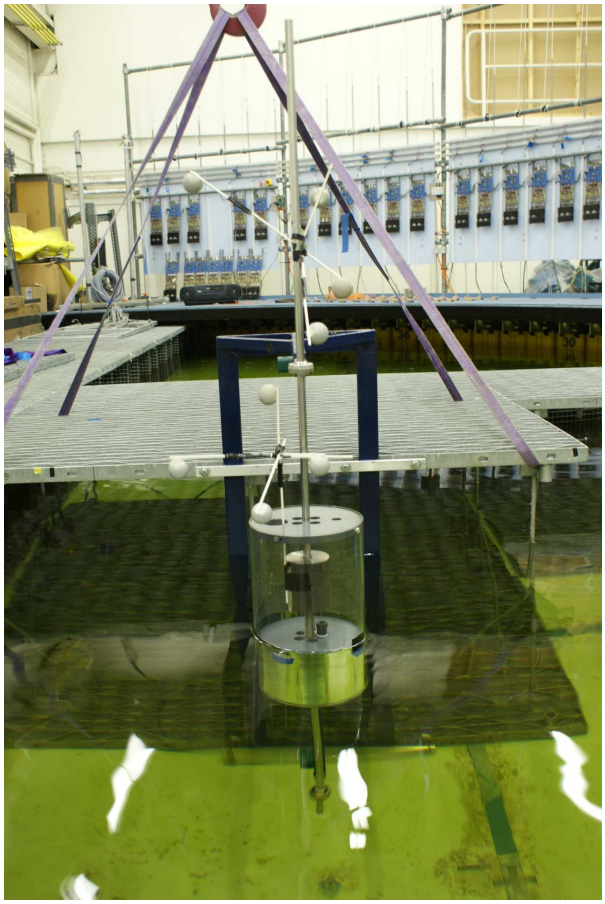

Figure 2: The experimental setup, along with the motion-detection markers.

weighs 6.721 kg and the external body without the internal mass weighs 4.856 kg. The size of the internal mass and spring constant were chosen from previous work [5] based on Falnes' work on two body systems [6]. Since the model is at a 1:40 scale, a full scale device would have a cylinder radius of 4.6 m and an internal mass of 430 tonnes.

The positions of the cylinder and internal mass are monitored via markers which are observed by a Qualisys Motion Capture [7] infrared tracking camera system. The markers are attached to the rod and on a light dowel attached to the internal mass which protrudes from the cylinder and can clearly be seen in Fig 2 as the white spheres. The data collection from the markers is linked to the wave tank activation signal allowing data to be collected at a known time in the wave cycle, hence allowing different setups to be compared since they experience the same waves.

2.2 Dampers

The dampers used are pneumatic and designed to have a linear response. They have the brand name Airpot [8]. Two types of dampers have been used: a compression damper, which provides a resisting force when the piston of the damper is compressed into the unit, and an expansion damper, which provides a resisting force when the piston is expanding from the unit. There

is a minimal constant resisting force in the opposite direction to the intended resisting force, this is generally assumed to be zero. The dampers are both adjustable via a screw to get a variety of damping constants. The dampers are sold as linear and there is a air spring effect of the dampers for the first 1-2 mm of motion.

2.3 Calibration of Dampers

The dampers were calibrated by rigidly fixing the body and using a 23 g and a 55 g mass that screws into the damper. A Qualisys marker is attached to the mass and the dampers are either manually extended or compressed (depending on which damper is being tested), released, and allowed to move under gravity due to the weight of the mass. The marker is tracked at 128 Hz and the extension / compression is repeated for a minimum of 128 s. For the damper where the marker is being recorded in compression, a plastic manual guide is used to keep the mass falling vertically, with as little interference to the motion as possible. The results are visually reviewed and individual results for which there has been difficulty obtaining a vertical descent are removed. Due to the manual input in this experiment the reliability of the dampers which produce force in compression is lower than the dampers that produce force in extension.

This obtains between 5 and 20 results for the mass falling under gravity which are averaged, and the overall damping factor is calculated using Equation 1.

$$c = \frac{m(g-a)}{v}, \tag{1}$$

where c [Ns/m] is the damping factor, m [kg] the combined weight of the mass and the marker, g [m/s^2] the acceleration due to gravity, a [m/s^2] the measured acceleration of the mass and v [m/s] the measured velocity of the mass. The resulting damping for each of the damper setups can be seen in Table 1.

Name	**Direction of force**	**Damping constant** [Ns/m]	**Approx error** [Ns/m]
Exp 1	Expansion	14.1	0.2
Exp 2	Expansion	31.1	0.5
Exp 3	Expansion	433	3
Com 1	Compression	26.8	5
Com 2	Compression	123	16

Table 1: Damping constants.

2.4 Friction

The main sources of unrequited friction and damping were in the two bearings which attach the rod to the fixed rig and the bearing between the internal mass and the rod. The damping and friction from the two rod end bearings has been reduced by having the bearings able to rotate and using the PTFE sleeve. The level of damping is still non-negligible and increases as the body tries to move in pitch, which has a resonant frequency of 1 Hz. Since it is a direct stainless steel / PTFE contact it would be reasonable to assume that it is Coulomb damping. However for the same cylinder motion, regardless of which damper is used, this damping will be constant and linear, and it would be reducing the motion of larger oscillations in a consistent way. Therefore this damping can be neglected and it would be likely that there would be higher response of the cylinder if this damping was not present.

The damping between the bearing on the internal mass and the steel rod is more problematic, since for all motion, whether the damper is expanding or compressing, there will be an assumed Coulomb damping acting upon it and in opposition to motion at all times. This will interfere with our ability at looking at the effects of a mono-directional damper. The ratio of this damping to the mono-directional damper damping is unknown. Efforts are still being made to appropriately quantify this effect.

3 Results and Discussions

3.1 Experimental accuracy and repeatability

To test the repeatability and accuracy of the experiment for a single damper, a PM spectrum with a peak frequency of 0.90 Hz was used for 128 s to look at the correlation for 5 identical runs with damper “Com 1”. The runs were taken in succession with no physical interference to the model occurring between runs.

The data sets were used to find the R correlation, which is a linear measure of the normalized strengths of the relationships between two data sets, were an outcome of 1 is for identical data sets. The R value for the cylinder was above 0.985, with an average of 0.9889. For tests with the internal mass the R values were above 0.975 with an average of 0.9863.

An estimation of the spread of the data sets was calculated from quataion 2,

$$\frac{1}{N}\sum_{i=1}^{N}\left|\frac{X_i - x_i}{X_i}\right|, \tag{2}$$

where X_i represents one data set, and x_i represents a different data set which is being compared to the first, with the subscript i representing the time series progression and N the length of the set.

The spread for the cylinder were between 5.8% and 2.5% with an average of 4.1% for a 50 sec section that avoids values that are close to zero. The results for the internal mass were found to be between 4.1% and 10.2% with an average of 5.7%. Since the average position of the internal mass was near to zero, the results were reduced by 30 mm to have an average that is approximately the same as the cylinder. This is to avoid having to devide by zero.

3.2 Response Amplitude Operator

The Response Amplitude Operator (RAO) is a ratio of the bodies response to the actual wave height and monochromatic waves have been used to obtain this. The waves were run for 16 s in order to reach steady state and results were recorded for the following 64 s. The average maximum response of both the internal mass and the cylinder were calculated. The wave heights were recorded using standard wave gauges. The wave heights were set to have an amplitude of 20 mm but the actually wave height varied around this value by a maximum of 4 mm. The results were obtained for 0.05 Hz to 1.10 Hz in 0.05 Hz increments, over the central range 0.67 Hz to 0.84 Hz which appeared to have the most significant response and further results where taken for each possible frequency of the wave tank. The wave tank is limited to produce waves of $\frac{n}{64}$ Hz, were n is an integer.

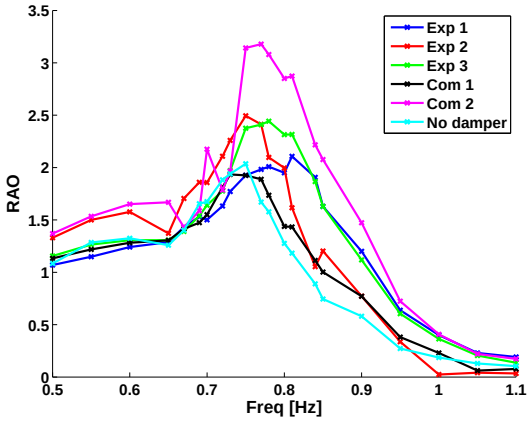

Figure 3: RAO of cylinder.

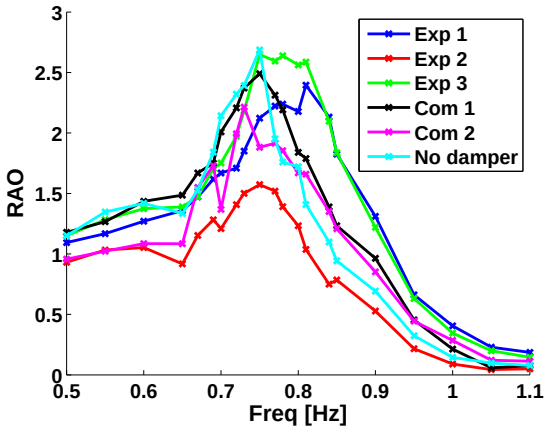

Figure 4: RAO of internal mass.

The results for the RAO of the cylinder are shown in Fig. 3 where each cross on the graph indicates a separate experiment. It can be seen that there is generally a greater response of the cylinder, when a damper is present to when there is no damper. This is seen for all dampers above 0.80 Hz and for two of the dampers below this frequency. There is not a simple pattern to

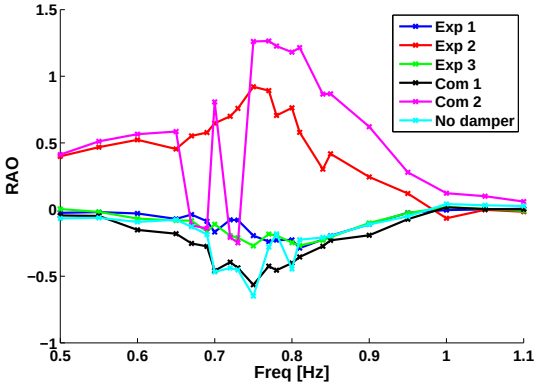

Figure 5: RAO of relative position.

how the different damping constants result in the different response to the waves. The compression damper with the higher damping results in a much greater cylinder response than the other dampers. The shape and height of the RAO of the three expansion dampers varies with the increase/decrease in damping. The non-simple nature of the response suggests that the link between the RAO of the cylinder and the damping factor is not linear.

Fig. 4 shows the RAO of the internal mass. It can be seen that for frequencies up to 0.75 Hz having no damper tends to have the highest motion, with higher frequencies having a more varied response. The results for both compression dampers are much more closely approximated to the case with no damper compared to the expansion damper. The higher damping constant compression damper does not get such a high response around the resonant peak for the internal mass but outside this frequency range it follows the device without a damper closer. The expansion dampers response varies a lot within the set and compared to the no damping case. The lower expansion damper of 14 Ns/m (Exp 1) has a 0.4 lower response ratio than the higher damped expansion damper of 433 Ns/m (Exp 3), while the lower value expansion damper of 31 Ns/m (Exp 2) has a 1.1 ratio lower response than both dampers although its damping constant is relatively close to the lower case. This implies that the response of the internal mass in this device and setup is quite sensitive to the actual damping constant and again indicates a nonlinear relationship between the response and the damping constant.

The relative position between the internal mass and cylinder is highly relevant to the potential amount of energy that can be extracted from the system. The ratio of this relative position to the wave height can be viewed in Fig. 5. It is hard to interpret any general trends from the damping values but it does show that for some cases of damping for both expansion and compression dampers a much higher relative motion occurs than with no dampers present. The apparently anomalous behavior of the cylinder and the internal mass for the damper "Com 2" is compounded here and shows a wild variation between 0.65 Hz and 0.75 Hz.

3.3 Time series response in irregular seas

The PM spectrum has been used with a variable peak frequency to test the response of the cylinders with different dampers. The University of Edinburgh curved tank [4] is a deterministic tank with a 64 s repeat period for all sea states. The waves are run for 16 s and then the data is recorded for a further 128 s, at 32 Hz. An example in the time domain for a section of the tests where the pattern of results is present can be seen in Fig. 7 for the response of the cylinder, Fig. 8 for the response of the internal mass and in Fig. 9 for the relative motion between the internal mass and cylinder.

It can be seen in Fig. 7 and Fig. 8 that although the results are generally similar that the heights and to a limited amount the phase of the cylinder varies. The heights relative to the cylinder without damping change, for some dampers on a wave to wave bases.

Fig. 9 shows the relative position, most notably Exp 2 is 180 degrees out of phase with the other cylinders. The higher damping expansion damper (Exp 3), for the larger responses tends to have a much smaller negative component in comparison to its positive component, with the negative component going no lower than -5 mm whilst the positive value reaches 15 mm. In contrast, the higher damped compression damper (Com 2) has a mainly negative relative position, for the larger responses, where it has a maximum value of 7 mm but a minimum of -20 mm. The other dampers do not tend to follow this trend with approximately equal positive and negative relative positions.

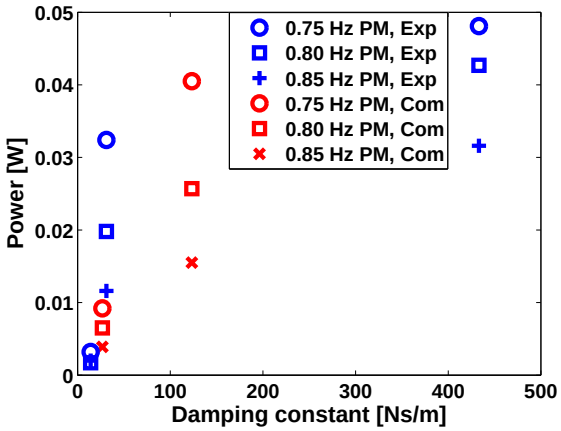

Figure 6: The time averaged power extracted for the dampers in different PM spectrums.

3.4 Power extraction

The power that is extracted has been calculated from the product of the square of the relative velocity and the damping constant when the velocity was in the direction that the damper was exerting a force, and zero for the opposite direction. It is calculated for three different PM spectrums with peak frequencies of 0.75 Hz, 0.80 Hz and 0.85 Hz. The tests were ran for 16 s to allow the system to establish and a further 128 s of data measurements. The time averaged power over this time frame has been calculated and presented in Fig. 6.

This figure shows the increase in the extracted power for stronger dampers, of both expansion and compression. These values would result in a full scale power of between 20 kW for Exp 3 in a 0.75 Hz peak frequency PM spectrum and 810 W for Exp 1 in the same sea. It should be noted that the bearing friction on the internal mass would not follow scaling laws, and hence it could be expected that these values would be higher for a full scale device.

Due to the limited number of samples, there is not a clear shape emerging and from the data available it appears that the optimal damping for a mono-directional damper would be greater than has currently been tried. However, as the damping increases further, the power would eventually decrease since no relative motion would be present.

3.5 General discussion

From studying Fig. 3 and Fig. 7 the cylinder is shown to consistently to have a higher response for most of the different dampers for the majority of the frequencies of interest than if it had no damper. This is not the intuitive result since by taking out energy from the system by having the dampers present, a lower response may have been expected. Although there is not clear evidence to confirm this, a possible explanation would be that the higher response from having the dampers present is due to some form of uncontrolled latching [9, 10] or partial latching of the internal mass occurring in the model.

This implies that for a self-contained inertial model where a control strategy is not to be implemented, a mono-directional damper may have a much higher power extraction than just half of that produced by a bi-directional damper. This will be further investigated in future work.

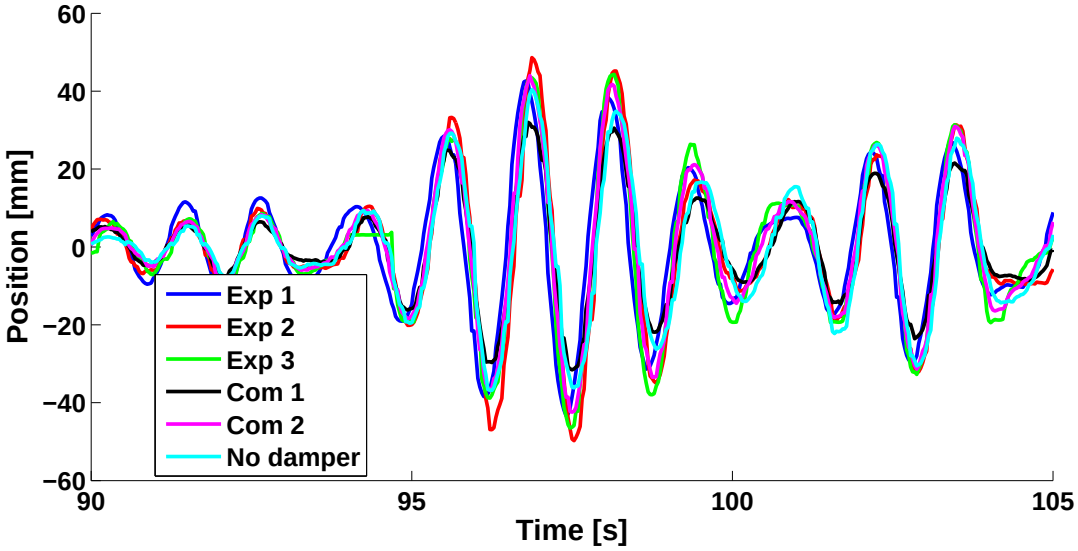

Figure 7: Position of cylinder for PM spectrum.

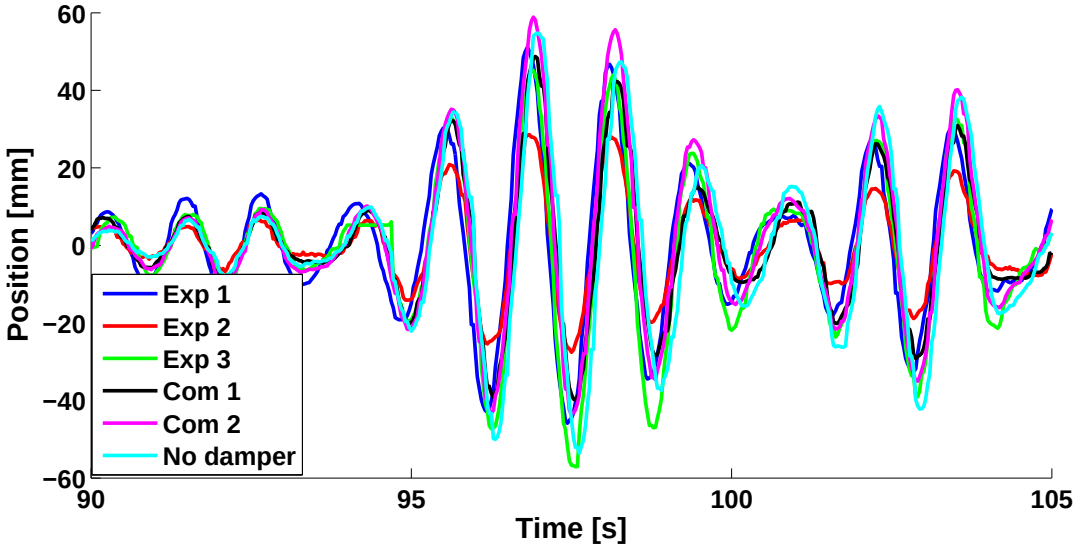

Figure 8: Position of internal mass for PM spectrum.

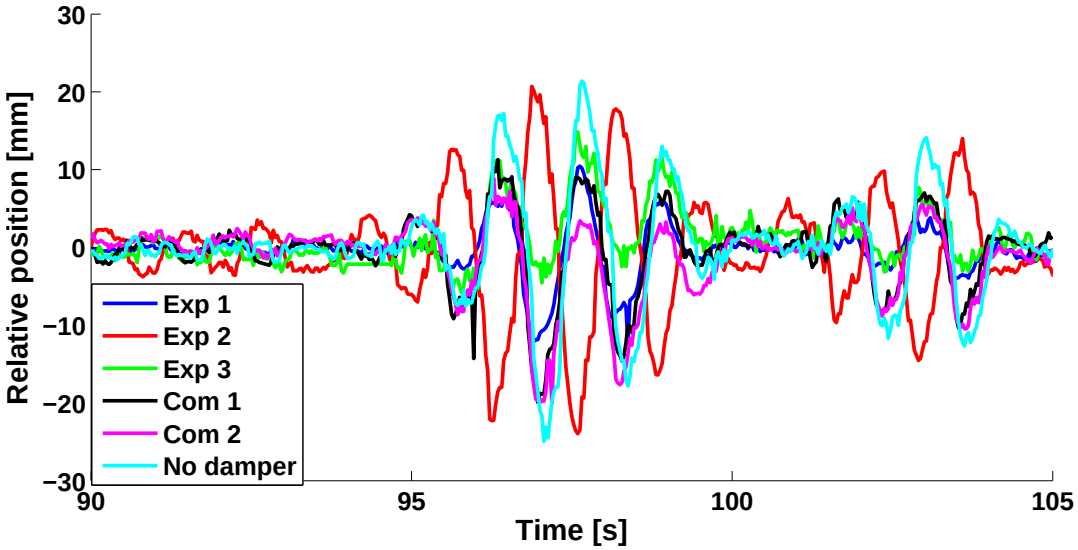

Figure 9: Relative position of internal mass to cylinder for PM spectrum.

4 Concluding comments

The results for regular and irregular waves for a mono-directional damper in an experimental setup comprised of a cylinder and an internal mass within the cylinder that both move in heave and relative to each other have been presented. The RAO for the internal mass, cylinder and the relative position between them have been given, showing that systems with the mono-directional damper has a higher response of the cylinder and often a higher relative motion.

A time series example of the results for a PM spectrum were presented, showing the varying heights across the different dampers and how the relative heights tended to change with time. The relative position between the internal mass and the cylinder showed that one the the expansion dampers was 180 degrees out of phase with all the other relative motions.

The power extracted from the recorded positions of the bodies and the dampers was presented, for 3 different PM sea states. This showed a general increase in the power extracted for increased damping and implied that further experimental testing was needed in order to find the optimal mono-directional damper for maximum power extraction.

The reason for the increase in amplitude of the motion of the cylinder when damping is present to when not present was discussed and it was postulated that this could be because of a "latching" effect, although it was noted that there is currently not sufficient evidence to confirm this.

Acknowledgments

The author acknowledges the support of the EPSRC research council for DTA funding (EP/P502454/1).

References

[1] T. Stallard, P. K. Stansby, and A. J. Williamson. An experimental study of closely spaced point absorber arrays. *Proceedings of the Eighteenth (2008) International Offshore and Polar Engineering Conference, Vol 1*, pages 417–424 699, 2008.

[2] Wave Power Langlee. http://langlee.no, Accessed April 2009.

[3] M. J. French. Tadpole: A design problem the mechanics of the use of sea wave energy. *Proceedings of the Institution of Mechanical Engineers Part a-Journal of Power and Energy*, 210(4):273–277, 1996.

[4] M. Rea J. Taylor and D. Rogers. The edinburgh curved tank. In *5th European Wave Energy Conference*, Cork, Ireland, 2003.

[5] H. Bailey and I.G. Bryden. Experimental testing on the effect of nonlinear power take off on the motions of wave energy converters. In *2nd International Conference on Ocean Energy*, Brest, France, 2008 - In press.

[6] J. Falnes. Wave-energy conversion through relative motion between two single-mode oscillating bodies. *Journal of Offshore Mechanics and Arctic Engineering-Transactions of the Asme*, 121(1):32–38, 1999.

[7] Qualisys motion capture. http://www.qualisys.com/, Accessed April 2009.

[8] Airpot. http://www.airpot.com/html/dashpot.html, Accessed April 2009.

[9] A. F. D. O. Falcao. Phase control through load control of oscillating-body wave energy converters with hydraulic pto system. *Ocean Engineering*, 35(3-4):358–366, 2008.

[10] U. A. Korde. Latching control of deep water wave energy devices using an active reference. *Ocean Engineering*, 29(11):1343–1355, 2002.

Experimental testing on the effect of nonlinear Power Take Off on the motions of Wave Energy Converters

H. Bailey,
University of Edinburgh,
School of Engineering & Electronics,
The King's Buildings, Mayfield Rd,
Edinburgh, EH9 3JL, UK
Helen.Bailey@ed.ac.uk

I.G. Bryden,
University of Edinburgh,
School of Engineering & Electronics
The King's Buildings, Mayfield Rd,
Edinburgh, EH9 3JL, UK
Ian.Bryden@ed.ac.uk

Abstract

This paper presents the effects of a nonlinear Power Take Off (PTO) on the response of a simple Wave Energy Converter (WEC) to the waves. The current WEC is a self – contained, slack moored point absorber, with the PTO operating from an inertial mass within the device.

A linear numerical model is used to choose the experimental model parameters - such as the internal mass, and spring constants – for both maximising the relative motion between the inertial mass and the body and maximising power extraction. A 1:40 scale experimental model has been built and tested in Edinburgh University's curved tank. The motions of the model for regular sinusoidal monochromatic waves have been observed and for different setups of the PTO. It was found that the amplitude of the device response varied but the frequency and shape of the response profile remained constant. A double frequency sea was also used to see if nonlinear effects were present in the overall motion and they were indeed found to be present in some of the setups. This shows that having some nonlinearities present in PTO has an effect on the overall motion.

1. INTRODUCTION

The PTO system in a WEC is required to transform the relative motion that occurs in most WECs into electricity. This power extraction due to the relative motion that occurs in the WEC influences the response of the WEC to waves.

There are a large number of different PTOs that are being researched, developed or used. These tend to fall into three categories – hydraulic, pneumatic or electromagnetic. Hydraulic PTOs [1] tend to use reservoirs of high and low pressure oil (or potentially sea water) and hydraulic machines to extract the energy. Pneumatic PTOs split into two main types, where one type uses a turbine, often a Wells turbine for fixed or floating OWCs. The other type takes advantage of the low head of water produced in an overtopping device. Electromagnetic or direct drive generators [2] have the motion of the device connected to a rotor, which moves relative to a stator without the aid of a gearbox to produce electricity. The relative motion in this case can be linear or rotational.

The PTO can be nonlinear due to several reasons:

- The flow rate of the oil in a hydraulic machine is directly proportional to the square of the pressure difference; hence, the force is proportional to the velocity squared.
- Some PTOs only operate during certain parts of the wave cycle, e.g. in only one direction.
- The PTO may have end-stop considerations to avoid damage in high-energy sea states.
- The PTO may be part of the control strategy, in order to extract more energy from the waves.

A reaction force is required by the PTO for it to act against in order to extract energy. For a point absorber (where the dimensions of the body are much less than the wavelength), this reaction force needs to be derived from either being rigidly fixed to a stationary platform such as the ocean floor, or from an inertial mass acting as either a separate but connected body to the device or from within the device, such as considered by French [3], Falnes [4], SEAREV [5], Beatty [6], Finervia Renewable's Aquabouy [7], Wavebob [8] among others. In this work, we consider the latter case, where the internal mass is within the body.

This work investigates a generic device, not directly related to a single technology development but a model relevant to a number of devices being developed. It is self-contained for ease of deployment and the interior of the device is dry which will aid reliability and lifespan. The device is slack moored hence the moorings will have limited affect on the motion and are not considered here. The device is operating offshore where a fixed mooring setup would be very expensive.

2. NUMERICAL MODEL

2.1. Linear Model

A linear model has been used to decide upon the parameters used to design the experimental model. A

linear model is considered valid for choosing the parameters due to the linear motion at and at small deflections from the still water level of the internal mass. When larger motions of the internal mass are present, the mass will contact the additional dampers and / or springs, which will lead to the nonlinear forces. The advantage of a linear model over a more accurate nonlinear model is the reduced computational time.

The model is based upon a mass – spring – damper system. A schematic view of this model can be seen in Figure 1, where an axi-symmetric cylinder houses the internal mass and between this and the cylinder a spring and damper act in parallel.

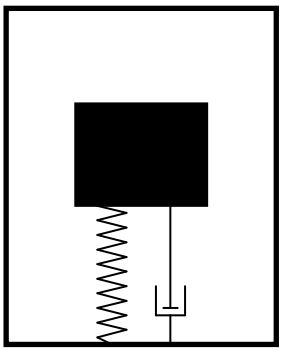

Figure 1: A schematic view

The linear model is developed in the frequency domain, and is strongly based upon the two-body problem by Falnes [4] where the bodies considered are separate bodies linked together, although Falnes refers to the case where the second body is within the first. These equations below are very similar to those in Falnes [4].

The equations of motion for the external cylinder and internal mass respectively are:

$$(m_e + A)\, i\omega U_e + BU_e + CU_e / i\omega + Z_L(U_e - U_i) = F_e \tag{1.1}$$

$$m_i i\omega U_i - Z_L(U_e - U_i) = 0 \tag{1.2}$$

and

$$Z_L = c + k / i\omega$$

Where:

m is the mass of the bodies

A is the added mass of the external body

i is $\sqrt{-1}$

ω is the incident wave angular frequency

U is the absolute velocities

B is the added damping of the body

C is the buoyancy of the body

F_e is the excitation force – the force required to keep the body stationary while experiencing incident waves

c is the damping constant

k is the spring constant

The subscripts *i* and *e* refer to the internal and external bodies respectively.

By introducing mechanical impedances, the abbreviated form of the equations of motion is:

$$\begin{pmatrix} Z_e + Z_L & -Z_L \\ -Z_L & Z_i + Z_L \end{pmatrix} \begin{pmatrix} U_e \\ U_i \end{pmatrix} = \begin{pmatrix} F_e \\ 0 \end{pmatrix} \tag{1.4}$$

Where the impedances are:

$$Z_e = B + i\omega(m_e + A - C/\omega^2) \tag{1.5}$$

$$Z_i = i\omega m_i \tag{1.6}$$

Therefore, the solution to this equation is:

$$\begin{pmatrix} U_e \\ U_i \end{pmatrix} = \frac{1}{D_{et}} \begin{pmatrix} Z_i + Z_L & Z_L \\ Z_L & Z_e + Z_L \end{pmatrix} \begin{pmatrix} F_e \\ 0 \end{pmatrix} \tag{1.5}$$

With the determinant being:

$$D_{et} = Z_e Z_i + Z_L Z_e + Z_L Z_i \tag{1.6}$$

Therefore, the relative motion is:

$$U_r = U_e - U_i = \frac{Z_i F_e}{Z_e Z_i + Z_L(Z_e + Z_i)} \tag{1.7}$$

The (time-averaged) power produced from the relative motion between the internal mass and external shell is:

$$P = \frac{1}{2}\mathrm{Re}\{Z_L\, U_r\, U_r^{*}\} = \frac{1}{2}\mathrm{Re}\{Z_L\}\left|U_r\right|^2 \tag{1.8}$$

The maximum power occurs when the force in the connection between the internal mass and external shell and the relative velocity are in phase.

The force within the PTO, $F_L = -Z_L\, U_r$ can be calculated from equation (1.4).

$$F_L = -\frac{1}{2}(F_e - Z_e\, U_e + Z_i\, U_i) \tag{1.9}$$

When the damping in the PTO is infinite, the force within the PTO is:

$$F_0 = \frac{F_e Z_i}{Z_e + Z_i} \tag{1.10}$$

So the relative velocity can also be written as:

$$U_r = \frac{F_0 (Z_e + Z_i)}{Z_e Z_i + Z_L (Z_e + Z_i)} \tag{1.11}$$

To ensure the maximum power, the relative velocity and force would need to be in phase, so that means:

$$Z_L = \left(\frac{Z_e Z_i}{Z_e + Z_i} \right)^* \tag{1.12}$$

Where the $(*)$ denotes a complex conjugate.

The internal mass, spring constant and damping constant can be chosen to ensure that the power extracted is maximal, for a set size of model. However, since we are interested in both maximising the power extracted **and** the relative motion. In order to get an indication of the ideal values and the sensitivity of the power and relative motion to these values, we have been looking at the actual power extracted rather than the maximum values.

For this linear model, the boundary element method commercial software WAMIT was used to obtain the added mass, added damping and excitation force for different frequencies.

2.3. Choice of constants

Two criteria are to be maximised, the power extracted from the model and the relative internal motion. Having large internal relative motion results in having control over the amount of nonlinearity present.

2.2.1. Influence of Mass

The effect of the size of the internal mass on the relative motion of the internal mass to the external body and the power dissipated in the PTO can be seen in Figure 2. Here the spring constant was 200 N/m, the damping constant was 50 Ns/m, the incident wave frequency was 4 rad/s, and the remaining mass to enable a draft of 0.25 m was rigidly attached to the external body.

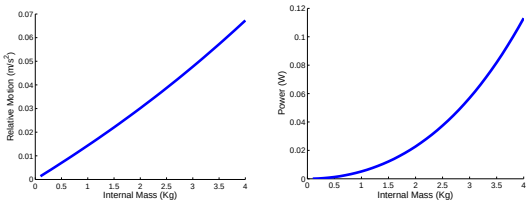

Figure 2: The influence of mass on
a) the relative motion, b) the power

Figure 2 shows that to both maximise the power extracted in the PTO and the relative motion the internal mass should be large.

2.2.2. Influence of Spring Constant

Figure 3 displays what happened when the spring constant was varied and the power extracted and the relative motion were observed. The black line is for an internal mass of 2 kg and a damping constant of 50 Ns/m. The red lines show the effect of varying the damping, the lower red line had the reduced damping of 20 Ns/m and the upper red line at 100 Ns/m. The blue lines show the influence of the mass, with the upper blue line having an internal mass of 3 kg and the lower blue line an internal mass of 1 kg. The incident wave frequency was 4 rad/s.

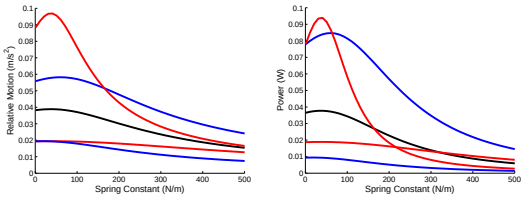

Figure 3: Influence of Spring Constant on the
a) relative motion, b) power

Both graphs show maxima of power and relative motion at a spring constant of between 40 N/m and 80 N/m. The exact values of the power and relative motion at the maxima varies considerably and the gradient of the reduction from the maxima varies but the spring constant that corresponds with the maxima values is relatively stable. These graphs show that the ideal value of the spring constant would be approximately 40 – 80 N/m depending on the other parameters chosen.

2.2.3. Influence of Damping

The amount of damping in the PTO will obviously affect both the amount of power produced and the relative motion. This is displayed in Figure 4, where the black line corresponds to a spring constant of 200 N/m and an internal mass of 2 kg for. The blue lines shows variation of the mass, with the upper blue line having an internal mass of 3 kg and the lower an internal mass of 1 kg. The red lines show the effect of the spring constant, with the upper red line having a spring constant of 150 N/m and the lower red line of 250 N/m. The incident wave frequency is 4 rad/s.

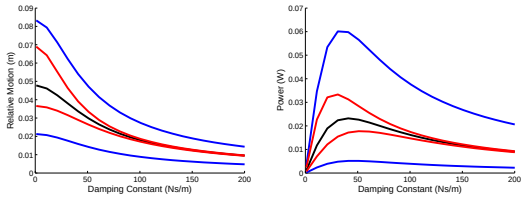

Figure 4: The influence of damping on
a) the relative motion, b) the power

As expected, the power extracted is zero when the damping is zero, and increases as the damping increases from zero until reaching a maxima and decreasing towards zero for higher values of damping. For maximum power extraction, the ideal damping constant is approximately 30 – 60 Ns/m. For maximum relative motion, the ideal damping would be zero – so a conflict is seen between these two criteria.

2.2.4. Practical considerations

To conclude, from looking at the influences of the parameters the ideal system for maximum power extraction and maximum relative position would be:

1. Largest mass possible
2. Spring constant of 40 – 80 N/m
3. Damping of 0 for maximum relative position or 30 – 60 Ns/m for maximum power extraction

However, to have a large mass and a small spring constant would require a very long, very weak spring. For example, a 50 N/m spring compressed by a 5 kg mass would reduce in length by 1 m, and further spring compression would occur when this mass is in motion with greater forces applied. The solid height of the spring and not wanting to operate the spring near to the fully compressed state, due to unknown nonlinearities needs to be considered. The above case would in reality call for a spring with a free length of at least 2 m.

The additional considerations related to the spring are: the wire diameter becoming excessively thin and liable to damage; the space restraints within the cylinder; the solid height of the spring; and the ability of the spring to be manufactured.

As a result of this a 200 N/m spring constant was chosen with a 2 kg mass. The spring has a wire diameter of 1.64 mm, is made from stainless steel and has a free length of 300 mm.

The 2 kg internal mass was also chosen due to previous experimental setups where a 4.4 kg mass and an 8.9 kg mass were used. Both of these masses were observed to have only very small relative motion with the larger mass having the least motion. However, the geometry of these masses was short and wide, which resulted in a short bush bearing in contact with the rod. Hence, it was likely that the masses experienced a higher amount of friction from the bearing, which resulted in the reduced relative motion observed. The 2 kg mass is designed to have a longer bearing with a PTFE sleeve acting as the bearing.

A damping system was chosen which has adjustable damping constants in order to achieve a large relative motion and power extraction. The damping suggested from the linear model would be larger than actually required due to power being dissipated in the dynamic and static friction between the internal mass and the rod as well as between the rod and the fixed bearings, which is especially problematic due to the scaled size of the model.

3. EXPERIMENTAL

The experimental model has undergone initial tests in Edinburgh University's curved wave tank, see Figure 5. It is a 1:40 scale model that is based upon the numerical model and restrained to allow only heave motion for both the internal mass and the external cylinder.

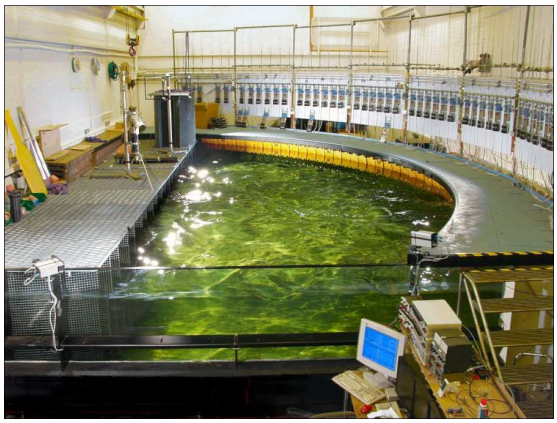

Figure 5: Curved tank at the University of Edinburgh

3.1. Experimental Setup

The model consists of a 16 mm diameter ground stainless steel rod. Rigidly attached to the central portion of the rod is a plastic cylinder, within which the internal mass resides also upon the rod. The main spring is also mounted on the central rod, between the internal mass and the external cylinder. The internal mass can be rigidly attached to a dashpot pneumatic damper. Two additional dampers are located above and below the mass – a small distance from the still water level of the mass. Floating bases within the cylinder are attached to these dampers. Two additional springs are (in some setups) located above and below the mass in a similar manor to the dampers, upon the floating bases. This setup causes the movement of the mass and its power extraction to be nonlinear.

The rod is held in place by two rod-end stainless steel bearings with PTFE inner sleeves. Hence, the cylinder and the internal mass can only move in heave. The advantages of using bearings that can freely rotate are that any misalignments can be adjusted for and do not result in excessive bearing friction.

The dampers used are Airpot Dashpot for the main damping and Airpot snubbers for the extremities damping [9]. These have a variable damping constant of (according to the company literature) 0 – 88 Ns/m for the main damper whilst the dampers at the extremities can dissipate energy at a rate of 0 – 41 N/m.

The position of the external cylinder is measured using two Qualisys [10] motion capture cameras via a reflective coated ball attached to the central rod, which enable the position to be known in three dimensions. The data is recorded at 64 Hz.

The experimental model varies from the numerical model for a variety of reasons besides the nonlinear PTO:

- The bearings both between the model and the attachment rig and between the internal mass and the rod will have some amount of static and dynamic friction.
- The model will also try to move in pitch. With the resonance for pitch near the resonant frequency for heave which will result in additional friction on the external bearings. This can be seen in Figure 6, which shows the pitch and heave response of the cylinder to waves.
- A linear irrotational sea has been assumed in the WAMIT modelling. Hence any turbulent effects or large motions will not be accounted for.

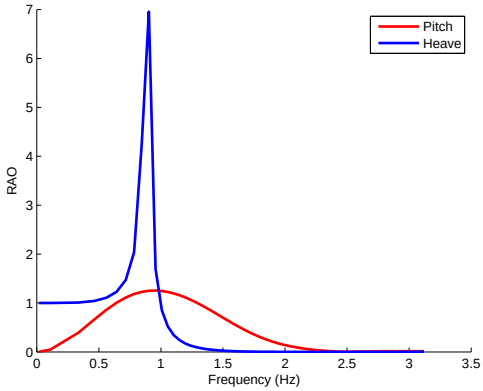

Figure 6: The heave and pitch response to waves

Table 1: Model dimensions

Model	Diameter	230 mm
	Height	500 mm
	Draft	300 mm
	Min weight	5.9 kg
	Additional mass	4.4 kg
Wave tank	Water depth	1.2 m
Internal mass	Radius	30 mm
	Height	101.5 mm
	Weight	2 kg
Spring	Spring constant	200 N/m
	Free length	300 mm

The dimensions of the model are shown in Table 1 and the experimental setup is shown in Figure 7. The cylinder is shown out of the water and the internal mass can be seen between the internal bases that make up the internal support structure. In Figure 8, the rig that holds the cylinder in place and only allows it to move in heave can be seen. This rig is attached to a thin-legged platform.

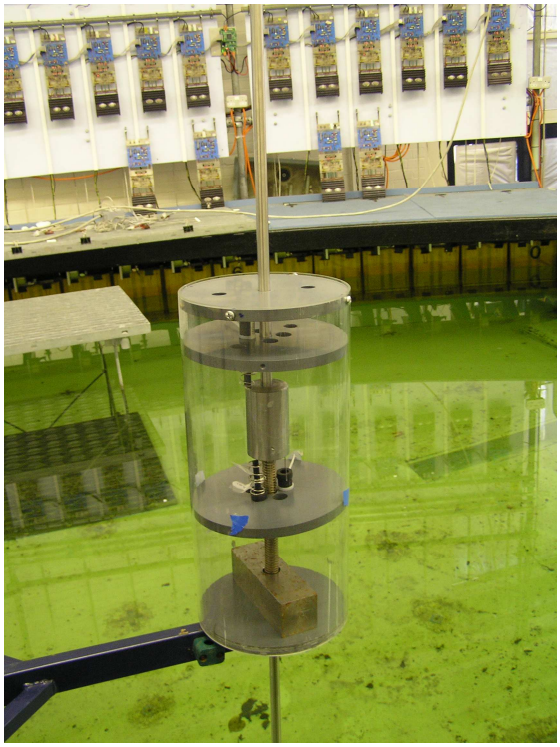

Figure 7: Picture showing the cylinder out of the water

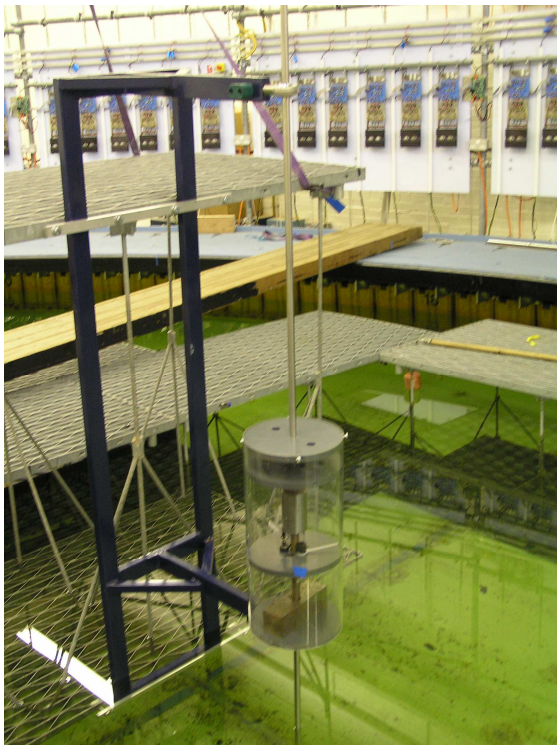

Figure 8: The cylinder and the attached rig both out of the water

3.2. Experimental results

Some different setups of the PTO where introduced to see how these affected the overall motion of the cylinder. They were:

1) The main spring and dampers at the extremities of the motion only.

2) The main spring, a damper throughout motion, and additional dampers at the extremities of the motion.

3) The main spring, with additional springs and dampers at the extremities of motion.

The three different setups for the cylinder were tested at a single frequency sinusoidal sea and with a double frequency sinusoidal sea where the frequencies were close together, in order to discern any nonlinearities.

The single frequency incident wave was at 0.80 Hz, with an approximate wave height of 0.04 m. The double frequencies both had a wave height of 0.01 m and the two frequencies are 0.7031 Hz combined with either 0.7188 Hz, 0.7344 Hz or 0.7500 Hz. These are all frequencies that the Edinburgh curved tank can produce exactly.

The motion of the external cylinder for the different setups and the single frequency incident wave can be seen in Figure 9. All the responses are approximately sinusoidal and of constant amplitude.

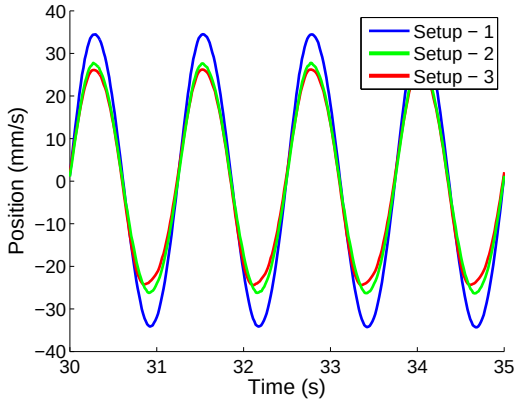

Figure 9: Device motions for the different setups and the single frequency incident wave

It is observed that the maximum amplitude varies for the different setups. There appears to be two possible explanations for the difference in height.

1. It could be that the dampers are removing part of the kinetic energy from the system, which results in less overall energy and a reduced height. Since currently, it is not possible to record the exact position of the internal mass it is hard to judge how much effect the main damper (when present) and the extremities dampers are having upon the internal mass.

2. The motion of the internal mass within the cylinder could effect the resonant response of the system – and since these results occur near resonance this could cause an effect.

The frequency content of the double frequency response can be observed in Figure 10.

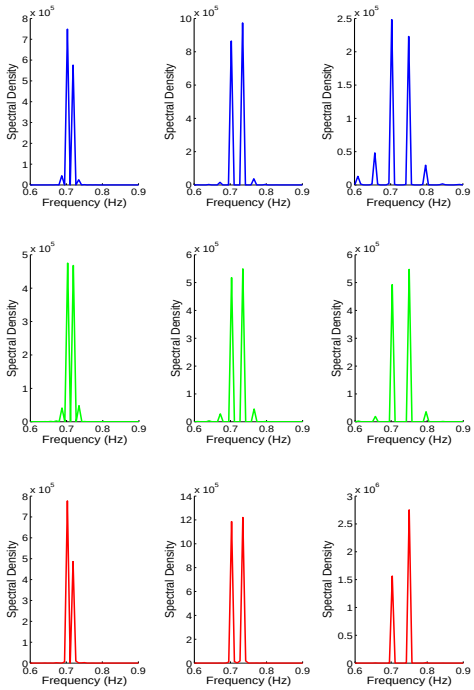

Figure 10: The frequency response to double frequencies. For (from top to bottom) setup 1,2 & 3, with (from left to right) 0.70 Hz with 0.71 Hz, 0.73 Hz & 0.75 Hz.

For setups 1 and 2, additional sub and super harmonic frequencies in addition to the two input frequencies are present. These imply that there are nonlinear effects influencing the system (these are not seen for a purely linear PTO with this model). This shows that by having a nonlinear PTO within the system it affects the overall system motion, which results in nonlinear effects for the entire system.

Setup 3 did not appear to have these indictors of nonlinear effects by the additional frequencies. However, there were some interesting effects with the amplitude of setup 3, as the amplitudes of the motion do not match the pattern of the amplitudes of the waves, as the other setups did. Examples of this are particularly notable for 0.70 Hz with 0.71 Hz and 0.73 Hz, as seen in Figure 11. It is currently not understood why this is occurring, it could be connected to the different amplitudes of the different frequency components, seen in Figure 10. However, the cylinder was spinning about its vertical axis in response to the waves – which did not occur for the other setups. This may also (partially) explain the curious outcome. It also meant that obtaining the data was difficult due to the reflective ball being out of line of sight to one of the cameras – so further clarification of these results have not been obtained.

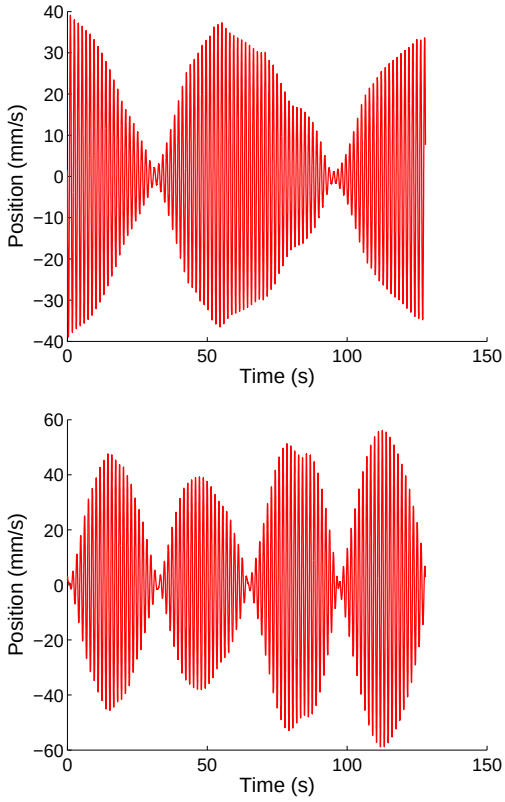

Figure 11: The response of setup 3 for the double frequency incident wave, with 0.7 Hz and 0.71 Hz (upper) and 0.73 Hz (lower)

3.3 Further Work

There is a large scope for further experiments to be performed on this model to fully investigate the influence of the nonlinear PTO:

- Varying the spring and damper combinations in the PTO.
- Increasing the internal mass, and with the appropriate spring seeing if the power extracted and relative motion can be increased.
- The position of the internal mass can be monitored.
- Finding the exact damping constants of the dampers used in the experiments would enable an approximately power extraction to be calculated.
- Since additional friction is experienced in the bearings from the cylinder attempting to move in pitch, separation of the heave and pitch resonant responses would be advantageous to reduce this friction.
- More investigations into the unexpected pattern of amplitudes as seen in setup 3.

4. CONCLUSIONS

The parameters for an experimental model of a point absorber limited to move in heave have been obtained by a linear numerical model. These parameters are used as part of the design process for a 1:40 scale model which has been tested in Edinburgh University's curved tank.

The experimental model has been built with the nonlinear PTO comprising a main spring and a combination of springs and dampers which work at the extremities of motion. The first tests on the model to demonstrate its nonlinear characteristics due to the PTO and its motion have been completed and recorded here for three different setups. Double frequency waves have been used to investigate in the frequency domain whether sub or super harmonic frequencies occur – an indication of nonlinearities. Further testing needs to be completed to fully understand this nonlinear system.

5. REFERNCES

[1] Falcao, A.F. de O. (2007) Modelling and control of oscillating-body wave energy converters with hydraulic power take-off and gas accumulator. Ocean Engineering Volume 34, Issues 14-15, October 2007, Pages 2021-2032.

[2] Mueller M.A., Baker N.J., (2005) Direct drive electrical power take-off for offshore marine energy converters. Proceedings of the I MECH E Part A Journal of Power and Energy, Volume 219, Number 3, March 2005 , pp. 223-234(12)

[3] French, M.J., (1996). Tadpole: a design problem in the mechanics of the use of sea wave energy. Proceedings of IMechE Part A, J Power Energy 210, 1996, pp. 273–277.

[4] Falnes, J. (1999). Wave-energy conversion through relative motion between two single-mode oscillating bodies. Journal of Offshore Mechanics and Arctic Engineering (ASME Transactions), Vol.121, pp.32-38, 1999.

[5] Babarit, A., Clement, A.H., (2006). Optimal latching control of a wave energy device in regular and irregular waves, Applied Ocean Research, Volume 28, Issue 2, , April 2006, Pages 77-91.

[6] Beatty, S.J., Buckham, B.J., Wild, P., (2008). Frequency response tuning for a two-body heaving wave energy converter. In Proc. of the International Offshore and Polar Engineering Conference, Vancouver, BC, Canada, July 2008.

[7] Finervia Renewables. http://www.finavera.com/en/wave , accessed Sept 2008

[8] Wavebob. http://www.wavebob.com/ , accessed Sept 2008

[9] Airpot Corporation dampers and snubbers. http://www.airpot.com/ , accessed Sept 2008

[10] Qualisys motion capture systems. http://www.qualisys.com , accessed Sept 2008

Nonlinear Modelling of Power Take Off Systems

Helen Bailey
Institute for Energy Systems
School of Engineering & Electronics
University of Edinburgh
Scotland, EH9 3JL
Email: Helen.Bailey@ed.ac.uk

Ian Bryden
Institute for Energy Systems
School of Engineering & Electronics
University of Edinburgh
Scotland, EH9 3JL
Email: Ian.Bryden@ed.ac.uk

***Abstract*—The motion of a simple inertial Wave Energy Converter (WEC) is studied to find the relative motion between an internal mass and an external body. The Power Take Off (PTO) system is deemed to connect the internal mass to the external body, modelled as a spring and damper in parallel. This PTO system is assumed to have both linear and nonlinear components, since this will result in a more accurate model. The nonlinearity of this model is a different approach to most other similar models. The known motion of the device allows an optimisation on the values of the spring and damper constants to be performed to maximise the power obtained from the device, for known wave and device properties.**

I. Nomenclature

k	=	linear spring constant (N/m)
j	=	nonlinear spring constant (N/m^2)
c	=	linear damping constant (kg/s)
d	=	nonlinear damping constant (kg/m)
x_i	=	displacement of internal mass (m)
ω	=	Period of oscillation (1/s)
t	=	time (s)
m	=	mass of internal mass (kg)
h	=	max wave height (m)
e	=	the limited relative displacement (m) between the internal mass and external shell

II. Introduction

Wave Energy Converters (WECs) need to be efficient in converting the power of the marine waves into electricity, in order to be economically viable. The overall efficiency of the device can be increased if the Power Take Off (PTO) system is optimised. To be able to optimise the PTO, knowledge about its movement and its response to waves is required.

The WEC being studied is a generic device. It is a slack moored, point absorber, that has an arbitrary shape and is seen to float on the surface of a sinusoidal wave. The motion of the external body of the device is purely sinusoidal, and the device is currently limited to move in heave.

The device is comprised of an internal mass supported inside an external shell. The mass of the internal mass is a significant proportion of the overall mass of the device. The internal mass is supported by the PTO system, that is modelled as a spring and damper in parallel. The spring and damper will initially be modelled linearly but the model will be developed to allow for significant nonlinearities.

The device is modelled as nonlinear, since it is assumed to be a more accurate method, due to the spring and damper having significant nonlinear components for large amplitude oscillations. This will enable a more precise model to find the motion and response of the internal mass, however it does increase the complexity of the model.
March 30, 2007

III. Model

A. Analytical Linear Model

A linear model was produced using purely analytical methods. This was achieved by calculating all the forces on the internal mass, shown in equation (1). The harmonic balance method was then used to obtain the equations of motion (2), for the internal mass relative to the external shell. The external input from the waves was modeled as a sinusoidal input on the external shell, with maximum height equal to h.

$$m\ddot{x}_i + c(\dot{x}_i - h\omega\cos(\omega t)) + k(x_i - h\sin(\omega t)) = 0 \quad (1)$$

$$\begin{aligned} x_i(t) &= A\cos(\omega t) + B\sin(\omega t) - h\sin(\omega t) \\ \dot{x}_i(t) &= -A\omega\sin(\omega t) + B\omega\cos(\omega t) - h\omega\cos(\omega t) \\ \ddot{x}_i(t) &= -A\omega^2\cos(\omega t) - B\omega^2\sin(\omega t) + h\omega^2\sin(\omega t) \end{aligned} \quad (2)$$

Where:

$$A = h - \frac{h\omega^2 m(m\omega^2 - c)}{(m\omega^2 - c)^2 + k^2\omega^2}$$

$$B = \frac{-h\omega^3 mk}{(m\omega^2 - c)^2 + k^2\omega^2}$$

The equations of motion are used to find the position, velocity and acceleration of the internal mass at any point in time.

The motivation for producing the analytical model was to compare this model to the purely linear parts of the numerical model. The analytical model should help to confirm results of the linear numerical model, so more

confidence can be placed in the nonlinear numerical model.

B. Linear Runge Kutta Model

A fourth order Runge Kutta analysis [1] was completed, on the same force equation (1) that was used in the analytical solution. This enabled the position, velocity and acceleration of the internal mass absolutely and relative to the external shell to be determined.

The initial conditions chosen were the values of the position and velocity when time was equal to zero, in the analytical model.

The time step size chosen is small enough so that reducing the step size by an order of magnitude, does not result in any noticeable change in the results, while it must be large enough not to lead to significantly increased computational time. The chosen time step used was 0.1 s.

C. Nonlinear Runge Kutta

The linear Runge Kutta analysis can be developed to include nonlinear terms. The force equation (1) is extended for quadratic terms, see equation (3) and cubic terms, see equation (4).

$$m\ddot{x}_i + c\dot{x}_i + d\dot{x}_i|\dot{x}_i| + k\dot{x}_i + jx_i|x_i| = 0 \tag{3}$$

$$m\ddot{x}_i + c\dot{x}_i + d\dot{x}_i^3 + k\dot{x}_i + jx_i^3 = 0 \tag{4}$$

The position, velocity and acceleration could then be determined, with considerations of the natural nonlinearities of the PTO.

IV. Optimising Methods

A. Linear Analytical Model

Obtaining the maximum amount of power from the device is desirable. To achieve this the values of the spring and damper need to be adjusted for known wave properties.

For the analytical model these values are calculated from setting a maximum value of the displacement of the internal mass relative to the external shell. Differentiating the equation of the relative position, with respect to time, and setting it equal to zero, finds the time when the maximum displacement occurs. This time can then be substituted back in to the original equation, and the results are shown in equation (5).

$$e^2 = A^2 + (B - h)^2 \tag{5}$$

The instantaneous power of the device is the product of the damping constant and the velocity squared [2]. The total power over one wave cycle can be calculated from integrating the instantaneous power with respect to time, over the cycle, and dividing this by the time of the cycle. The values of the spring and damper constants that produce the maximum amount of power can then be found, by differentiating this with respect to the spring constant and setting this equation to zero.

B. Runge Kutta Model

The numerical solution is optimised in the same way as the analytical model by limiting the maximum relative motion of the external shell and the internal mass and finding the maximum power over a wave cycle.

The power that is obtainable from the linear term has been calculated from the power being the product of the linear damping constant and the velocity squared, as discussed before. The amount of power obtained from the nonlinear component of the damper also needs to be calculated. A dimensional analysis is performed on the nonlinear term and it is found that the power of the nonlinear term is equal to the product of nonlinear damping constant and the velocity cubed for the quadratic case, and the product of the velocity to the power of four, and the nonlinear damping constant, for the cubic case.

The algorithm which performs this optimisation uses the following method:

1) Suggests a value for the spring constant, starting from an initial given value

2) Suggests a value of damping constant, initially based on the linear analytical value.

3) An optimisation is performed by changing the value of the damping constant, so that the maximum relative displacement is equal to a predetermined value.

4) Using this spring and damper combination, finds the amount of power within the system is found, by adding up all the instantaneous powers over the second cycle of the device.

5) An optimisation algorithm is used to find the maximum power by changing the spring constant and repeating steps 2 to 4, to find the associated damping constant and the new power.

V. Results

A. Linear Models

The values of the constants were chosen based on the device being spherical, with a radius of 2 meters, with ten percent of the sphere submerged. Therefore the internal mass can be calculated to be 3000 kg. The maximum wave height, of

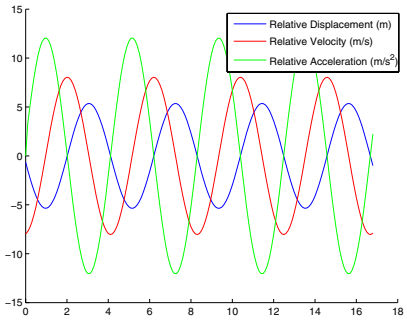

Fig. 1. The motion of the internal mass, with the Spring Constant = 500 (N/m) & the Damping Constant = 500 (kg/s)

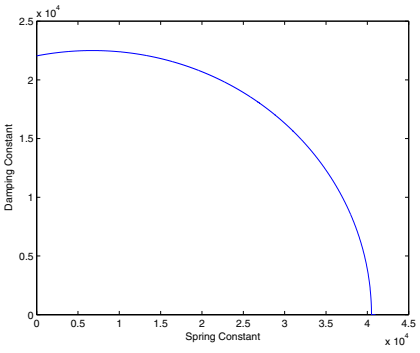

Fig. 2. The relationship between the Spring and Damping Constants

regular seas was assumed to be 5 meters, with a wave period of about 4 seconds. The maximum relative motion between the internal mass and the external shell is chosen to be 1 meter.

Both the analytical and the Runge Kutta analysis produce results that show the position, velocity and acceleration of the internal mass relative to the external shell. The results for the purely linear terms are practically identical, with negligible difference between the two values, throughout the cycle. The motion can be seen, in figure 1, with arbitrarily chosen spring and damper constants.

Limiting the maximum relative displacement of the external shell to the internal mass, causes a relationship between the spring and damping constants, as seen in figure 2. It is seen that an increase in the value of one constant leads to a reduction in the other constant. These results were consistent for both the analytical and the numerical Runge Kutta model.

The relationship between the power obtained from the device and the spring constant can be seen in figure 3. The power initially increases with a shallow slope, up approximately 0.7×10^4N/m, after which the power decreases, with the gradient increasing for higher values of the spring constants. This graph shows that the power would be near to its maximum value for any spring constant below

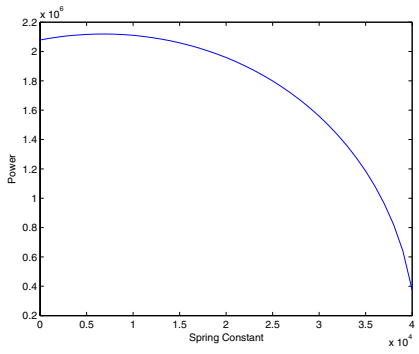

Fig. 3. The relationship between the Spring Constant and the Power Obtainable

TABLE I
OPTIMISED VALUES FOR THE SPRING AND DAMPING CONSTANTS, FOR DIFFERENT MODELS

Model	Spring Constant (N/m)	Damping Constant (kg/s)
Analytical	6750.0	22500
Runge Kutta	6782.4	22500

TABLE II
OPTIMISED VALUES OF THE SPRING AND DAMPING CONSTANTS FOR QUADRATIC NONLINEARITIES

Non-Linearity	Linear Spring (N/m)	Nonlinear Spring (N/m^2)	Linear Damping (kg/s)	Nonlinear Damping (kg/m)
10%	7855	786	20050	12005
100%	6620	6620	10621	10621

1.5×10^4N/m. Increasing the spring constant to values much higher than this leads to a drop in the power obtainable.

The optimised values of the spring and damper constants, for the different models can be seen in table 1.

B. Nonlinear Models

The nonlinear parts of the model are deemed to be a certain proportion of the linear parts, for both the spring and the damper. Using these set proportions the movement of the internal mass relative to the external shell can be predicted, this is shown in figures 4 & 5. The values of the optimised spring and damping constants can be seen in tables 2 & 3, for the quadratic and cubic case respectively.

For large amounts of nonlinearities (much greater than 100%), there can be an initial large jump in the acceleration, and initial noncyclic occurrences for the position and velocity. This is probably due to the initial conditions being inaccurate as they are calculated from the linear analytical solution, so for large nonlinearities, these values would be more inaccurate. Since the initial conditions are very important

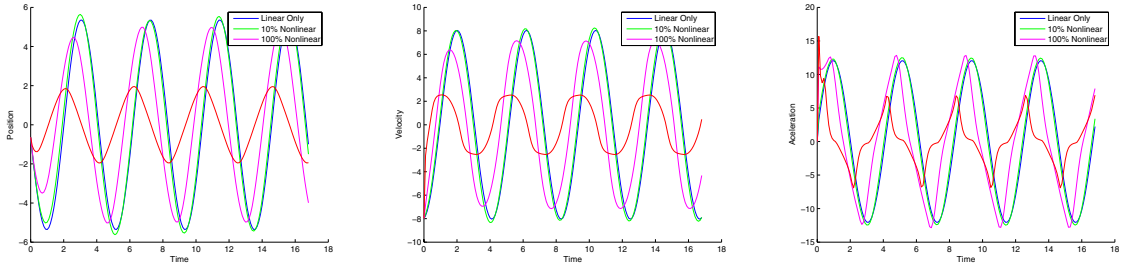

(a) x_i (b) $\dot{x}_i$ (c) $\ddot{x}_i$

Fig. 4. Quadratic Nonlinearities

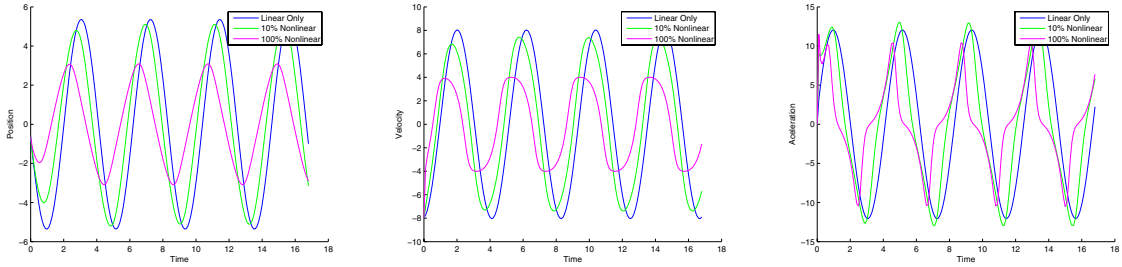

(a) x_i (b) $\dot{x}_i$ (c) $\ddot{x}_i$

Fig. 5. Cubic Nonlinearities

TABLE III
OPTIMISED VALUES OF THE SPRING AND DAMPING CONSTANTS FOR CUBIC NONLINEARITIES

Non-Linearity	Linear Spring (N/m)	Nonlinear Spring (N/m^2)	Linear Damping (kg/s)	Nonlinear Damping (kg/m)
10%	5959	596	19951	1995
100%	7057	7057	9080	9080

in a numerical model, this leads to the start of the model being inaccurate and reduces the certainty that the rest of the model is accurate, for large nonlinearities. However for the majority of the nonlinear models, except the very large (approximately 1000%), after the initial non-cyclic or large jump in the results, the results appear cyclic as expected.

This large jump in acceleration occurs in the cubic model when the proportion of nonlinearity is 1000%. The maximum acceleration that occurs at the jump is 100 m/s. This is the reason that the results for the cubic model (see figure 5), only show nonlinearities up to 100%.

VI. Further Work

Attempts will be made to develop a nonlinear analytical model, ideally fully analytical but potentially with some numerical parts to it. This will be a more accurate and reliable model since it will not rely as much on having the correct initial conditions. The links between the constants and the movement of the device will be simpler to understand.

Experimental testing of PTOs will be done to confirm these results.

VII. Conclusion

A linear analytical and linear numerical Runge Kutta model have been developed that show the position, velocity and acceleration of an internal mass relative to an external shell. These are optimised based on the need for a limited maximum relative displacement and to maximise the power obtained from the device. This is achieved by changing the spring and damper constants.

The Runge Kutta model is extended with quadratic and cubic nonlinear terms, and the new positions, velocities and accelerations studied. Using nonlinear components improves the accuracy of the model. The optimisation algorithm is repeated for this model and finds new values of the spring and damper constants for the maximum power extractable, with set proportions of linear to nonlinear terms.

REFERENCES

[1] Michael D. Greenberg, *Advanced Engineering Mathematics*, 2nd ed. Cambridge, England: Cambridge University Press, 2002.

[2] Johannes Falnes, *Ocean Waves and Oscillating Systems*, 1st ed. New Jersey, USA: Prentice Hall, 1998.